UNIVERSITÉ DE MONTRÉAL

GUIDAGE MAGNÉTIQUE PAR CHAMPS DE DIPÔLES POUR L'ADMINISTRATION CIBLÉE D'AGENTS THÉRAPEUTIQUES

MAXIME LATULIPPE
INSTITUT DE GÉNIE BIOMÉDICAL
ÉCOLE POLYTECHNIQUE DE MONTRÉAL

THÈSE PRÉSENTÉE EN VUE DE L'OBTENTION
DU DIPLÔME DE PHILOSOPHIÆ DOCTOR
(GÉNIE BIOMÉDICAL)
AOÛT 2017

UNIVERSITÉ DE MONTRÉAL

ÉCOLE POLYTECHNIQUE DE MONTRÉAL

Cette thèse intitulée :

GUIDAGE MAGNÉTIQUE PAR CHAMPS DE DIPÔLES POUR L'ADMINISTRATION CIBLÉE D'AGENTS THÉRAPEUTIQUES

présentée par : LATULIPPE Maxime
en vue de l'obtention du diplôme de : Philosophiæ Doctor
a été dûment acceptée par le jury d'examen constitué de :
M. KADOURY Samuel, Ph. D., président
M. MARTEL Sylvain, Ph. D., membre et directeur de recherche
M. SIROIS Frédéric, Ph. D., membre
M. FERREIRA Antoine, Doctorat, membre externe

REMERCIEMENTS

C'est avec beaucoup de fierté que je termine le long parcours doctoral, lequel est à la fois enrichissant et stimulant, mais aussi parfois parsemé d'embûches. Je ne me serais probablement pas rendu aussi loin sans le précieux soutien de mes proches, collègues, famille et amis.

Je suis d'abord extrêmement reconnaissant d'avoir eu la chance de travailler sur ce projet de recherche si unique et innovateur et, disons-le tout de même, un peu « flyé » qu'est de naviguer des petits robots dans les vaisseaux sanguins. Je tiens à remercier sincèrement Sylvain, mon directeur de recherche, pour la confiance qu'il m'a accordée et pour m'avoir donné la chance d'embarquer dans cette aventure. Déterminé et visionnaire, celui-ci demeurera certainement une source d'inspiration. Comme tu le dis toujours Sylvain, rien n'est impossible, il faut juste trouver les solutions !

Je tiens aussi à remercier toute l'équipe du laboratoire pour les nombreuses discussions enrichissantes, qui auront autant permis de résoudre des problèmes coriaces que de détendre un peu l'atmosphère. En particulier, Charles, Mahmood et Dumitru : on en aura dit des choses (toujours intelligentes bien sûr) autour de bons « cafés gratuits » ! J'ai vraiment apprécié cette ambiance où travail productif peut cohabiter avec humour et rigolade.

Je me dois aussi de souligner le support constant des membres de ma famille et amis, qui n'ont cessé de m'encourager et de démontrer un intérêt marqué pour mon projet. Un tel appui est motivant, je suis très heureux d'être si bien entouré !

Enfin, je suis plus que reconnaissant envers ma copine Jany, qui a fait preuve d'énormément de support et de compréhension durant ces quatre années. Merci de m'avoir accompagné dans cette aventure, merci d'être là, avec comme toujours ton sourire et ta bonne énergie !

Par ailleurs, pour se consacrer à ces longues heures d'études parfois prenantes, le soutien financier fait toute la différence. Je tiens donc à remercier les organismes m'ayant accordé des bourses et de l'aide financière, soient le Fond de recherche du Québec - Nature et technologies, Hydro-Québec ainsi que la chaire de recherche du Canada en nanorobotique médicale.

RÉSUMÉ

Les chimiothérapies modernes utilisées pour le traitement des cancers consistent souvent à l'injection systémique de molécules toxiques dont généralement une infime partie atteint la tumeur. Pour augmenter l'efficacité de ces traitements et réduire leurs effets secondaires, une solution consiste à guider magnétiquement des agents thérapeutiques afin de les diriger dans le réseau vasculaire, à partir du point d'injection directement vers la zone à traiter. Ceci peut être accompli en appliquant des champs et des gradients magnétiques de manière contrôlée sur les agents, qui sont alors soumis à des forces de propulsion permettant de les attirer à travers les bifurcations artérielles désirées. Pour le guidage de micro-agents, cette approche requiert des champs et des gradients magnétiques forts. Le champ permet de magnétiser les agents et doit idéalement être suffisamment fort pour les amener à saturation magnétique. Les gradients (variations spatiales du champ) peuvent alors induire des forces magnétiques de propulsion, mais doivent atteindre une certaine amplitude pour que ces forces soient suffisantes. Avec les limites technologiques actuelles, il est difficile de rencontrer ces deux critères pour le guidage de micro-agents à l'échelle humaine. Dans les tissus profonds, les méthodes existantes sont généralement limitées à des champs de $<0.1\,\mathrm{T}$ et des gradients de $<400\,\mathrm{mT/m}$, ou peuvent générer un champ assez fort pour obtenir une magnétisation à saturation mais au détriment de gradients faibles (e.g. $<100\,\mathrm{mT/m}$ ou typiquement $<40\,\mathrm{mT/m}$).

Dans le cadre de ce projet de recherche, une nouvelle méthode de guidage magnétique, baptisée guidage par champs de dipôles, ou *Dipole Field Navigation* (DFN), est proposée et étudiée pour surmonter les limitations des méthodes précédentes pour le guidage de micro-agents. Contrairement aux autres méthodes de guidage magnétique, DFN bénéficie à la fois d'un champ magnétique fort et de gradients d'amplitudes élevées dans les tissus profonds chez l'humain. Ceci est accompli à l'aide de corps ferromagnétiques précisément positionnés autour du patient à l'intérieur d'un appareil clinique d'imagerie par résonance magnétique. Ces appareils génèrent un puissant champ magnétique, typiquement de 1.5-3 T, qui est suffisant pour atteindre la saturation magnétique des agents. Les corps ferromagnétiques ont pour effet de distordre le champ de l'appareil de sorte que des gradients excédant $400\,\mathrm{mT/m}$ peuvent être générés à une profondeur de $10\,\mathrm{cm}$ dans le patient. Grâce aux distorsions complexes du champ autour de ceux-ci, il est théoriquement possible d'induire, dans une certaine mesure, les forces magnétiques nécessaires au guidage des agents le long de trajectoires prédéfinies dans le réseau vasculaire.

Le paramétrage adéquat d'une disposition de corps ferromagnétiques, dont le nombre requis est a priori inconnu, est toutefois complexe et doit être effectué en fonction de la trajectoire vasculaire désirée, spécifique à chaque patient. Différentes contraintes reliées à l'environnement d'IRM, dont l'espace restreint à l'intérieur de l'appareil, doivent également être prises en compte. Ainsi, des modèles et algorithmes d'optimisation permettant de résoudre ce problème sont développés et présentés. Le fonctionnement de la méthode est validé in vitro par le guidage de particules à travers des réseaux ayant jusqu'à trois bifurcations consécutives avec un taux de ciblage supérieur à 90%. Il est démontré que la taille et la forme des corps ferromagnétiques peuvent être variées afin d'augmenter les capacités de génération de gradients. En particulier, les formes de disque et de demie-sphère sont identifiées comme étant les plus efficaces. Par ailleurs, l'environnement d'IRM n'étant typiquement pas compatible avec la présence de matériaux magnétiques, les effets des corps ferromagnétiques sur l'imagerie sont étudiés. Il est démontré que l'imagerie demeure possible, dans une certaine mesure malgré les distorsions, dans des régions spécifiques autour d'une sphère magnétisée à l'intérieur de l'appareil. La qualité des images obtenues dans ces conditions est suffisante pour permettre de valider le succès du ciblage. Ainsi, des vérifications périodiques du déroulement de l'intervention seraient possibles en éloignant momentanément le ou les corps ferromagnétiques du patient. D'autre part, à cause des forces magnétiques exercées sur ceux-ci, le nombre et la taille des corps ferromagnétiques doivent être limités afin de faciliter leur insertion et leur positionnement sécuritaire dans l'appareil. Bien que certaines trajectoires puissent nécessiter plusieurs corps ferromagnétiques de grande taille, un certain compromis doit donc être recherché par rapport à la qualité des gradients générés. Enfin, le potentiel de la méthode pour le guidage de micro-agents dans les tissus profonds chez l'humain est évalué en utilisant un modèle du réseau vasculaire du foie d'un patient. Les résultats indiquent que, pour des trajectoires vasculaires multi-bifurcations relativement complexes, un compromis est inévitable entre les amplitudes et la précision angulaire des gradients générés. Par exemple, des gradients d'environ 150 mT/m ont été obtenus pour le guidage à travers trois bifurcations consécutives dans ce modèle, mais avec une erreur angulaire moyenne d'environ 20°. Finalement, les capacités de DFN à générer des gradients forts dépendent de nombreux paramètres, comme la complexité et la profondeur de la trajectoire vasculaire visée, mais peuvent, selon les conditions, surpasser grandement celles des méthodes existantes pour le guidage de micro-agents dans les tissus profonds. À la lumière des résultats présentés dans cette thèse, le potentiel de la méthode est prometteur et justifie la poursuite du projet, notamment vers la réalisation des premiers essais in vivo. À ce titre, différentes pistes de recherches et de travaux futurs sont discutées.

ABSTRACT

Modern chemotherapies used in cancer treatment often involve the systemic administration of toxic molecules, of which usually a tiny fraction reaches the tumor. To increase the efficacy of these treatments while significantly reducing their secondary effects, a solution consists in magnetically guiding therapeutic agents in the vascular network, from an injection point directly towards the diseased site. This can be accomplished by applying controlled combinations of magnetic fields and gradients on the agents, which are then subjected to propulsive directional forces that can be used to steer them through the desired arterial bifurcations. For the navigation of micro-agents, this approach requires both a strong magnetic field and high gradients. The field strength is required to magnetize the agents and is ideally high enough to bring them at saturation magnetization. The gradients (spatial variations of the field) can then induce magnetic propulsion forces, but must reach a certain magnitude so that these forces are sufficient. Because of current technological limitations, it is challenging to meet both criteria for the navigation of micro-agents at the human scale. In deep tissues, current methods are in fact usually limited to $<0.1\,\mathrm{T}$ fields and $<400\,\mathrm{mT/m}$ gradients, or can provide the field to reach saturation magnetization but at the expense of weak gradients (e.g. $<100\,\mathrm{mT/m}$ or typically $<40\,\mathrm{mT/m}$).

In this research project, a new method dubbed Dipole Field Navigation (DFN) is proposed and studied to overcome the limitations of existing magnetic navigation methods for guiding micro-agents. Unlike other methods, DFN can provide both a strong magnetic field and high gradients in deep tissues for whole-body interventions. This is achieved by precisely positioning ferromagnetic cores around the patient inside a clinical magnetic resonance imaging scanner. Conventional scanners generate a strong magnetic field, typically of 1.5-3 T, which is sufficient to bring the agents at saturation magnetization. The ferromagnetic cores distort the scanner's field such that gradients exceeding $400\,\mathrm{mT/m}$ can be generated at a $10\,\mathrm{cm}$ depth inside the patient. Due to the complex distortion patterns around the cores, it is theoretically possible to induce, to a certain extent, the magnetic forces required for navigating agents along predefined vascular routes.

The parameterization of core configurations, in which the required number of cores is a priori unknown, is however complex and must be performed according to the specific vasculature of a given patient. Several constraints related to the MRI environment must also be considered, such as the limited space inside the scanner. Therefore, models and optimization algorithms

are developed and presented for solving this problem. The feasibility of the method is validated in vitro by guiding particles through up to three consecutive bifurcations, achieving a targeting efficiency of over 90%. It is shown that the size and shape of the cores can be varied to increase the capabilities of the method for generating gradients. In particular, discs and hemispheres are shown to be the most effective shapes. Moreover, the MRI environment typically no being compatible with the presence of magnetic materials, the effects of the cores on imaging are studied. It is shown that, despite distortions, imaging is still possible, to a certain extent, in specific regions around a magnetized sphere placed in the scanner. The images obtained in these conditions are of sufficient quality for targeting assessment. Thus, periodic validations of the procedure could be achieved by momentarily moving the cores away from the patient. On another hand, due to the potentially strong magnetic forces exerted on the cores, their number and sizes must be limited to ensure their safe insertion and positioning in the scanner. Consequently, although the navigation in some vascular routes may require several large ferromagnetic cores, a certain compromise must be made with respect to the quality of the gradients generated. Finally, the potential of the method for guiding micro-agents in a human vasculature in deep tissues is evaluated using the vascular model of a patient liver. The results indicate that, for relatively complex vascular routes having multiple bifurcations, a compromise is also required between the amplitudes and the angular precision of the gradients. For example, gradient strengths around 150 mT/m were obtained for routes having three consecutive bifurcations in this model, but with an average angular error of about 20°. Overall, the capabilities of DFN for generating strong gradients depend on several parameters, such as the complexity and depth of the desired vascular route, but can in a range of cases greatly exceed those achievable by previous methods for the navigation of micro-agents in deep tissues. In view of the results presented in this thesis, the promising potential of DFN motivates the continuation of this project, in particular towards the first in vivo experiments. As such, different avenues of research and future works are discussed.

TABLE DES MATIÈRES

REMERCIEMENTS iii

RÉSUMÉ iv

ABSTRACT vi

TABLE DES MATIÈRES viii

LISTE DES TABLEAUX xii

LISTE DES FIGURES xiii

LISTE DES SIGLES ET ABRÉVIATIONS xvi

CHAPITRE 1 INTRODUCTION 1
1.1 Hypothèses et objectifs 3
1.2 Plan de la thèse 4

CHAPITRE 2 REVUE DE LITTÉRATURE 5
2.1 Principe d'actionnement magnétique 5
2.1.1 Types de matériaux magnétiques 6
2.1.2 Aspects d'application au guidage endovasculaire 7
2.2 Agents thérapeutiques magnétiques 8
2.2.1 Microtransporteurs thérapeutiques magnétiques 8
2.3 Microrobots magnétiques 9
2.4 Méthodes de guidage magnétique 11
2.4.1 Guidage avec aimants permanents 11
2.4.2 Utilisation d'aimants supraconducteurs 13
2.4.3 Systèmes à actionnement électromagnétique 15
2.4.4 Navigation par résonance magnétique 18
2.4.5 *Magnetic Resonance Targeting* 20
2.5 Cartographie du réseau vasculaire et suivi des agents thérapeutiques pendant le guidage 21

CHAPITRE 3 DÉMARCHE SCIENTIFIQUE ET PRÉSENTATION DES ARTICLES 24
3.1 Positionnement des corps ferromagnétiques et preuve de concept: article « *Dipole Field Navigation: Theory and Proof of Concept* » 24
3.2 Imagerie en présence de corps ferromagnétiques: article « *Enabling automated magnetic resonance imaging-based targeting assessment during dipole field navigation* » 25
3.3 Paramétrage de configurations de corps ferromagnétiques: article « *A Progressive Multidimensional Particle Swarm Optimizer for Magnetic Core Placement in Dipole Field Navigation* » 26
3.4 Forme des corps ferromagnétiques: article « *Seeking Optimal Magnetic Core Shapes for Strong Gradient Generation in Dipole Field Navigation* » 26
3.5 Potentiel de la méthode pour des interventions réelles: article « *Evaluation of the Potential of Dipole Field Navigation for the Targeted Delivery of Therapeutic Agents in a Human Vascular Network* » 27

CHAPITRE 4 ARTICLE 1: DIPOLE FIELD NAVIGATION: THEORY AND PROOF OF CONCEPT 28
4.1 Abstract 28
4.2 Introduction 28
4.3 Dipole Field Navigation 32
4.3.1 Magnetic Models 32
4.3.2 Magnetic Interactions 34
4.3.3 Single Core Positioning 35
4.4 Multi-Core DFN Positioning 36
4.4.1 Optimization Problem Formulation 38
4.4.2 Alternating Optimizations 39
4.4.3 Search Algorithm 40
4.4.4 Exploiting Positioning Region Intersections 43
4.5 Algorithm Implementation 43
4.6 *In Vitro* Navigation Experiment 45
4.6.1 Setup 46
4.6.2 Results 49
4.7 Discussion 51
4.8 Conclusion 52

4.9 References 52

CHAPITRE 5 ARTICLE 2: ENABLING AUTOMATED MAGNETIC RESONANCE IMAGING-BASED TARGETING ASSESSMENT DURING DIPOLE FIELD NAVIGATION 56
5.1 Abstract 56
5.2 Main text 56
5.3 References 65

CHAPITRE 6 ARTICLE 3: A PROGRESSIVE MULTIDIMENSIONAL PARTICLE SWARM OPTIMIZER FOR MAGNETIC CORE PLACEMENT IN DIPOLE FIELD NAVIGATION 67
6.1 Abstract 67
6.2 Introduction 67
6.3 Previous Works 69
6.3.1 Magnetic Models for Dipole Field Navigation 69
6.3.2 Magnetic Core Positioning in DFN 71
6.3.3 Particle Swarm Optimization 72
6.4 Progressive Multidimensional PSO 72
6.5 Core Placement in DFN Using PMD-PSO 74
6.5.1 Proposed Fitness Function 74
6.5.2 Core Positioning Constraints 76
6.5.3 Application of PMD-PSO to DFN 77
6.6 Experiments 77
6.6.1 Test Framework 78
6.6.2 Tested algorithms 79
6.6.3 Parameters Selection 79
6.6.4 Results 80
6.7 Discussion and Conclusion 82
6.8 References 84

CHAPITRE 7 ARTICLE 4: SEEKING OPTIMAL MAGNETIC CORE SHAPES FOR STRONG GRADIENT GENERATION IN DIPOLE FIELD NAVIGATION 87
7.1 Abstract 87
7.2 Introduction 87
7.3 Magnetic Gradients in Dipole Field Navigation 89

7.3.1 Considerations on Magnetic Gradients 90
7.3.2 Expected Effect of Core Shape on Gradients 91
7.4 Investigation of Core Shapes 92
7.4.1 Gradient Calculations 92
7.4.2 Tested Core Shapes 93
7.4.3 Results 94
7.5 Discussion 95
7.6 Conclusion 96
7.7 References 101

CHAPITRE 8 ARTICLE 5: EVALUATION OF THE POTENTIAL OF DIPOLE FIELD NAVIGATION FOR THE TARGETED DELIVERY OF THERAPEUTIC AGENTS IN A HUMAN VASCULAR NETWORK 104
8.1 Abstract 104
8.2 Introduction 104
8.3 Background on Dipole Field Navigation 108
8.3.1 Optimization of Core Configurations 109
8.4 Magnetic Models 110
8.4.1 Magnetic Field of Disc Cores 111
8.4.2 Gradient Calculations 112
8.4.3 Magnetic Interactions 113
8.5 Achievable Gradient Strengths 115
8.5.1 Gradient Optimization Approach 115
8.5.2 Single bifurcation 116
8.5.3 Two bifurcations 117
8.6 Real Case Scenario - Targeting in the Human Liver with Dipole Field Navigation 120
8.7 Discussion 125
8.8 References 130

CHAPITRE 9 DISCUSSION GÉNÉRALE 134

CHAPITRE 10 CONCLUSION ET RECOMMANDATIONS 139

RÉFÉRENCES 141

LISTE DES TABLEAUX

Table 4.1 Parameters of the Navigation Experimental Setup 47

Table 6.1 Overall performance of the tested algorithms on the 300 randomly generated navigation problems. 82

Table 7.1 Dimensions of the different core shapes tested, for a constant volume of ferromagnetic material in each core. 94

Table 8.1 Target Gradient Parameters and Characteristics for the Seven Vascular Routes Tested in the Human Liver Model. 124

Tableau 9.1 Avantage et inconvénients de la méthode proposée, DFN, en comparaison avec la méthode MRN. 138

LISTE DES FIGURES

Figure 1.1 Illustration du ciblage direct, approche dans laquelle des forces de guidage permettent de propulser les agents thérapeutiques dans les branches vasculaires désirées jusqu'à une région ciblée. 2
Figure 1.2 Illustration du fonctionnement de la méthode *Dipole Field Navigation*. 3
Figure 1.3 Interconnexion entre les objectifs du projet et les articles publiés/soumis. 4
Figure 2.1 Couple et force magnétiques induits sur un moment magnétique plongé dans un champ $\mathbf{B}$. 6
Figure 2.2 Illustration des courbes de magnétisation de quelques types de matériaux magnétiques, en fonction de la force du champ appliqué H. 7
Figure 2.3 Illustration des *therapeutic magnetic microcarriers*. 10
Figure 2.4 Exemples de microrobots inspirés des mécanismes de propulsion de bactéries. Images reproduites avec permissions. 11
Figure 2.5 Illustration du ciblage de particules magnétiques à l'aide d'un aimant permanent positionné à la surface du patient, très près de la zone ciblée. 13
Figure 2.6 Image du système Niobe de Stereotaxis, permettant d'orienter un cathéter. 14
Figure 2.7 Image du système Octomag, pour le contrôle d'un petit dispositif à des fins de microchirurgies oculaires. 16
Figure 2.8 Système à actionnement électromagnétique développé par Jeong *et al.* pour diriger un dispositif dans les artères. 17
Figure 2.9 Deux points de vue de la plateforme commerciale de guidage de cathéter Aeon Phocus de Aeon Scientific. 17
Figure 2.10 Méthode de navigation par résonance magnétique. 19
Figure 2.11 Exemple d'angiographie numérique par soustraction. 22
Figure 4.1 Magnetic gradient field around a magnetized spherical core. 33
Figure 4.2 Convention used for spherical coordinates. 34
Figure 4.3 Range of gradient magnitudes achievable around a core having a magnetization $M = 1.43 \times 10^6\,\mathrm{A/m}$, as a function of the distance from the surface of the core, for different core radii. 37
Figure 4.4 Illustration of positioning regions in 2D (gray areas), inside which a given core can induce a gradient at point $\mathbf{p}$ that meet the desired gradient $\mathbf{G}$. 38

Figure 4.5 Examples of core configurations found by the positioning algorithm for three different scenarios. 45
Figure 4.6 Tube network used for the navigation experiment. 47
Figure 4.7 Top and side views illustrating the experimental setup. 48
Figure 4.8 Experimental setup and results. 50
Figure 5.1 To assess targeting in DFN, the core can be moved between locations optimized for navigation and for imaging. 58
Figure 5.2 Simulated offset of the Larmor frequency of hydrogen around a chrome steel core. 59
Figure 5.3 MR coronal images of an orange, acquired in presence of a 3.81 cm chrome steel core located at different positions. 61
Figure 5.4 Experimental setup used for the navigation and imaging experiment. . 63
Figure 5.5 Coronal images of the phantom resulting from the combination of slice images acquired during the navigation experiment, with the core located at its imaging position. 64
Figure 5.6 Post injection photograph of phantom showing particles in targeted branches. 64
Figure 6.1 In DFN, ferromagnetic cores positioned around the patient in an MRI scanner generate gradients (arrows) for navigation towards a target. . . 68
Figure 6.2 Examples of randomly generated vasculatures that were used to test the algorithms. 78
Figure 6.3 Distribution of solution fitnesses (the closer to $F = 1$ the better) over the 300 problems solved, for different numbers of cores. 81
Figure 6.4 Illustration of the tradeoff in the number of cores using an example of the best solutions found by PMD-PSO on a 2-D problem. 83
Figure 7.1 Magnetic gradient field lines around a magnetized sphere in a uniform field $\mathbf{B}_0$. 90
Figure 7.2 Plane delimiting the gradients that are accessible (in blue, normalized) inside the body for DFN. 91
Figure 7.3 Tested core shapes and their natural alignment with $\mathbf{B}_0$. 93
Figure 7.4 Example of gradient orientation isolines, which were used to compare gradient strengths across tested shapes given a desired gradient orientation. 96
Figure 7.5 Results of the calculated gradients in the navigation gradient region, for the different core shapes tested. 97

Figure 7.5 (Cont.) . . . 98
Figure 7.6 Gradient strengths and gains relative to the sphere obtained for the core shapes tested as a function of the depth inside the navigation gradient region. . . . 99
Figure 7.6 (Cont.) . . . 100
Figure 8.1 In Dipole Field Navigation, ferromagnetic cores are positioned around the patient inside an MRI scanner to distort the field. . . . 107
Figure 8.2 Coordinate system used in DFN and alignment of a disc in the scanner's field. . . . 110
Figure 8.3 Validation of the field and gradient calculation approach, performed for a spherical core ($R = 4\,\text{cm}$) by comparison with analytical values. . . . 112
Figure 8.4 Results of the finite element modeling of the interactions forces between two discs and the variations from the expected magnetizations. . . . 114
Figure 8.5 Illustration of the achievable gradient tests. . . . 116
Figure 8.6 Maximum gradient strengths obtained using disc core(s) constrained to lie above a horizontal plane (approximation of patient body) as a function of the desired gradient orientation. . . . 118
Figure 8.7 Performances comparison between different disc core sizes for generating desired gradient orientations at a 10 cm depth. . . . 119
Figure 8.8 Maximum gradient strengths obtained for generating a 180° variation (worst case) of the gradient over a distance d_{sep} using disc cores constrained to lie above a horizontal plane. . . . 121
Figure 8.9 Performance comparison between different disc core sizes for generating 180° variations of the gradient. . . . 122
Figure 8.10 Realistic scenario tested for DFN in a real human liver model, taking into account the limited space around the patient body inside an MRI scanner. . . . 123
Figure 8.11 Results of different compromises between the average error angle and the average strength of the resulting gradients on the vascular routes in the liver model. . . . 125
Figure 8.12 Example core configurations obtained for three vascular routes in the liver model. . . . 126
Figure 9.1 Forces d'insertion de disques ferromagnétiques dans un appareil d'IRM de modèle MAGNETOM Skyra 3 T. . . . 136

LISTE DES SIGLES ET ABRÉVIATIONS

Principaux acronymes utilisés :

2D	Deux dimensions
3D	Trois dimensions
AEM	Actionnement électromagnétique
AO	*Alternating Optimization*
CGCI	*Catheter Guidance Control and Imaging*
CT-scan	Tomographie assistée par ordinateur
DFN	*Dipole Field Navigation* (guidage par champs de dipôles)
DT	*Direct Targeting*
EMA	*Electromagnetic actuation*
FEM	*Finite element modeling*
FFN	*Fringe Field Navigation*
IRM	Imagerie par résonance magnétique
MGCE	*Magnetically-Guided Capsule Endoscope*
MNP	*Magnetic nanoparticles*
MPI	*Magnetic Particle Imaging*
MRI	*Magnetic resonance imaging*
MRN	*Magnetic Resonance Navigation*
MRT	*Magnetic Resonance Targeting*
MS-SET	*Magnetic Signature Selective Excitation*
NGR	*Navigation Gradient Region*
PHA	*Proper hepatic artery*
PMD-PSO	*Progressive Multidimensional Particle Swarm Optimization*
PSO	*Particle Swarm Optimization*
TMMC	*Therapeutic magnetic microcarriers*

Principaux symboles utilisés :

$\mathbf{B}$	Champ d'induction magnétique [T]
$\mathbf{B}_0$	Champ magnétique principal d'un appareil d'IRM [T]
$\mathcal{C}$	Ensemble de paramètres d'un corps ferromagnétique
D	Dimensionnalité de l'espace de recherche
$\mathbf{F}_{mag}$	Force magnétique [N]
$\mathbf{G}$	Gradient magnétique [T/m]
$\mathbf{H}$	Champ d'excitation magnétique [A/m]
$\mathbf{m}$	Moment magnétique [A·m^2]
$\mathbf{M}$	Magnétisation du matériau [A/m]
N	Nombre de corps ferromagnétiques
$\mathbf{p}$	Position d'un point dans l'espace [m]
$\mathbf{r}$	Coordonnées relatives d'un point par rapport à la position d'un corps ferromagnétique [m]
R	Rayon d'un corps ferromagnétique [m]
V_{mag}	Volume de matériau magnétique [m^3]
∇	Opérateur gradient
μ	Perméabilité magnétique [H/m]
μ_0	Perméabilité magnétique du vide [H/m]
ξ	Erreur angulaire sur la direction d'un gradient généré
$\boldsymbol{\tau}_{mag}$	Couple magnétique [N·m]
χ_m	Susceptibilité magnétique [H/m ou H·m^2/kg]

CHAPITRE 1 INTRODUCTION

Les statistiques publiées par l'Organisation mondiale de la Santé montrent que l'incidence du cancer est globalement en augmentation dans le monde [1]. Au Canada par exemple, on prévoit que deux personnes sur cinq seront atteintes d'un cancer au cours de leur vie et qu'une sur quatre en mourra. D'après les données colligées dans le cadre du projet GLOBOCAN 2012, portant sur 28 types de cancers dans 184 pays, le fardeau mondial du cancer en 2012 est estimé à 14.1 millions de nouveaux cas et 8.2 millions de décès [2].

Il n'existe aucun traitement parfaitement efficace contre cette maladie à l'heure actuelle. En complémentarité avec la chirurgie et la radiothérapie, les traitements modernes ont souvent recours à la chimiothérapie, lors de laquelle des molécules cytotoxiques sont administrées au patient, le plus souvent de manière systémique. Bien que les cancers soient en majorité (>80%) initialement localisés dans une région précise, ces molécules se retrouvent alors en libre circulation dans le système vasculaire et peuvent causer des dommages aux tissus et organes sains avant d'être éliminées par l'organisme. Même si certains agents thérapeutiques sont étudiés pour augmenter leur spécificité aux cellules cancéreuses et allonger leur durée de vie en circulation [3], leur taux d'efficacité demeure très faible, 1-2% atteignant la tumeur. Les effets secondaires causés par la toxicité de ces traitements se traduisent à la fois en un risque et une perte de qualité de vie substantiels pour les patients [4].

Une solution prometteuse pour cibler plus efficacement une région spécifique à traiter est le ciblage direct, illustré à la Fig. 1.1, qui consiste à diriger les agents thérapeutiques dans le réseau vasculaire à partir d'un point d'injection directement vers la région ciblée. Pour ce faire, les agents, transportés par le débit sanguin, doivent être propulsés dans les branches désirées du réseau vasculaire le long d'une trajectoire prédéterminée. Étant données les contraintes technologiques actuelles limitant la miniaturisation de robots qui seraient capables de naviguer et de s'orienter jusque dans les petites artères ou artérioles ($<100\,\mu$m), l'approche privilégiée pour réaliser le guidage direct est basée sur l'actionnement magnétique de micro-agents magnétiques [5]. En soumettant ces derniers à des champs magnétiques, il est en effet possible d'induire des forces et des couples magnétiques permettant de les propulser et de les contrôler à distance. Dans le cas spécifique du guidage endovasculaire de micro-agents thérapeutiques, un champ magnétique fort combiné à des gradients magnétiques (variations spatiales du champ) d'amplitudes élevées sont requis afin d'induire des forces de propulsion suffisantes pour les diriger efficacement en présence des débits sanguins relativement élevés.

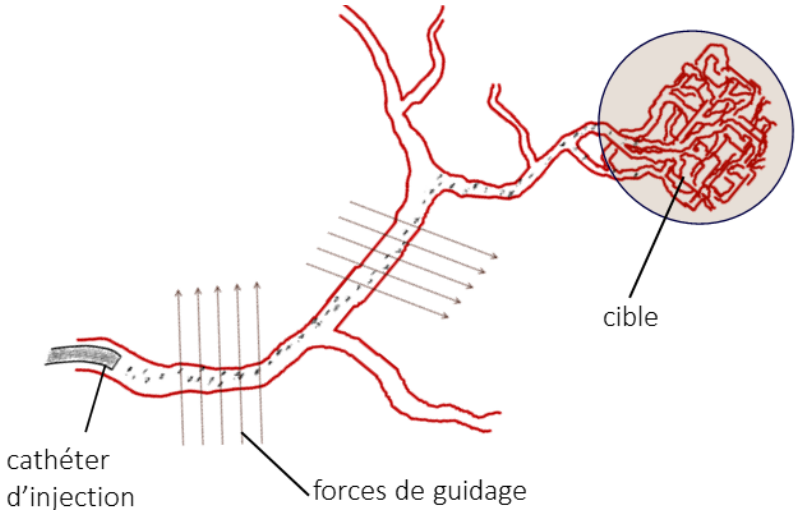

Figure 1.1 Illustration du ciblage direct, approche dans laquelle des forces de guidage permettent de propulser les agents thérapeutiques dans les branches vasculaires désirées jusqu'à une région ciblée.

De nombreuses méthodes basées sur le guidage magnétique ont été proposées par le passé pour diverses applications biomédicales, avec un essor marqué dans la dernière décennie. Néanmoins, pour le guidage de micro-agents thérapeutiques dans les tissus profonds à l'échelle humaine, la génération de champs et de gradients magnétiques suffisamment élevés demeure un défi technologique important.

Dans cette thèse, une nouvelle méthode de guidage magnétique est proposée et étudiée afin de surmonter les limitations des solutions existantes pour le guidage endovasculaire d'agents thérapeutiques. Cette méthode, nommée guidage par champs de dipôles, ou *Dipole Field Navigation* (DFN), exploite le puissant champ homogène généré par un appareil d'imagerie par résonance magnétique (IRM). Ce champ garantit la haute magnétisation (saturation magnétique) des agents, indépendamment de la profondeur à laquelle ils se trouvent dans le corps du patient. Les gradients sont générés en distordant le champ de l'appareil de manière contrôlée à l'aide de corps ferromagnétiques précisément positionnés autour du patient, à l'intérieur de l'appareil. En utilisant des corps ferromagnétiques suffisamment gros, les gradients magnétiques résultants dans les tissus profonds peuvent induire des forces de guidage suffisantes sur des micro-agents jusque dans les tissus profonds du corps humain. Le principe de fonctionnement de la méthode est illustré à la Fig. 1.2.

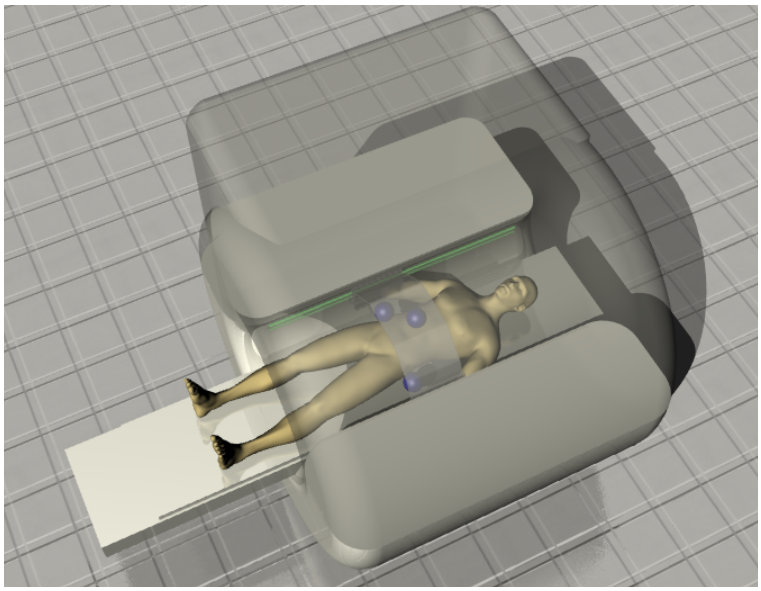

(a)

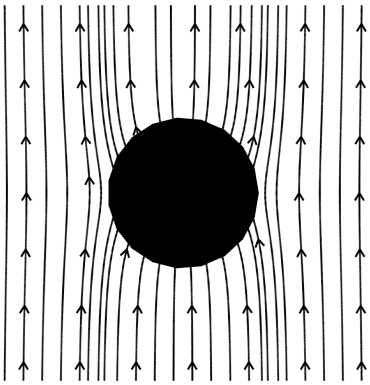

(b)

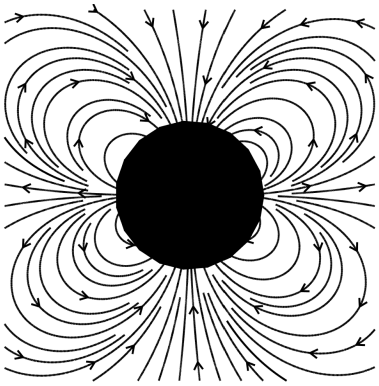

(c)

Figure 1.2 Illustration du fonctionnement de la méthode *Dipole Field Navigation*. a) Des corps ferromagnétiques (en bleu) sont positionnés précisément autour d'un patient à l'intérieur d'un appareil d'imagerie par résonance magnétique. b) Distorsion du champ autour d'un corps ferromagnétique plongé dans un champ de 3 T ; c) Gradients générés par la distorsion. Les forces magnétiques exercées sur les agents navigués suivent la direction des gradients.

1.1 Hypothèses et objectifs

Les fortes distorsions du champ autour d'un corps ferromagnétique produisent un motif de gradients relativement complexe (Fig. 1.2c) permettant de générer à la fois des forces attractives et répulsives, selon la position du corps ferromagnétique par rapport aux agents navigués. Ainsi, la première hypothèse de recherche émise est la suivante :

Hypothèse 1 : *En paramétrant adéquatement un ensemble de corps ferromagnétiques (nom-*

bre, tailles, positions, etc.), il est possible de générer, dans une certaine mesure, les gradients nécessaires au guidage de micro-agents thérapeutiques le long d'une trajectoire vasculaire désirée.

Le fait de positionner plusieurs corps ferromagnétiques pour générer des variations complexes de gradients dans le patient implique que les gradients générés par chacun des corps s'annulent partiellement ou totalement à certains endroits. Par conséquent, une deuxième hypothèse est :

Hypothèse 2 : *Les gradients générés dans les tissus profonds par les corps ferromagnétiques peuvent surpasser ceux obtenus par les méthodes existantes, avec toutefois des limitations sur la complexité des trajectoires vasculaires navigables (nombre de bifurcations, orientation des bifurcations, etc.).*

Conséquemment, les principaux objectifs du projet sont les suivants :

Objectif 1 : *Développer des modèles et algorithmes permettant de déterminer des configurations adéquates de corps ferromagnétiques étant donnée une trajectoire désirée dans un réseau vasculaire.*

Objectif 2 : *Valider expérimentalement la faisabilité de la méthode.*

Objectif 3 : *Évaluer le potentiel de la méthode, par rapport aux autres solutions existantes, pour le guidage de micro-agents dans le réseau vasculaire.*

1.2 Plan de la thèse

Cette thèse se présente sous la forme de thèse par articles, dont les interconnexions avec les objectifs sont illustrées à la Fig. 1.3. Le Chapitre 2 introduit d'abord des notions de base et présente une revue critique de la littérature sur le guidage magnétique. Le Chapitre 3 détaille la démarche scientifique et la pertinence des travaux menés dans les articles, qui sont ensuite présentés aux Chapitres 4 à 8. Une discussion générale est présentée au Chapitre 9. Enfin, le Chapitre 10 propose des recommandations sur les travaux futurs et conclut.

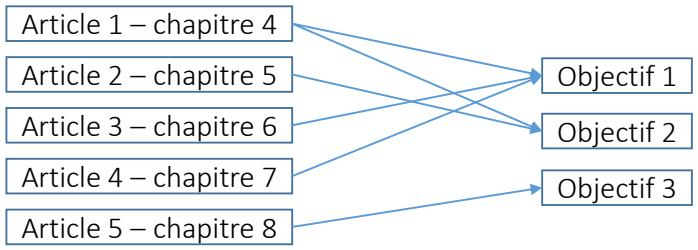

Figure 1.3 Interconnexion entre les objectifs du projet et les articles publiés/soumis.

CHAPITRE 2 REVUE DE LITTÉRATURE

2.1 Principe d'actionnement magnétique

L'actionnement magnétique est gouverné par les équations de la force $\mathbf{F}_{mag}$ et du couple $\boldsymbol{\tau}_{mag}$ induits sur un agent, lorsque celui-ci est magnétisé et plongé dans un champ magnétique :

$$\mathbf{F}_{mag} = \nabla (\mathbf{m} \cdot \mathbf{B}) \tag{2.1}$$

$$\boldsymbol{\tau}_{mag} = \mathbf{m} \times \mathbf{B} \tag{2.2}$$

où $\mathbf{m}$ est le moment magnétique de l'agent et $\mathbf{B}$ la densité du champ magnétique appliqué. L'opérateur gradient, ∇, retourne une grandeur vectorielle qui correspond ici à la variation spatiale son opérande et est défini comme

$$\nabla = \begin{bmatrix} \dfrac{\partial}{\partial x} & \dfrac{\partial}{\partial y} & \dfrac{\partial}{\partial z} \end{bmatrix}^T \tag{2.3}$$

Dans le cas particulier où l'agent est magnétisé par le champ $\mathbf{B}$, l'Eq. (2.1) se simplifie à

$$\mathbf{F}_{mag} = \nabla (mB \cos 0) = m \nabla B \tag{2.4}$$

Le moment magnétique de l'agent est quant à lui proportionnel à son volume magnétique V et à sa magnétisation $\mathbf{M}$:

$$\mathbf{m} = V\mathbf{M} \tag{2.5}$$

Pour un agent magnétique donné, la force induite est donc fonction de l'amplitude de la magnétisation et du gradient du champ magnétique. Quant au couple, celui-ci est généré de sorte que la direction de la magnétisation tende à s'aligner avec celle du champ appliqué. Ces comportements sont illustrés à la Fig. 2.1. Puisque les champs magnétiques pénètrent facilement le corps humain, l'actionnement magnétique est particulièrement adapté au contrôle à distance de petits dispositifs ou micro-agents à des fins de diagnostics ou de traitements médicaux minimalement invasifs [5, 6].

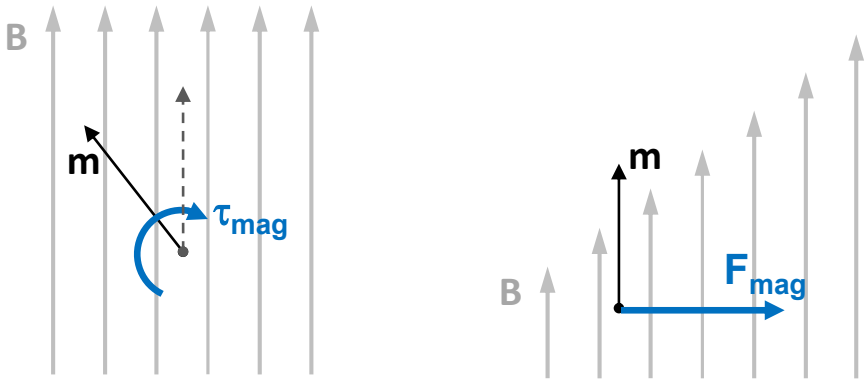

Figure 2.1 Couple et force magnétiques induits sur un moment magnétique plongé dans un champ **B**. La longueur des flèches du champ **B** est proportionnelle à l'intensité du champ. À gauche, le moment magnétique en pointillé représente l'état d'équilibre ($\tau_{mag} = 0$). À droite, pour un moment magnétique aligné avec **B**, une force directionnelle est générée dans la direction où l'intensité du champ augmente.

2.1.1 Types de matériaux magnétiques

À l'exception des matériaux magnétisés de manière permanente (ex : aimant permanent), la magnétisation **M** dépend elle-même de l'intensité du champ magnétique appliqué. La Fig. 2.2 illustre des courbes typiques de la magnétisation en fonction de l'intensité du champ appliqué $H = B/\mu$, où μ est une propriété du matériau appelée la perméabilité magnétique, pour les principaux types de matériaux magnétiques d'intérêt dans cet ouvrage.

Les matériaux ferromagnétiques sont facilement magnétisés lorsque immergés dans un champ magnétique. Ils sont caractérisés par une courbe de magnétisation non linéaire atteignant, à partir d'une certaine valeur de H, une valeur maximale de magnétisation M_{sat} typiquement élevée, appelée saturation magnétique. Pour ces matériaux, la courbe $M(H)$ est aussi caractérisée par une hystérésis, signifiant que le chemin emprunté lors de la magnétisation diffère de celui emprunté lors de la démagnétisation. Une magnétisation rémanente M_r, plus ou moins grande, perdure donc dans le matériau même lorsque celui-ci est retiré du champ magnétique. L'hystérésis des matériaux ferromagnétiques *durs* est en général très prononcée (rémanence élevée), alors que celle des ferromagnétiques *mous* est très faible (rémanence faible).

Les matériaux paramagnétiques ne présentent quant à eux aucune hystérésis, leur magnétisation variant approximativement linéairement en fonction du champ appliqué selon $M = \chi_m H$, où χ_m est la susceptibilité magnétique du matériau. Pour les matériaux paramagnétiques, la valeur de χ_m est toutefois typiquement très basse, engendrant une magnétisation relativement faible même en présence de champs magnétiques très forts.

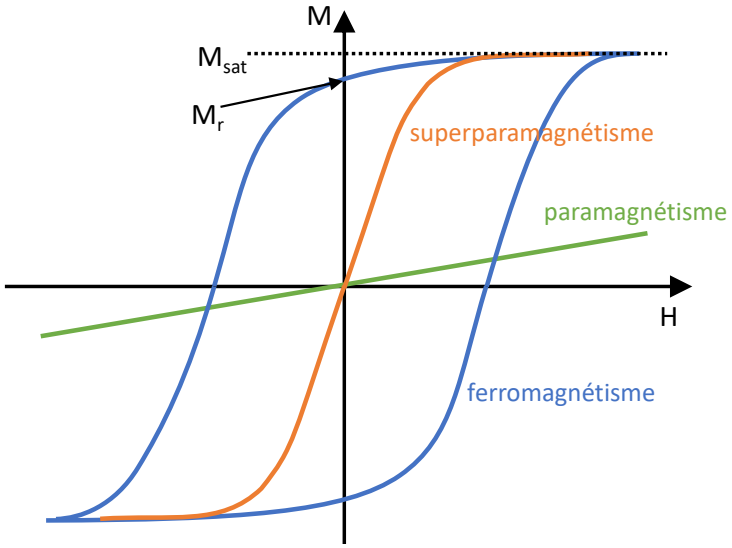

Figure 2.2 Illustration des courbes de magnétisation de quelques types de matériaux magnétiques, en fonction de la force du champ appliqué H.

Les matériaux ferri- ou ferromagnétiques, lorsque sous la forme de particules suffisamment petites (généralement de quelques dizaines de nanomètres) deviennent superparamagnétiques. Dans cet état, tous les moments magnétiques atomiques d'une particule ont la même direction, formant un seul *domaine magnétique*. Ceci n'est pas le cas dans des volumes plus gros qui, à moins d'être à saturation magnétique, se caractérisent plutôt par l'existence de nombreux domaines magnétiques dont les directions de magnétisation varient autour d'une direction moyenne. Comme les matériaux paramagnétiques, les particules superparamagnétiques ne présentent aucune hystérésis. En absence de champ magnétique externe, elles ont donc une magnétisation nulle ($M_r = 0$). Ces particules peuvent quand même être magnétisées par un champ externe, en s'alignant parfaitement avec celui-ci, avec une grande susceptibilité magnétique et une saturation magnétique élevée, similaires à celles des matériaux ferromagnétiques.

2.1.2 Aspects d'application au guidage endovasculaire

Pour le guidage endovasculaire, une caractéristique importante des agents injectés est l'absence de magnétisation rémanente. En effet, pour des micro-agents thérapeutiques, une magnétisation rémanente, même faible, favoriserait leur agrégation permanente une fois retirés du champ magnétique, ce qui pourrait entraîner le blocage des vaisseaux et empêcher leur dispersion dans la région ciblée [7]. Étant donné le très faible volume magnétique des micro-agents nécessaires au guidage endovasculaire ($<100\,\mu$m), ceux-ci doivent également atteindre des

magnétisations élevées afin que les forces magnétiques induites (Eq. (2.4)) soient suffisantes pour les diriger efficacement en présence des débits sanguins relativement élevés.

Par conséquent, les agents thérapeutiques sont typiquement constitués de nanoparticules superparamagnétiques afin d'obtenir à la fois une magnétisation rémanente nulle et une saturation élevée [7, 8]. Un exemple de telles particules sont celles d'oxyde de fer Fe_3O_4, aussi appelé magnétite. Celles-ci sont d'ailleurs utilisées dans des applications biomédicales variées, notamment comme agents de contraste IRM, comme vecteurs de transport de médicaments ou pour l'hyperthermie [9]. Pour le guidage magnétique, ces particules doivent idéalement atteindre la saturation magnétique afin de maximiser les forces induites, ce qui peut nécessiter une densité de champ magnétique externe B de plusieurs centaines de milliteslas ou plus. Selon l'Eq. (2.4), elles peuvent ensuite être tirées vers les directions désirées par des gradients magnétiques. Encore une fois, le faible volume magnétique des agents thérapeutiques, qui peuvent être constitués à partir de ces particules, implique la nécessité d'appliquer des gradients forts pour générer des forces de guidage suffisantes. Cette particularité est une source de difficulté importante du guidage magnétique d'agents thérapeutiques qui, pour être efficace, requiert donc à la fois un champ magnétique fort et des amplitudes de gradients élevées dans toute la zone d'intervention.

2.2 Agents thérapeutiques magnétiques

Des agents thérapeutiques magnétiques peuvent être obtenus en attachant simplement des molécules thérapeutiques à des nanoparticules magnétiques [10, 11]. Néanmoins, le guidage endovasculaire de telles particules dispersées requiert des amplitudes de gradients extrêmement élevées. Plus spécifiquement, des études suggèrent que, pour des nanoparticules magnétisées par un champ d'environ 200 mT, des gradients de 8-100 T/m sont requis, dépendamment de la vitesse du débit sanguin [12]. Ces amplitudes de gradients ne peuvent être atteintes qu'à de très petites distances de sources magnétiques.

2.2.1 Microtransporteurs thérapeutiques magnétiques

Pour diriger efficacement les agents avec des gradients plus faibles, et donc plus facilement atteignables à l'échelle humaine, il est nécessaire d'augmenter le volume magnétique de chaque agent individuel en regroupant plusieurs particules. Une alternative plus adaptée au guidage endovasculaire consiste donc à encapsuler des nanoparticules superparamagnétiques et des molécules thérapeutiques dans des microtransporteurs thérapeutiques magnétiques, connus

sous le nom de *therapeutic magnetic microcarriers* (TMMC) [13, 14]. Ceux-ci, présentés à la Fig. 2.3, sont constitués d'une membrane biodégradable permettant la libération progressive de la charge thérapeutique. La proportion de la charge magnétique dans les TMMCs doit être suffisante pour obtenir un moment magnétique élevé, mais en même temps minimisée pour permettre d'y intégrer une charge thérapeutique importante. Des résultats expérimentaux suggèrent que, pour des TMMCs ou des agrégats de microparticules à saturation magnétique, des gradients de l'ordre de 200-400 mT/m sont nécessaires [15, 16]. En particulier, des gradients d'environ 300 mT/m ont permis de guider des TMMCs de ~50 μm de diamètre et chargés à 30% de nanoparticules de fer cobalt (FeCo) vers un lobe prédéterminé du foie chez des lapins à partir l'artère hépatique (une seule bifurcation) [16].

2.3 Microrobots magnétiques

Plutôt que de guider des agents thérapeutiques comme ceux décrits ci-dessus, une approche différente consiste à actionner des microrobots magnétiques capables de libérer activement une charge thérapeutique contenue dans un réservoir, lorsque arrivés dans une région ciblée [17–19]. Les défis reliés à la miniaturisation de ces robots et à leur fabrication en grand nombre peuvent cependant limiter leur applicabilité pour le ciblage endovasculaire. Par exemple, des microrobots constitués d'un compartiment cylindrique et d'un bouchon en forme de vis pour le refermer ont été fabriqués [19]. Tout comme le déplacement du robot, l'ouverture du compartiment est actionnée magnétiquement afin d'en libérer le contenu une fois la cible atteinte. Une technique de fabrication au laser a permis de réduire les dimensions du microrobot à environ $40\times200\,\mu$m. Ce processus de fabrication complexe est toutefois contraignant pour la production en grand nombre de ces microrobots.

Des microrobots inspirés de la nature ont également été proposés. Conçus selon des modèles plus simples, ceux-ci peuvent atteindre des tailles beaucoup plus petites, de quelques dizaines de micromètres ou moins. En particulier, des microrobots imitant le mécanisme de propulsion de flagelles de bactéries ont été proposés, adoptant des mouvements de rotation d'une structure hélicoïdale [20–22] ou de battements d'un cil [23, 24]. Les premiers sont actionnés à l'aide de champs magnétiques rotatifs faibles (<10 mT), sous l'influence desquels un mouvement de rotation du robot est induit et se traduit en déplacement translationnel le long de l'axe de rotation. De manière similaire, les microrobots à battements sont actionnés par des champs oscillants induisant un mouvement d'ondulation du flagelle artificiel qui génère alors la propulsion. La Fig. 2.4 présente un exemple de microrobot de chaque catégorie. Des

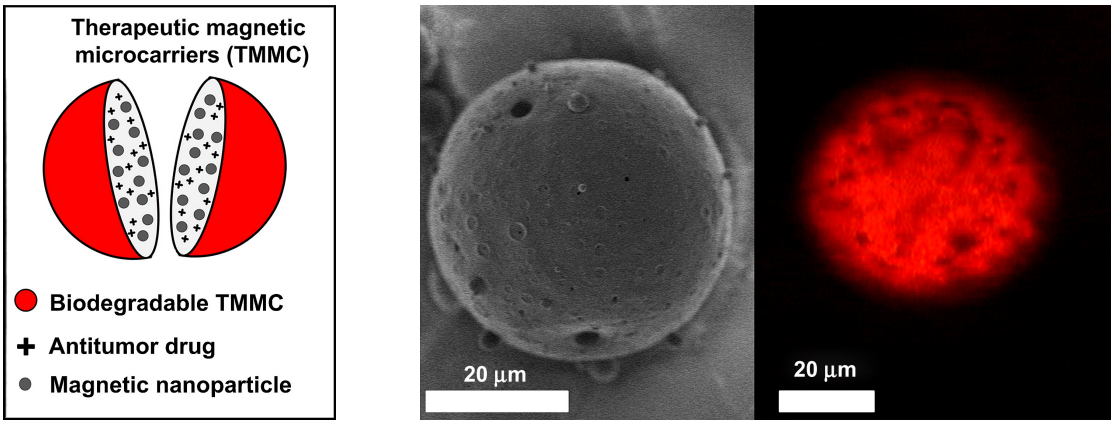

(a) (b)

Figure 2.3 La livraison ciblée de médicaments peut être réalisée par le guidage de micro-transporteurs thérapeutiques magnétiques comme les TMMCs, qui enferment des particules magnétiques et des molécules thérapeutiques dans une capsule biodégradable. a) Illustration des TMMCs ; b) Image de microscopie électronique à balayage d'un TMMC (gauche) et image de la fluorescence émise par le médicament (doxorubicine) encapsulé dans un TMMC (droite). Images adaptées de [16] avec permission.

microrobots inspirés de bactéries capables de changer de morphologie pour adapter leurs caractéristiques de mobilité à différents microenvironnements ont également été proposés [25]. Sous l'effet de la chaleur, ceux-ci peuvent passer d'une forme allongée, exposant un flagelle artificiel leur permettant de nager plus rapidement, à une forme compacte sans flagelle apparent. Ces structures plus complexes sont néanmoins plus grosses (~0.5×2 mm) et plus difficiles à produire en grand nombre avec une bonne répétabilité de leurs caractéristiques [25]. Par ailleurs, les forces translationnelles de propulsion générées par des flagelles artificiels sont plutôt faibles. Ceci limite grandement leur efficacité en présence des vitesses de flots relativement rapides du réseau vasculaire. Pour cette raison, ce type de microrobots est davantage adapté aux microenvironnements avec des débits de fluides nuls ou faibles.

Pour éviter les difficultés associées à la fabrication de microrobots suffisamment petits et puissants, certains travaux se tournent vers la nature et exploitent des bactéries magnétotactiques comme transporteurs [26]. Ces bactéries, qui possèdent une chaîne de nanoparticules magnétiques jouant le rôle d'une boussole, nagent naturellement dans la direction du champ magnétique ambiant. En les soumettant à des séquences de champs spécifiques, il est possible de les amener à converger vers une région désirée [27, 28]. Ces bactéries pourraient donc livrer des cargaisons de médicaments vers une zone ciblée. Des résultats prometteurs ont d'ailleurs été obtenus récemment pour le traitement de tumeurs chez des souris [29]. Cette approche est

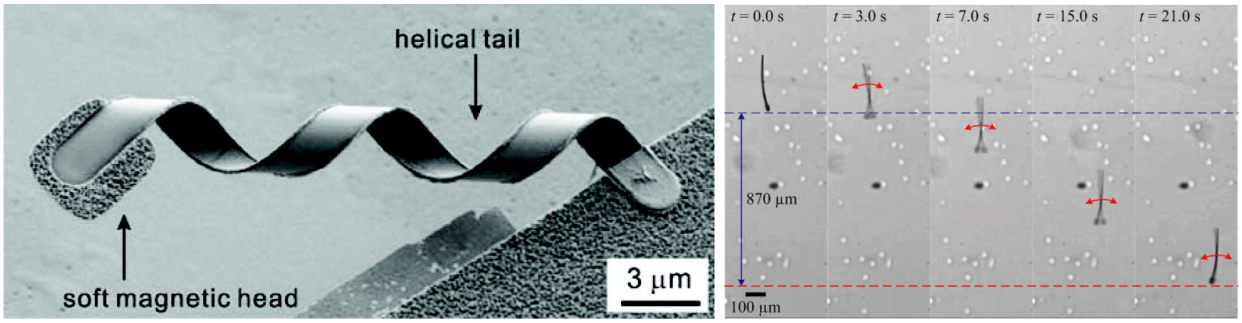

(a) Microrobot hélicoïdal [20] (b) MagnetoSperm [24]

Figure 2.4 Exemples de microrobots inspirés des mécanismes de propulsion de bactéries. Images reproduites avec permissions.

cependant uniquement applicable lorsque l'injection péritumorale des bactéries est possible, c'est-à-dire dans les régions où les vitesses de flots sont moindres. Autrement, ces dernières sont, tout comme les microrobots à flagelles artificiels mentionnés ci-haut, déportées par le flot.

En résumé, pour réussir à les guider efficacement, les micro-agents doivent être adaptés aux conditions de leur environnement. Étant données les limitations des microrobots magnétiques mentionnées ci-dessus et considérant les débits sanguins potentiellement élevés dans le réseau vasculaire, l'utilisation d'agents thérapeutiques magnétiques comme les TMMCs est donc davantage appropriée pour le guidage à l'intérieur du réseau vasculaire.

2.4 Méthodes de guidage magnétique

2.4.1 Guidage avec aimants permanents

L'idée d'utiliser des champs magnétiques pour concentrer, dans une zone ciblée, des particules transportant des molécules thérapeutiques a été évoquée dès 1960 [30]. L'intérêt pour cette approche s'est toutefois principalement développé vers la fin des années 1970 [31–35]. Les premières méthodes consistaient à placer un aimant permanent près de la région ciblée afin d'y attirer des particules magnétiques, associées à des médicaments, après leur injection dans le système vasculaire. Les résultats obtenus étaient prometteurs, quoique limités au ciblage de régions situées en surface ou très près de l'aimant. Plusieurs années se sont écoulées par la suite, avec peu de nouveaux développements dans le domaine [36], jusqu'à ce que les premiers essais cliniques soient publiés en 1996 [37]. Ces essais ont été conduits sur 14 patients atteints de tumeurs solides. Des aimants relativement gros ($8\times4\times2$ cm) placés à moins de 0.5 cm

des tumeurs ont permis d'y attirer avec succès des nanoparticules de magnétite liées à un médicament anticancéreux (épirubicine) chez la moitié des patients. Les résultats obtenus, bien que suggérant l'innocuité de cette approche, n'ont toutefois pu confirmer clairement l'efficacité supérieure de cette méthode par rapport aux traitements conventionnels de chimiothérapie. D'autres travaux ont ensuite été menés avec des aimants permanents, portant notamment sur l'étude de la rétention des médicaments après le ciblage [39], le développement d'une plateforme d'intervention [38] (illustrée à la Fig. 2.5) et le guidage de particules dans des poumons de souris [40, 41]. Des études portant sur la disposition optimale de plusieurs aimants à la surface de la peau ont également été menées [42].

L'utilisation d'aimants permanents positionnés de manière statique à la surface du patient a l'avantage d'être simple et très peu coûteuse. Cependant, cette approche est fortement limitée en termes de capacités de contrôle puisque, en général, seules des forces d'attraction magnétique vers l'aimant peuvent être générées. Une exception est la méthode proposée par Shapiro *et al.* [43] qui, à l'aide de deux aimants positionnés à angle l'un de l'autre d'une manière spécifique, est aussi capable de repousser des particules magnétiques. En général, le ciblage de tumeurs avec ces méthodes est basé sur l'extravasation des particules vers l'extérieur des vaisseaux sanguins lorsque celles-ci circulent dans la région soumise au champ magnétique, puis par leur diffusion à travers les tissus dans la direction de l'aimant. Étant donné que les agents thérapeutiques ne sont pas guidés directement à partir du point d'injection vers une cible, il peut en résulter une toxicité secondaire affectant les tissus et organes sains, même si leur concentration est supérieure dans la région ciblée.

Pour le guidage magnétique de dispositifs en général, de meilleures capacités de contrôle et une plus grande flexibilité peuvent être obtenues en contrôlant robotiquement la position d'un ou plusieurs aimants. Ainsi, des systèmes de guidage de capsules endoscopiques ont été proposés [44–47], de même que pour la manipulation de tiges élastiques pour des tâches chirurgicales [48] ou la propulsion d'un microrobot hélicoïdal [49]. La plateforme commerciale de guidage de cathéter Niobe de Stereotaxis [50], dont une image est présentée à la Fig. 2.6, fonctionne également sous ce principe en contrôlant l'orientation de deux gros aimants, placés de chaque côté du patient et générant un champ uniforme d'environ 0.08 T, afin d'orienter l'embout magnétique d'un cathéter. En général, ces systèmes robotiques permettent de contrôler la pose d'un dispositif magnétique avec jusqu'à cinq degrés de liberté (3 translations et 2 rotations). Le sixième, plus difficile à contrôler, correspond à la rotation du dispositif autour de son axe de magnétisation. Le niveau de contrôle de ces méthodes demeure néanmoins limité par des changements de direction plutôt lents des forces induites sur les agents magnétiques.

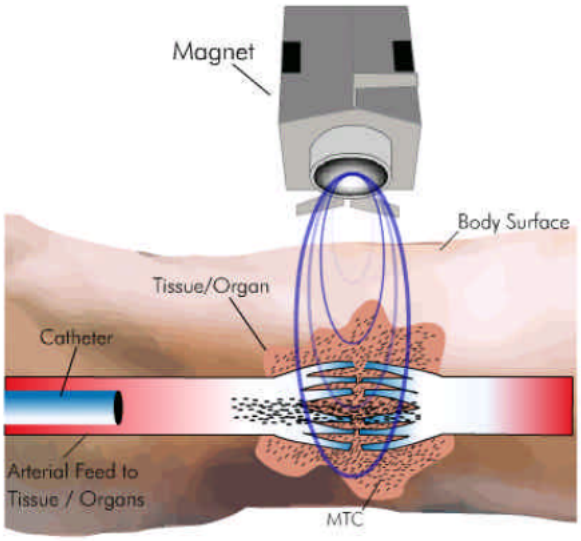

Figure 2.5 Illustration du ciblage de particules magnétiques à l'aide d'un aimant permanent positionné à la surface du patient, très près de la zone ciblée. Image tirée de [38].

Elles sont donc adaptées davantage au guidage de dispositifs se déplaçant relativement lentement, comme les capsules endoscopiques ou les embouts de cathéters, plutôt qu'à des agents transportés par des débits sanguins rapides dans le réseau vasculaire.

Dans tous les cas, la principale limitation des méthodes utilisant des aimants permanents est reliée à la décroissance rapide (exponentielle) du champ et du gradient magnétique en fonction de la distance. D'une part, le faible champ généré dans les tissus profonds ($<0.1\,\mathrm{T}$) ne suffit pas à saturer la magnétisation des agents. D'autre part, les gradients résultants dans les tissus profonds sont aussi trop faibles pour induire des forces de propulsion suffisantes sur des nanoparticules ou micro-agents magnétiques. Cette approche, qui est donc fortement affectée par la profondeur, est par conséquent limitée au ciblage d'agents thérapeutiques dans les tissus de surface, au guidage de dispositifs plus gros (ex : capsules) aimantés de manière permanente, ou encore au guidage de dispositifs plus petits (ex : embouts de cathéters) mais qui ne peuvent être qu'orientés par des couples magnétiques.

2.4.2 Utilisation d'aimants supraconducteurs

Récemment, une méthode baptisée Fringe Field Navigation (FFN) [51] a été proposée afin d'opérer dans un champ magnétique plus fort avec des gradients élevés. Celle-ci consiste à positionner le patient dans le champ de franges d'un aimant supraconducteur, comme par exemple l'électroaimant principal d'un appareil d'imagerie par résonance magnétique (IRM).

Figure 2.6 Système Niobe de Stereotaxis, composé d'une paire d'aimants permanents dont les rotations sont contrôlées afin d'orienter un dispositif magnétique (cathéter ou capsule endoscopique) dans le corps d'un patient [50].

Le champ généré par un aimant supraconducteur est en effet beaucoup plus puissant que celui des aimants conventionnels. En utilisant un appareil d'IRM clinique de 1.5 T, par exemple, le champ magnétique peut atteindre 0.5 T dans les tissus profonds, avec des amplitudes de gradients élevées de 1-2 T/m. Les variations d'amplitude et de direction des forces et des couples induits sont obtenues en déplaçant et en réorientant le patient, de manière robotisée, dans la région périphérique de l'aimant. Cette méthode est donc limitée par des changements de direction des forces plutôt lents qui ne permettent pas le guidage d'agents autonomes dans des réseaux vasculaires complexes. Pour cette raison, la méthode FFN est destinée principalement au guidage de cathéters.

Des aimants supraconducteurs en bloc peuvent aussi générer des champs magnétiques nettement supérieurs à ceux des aimants permanents conventionnels. Des travaux utilisant un aimant supraconducteur de 4.5 T pour le ciblage de nanoparticules ont d'ailleurs été menés [52], dans lesquels des nanoparticules de magnétite ont été guidées à travers une bifurcation avec une efficacité de 67%, malgré une vitesse de flot de 20 cm/s, par un champ et un gradient de 0.088 T et 4.3 T/m à une distance de 5 cm de l'aimant. Des aimants supraconducteurs plus puissants, avec un champ interne pouvant atteindre jusqu'à plus de 17 T [53, 54], pourraient potentiellement être utilisés pour augmenter davantage les forces de guidages dans les tissus profonds. De tels aimants peuvent cependant être plus complexes à fabriquer et à magnétiser,

en plus de devoir demeurer refroidis sous une température critique, ce qui peut nécessiter des équipements relativement encombrants et contraignants pour leur placement très près du corps du patient. Par ailleurs, tout comme les aimants permanents conventionnels, les capacités de contrôle pour le guidage endovasculaire demeurent limitées par des forces attractives principalement vers l'aimant.

2.4.3 Systèmes à actionnement électromagnétique

Pour réaliser le contrôle plus rapide et précis de dispositifs magnétiques, des systèmes à base de bobines électromagnétiques ont été proposés. Ces systèmes, dits à actionnement électromagnétique (AEM), permettent d'induire des variations rapides du champ et des gradients dans un certain volume de travail en faisant fluctuer le courant électrique circulant dans chacune des bobines. Comme les systèmes à aimants permanents robotisés, ils permettent de contrôler en général jusqu'à cinq degrés de liberté (3 translations et 2 rotations), selon le nombre de bobines employées [55]. Le contrôle des six degrés de liberté peut être réalisé, mais requiert une magnétisation non uniforme de l'agent [56, 57]. Parce que la flexibilité et les fréquences de contrôle sont potentiellement beaucoup plus élevées que les systèmes à aimants permanents, les systèmes à AEM sont mieux adaptés aux tâches de guidage complexes.

De nombreuses variantes de systèmes à AEM, composés de différents arrangements de bobines, ont été proposées pour diverses applications. Le système Octomag [58], par exemple, est une plateforme à huit bobines positionnées autour de la tête du patient qui a été proposée pour contrôler, selon cinq degrés de liberté, un petit dispositif injecté dans l'œil afin de réaliser des chirurgies intraoculaires minimalement invasives. L'efficacité de ce système a été validée in vivo en contrôlant un petit outil chirurgical cylindrique de $0.3\times1.8\,\mathrm{mm}$ inséré dans l'œil de lapins [59]. Les gradients magnétiques générés par les bobines atteignent jusqu'à $1\,\mathrm{T/m}$ dans un volume de travail d'environ $20\,\mathrm{mm}$ de diamètre, mais avec un champ faible de $40\,\mathrm{mT}$ [59]. Une photographie du système est présentée à la Fig. 2.7. Similaire, le Minimag est une version miniaturisée du Octomag qui a été proposée pour la micromanipulation de particules ou de cellules biologiques [60] et qui peut dans son cas atteindre des amplitudes de champ et de gradient allant jusqu'à $50\,\mathrm{mT}$ et $5\,\mathrm{T/m}$ dans une zone de travail de $10\,\mathrm{mm}$ de diamètre. Des systèmes électromagnétiques ont également été proposés pour le guidage de capsules endoscopiques [17, 61–63]. En particulier, le Magnetically Guided Capsule Endoscope (MGCE) [61], développé conjointement par Siemens et Olympus, a été évalué positivement dans une étude clinique. Dans [62], l'utilisation de bobines mobiles (plutôt que fixes) est proposée pour augmenter la flexibilité de contrôle et réduire le nombre de bobines requises.

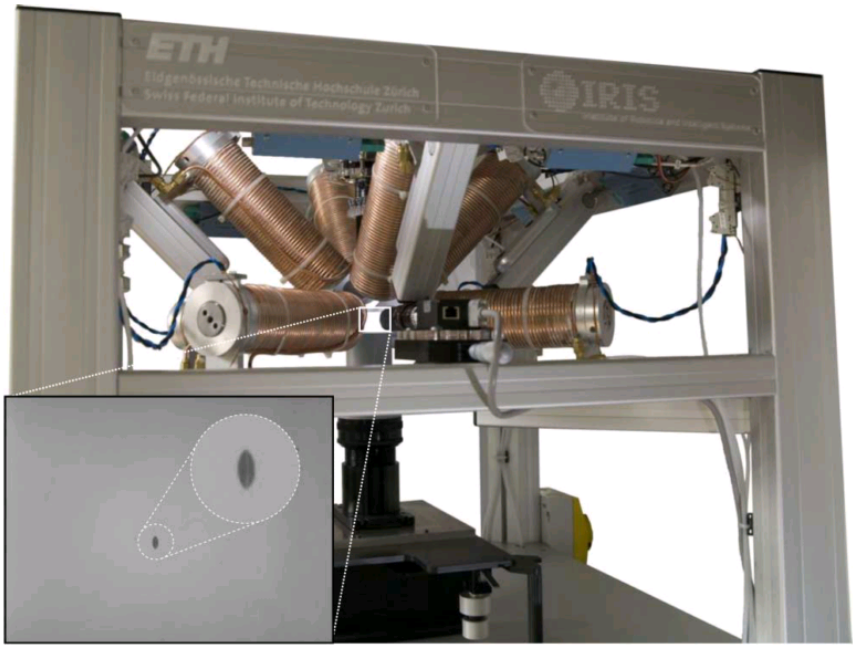

Figure 2.7 Le système Octomag, composé de huit bobines électromagnétiques, permet le contrôle avec cinq degrés de liberté d'un petit dispositif pour accomplir des microchirurgies oculaires. Image tirée de [58].

D'autres plateformes basées sur l'actionnement électromagnétique ont été développées pour le guidage de dispositifs à l'intérieur des vaisseaux sanguins [64–67]. En particulier, des résultats intéressants ont été obtenus récemment pour le traitement in vivo d'une thromboembolie artificielle dans une artère de cochon à l'aide d'un outil magnétique en forme de projectile de 2 mm de diamètre par 15 mm de longueur [68]. Le système utilisé, illustré à la Fig. 2.8, est composé de deux paires de bobines fixes et de deux paires de bobines rotatives pouvant tourner autour du patient. Ces dernières permettent d'augmenter à cinq le nombre de degrés de liberté (par rapport à trois si elles étaient fixes), mais en sacrifiant toutefois de la rapidité pour induire des variations de forces et de couples dans certaines directions. Les systèmes commerciaux de guidage de cathéter Aeon Phocus de Aeon Scientific [69] et CGCI de Magnetecs [70] exploitent également la propulsion par AEM. Le système Aeon Phocus, composé de huit bobines (cinq degrés de liberté), est illustré à la Fig. 2.9. Avec une approche différente, une configuration orthogonale de six bobines entourant un corps ferromagnétique a été proposée sous le nom de Omnimagnet [71]. Ce dernier permet de générer un dipôle magnétique dont la direction et l'amplitude peuvent être variées en contrôlant le courant dans les bobines. L'Omnimagnet permet de guider selon trois degrés de liberté un dispositif situé à l'extérieur de cet assemblage de bobines. La combinaison de plusieurs Omnimagnets, dont la configuration

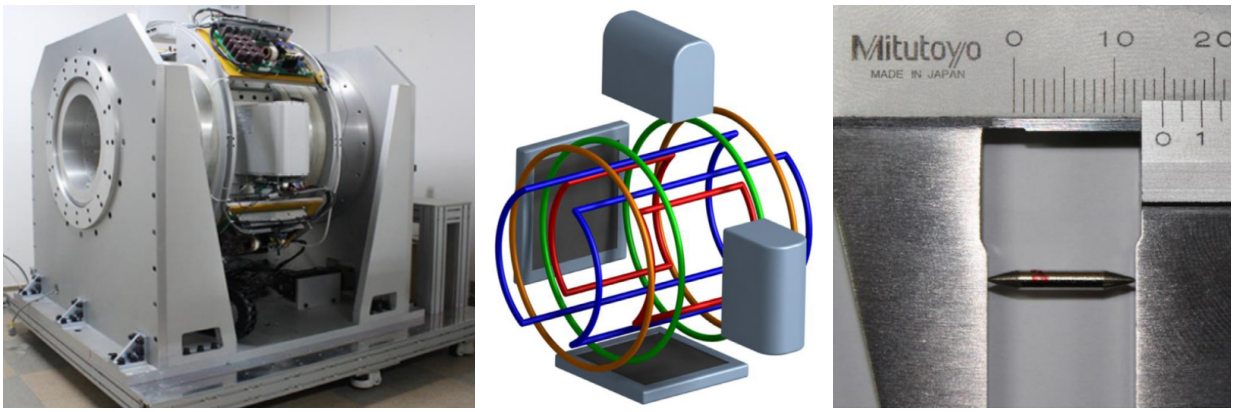

(a) (b) (c)

Figure 2.8 Système à actionnement électromagnétique développé par Jeong *et al.* pour diriger un dispositif dans les artères [68]. a) Photo du prototype ; b) Schéma de la configuration des bobines fixes (oranges et vertes) et rotatives (bleues et rouges). Des sources et détecteurs de rayons X (en gris) permettent le suivi du dispositif ; c) Dispositif, usiné dans un aimant permanent, dirigé avec succès dans une artère de cochon. Images tirées de [68] avec permission.

(a) (b)

Figure 2.9 Deux points de vue de la plateforme commerciale de guidage de cathéter Aeon Phocus de Aeon Scientific [69]. Le système est composé de huit bobines électromagnétiques et permet de guider un embout de cathéter avec cinq degrés de liberté. Images tirées de [69].

spatiale peut être optimisée selon l'application visée, a ensuite été proposée pour atteindre cinq degrés de liberté de guidage et réduire les singularités de contrôle [72]. Des travaux récents suggèrent par ailleurs l'actionnement électromagnétique en utilisant le principe de fonctionnement d'une nouvelle modalité d'imagerie de nanoparticules connue sous le nom de Magnetic Particle Imaging (MPI) [73]. Les systèmes de MPI génèrent, à l'aide de bobines, des champs magnétiques opposés s'annulant à un point appelé *field free point*. L'actionnement par MPI est réalisé en déplaçant la position de ce point afin de placer les particules dans une zone de fort gradient. Cette stratégie a permis de guider et de localiser en alternance

un agrégat de nanoparticules dans un tube avec des gradients magnétiques de 3.5-8.75 T/m, mais dans un petit volume de travail d'environ 4 cm de diamètre et avec une fréquence de rétroaction de contrôle de 2 Hz seulement.

À l'instar des méthodes utilisant des aimants permanents, la limitation majeure des systèmes à AEM pour le guidage de micro-agents dans les tissus profonds est reliée aux valeurs de champs et de gradients devenant insuffisantes lorsque ceux-ci sont mis à l'échelle avec des volumes de travail assez grands pour accueillir un humain. En effet, bien que les forces de contrôle puissent atteindre des amplitudes élevées dans des volumes restreints, comme c'est le cas du Octomag par exemple, les systèmes à AEM dimensionnés à l'échelle humaine sont actuellement limités à des champs de ~0.1 T et des gradients <400 mT/m dans les tissus profonds [74]. La plateforme Aeon Phocus mentionnée plus haut, par exemple, génère des gradients de 350 mT/m, mais un champ faible (<0.1 T), insuffisant pour atteindre la saturation magnétique des agents. En règle générale, pour des interventions dans les tissus et organes profonds, les systèmes à AEM sont par conséquent mieux adaptés à la navigation de dispositifs relativement gros, ayant des dimensions de quelques millimètres ou plus. Dans plusieurs cas, les dispositifs sont aussi constitués d'un aimant permanent afin de garantir une magnétisation élevée et des forces de guidage suffisantes.

2.4.4 Navigation par résonance magnétique

Pour le guidage de micro-agents dans les tissus profonds à l'échelle humaine, il est particulièrement difficile d'atteindre les champs de plusieurs centaines de milliteslas (et plus) requis pour amener les agents à leur saturation magnétique. Pour surmonter ce problème, une méthode connue sous le nom de *Magnetic Resonance Navigation* (MRN) a été proposée [75] (Fig. 2.10a), dans laquelle le puissant champ magnétique généré par l'aimant supraconducteur à l'intérieur d'un appareil d'IRM est utilisé pour saturer les agents (ex : TMMCs) à naviguer. Les appareils cliniques conventionnels génèrent en effet un champ statique et uniforme très fort, typiquement de l'ordre de 1.5-3 T, qui est plus que suffisant pour atteindre la saturation magnétique de la majorité des matériaux magnétiques indépendamment de la profondeur à laquelle ils se trouvent dans le corps du patient. Les appareils d'IRM sont composés également de bobines électromagnétiques servant à générer les gradients magnétiques nécessaires aux séquences d'imagerie. Il a été démontré que ces bobines peuvent être utilisées pour générer et contrôler en temps réel les forces de guidage [77–79]. Parce que la direction du champ magnétique dans l'appareil est fixe, MRN ne permet d'induire que des forces directionnelles de guidage (trois degrés de liberté). La faisabilité de cette méthode a été démontrée in vivo,

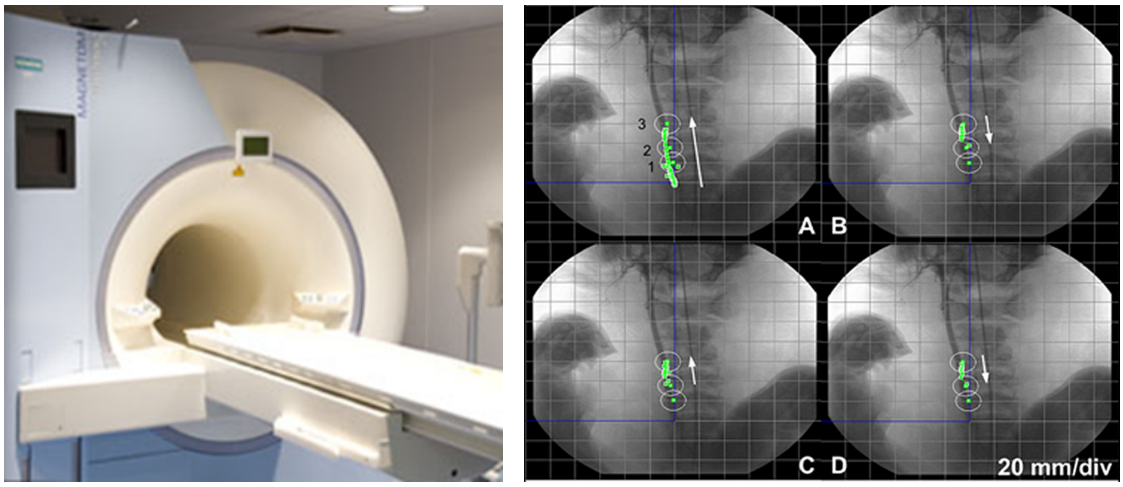

(a) Appareil clinique d'IRM (gauche) et guidage in vivo d'une bille ferromagnétique dans l'artère carotide d'un cochon (droite, image tirée de [75]).

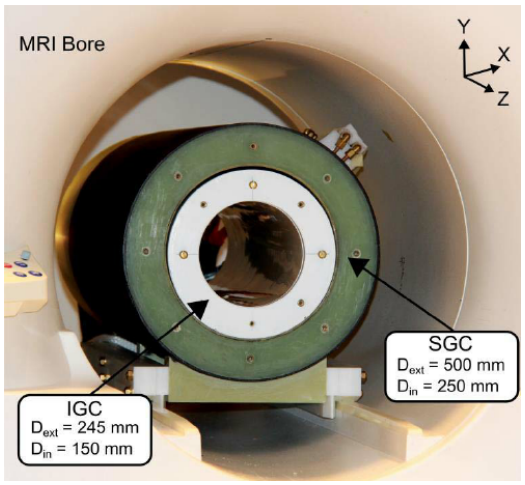

(b) Bobines de propulsion capables de générer des gradients de 300 mT/m. Image tirée de [76].

Figure 2.10 a) La méthode de navigation par résonance magnétique exploite le puissant champ généré par un appareil d'IRM. b) Des bobines pouvant générer des gradients plus forts peuvent être ajoutées, mais en sacrifiant une grande partie de l'espace disponible dans le tunnel.

d'abord par la navigation d'une bille ferromagnétique de 1.5 mm dans l'artère carotide d'un cochon [75], puis par le guidage de TMMCs vers un lobe ciblé du foie chez des lapins [16, 80].

La limitation majeure de MRN est liée aux amplitudes maximales des gradients pouvant être générés par les appareils d'IRM cliniques conventionnels. Ceux-ci sont actuellement limités à des maximums de l'ordre de 40-80 mT/m [81–83]. La surchauffe des bobines de gradients représente par ailleurs un problème potentiel qui limite davantage les amplitudes de gradients utilisables et/ou les durées d'intervention possibles [76]. Même avec la saturation magnétique

des agents, les amplitudes de gradients atteignables avec MRN, qui sont par conséquent significativement inférieures aux 200-400 mT/m désirés (voir Section 2.2.1), ne permettent de réduire le diamètre des agents qu'à quelques centaines de micromètres, limitant ainsi la navigation aux artères. Pour naviguer efficacement des TMMCs de plus petit diamètre ($<$100 μm) avec cette méthode, le débit sanguin doit être significativement réduit à l'aide d'un cathéter ballon afin d'augmenter la durée de l'effet des gradients pour attirer les TMMCs vers la branche vasculaire désirée. Bien qu'il existe des appareils d'IRM à ultra-hauts gradients capables d'atteindre des amplitudes de 300 mT/m [84], ces systèmes, présentement dédiés surtout à la recherche, sont beaucoup plus coûteux et ne sont pas largement disponibles. Comme solution plus accessible, des bobines de gradients additionnelles, dédiées à la propulsion des micro-agents, ont été ajoutées dans un appareil d'IRM [15] (voir Fig. 2.10b). Celles-ci permettent de générer des gradients de 300+ mT/m, mais le diamètre interne du tunnel (~15 cm) devient alors trop petit pour mener des interventions chez l'humain.

D'autre part, une difficulté fondamentale de MRN concerne la synchronisation des gradients pendant le guidage afin d'effectuer les changements de directions aux moments appropriés lors du transit des particules le long de trajectoires vasculaires complexes. Jusqu'à maintenant, MRN a pu être validée in vivo pour une seule bifurcation [16, 80]. Le guidage multi-bifurcations a été réalisé in vitro [85], mais en synchronisant les moments de transition des gradients manuellement, par essais et erreurs, et non de manière automatique. Considérant la complexité de l'environnement vasculaire, cet aspect représente un défi important pour la réussite de MRN in vivo dans les trajectoires multi-bifurcations.

2.4.5 *Magnetic Resonance Targeting*

Il est pertinent de mentionner également une autre méthode de ciblage, similaire à MRN mais différente, utilisant un appareil d'IRM. Celle-ci, appelée *Magnetic Resonance Targeting* [86], utilise les bobines d'imagerie de l'appareil pour générer des gradients pulsés et orientés vers une zone ciblée afin d'y favoriser l'accumulation de particules magnétiques. Contrairement à MRN, ces particules sont cependant injectées de manière systémique dans le réseau sanguin. Cette méthode, qui a été testée avec succès in vivo en utilisant des gradients de 300 mT/m à l'aide d'un appareil d'IRM préclinique ne pouvant accueillir que de très petits animaux comme des souris, possède les mêmes limitations que MRN en ce qui concerne les gradients pouvant être générés à l'échelle humaine.

2.5 Cartographie du réseau vasculaire et suivi des agents thérapeutiques pendant le guidage

Pour réaliser le guidage endovasculaire d'agents thérapeutiques, la cartographie tridimensionnelle du réseau vasculaire reliant le point d'injection à la région ciblée est requise. Cette information doit être suffisamment précise pour permettre d'identifier correctement tous les points de bifurcations sur la trajectoire menant à la cible. D'autre part, les agents navigués doivent idéalement pouvoir être localisés pendant le guidage afin de permettre d'ajuster si nécessaire les paramètres de contrôle et ainsi d'assurer le succès de l'intervention.

Traditionnellement, des angiographies peuvent être obtenues par rayons X avec l'injection d'un agent de contraste dans les vaisseaux sanguins. Pour obtenir des images en trois dimensions, la tomographie assistée par ordinateur (*CT-scan*) consiste à reconstruire une image 3D à partir de plusieurs images 2D acquises, correspondant à plusieurs projections selon différentes orientations autour du patient. De façon similaire, l'angiographie numérique par soustraction permet de rehausser le contraste des vaisseaux en calculant la différence entre des images acquises avec et sans agent de contraste. Un exemple d'image obtenue avec cette méthode est présenté à la Fig. 2.11. La résolution maximale des images est typiquement d'environ 200 μm, ce qui permet de cartographier les petites artères mais reste insuffisant pour visualiser les artérioles. Par ailleurs, le principal inconvénient de cette technique est l'exposition du patient à des doses de radiations ionisantes, même si les systèmes modernes permettent de réduire grandement ces dernières par rapport aux systèmes plus anciens [87].

Une alternative sans radiations ionisantes est l'angiographie par IRM, avec ou sans agent de contraste. La résolution obtenue par les séquences d'imagerie conventionnelles est cependant inférieure à celle de l'imagerie par rayons X, soit d'environ 500 μm. Pour permettre la détection de plus petits vaisseaux, une solution possible consiste à utiliser des particules magnétiques comme agents de contraste. En effet, étant donné que cette modalité d'imagerie est très sensible aux inhomogénéités du champ magnétique, les distorsions locales causées par ces particules peuvent générer des artéfacts plus gros que la résolution (i.e. taille d'un voxel), ce qui permet de les détecter dans les images. Cette distorsion peut d'ailleurs servir à valider le succès du ciblage pendant ou après le guidage [41, 80]. Ainsi, ce phénomène pourrait être exploité pour visualiser les petits vaisseaux sanguins ($<$100 μm) avec une résolution beaucoup plus fine. Cette idée a été démontrée in vitro en injectant des agrégats de nanoparticules de magnétite puis en les imageant à l'aide de séquences d'IRM rapides pendant leur transit dans un réseau de tubes en verre, ce qui a permis de cartographier progressivement ce dernier [89]. Par ailleurs, basée sur

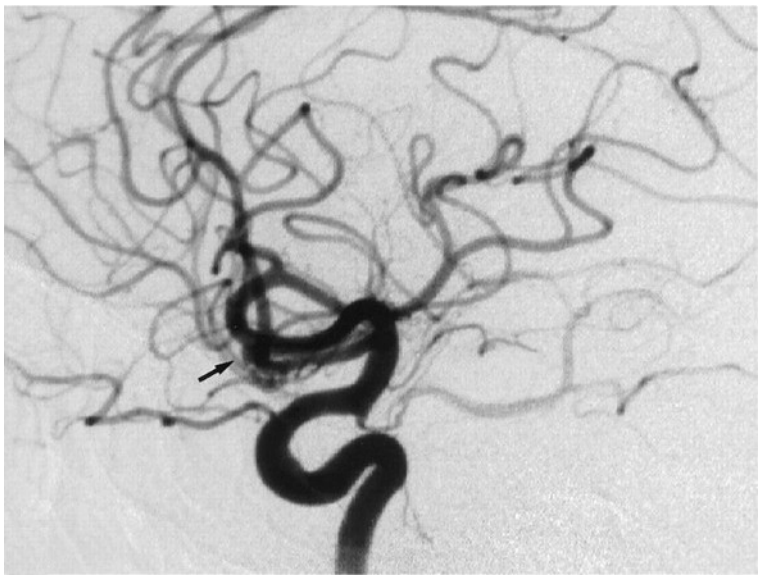

Figure 2.11 Exemple d'angiographie numérique par soustraction. Image tirée de [88].

le même phénomène, une séquence d'imagerie nommée *Magnetic Signature Selective Excitation* (MS-SET) [90] a été proposée pour localiser rapidement des particules magnétiques en trois dimensions. Pour la méthode MRN, cette capacité permet notamment le contrôle en boucle fermée d'agents le long d'une trajectoire prédéfinie, en alternant des phases de propulsion et des phases d'imagerie [77, 79]. Originellement, la séquence MS-SET a permis de localiser une bille ferromagnétique de 1.5 mm avec une fréquence de rafraichissement de 24 Hz. Pour de petites particules, toutefois, le temps de localisation augmente significativement, réduisant par exemple cette fréquence à environ 3 Hz pour des particules de 900 μm [91]. Cette diminution importante du taux de rafraichissement est problématique pour le guidage de particules encore plus petites. Récemment, il a été démontré que les gradients de propulsion peuvent être intégrés à même la séquence MS-SET afin de réaliser l'imagerie et la propulsion simultanément [92]. Dans ce cas, la localisation de l'agent est réalisée selon une seule dimension, soit dans la direction de son déplacement, ce qui permet du même coup d'augmenter significativement la fréquence de rafraîchissement. Alors qu'avec la séquence d'origine aucune force de propulsion n'est générée pendant la phase d'imagerie, cette séquence modifiée permet de générer 90% de la force correspondant à un gradient constant pour une fréquence de contrôle de 52 Hz, et 63% de la force à 182 Hz (bille de 2 mm).

Par ailleurs, une autre technique prometteuse et présentement à l'étude pour l'imagerie des vaisseaux sanguins est l'angiographie par MPI [93]. Cette méthode, qui utilise des nanoparticules magnétiques comme traceurs, a le potentiel de permettre de cartographier les

vaisseaux avec une bonne résolution spatiale et une plus grande rapidité que l'IRM, toujours sans émettre de radiations ionisantes [93]. De par son principe de fonctionnement, cette méthode permet également de suivre des agents navigués [73]. À cet égard, il faut toutefois noter que, comme les autres systèmes à AEM et tel que mentionné à la Section 2.4.3, il est probable que l'efficacité d'un appareil de MPI pour guider des micro-agents à l'échelle humaine dans les tissus profonds demeure fortement limitée.

CHAPITRE 3 DÉMARCHE SCIENTIFIQUE ET PRÉSENTATION DES ARTICLES

En distordant le puissant champ d'un appareil d'IRM, le guidage par champs de dipôles (DFN) permet de garantir la magnétisation à saturation des agents magnétiques, indépendamment de leur profondeur dans le patient, tout en ayant le potentiel de générer des gradients forts dans les tissus profonds. Le paramétrage adéquat des corps ferromagnétiques (nombre, tailles, positions, formes, etc.) requiert toutefois des modèles et algorithmes complexes et doit être effectué en tenant compte des caractéristiques spécifiques de la trajectoire à suivre dans le réseau vasculaire. Par ailleurs, les matériaux magnétiques étant typiquement incompatibles avec l'environnement d'IRM, ceux-ci peuvent représenter un certain risque et affecter l'imagerie. Les meilleures performances possibles doivent donc être recherchées tout en minimisant la quantité de matériau magnétique insérée dans l'appareil.

Les principaux aspects de DFN abordés dans cette thèse sont le positionnement adéquat des corps ferromagnétiques étant donnée une trajectoire vasculaire à suivre, les effets de leur présence dans l'appareil d'IRM sur les capacités à utiliser cette modalité d'imagerie, l'influence de la forme des corps ferromagnétiques sur les gradients générés dans les tissus profonds ainsi que les capacités et limites de la méthode pour le guidage multi-bifurcations le long de trajectoires vasculaires complexes. Ce qui suit présente les articles, publiés ou en cours d'évaluation, dans lesquels les principaux résultats ont été rapportés.

3.1 Positionnement des corps ferromagnétiques et preuve de concept : article « *Dipole Field Navigation : Theory and Proof of Concept* »

Cet article a été publié en novembre 2015 dans la revue *IEEE Transactions on Robotics* [94]. Ces travaux sont la suite d'un premier article publié en août 2014 dans *IEEE International Conference on Biomedical Robotics and Biomechatronics* (BioRob) [95], mais non inclus ici par souci de concision car la plupart des aspects présentés sont repris dans le deuxième. En quelques mots, le premier article présentait des travaux exploratoires et une modélisation de base permettant de valider le principe de fonctionnement de DFN. Il y est montré que les amplitudes de gradients peuvent excéder 300 mT/m dans les tissus profonds (~10 cm) en utilisant un corps ferromagnétique sphérique de 4 cm de rayon.

L'article de novembre 2015 présente des modèles et un algorithme permettant de positionner

adéquatement un ensemble de corps ferromagnétiques en fonction d'un ensemble de gradients désirés à des endroits spécifiques (*points de contrôle*). En formulant le problème de positionnement des corps ferromagnétiques comme un problème d'optimisation non linéaire et non convexe, l'algorithme proposé combine un arbre de recherche avec des optimisations locales alternées. Cet algorithme permet aussi de minimiser le nombre de corps ferromagnétiques utilisés. La faisabilité de DFN est démontrée par le guidage de particules à travers trois bifurcations consécutives dans un réseau in vitro en trois dimensions. Les corps ferromagnétiques utilisés sont des billes placées au-dessus d'un plan imaginaire représentant la surface du corps d'un patient. Le taux de ciblage obtenu est supérieur à 90%.

3.2 Imagerie en présence de corps ferromagnétiques : article « *Enabling automated magnetic resonance imaging-based targeting assessment during dipole field navigation* »

Cet article a été publié en février 2016 dans la revue *Applied Physics Letters* [96]. Tel que mentionné précédemment, les agents thérapeutiques doivent idéalement pouvoir être localisés pendant le guidage afin d'apporter les ajustements nécessaires. Or, les fortes distorsions du champ autour des corps ferromagnétiques sont susceptibles de rendre impraticable l'imagerie durant le guidage. En effet, la reconstruction des images en IRM requiert traditionnellement un champ magnétique (presque) parfaitement homogène. Les inhomogénéités du champ, engendrées par des implants métalliques par exemple, causent des artéfacts dans les images. Cet article démontre que l'imagerie autour d'un corps ferromagnétique est en fait possible, dans une certaine mesure, dans des régions spécifiques et suffisamment éloignées. Dans ces régions, la qualité des images obtenues est suffisante pour permettre de valider l'atteinte de la cible par les agents navigués. Des expérimentations in vitro démontrent la faisabilité d'une stratégie dans laquelle un corps ferromagnétique serait périodiquement et automatiquement éloigné du patient (tout en demeurant dans le tunnel de l'appareil) et positionné de sorte à minimiser les effets de la distorsion dans la région d'intérêt à imager. Ces résultats, bien que démontrant que des validations ponctuelles du ciblage sont envisageables, renforcent donc la dépendance de DFN sur des modèles et algorithmes précis pour assurer le succès du guidage, puisque celui-ci doit être réalisé principalement à l'aveugle, sans rétroaction en temps réel.

3.3 Paramétrage de configurations de corps ferromagnétiques : article « *A Progressive Multidimensional Particle Swarm Optimizer for Magnetic Core Placement in Dipole Field Navigation* »

Cet article de conférence a été présenté et publié en octobre 2016 dans *IEEE/RSJ International Conference on Intelligent Robots and Systems* (IROS) [97]. Bien qu'efficace, le premier algorithme de positionnement de corps ferromagnétiques, introduit ci-dessus, comporte certaines limitations, notamment en termes de complexité algorithmique lorsque le nombre de points de contrôle des gradients augmente, ou lorsque plusieurs tailles de corps ferromagnétiques sont considérées. La seconde approche, décrite dans cet article et proposée pour pallier certaines limitations de la première, est basée sur une nouvelle variante proposée de l'optimisation par essaims particulaires (PSO). Cette variante multidimensionnelle de PSO, abrégée PMD-PSO, permet d'augmenter progressivement la dimensionnalité de l'espace de recherche et retourne la meilleure solution trouvée pour chaque dimensionnalité considérée. Une série de tests effectués sur des réseaux vasculaires générés aléatoirement démontre que cette variante converge mieux et plus rapidement que l'algorithme PSO standard pour le problème de positionnement de corps ferromagnétiques. De plus, PMD-PSO permet d'effectuer un compromis entre la qualité des gradients générés et le nombre de corps ferromagnétiques utilisés (i.e. nombre de dimensions) à partir de l'ensemble des solutions retournées.

3.4 Forme des corps ferromagnétiques : article « *Seeking Optimal Magnetic Core Shapes for Strong Gradient Generation in Dipole Field Navigation* »

Cet article de conférence a été accepté pour présentation et publication (juillet 2017) dans *IEEE International Conference on Manipulation, Automation and Robotics at Small Scales* (MARSS) [98]. Différentes formes de corps ferromagnétiques sont évaluées et comparées pour maximiser les amplitudes de gradients générés dans le patient. Les résultats, basés sur le calcul par éléments finis des gradients générés autour des différentes formes, montrent que les corps ferromagnétiques en forme de disque ou de demie-sphère génèrent, à volume égal, des gradients significativement supérieurs (gains >50%) aux corps sphériques dans les tissus profonds. Ces formes plus performantes permettent donc d'induire des forces de guidage plus élevées, ou encore de réduire la quantité de matériau ferromagnétique insérée dans l'appareil d'IRM. Ce dernier aspect, discuté plus en détail à la Section 9, est important afin de minimiser, d'une part, les forces d'attraction vers l'appareil lors de l'insertion des corps ferromagnétiques, et d'autre part, les forces d'interactions magnétiques s'exerçant entre ceux-ci lorsque magnétisés.

3.5 Potentiel de la méthode pour des interventions réelles : article « *Evaluation of the Potential of Dipole Field Navigation for the Targeted Delivery of Therapeutic Agents in a Human Vascular Network* »

Cet article a été soumis le 9 juin 2017 pour publication dans la revue *IEEE Transactions on Magnetics*. En utilisant des corps ferromagnétiques en forme de disques et en considérant les principales contraintes reliées à l'environnement d'IRM (ex : espace restreint autour du patient dans l'appareil), les amplitudes de gradients maximales pouvant être obtenues pour le guidage à une seule et à plusieurs bifurcations sont étudiées. Dépendamment de la distance séparant deux bifurcations, des gradients nettement supérieurs à MRN peuvent être générés, même dans les tissus profonds. Les résultats révèlent que certaines orientations de gradients sont cependant beaucoup plus difficiles à obtenir. Il est démontré que le fait de diviser un disque en deux disques plus petits, mais de volume total égal, peut améliorer significativement les performances de DFN pour générer certaines orientations de gradients. Le potentiel de la méthode pour le guidage de micro-agents dans un réseau vasculaire humain est évalué à l'aide d'un modèle d'artères hépatiques et de la surface du corps d'un patient, segmentés à partir de données *CT-scan* cliniques. Pour sept trajectoires vasculaires considérées dans ce modèle, dont six impliquent trois bifurcations, les amplitudes de gradients peuvent excéder 100-200 mT/m, mais au prix d'erreurs angulaires sur les directions de gradients générés. Ces tests confirment que, pour le guidage multi-bifurcations avec DFN, un compromis doit être fait entre l'amplitude et la précision des gradients générés le long de la trajectoire à suivre.

CHAPITRE 4 ARTICLE 1: DIPOLE FIELD NAVIGATION : THEORY AND PROOF OF CONCEPT

Maxime Latulippe and Sylvain Martel
IEEE Transactions on Robotics

4.1 Abstract

To achieve effective navigation of microscale agents in the vascular network, a high magnetic field strength with high directional magnetic gradients are required. So far, the methods that have been investigated support only one of these specifications but not both. Here, we propose a new method dubbed Dipole Field Navigation (DFN) that provides high field strength to bring magnetic agents at saturation magnetization with gradients exceeding 300 mT/m at any depth within the human body. For DFN, the high field strength is achieved by placing the patient in the tunnel of a clinical MRI scanner while high gradients are generated by the distortions of the scanner's homogeneous field from larger ferromagnetic cores placed at specific locations outside the patient. The main challenge of DFN lies in the methods required to adequately place the cores in the tunnel. Here, a first method is presented to solve the inverse magnetic problem of positioning such a set of cores so that microscale agents could be guided through a desired path in the vascular network. As a first proof of concept, magnetic particles were steered successfully in three consecutive bifurcations in a 3D in vitro network.

4.2 Introduction

Magnetic navigation of untethered devices in the human body is a promising technique for the development of new targeted, more efficient and less invasive medical interventions. In cancer therapy for instance, although most cancers are initially localized, modern treatments often involve the systemic administration of chemotherapeutics. Not only this approach generally leads to a tiny amount of the drugs reaching the tumor, but since these drugs do not differentiate between normal and cancerous cells, severe side effects arise due to healthy organs and tissues being affected. The design of therapeutics with enhanced specificity to tumor cells, known as active targeting, constitutes an important research field which has seen significant developments in the last decade [1, 2]. However, even these new anticancer drugs lead to suboptimal targeting levels when they are injected systemically [2]. As one possible solution, the controlled endovascular navigation of therapeutic agents, directly from

the injection site toward the region to be treated, is expected to yield enhanced therapeutic outcomes while minimizing secondary toxicity effects.

Such navigation is known as direct targeting and typically relies on the remote magnetic navigation of therapeutic agents consisting of magnetic nanoparticles (MNPs) embedded with drugs in a spherical matrix [3]. The MNPs are typically superparamagnetic, which makes them highly magnetizable when subject to a magnetic field, yet without remanent magnetization once removed from the field. This property provides a means of inducing pulling forces on the agents using magnetic gradients, and prevents their aggregation in the patient after the intervention. In addition, MNPs can act as magnetic resonance imaging (MRI) contrast agents for tracking or targeting efficiency evaluation [4, 5].

The simplest form of remote magnetic navigation, initially introduced more than 30 years ago [6–8] but also being developed more recently [9–11], consists in positioning a permanent magnet next to the targeted region in order to attract the agents. This approach, however, suffers from the rapid decay of the magnetic gradient and field strengths, thus preventing the navigation of MNPs in deep tissues. Moreover, due to the slow or lack of directional changes of the gradients, the control capabilities in complex vascular networks are very limited. Multicoil-based platforms, such as electromagnetic actuation systems [12–14] or the OctoMag [15] and MGCE [16] platforms, can provide fast variations of strong gradients by controlling currents in the coils, but still lack the magnetic field strength required to operate microscale agents at deeper regions in the body. Alternatively, Fringe Field Navigation was proposed recently [17], where the patient is positioned within the external fringe field of an MRI scanner and robotically moved in 6 degrees of freedom to induce variations of the gradients at the intervention site. Although it benefits from very high gradients, this approach achieves field strengths that are higher than all methods but Magnetic Resonance Navigation (MRN) [18, 19], while being limited by relatively slow directional changes of the gradients.

The most effective method to date to achieve direct targeting of therapeutic agents in the arterial network down to the arterioles is MRN, where the high uniform field generated by the superconducting magnet of an MRI scanner (1.5 T or higher) is sufficient to induce the depth-independent saturation magnetization of the MNPs, while directional imaging gradients offer fast variation capabilities. Conventional clinical MRI scanners are however typically limited to gradient magnitudes around 40 mT/m, which limits the velocity at which microscale agents can be navigated in the vascular network using MRN. This in turn extends the interventional time required to deliver a sufficient dose to the targeted area, especially when the total number of injections becomes significant. To shorten the total time required

for the navigation of microscale therapeutic agents, it was previously shown that gradients of the order 200-400 mT/m are required [20, 21]. Additional coil inserts capable of generating such gradients can be added in the tunnel of the scanner [20], but the resulting smaller diameter prevents whole-body interventions to be conducted. Although ultra-high gradient MRI scanners exist [22], these are much more expensive platforms and are not widely available. Furthermore, fast-switching gradients in MRN cause excessive heating of the coils [23], which limits the operating time for navigation in complex networks, and could potentially, with further advances in coil technology capable of much higher slew rates, induce peripheral nerve stimulation.

In this paper, we present new developments of the method Dipole Field Navigation (DFN), introduced recently to overcome the aforementioned constraints [24]. In DFN, the patient is positioned inside the tunnel of a clinical MRI scanner and therefore, as in MRN, the MNPs reach their saturation magnetization. The directional gradients are generated by positioning soft ferromagnetic cores at specific locations around the patient. These cores of a few centimeters in diameter induce a distortion of the uniform field in the scanner, which creates a magnetic path guiding the therapeutic agents. The main advantages of DFN are (1) depth-independent saturation magnetization of the MNPs, (2) strong directional gradients exceeding 300 mT/m in deep tissues, (3) whole-body interventions, (4) no peripheral nerve stimulation caused by fast switching gradients and (5) low cost of implementation (MRI are widely available platforms). An important challenge of DFN lies in the development of the models needed to predict the effect of the cores on the agents being navigated. In particular, in order to account for variations of the anatomy between patients and to be adapted to any targeted region in general, a method is needed to find working combinations of core positions and characteristics based on a desired vascular path. The accuracy of the models is crucial since real-time tracking of the agents through MR imaging would typically not be possible due to the field distortions in the scanner.

DFN can be categorized as static or dynamic. For static DFN (DFN-S), the magnetic cores are statically positioned and remain in the same position during the whole intervention. The main advantage of DFN-S is that continuous injections of the microscale agents are possible. To add flexibility to cope with various vascular configurations, dynamic DFN (DFN-D) could be considered where one or more cores are moved during the navigation process using, for example, the gradients generated by the MR-imaging coils. In DFN-D, continuous injection would not be possible. For more than one core operating under DFN-D, the cores should be encased in a special assembly with static and/or moving parts allowing independent

displacements of a particular core (addressability). A hybrid implementation dubbed DFN-H is also possible, where the navigation would be performed using both statically positioned and moving cores. This solution would add some flexibility without the increased complexity of navigating the agents using many moving cores. The proof of concept presented in this paper has been initially done with DFN-S only. The two other approaches (DFN-D and DFN-H) will be investigated in future studies.

Previous works have addressed the problem of parameterizing a set of magnetic sources in order to generate a given magnetic field. One possible solution when the positions of the sources are known is to build a matrix linear equation describing the system and solve it using the pseudo-inverse to find the optimal solutions [15, 25]. Although in [25] the electromagnetic coils used are allowed to move, the matrix equation is built once their positions are set, i.e., the coil positions and orientations are not part of the inverse problem. Other methods exist to localize and characterize dipoles from a set of measurements of the magnetic field, e.g., for the modeling of the magnetic field measured above the earth surface [26], for the electro- and magneto-encephalographic source localization [27] and for the modeling of the magnetic cleanliness of spacecrafts [28]. Here, we aim at developing a method specific to DFN such that the particularities of the core positioning problem are taken into account. In particular, a minimum separating distance must be respected between the centers of the cores to avoid unfeasible placements, the possible magnetic interactions must be considered, the solutions should consist of a minimal number of cores, and due to the nature of drug delivery there should be more importance accorded to achieving the first bifurcations on a vascular path.

In [24], we presented a solution to the magnetic inverse problem for positioning a single core and demonstrated the feasibility of DFN for guiding magnetic agents in one bifurcation. This paper presents a method for positioning multiple cores in DFN-S in order to guide therapeutic agents through consecutive bifurcations in a vascular network. Due to the cumulative contributions of the cores to the total gradients, and because of the possible magnetic interactions between them, the former method cannot be used directly to determine the positions of multiple cores. Here, we propose an incremental positioning algorithm, where cores are progressively added to a *core configuration* until the desired resulting magnetic gradients are met. Then, we present experimental results for the *in vitro* navigation of magnetic particles through three consecutive bifurcations in a 3D network.

4.3 Dipole Field Navigation

4.3.1 Magnetic Models

In presence of a static and homogeneous external magnetic field $\mathbf{B}_0$, a spherical ferromagnetic core becomes uniformly magnetized. For a core of radius R, the magnetic field generated is equivalent to that of a magnetic dipole and is given, at any point $\mathbf{r} = (x, y, z)$ around the core, by

$$\mathbf{B}(r > R) = \frac{\mu_0}{4\pi}\left[3\frac{(\mathbf{m}\cdot\mathbf{r})\mathbf{r}}{r^5} - \frac{\mathbf{m}}{r^3}\right] \tag{4.1}$$

where $\mu_0 = 4\pi \times 10^{-7}\,\mathrm{H/m}$ is the vacuum permeability, $r = \|\mathbf{r}\|$ and $\mathbf{m}$ is the magnetic moment of the core (parallel to $\mathbf{B}_0$), which in the case of a sphere has a magnitude

$$m = \frac{4\pi R^3}{3}M \tag{4.2}$$

The volume magnetization M of the core depends on the external field strength and on the ferromagnetic material used.

The addition of the field $\mathbf{B}$ to the external field $\mathbf{B}_0$ induces a distortion of the total magnetic field around the core. This distortion generates magnetic gradients that can be used to induce directional forces on magnetic particles circulating in the vicinity of the core. For a particle of magnetic moment $\mathbf{m}_p$, the magnetic force is

$$\mathbf{F}_{mag} = \nabla(\mathbf{m}_p \cdot \mathbf{B}_{tot}) \tag{4.3}$$

where $\mathbf{B}_{tot} = \mathbf{B}_1 + \mathbf{B}_2 + ... + \mathbf{B}_N$ is the summation of the magnetic fields generated by N cores. The field $\mathbf{B}_0$ can be omitted from the equation since it is homogeneous.

When the magnetic dipole-dipole interactions between cores and between cores and particles are negligible, (4.1) and (4.2) hold and all the magnetizations are approximately parallel to $\mathbf{B}_0$. This assumption can be respected for DFN in practice as explained below in Section 4.3.2. Let $\mathbf{B}_0 = B\hat{\mathbf{z}}$ be aligned with the z-axis. Therefore, (4.3) simplifies to

$$\mathbf{F}_{mag} \approx m_p \nabla B_{tot,z} = m_p \mathbf{G}_{tot} \tag{4.4}$$

which means that the force exerted on a magnetic particle depends on the gradient $\mathbf{G}_{tot}$ of the z-component of $\mathbf{B}_{tot}$ at the particle's location.

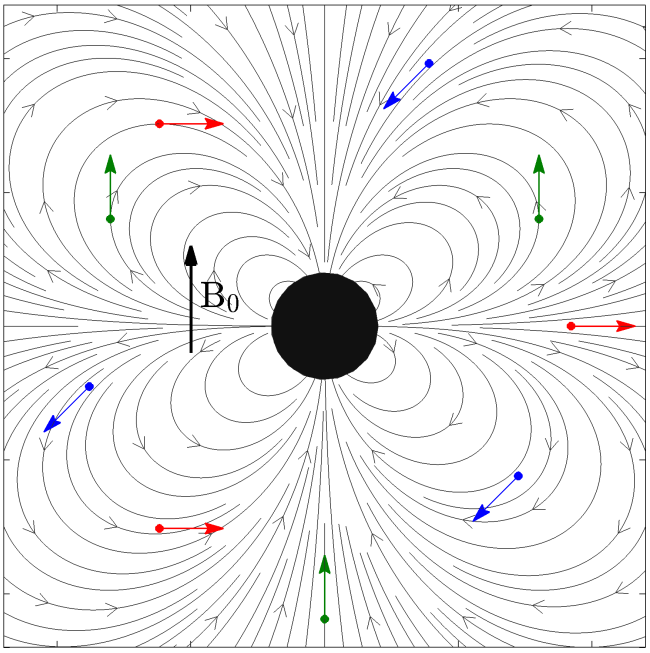

Figure 4.1 Magnetic gradient field around a magnetized spherical core. Arrows depict locations of same gradient orientations (same colors) and magnitudes.

For a core with $\mathbf{m} = m\hat{\mathbf{z}}$, (4.1) can be expressed as

$$\mathbf{B} = \frac{\mu_0 m}{4\pi r^5}\left[3xz\hat{\mathbf{x}} + 3yz\hat{\mathbf{y}} + (3z^2 - r^2)\hat{\mathbf{z}}\right] \tag{4.5}$$

Calculating the gradient of B_z yields

$$\begin{aligned}\mathbf{G} &= \nabla\left(\frac{\mu_0 m}{4\pi}\frac{3z^2 - r^2}{r^5}\right) \\ &= \frac{3\mu_0 m}{4\pi r^7}\begin{bmatrix} x\left(r^2 - 5z^2\right) \\ y\left(r^2 - 5z^2\right) \\ z\left(3r^2 - 5z^2\right)\end{bmatrix}^T\end{aligned} \tag{4.6}$$

This gradient field is symmetric around $\hat{\mathbf{z}}$, as illustrated in Fig. 4.1. For later convenience, (4.6) is converted to spherical coordinates using the convention illustrated in Fig. 4.2:

$$\mathbf{G} = \frac{3\mu_0 m}{4\pi r^4}\begin{bmatrix} \sin\theta\cos\phi\left(1 - 5\cos^2\theta\right) \\ \sin\theta\sin\phi\left(1 - 5\cos^2\theta\right) \\ \cos\theta\left(3 - 5\cos^2\theta\right)\end{bmatrix}^T \tag{4.7}$$

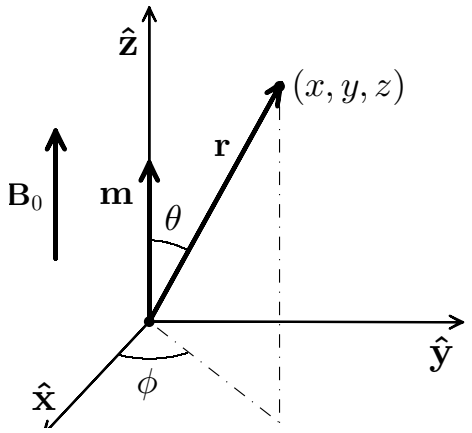

Figure 4.2 Convention used for spherical coordinates.

with $\mathbf{r} = (r, \theta, \phi)$ defined relative to the center of the core.

Finally, from the superposition principle, the total gradient resulting from N magnetized cores is

$$\mathbf{G}_{tot} = \sum_{n=0}^{N} \mathbf{G}_n \tag{4.8}$$

From the above equations, a set of adequately positioned ferromagnetic cores could shape the magnetic gradient field such that magnetic agents would preferentially follow a desired path in a vascular network. But such positioning of the cores is subject to physical constraints, e.g., cores cannot overlap on each other or be positioned inside the patient's body. These constraints may limit the number and complexity of the possible vascular paths through which agents can be guided. The feasibility of a path probably depends on several parameters, such as its depth in the patient's body, the number of bifurcations and the distance between those bifurcations.

Additionally, the magnitudes of the gradients generated are maximized when the core's material is at saturation magnetization. Since the high field (1.5 T or more) of a conventional MRI scanner is strong enough to saturate most magnetic materials, we assume in DFN that cores are at saturation magnetization.

4.3.2 Magnetic Interactions

Magnetic dipole-dipole interactions are possible in DFN if two magnetized cores are located close to each other. Such interactions can not only induce strong attractive or repulsive forces between the cores, but can also alter the magnitude and orientation of the magnetization

of the core material. This alteration can lead to the inaccuracy of the analytical models such as (4.1) and (4.2). For example, the actual average magnetization of two spheres in the attractive mode may be underestimated, whereas in repulsive mode it may be overestimated. No analytical models exist to calculate the magnetization of cores under interactions in general, thus these calculations are only available from numerical simulations.

Dipole-dipole interactions have been studied, for example for the calculation of attractive or repulsive forces between magnetized cores [29–31]. In particular, Mehdizadeh *et al.* [31] have shown that the magnetic dipole approximation for two identical soft ferromagnetic spheres immersed in an external field is reasonably accurate for $r/R > 4$, where r is the center-to-center distance between the spheres. Their work however addressed the case where the magnetizations of the spheres lie within the linear zone of the magnetization curve (M-H), where the variation of M is the largest as a function of the external field strength. In DFN, because the cores are close to or at full saturation magnetization (i.e., on the plateau region of M-H), we hypothesize that the interaction effects on the validity of the models could be less significant. In fact, as the strength of $\mathbf{B}_0$ increases over the material's saturation limit, the field generated by a core becomes less significant relative to $\mathbf{B}_0$ and the distortion is reduced (while gradient orientations and magnitudes remain constant around the core). Thus, in DFN, the dipole approximation limit $r/R > 4$ could be set at a closer distance between the cores. Nevertheless, this constraint is used throughout this work as a worst case since we do not want to address the problem of dipole-dipole interactions here. At distances over this limit, the magnetizations of cores and particles can be assumed to be parallel to $\mathbf{B}_0$, the dipole model (4.1) can be used and the approximation in (4.4) is valid.

4.3.3 Single Core Positioning

The method for positioning a single core presented in [24] is recalled here as it constitutes the basis for the multi-core positioning method presented in Section 4.4.

Let $\mathbf{G} = (G, \vartheta, \varphi)$ be the magnetic gradient desired at a point $\mathbf{p} = (x, y, z)$ in space, where ϑ and φ are the θ and ϕ equivalents used for the notation of a gradient orientation. As depicted in Fig. 4.1, for any given $\mathbf{G}$, there are always three positions around a spherical core where this gradient is met. The (ill-posed) problem of positioning a core requires the inversion of (4.6) in order to find these three possible solutions.

By exploiting the symmetry of the gradient around $\hat{\mathbf{z}}$, this inverse problem can first be solved in 2D in the xz-plane and then extended to 3D by performing a rotation of the solutions

around the z-axis. From (4.7), the gradient angle ϑ is related to the angle θ by the equation

$$\tan\vartheta = \frac{\sin\theta\,(1-5\cos^2\theta)}{\cos\theta\,(3-5\cos^2\theta)} = \frac{a}{b} \tag{4.9}$$

The three values θ_1, θ_2 and θ_3 solving this equation for any given angle ϑ can be found numerically (e.g., by interpolating in a lookup table). Then, for each of these solutions θ_i,

$$r_i = \left[\frac{3\mu_0 m}{4\pi G}\sqrt{a_i^2+b_i^2}\right]^{1/4}\ ,\ \ (i=1,2,3) \tag{4.10}$$

The three positions where $\mathbf{G}$ is found around the core are thus (Cartesian coordinates in the xz core's local frame)

$$\mathbf{r}_i = \begin{bmatrix} r_i\sin\theta_i \\ r_i\cos\theta_i \end{bmatrix}\ ,\ \ (i=1,2,3) \tag{4.11}$$

Finally, the possible core positions $\mathbf{d}_i = (x_i, y_i, z_i)$ in the 3D global reference frame are found by rotating solutions from (4.11) by the angle φ around $\hat{\mathbf{z}}$ and translating them by $\mathbf{p}$:

$$\mathbf{d}_i = \mathbf{R}_z(\varphi)\begin{bmatrix} -r_i\sin\theta_i \\ 0 \\ -r_i\cos\theta_i \end{bmatrix} + \mathbf{p}\ ,\ \ (i=1,2,3) \tag{4.12}$$

where $\mathbf{R}_z(\varphi)$ is the rotation matrix around the z-axis. The negative signs in (4.12) come from the required change in perspective to express the position of the core's center relative to each solution in (4.11).

Notice that the gradient magnitude is not constant as a function of θ for a fixed distance r. In fact, it is maximized at $\theta = 0$ and $\theta = \pi$, whereas it is minimized at $\theta \approx \pm 0.352\pi$ and $\theta \approx \pm 0.648\pi$. Fig. 4.3 shows the range of gradient magnitudes achievable around cores having a magnetization [1] $M = 1.43\times10^6\,\mathrm{A/m}$ and different radii, as a function of the distance to the surface of the core. Using this ferromagnetic material, a core of radius $R \approx 4\,\mathrm{cm}$ can generate gradients exceeding $300\,\mathrm{mT/m}$ $10\,\mathrm{cm}$ deep in the patient's body.

4.4 Multi-Core DFN Positioning

Although in some situations two or more bifurcations may be possible using one core, in general, single-core DFN-S allows to navigate magnetic agents in one bifurcation. In order

1. This magnetization corresponds to carbon steel cores from our lab.

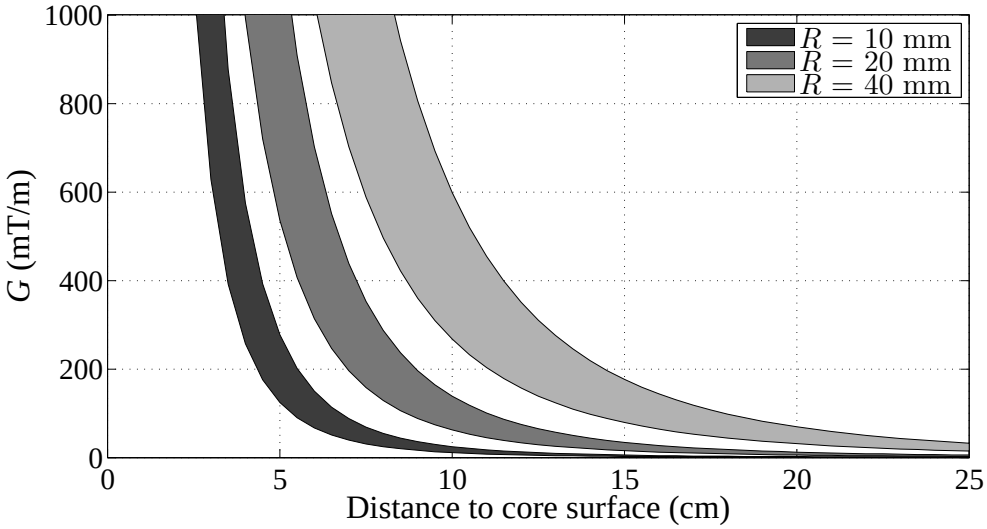

Figure 4.3 Range of gradient magnitudes achievable around a core having a magnetization $M = 1.43 \times 10^6$ A/m, as a function of the distance from the surface of the core, for different core radii.

to control particles through multiple consecutive bifurcations in the general case, multiple cores are needed to generate the required field of gradients. In this work, the magnetic path to be created is simplified as a set of *target gradients*, defined at some points along the desired vascular path. The following addresses the multi-core DFN-S positioning problem for generating these gradients.

A target gradient is defined as $\mathcal{T} = \{\mathbf{p}, \mathbf{G}, \xi_{max}\}$, meaning that a magnetic gradient $\mathbf{G} = (G_{min}, \vartheta, \varphi)$ is required at location $\mathbf{p} = (x, y, z)$ in space, where ξ_{max} is the maximum tolerance angular error on the gradient orientation and G_{min} is the minimum gradient magnitude. Hereinafter, the target gradient's location $\mathbf{p}$ is also called the *target point*. Note that ξ_{max} and G_{min} act as bound constraints, meaning that correct core positions for this target gradient can be represented by closed regions in space (see Fig. 4.4). A minimum distance r is also required to avoid the overlapping of the core on the target point, which narrows these positioning regions. Here, the dipole approximation limit constraint $r/R > 4$ considered throughout this work is used.

When positioning regions of different target gradients partially overlap, a single core positioned in the intersection area can generate gradients that are within the tolerance of both desired gradients. In this case, the position of the core can be calculated directly. Conversely, when multiple cores are needed, the positioning problem becomes much more complex due to the cumulative contribution of each core to the total gradients. In fact, this problem cannot be

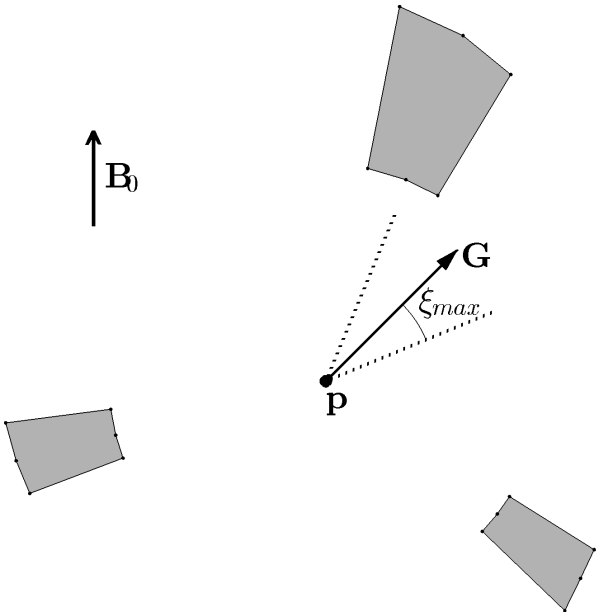

Figure 4.4 Illustration of positioning regions in 2D (gray areas), inside which a given core can induce a gradient at point **p** that meet the desired gradient **G**.

solved directly, can be highly nonlinear, and the solution may not be unique.

To solve this inverse problem, we propose a search algorithm that combines tree search and nonlinear optimization. The tree search allows to solve the positioning problem incrementally, from the injection point towards the target, and to initialize core positions strategically using (4.12), while the optimization is used to adjust these initial positions at each step. The algorithm allows to search for working configurations of cores having different characteristics (e.g., radius, magnetization, etc.) and attempts to minimize the required number of cores by exploiting positioning region intersections. In the following, the optimization procedure is described first, followed by the search algorithm details.

4.4.1 Optimization Problem Formulation

Let $\mathbf{G}' = (G', \vartheta', \varphi')$ be the actual total magnetic gradient at a target point, resulting from a certain core configuration $\{\mathcal{C}_1, \mathcal{C}_2, ..., \mathcal{C}_N\}$, where a core $\mathcal{C}_n = \{\mathbf{d}_n, R_n, M_n\}$ is defined by its position $\mathbf{d}_n$, its radius R_n and its volume magnetization M_n. The error angle ξ_k is the angle between a vector $\mathbf{G}'_k$ and the corresponding desired gradient $\mathbf{G}_k$. From the spherical law of cosines,

$$\cos\xi_k = \sin\vartheta_k \sin\vartheta'_k \cos(\varphi_k - \varphi'_k) + \cos\vartheta_k \cos\vartheta'_k \tag{4.13}$$

We formulate the general optimization problem of positioning N cores to generate K target gradients $\{\mathcal{T}_1, \mathcal{T}_2, ..., \mathcal{T}_K\}$ as

$$\mathcal{X}^* = \underset{\mathcal{X}}{\operatorname{argmax}} \sum_{k=1}^{K} \cos \xi_k \tag{4.14}$$

where $\mathcal{X}^*$ denotes the set of optimal (unknown) positioning parameters $\mathcal{X} = \{\mathbf{d}_1, \mathbf{d}_2, ..., \mathbf{d}_N\}$, subject to the constraints

$$G'_k \geq G_{min,k} \qquad \forall k \in [1, K] \tag{4.15}$$

$$\|\mathbf{d}_n - \mathbf{p}_k\| \geq 4R_n \qquad \forall n \in [1, N], \forall k \in [1, K] \tag{4.16}$$

$$\|\mathbf{d}_n - \mathbf{d}_m\| \geq 4 \max(R_n, R_m) \qquad \forall n, m \in [1, N] / n \neq m \tag{4.17}$$

Maximizing the objective function corresponding to (4.14) minimizes the error angles ξ_k, with more emphasis on large errors. The gradient magnitudes are excluded from the objective function to avoid the compensation of a bad gradient orientation (large ξ_k) by a greater gradient magnitude G'_k. Instead, G_{min} values are ensured by the constraints in (4.15).

The constraints in (4.16) and (4.17) arise from the aforementioned dipole approximation limit $r/R > 4$. Those in (4.16) allow to accurately predict the magnetization of the magnetic particles when they reach a target point. Here, we consider the largest of two cores to compute the minimum separating distances. Note that even without the dipole approximation limit, these two constraints would be necessary to avoid physically unfeasible core placements. The minimum value of the right-hand sides of the inequalities would then be R_n for (4.16) and $R_n + R_m$ for (4.17).

Other constraints can be defined in addition to (4.15)-(4.17) to ensure that the cores lie outside the patient's body. Finally, the optimization of (4.14) is considered as successful when the resulting errors ξ_k are bellow their respective $\xi_{max,k}$ values.

4.4.2 Alternating Optimizations

The above optimization problem is nonlinear and non-convex. To reduce its complexity when multiple cores are involved, one solution is to optimize (4.14) using an alternating optimization scheme. This strategy is explained here as it is employed in the search algorithm described next.

Alternating optimization (AO) consists in successively optimizing an objective function with respect to individual non-overlapping subsets of the parameters, $\mathcal{S}_1, \mathcal{S}_2, ..., \mathcal{S}_N$, while the

remaining parameters are fixed. This succession of restricted optimizations on $\mathcal{S}_i$ $(i = 1..N)$ is repeated iteratively until a stopping criterion is met. It was previously demonstrated that AO is guaranteed to converge, either to a local or global optimum, for any partitioning of the parameters [32].

For our application, a subset of parameters is created for each core position, i.e., the subset $\mathcal{S}_n = \mathbf{d}_n = \{x_n, y_n, z_n\}$ corresponds to core $\mathcal{C}_n$. During AO, instead of cycling over all subsets, the subset for which the parameters are optimized at each iteration is selected based on the gradients resulting from the current core configuration. As will be detailed in Section 4.4.3, the positioning algorithm associates each target gradient with a core in the configuration. The subset selected is the one corresponding to the core that is associated with the target gradient for which the current angular error ξ_k is the largest. Target gradients for which the resulting gradient orientation has little varied (threshold δ_{min}) during the previous iteration (i.e., due to the last modification to the configuration) are ignored in order to avoid selecting repeatedly the same subsets when some errors ξ_k cannot be decreased further. This subset selection strategy allows to focus the optimization on the parameters that are likely to improve the most the quality of the core configuration at each AO iteration. The AO process stops when the largest angular error is below a threshold ε_{tol}. The pseudo-code for this AO algorithm is presented in Algorithm 1. The input parameter *node* is a tree search node structure containing the parameters for the current configuration (see Section 4.4.3). Note that the input set of target gradients $\{\mathcal{T}_1, \mathcal{T}_2, ..., \mathcal{T}_j\}$, where $j \leq K$, does not necessarily contain the whole set of target gradients defined on the vascular path.

4.4.3 Search Algorithm

Given a set of target gradients, the goal is to find a working configuration of cores that will distort the magnetic field $\mathbf{B}_0$ such that the required gradients are generated. As mentioned earlier, solving this problem is not trivial due to the cumulative contribution of each core to the total gradients, to the physical constraints on core positions and because of the possible dipole-dipole interactions that can alter the accuracy of the mathematical models. In particular, whenever a modification is made to a core configuration to adjust the resulting gradient at a given target point (e.g., a core is moved or a new core is added), significant variations of the total resulting gradients at the other target points may be induced. Although a core configuration can theoretically be found by optimizing (4.14) for a given number of cores, the odds of converging to an unsatisfactory local optimum are high and increase with the number of cores. Moreover, the required number of cores is *a priori* unknown, as well as

Algorithm 1 DFNAlternatingOptim

Inputs: $node$, $\{\mathcal{T}_1, \mathcal{T}_2, ..., \mathcal{T}_j\}$, $maxIter$, ε_{tol}, δ_{min}

```
parent ← the parent node of node
for k = 1 to j do                                   ▷ Get previously obtained gradients
    G'_{prev,k} ← TotalGradientAt(parent.cores, T_k.p)
end for
n ← 0
while n < maxIter do
    for k = 1 to j do
        G'_k ← TotalGradientAt(node.cores, T_k.p)
        ξ_k ← AngleBetweenVectors(G'_k, T_k.G)
        δ_k ← AngleBetweenVectors(G'_k, G'_{prev,k})
    end for
    m ← argmax_m (ξ_m) subject to δ_m ≥ δ_min
    if ξ_m < ε_tol then
        break                                       ▷ Done optimizing this core configuration
    else
        C ← core associated with T_m
        Optimize(C, {T_1, T_2, ..., T_K})           ▷ See (4.14)-(4.17)
        for k = 1 to j do
            G'_{prev,k} ← G'_k
        end for
    end if
    n ← n + 1
end while
```

their characteristics. Especially, combining cores of different radii in a configuration adds some flexibility for solving the problem and thus may increase the number of possible solutions. In this regards, we state that a configuration is a valid solution when the target gradients and all other constraints are met. Thus, assuming that target gradients are chosen properly, there may be multiple equivalent solutions for navigating agents in a given vascular network.

These particularities motivated an incremental approach for the positioning algorithm, where the target gradients defined along the desired vascular path are met successively. Thus, new cores are progressively added to the configuration in order to meet the following target gradient(s) on path at each step. This approach allows to explore solutions using different core positions and characteristics while progressing on the path. The different combinations of core characteristics available (radius, magnetization, etc.) are referred to as *core prototypes*. These are the core samples that are provided to the search algorithm to solve a given problem.

During the search, every target gradient $\mathcal{T}_k$ is associated with the ferromagnetic core $\mathcal{C}_n$ that was added to meet this target gradient. When positioning regions of different target gradients intersect, multiple target gradients can be associated with the same core (if this core is positioned in the intersection area). This can serve as a heuristic to orient the search while reducing the number of cores in the configuration. For simplicity, the search algorithm is first described for unitary associations only.

Starting from the first target gradient on path ($k = 1$), cores $\mathcal{C}_k$ are added incrementally for each target gradient. Let $\mathcal{T}_k$ be the next target gradient on path and $\mathbf{G}'_k$ be the current total gradient at $\mathbf{p}_k$, resulting from the current configuration of cores $\mathcal{C}_1, \mathcal{C}_2, ..., \mathcal{C}_{k-1}$. The additional gradient required at $\mathbf{p}_k$ to obtain $\mathbf{G}_k$ is (when expressed in Cartesian coordinates)

$$\mathbf{G}_{k,add} = \mathbf{G}_k - \mathbf{G}'_k \tag{4.18}$$

The new core $\mathcal{C}_k$, selected among the core prototypes, is associated with $\mathcal{T}_k$ and added at one of the three theoretical possible positions $\mathbf{d}_{k,i}$ yielding the required additional gradient, which are calculated using (4.12). Two issues may then arise: (1) the position of $\mathcal{C}_k$ may not respect some of the physical constraints in (4.16)-(4.17); and (2) the total gradients previously generated at $\mathbf{p}_1, ..., \mathbf{p}_{k-1}$ may have been altered. To overcome the first issue, a physical constraint check is performed when adding a core and, if a constraint is violated, the restricted optimization of (4.14) with respect to $\mathcal{C}_k$ and $\mathcal{T}_k$ only is performed in order to adjust the position of $\mathcal{C}_k$ to a local optimum satisfying the constraints. Then, to solve the second issue, the AO process described previously is performed by taking into account the target gradients $\mathcal{T}_1, \mathcal{T}_2, ..., \mathcal{T}_k$. If the resulting configuration containing the new core is valid (i.e., target gradients $\mathcal{T}_1, \mathcal{T}_2, ..., \mathcal{T}_k$ are met and all constraints are satisfied), the search continues to the following target gradient $\mathcal{T}_{k+1}$ on path, if any. Otherwise, a different initial position $\mathbf{d}_{k,i}$ of $\mathcal{C}_k$ is tested (or a different core prototype when all three positions have been tried). If no valid configuration is found for $\mathcal{T}_k$, the search backtracks to $\mathcal{T}_{k-1}$ and tries a different setting for $\mathcal{C}_{k-1}$.

This search algorithm can be implemented as a tree search, where the root node is initialized with the list of all target gradients ($tgList = \{\mathcal{T}_1, \mathcal{T}_2, ...\mathcal{T}_K\}$) and an empty core configuration. The pseudo-code of the functions used to expand and process a search node are presented in Algorithms 2 and 3.

An interesting feature of this incremental search strategy is that it always meet the previous target gradients when moving to the next one on path. As a result, even when no solution

is found to a particular problem, the algorithm can still provide a core configuration that allows to guide particles through as many bifurcations as possible towards the target, which is particularly adapted to targeted drug delivery.

4.4.4 Exploiting Positioning Region Intersections

One drawback of the algorithm as presented above is that the number of cores in the solutions is equal to the number of target gradients. This can become cumbersome and prevent, due to the physical constraints, the existence of valid solutions if many target gradients are defined on the path.

The intersections between positioning regions of different target gradients, if any, can be exploited to orient the search toward solutions using fewer cores ($N < K$). If, for example, a positioning region of $\mathcal{T}_k$ intersect with another from a farther target gradient $\mathcal{T}_p$ on path, then the new core to be added can be positioned in the intersection area and associated with both target gradients. This possibility can be added in the search tree as an additional child node for $\mathcal{T}_k$. Thus, one strategy is to include, in the function *DFNChildNodes*, a test for the positioning region intersections between $\mathcal{T}_k$ and $\mathcal{T}_{k+1}, \mathcal{T}_{k+2}, ..., \mathcal{T}_K$ once a core prototype is selected. Note that this test must take into account the additional gradients needed at $\mathbf{p}_k, \mathbf{p}_{k+1}, ..., \mathbf{p}_K$ according to the current core configuration. The tree search algorithm can then be configured to explore the nodes corresponding to intersections first.

4.5 Algorithm Implementation

The positioning algorithm for multi-core DFN-S was implemented in MATLAB® R2013a. The optimizations of (4.14) were realized using the sequential quadratic programming (SQP) solver available using the MATLAB function *fmincon* from in the Optimization Toolbox. The parameters used for the AO algorithm are $\varepsilon_{tol} = \delta_{min} = 0.01\,\text{rad}$ and $maxIter = 10$.

The positioning algorithm was implemented in 2D and 3D. Fig. 4.5 presents example solutions found by the algorithm for three scenarios, including solutions using positioning region intersections and cores of different radii. For demonstration purposes, examples are only provided in 2D to keep the visualization simple. Equivalent results are obtained in 3D.

Algorithm 2 DFNChildNodes

Inputs: *node*, *corePrototypes*
Output: *children*

$\mathcal{T} \leftarrow$ next target gradient in *node.tgList*
$\boldsymbol{G}' \leftarrow$ TotalGradientAt(*node.cores*, $\mathcal{T}.\boldsymbol{p}$)
$\boldsymbol{G}_{add} \leftarrow \mathcal{T}.\boldsymbol{G} - \boldsymbol{G}'$ ▷ additional gradient needed at $\mathcal{T}.\boldsymbol{p}$
children $\leftarrow$ empty
for all $\mathcal{C}_P$ in *corePrototypes* **do**
  $\boldsymbol{d}_1, \boldsymbol{d}_2, \boldsymbol{d}_3 \leftarrow$ CorePos($\mathcal{C}_P$, $\boldsymbol{G}_{add}$, $\mathcal{T}.\boldsymbol{p}$) ▷ See (4.12)
  for $i = 1$ to 3 **do**
    $\mathcal{C} \leftarrow$ copy of $\mathcal{C}_P$ at position $\boldsymbol{d}_i$
    Associate $\mathcal{C}$ with $\mathcal{T}$
    child $\leftarrow$ copy of *node*
    child.cores.Add($\mathcal{C}$)
    child.tgList.Remove($\mathcal{T}$)
    children.Add(*child*)
  end for
end for
return *children*

Algorithm 3 DFNProcessNode

Inputs: *node*, $\{\mathcal{T}_1, \mathcal{T}_2, ..., \mathcal{T}_K\}$

$\mathcal{C} \leftarrow$ the lastly added core in *node.cores*
$\mathcal{T} \leftarrow$ the target gradient associated with $\mathcal{C}$
$b \leftarrow$ CheckPhysConstr(*node.cores*, $\{\mathcal{T}_1, \mathcal{T}_2, ..., \mathcal{T}_K\}$)
if $b =$ `False` **then**
  Optimize($\mathcal{C}$, $\mathcal{T}$) ▷ See (4.14)-(4.17)
end if
$j \leftarrow$ index of $\mathcal{T}$
DFNAlternatingOptim(*node.cores*, $\{\mathcal{T}_1, \mathcal{T}_2, ..., \mathcal{T}_j\}$)
$b \leftarrow$ IsConfigValid(*node.cores*, $\{\mathcal{T}_1, \mathcal{T}_2, ..., \mathcal{T}_K\}$)
if $b =$ `True` **then**
  if $j = K$ **then** ▷ All target gradients are met
    Label *node* as `Solution`
  else
    node.children $\leftarrow$ DFNChildNodes(*node*)
  end if
else
  Label *node* as `Failure`
end if

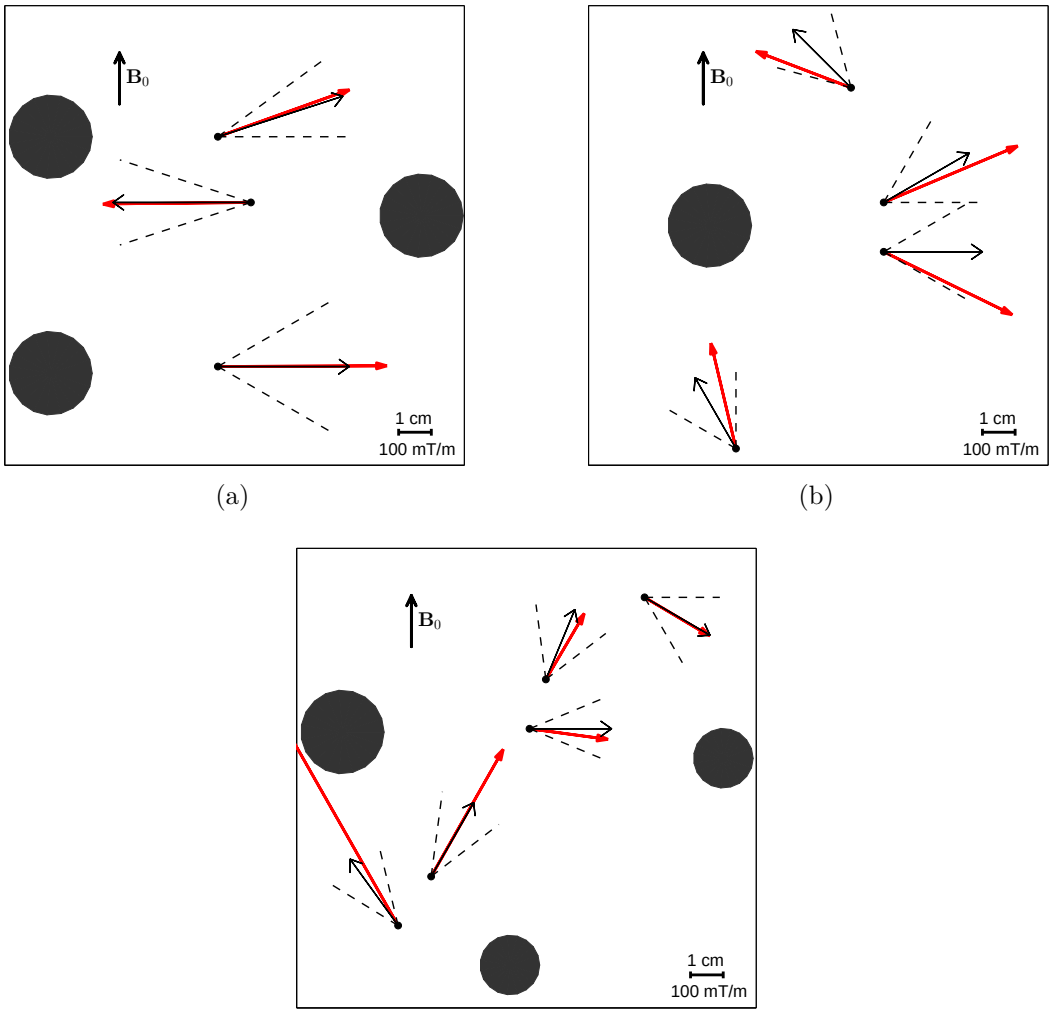

Figure 4.5 Examples of core configurations found by the positioning algorithm for three different scenarios. Black open-tip arrows show the desired gradients, while red filled arrows show the resulting gradients. Dashed lines show the error tolerance on gradient orientations. In (b) and (c), positioning region intersections allowed to reduce the number of required cores. In (c), two core prototypes of different radii were provided to the algorithm.

4.6 *In Vitro* Navigation Experiment

An *in vitro* experiment was conducted in order to evaluate the feasibility of DFN to guide magnetic agents through multiple bifurcations in a vascular network. The experiment consisted in the navigation of magnetic particles in three consecutive bifurcations in a 3D network, using a core configuration found by the algorithm presented in Section 4.4.

4.6.1 Setup

Transparent plastic tubes, having an inner diameter of 1.59 mm, were connected using Y-junctions of equal inner diameter and formed a network with multiple bifurcations. For each junction, the angle between the two bifurcations was 60°. The desired path of the particles in the network comprised three consecutive bifurcations, respectively left, up and then right. These three junctions were glued on LEGO® blocks and the setup was mounted on a baseplate in order to fix their positions in space (see Fig. 4.6). The distance between the first and the second bifurcations was ~4.7 cm, whereas the distance between the second and the third was ~3.2 cm.

The setup was centered in the tunnel of a 1.5 T Siemens Sonata clinical MRI scanner and oriented such that the baseplate lied on the xz-plane and the direction of $\mathbf{B}_0 = B_0\hat{\mathbf{z}}$ was perpendicular to the general direction of the flow, as shown in Fig. 4.6. A target gradient was defined for each bifurcation, with the target points set 5 mm upstream of the junctions. This setting was based on the concept of transit time allowed to the particles to shift on the desired side of the tube's centerline before reaching the bifurcation point [20], although the distance of 5 mm was chosen arbitrarily. The required magnetic gradients were oriented perpendicular to the flow and in the direction of the desired bifurcation. For each target gradient, we set $G_{min} = 400\,\mathrm{mT/m}$ and $\xi_{max} = \pi/6$.

The available ferromagnetic cores for the experiment were carbon steel spherical cores, having a radius $R = 1.27\,\mathrm{cm}$ and a saturation magnetization $M_{sat} = 1.43 \times 10^6\,\mathrm{A/m}$ reached at $B \approx 1.3\,\mathrm{T}$. Thus, the cores were at saturation magnetization inside MRI tunnel. To make the experiment more akin to a real intervention setup, a physical constraint was used in addition to (4.15)-(4.17) to simulate the presence of a patient's body. As such, the cores were constrained to be located above an imaginary plane (outside the "body" parallel to xz and set 5 mm above the highest target point with respect to the y-axis. The multi-core DFN positioning algorithm presented in Section 4.4 was allowed to explore the whole search tree of this positioning problem. Three different solutions were found, one of which required only two cores (from the use of positioning region intersections). The other two solutions, composed of three cores, were nevertheless preferred here in order to test DFN using a more complex core configuration. The solution retained among these two was the one yielding the smallest angular errors on the desired gradients. Table 4.1 presents the various parameters of the experimental setup, including the core positions of the solution used, the resulting gradients at the target points and the angular errors. Note that the first target point was used as the

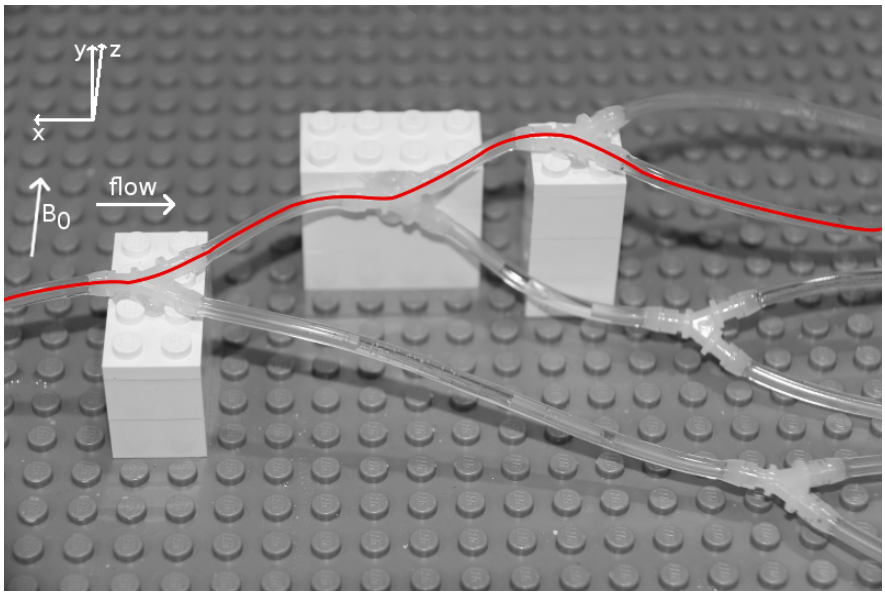

Figure 4.6 Tube network used for the navigation experiment. The red line depicts the desired path of the magnetic particles.

Table 4.1 Parameters of the Navigation Experimental Setup

Bifurcation	Target gradient[a,b]			Associated core[a,c]		Resulting gradient[b]	
	p	**G**	ξ_{max}	R	**d**	**G′**	ξ
1	$(0, 0, 0)$	$(400, 0, 0)$	$\pi/6$	1.27	$(-3.9, 2.8, -2.4)$	$(405, 0.10, -0.47)$	0.10
2	$(-4.2, -0.1, 2.2)$	$(400, \pi/2, \pi/2)$	$\pi/6$	1.27	$(-9.5, 2.6, -2.8)$	$(543, 1.91, 1.50)$	0.35
3	$(-7.2, 0.9, 2.4)$	$(400, \pi, 0)$	$\pi/6$	1.27	$(-8.0, 6.1, 3.1)$	$(400, 3.07, 0.41)$	0.07

[a] Position (x, y, z) in cm. [b] Gradient (G, ϑ, φ), magnitude in mT/m and all angles in radians.
[c] Radius in cm.

origin of the global xyz-frame. Fig. 4.7 illustrates the core configuration positioned above the tube network and depicts the theoretical total resulting gradients along the desired path.

The cores were added to the setup by placing them in small boxes made of LEGO blocks and their positions were precisely adjusted using shims (see Fig. 4.8a). The positioning precision of bifurcations and cores in the final setup was 1-2 mm.

A blood analogue fluid of dynamic viscosity 3.5 mPa·s consisting of 36% glycerol in water was used as the circulating fluid in the tubes. A syringe pump (Harvard Apparatus PHD 2000) set in refill mode was connected to the outputs of the network such that a constant and equal flow was delivered in both branches for each junction. This ensured that no preferential flow path existed in the network. The flow was set to 20 mL/min before the first bifurcation. This

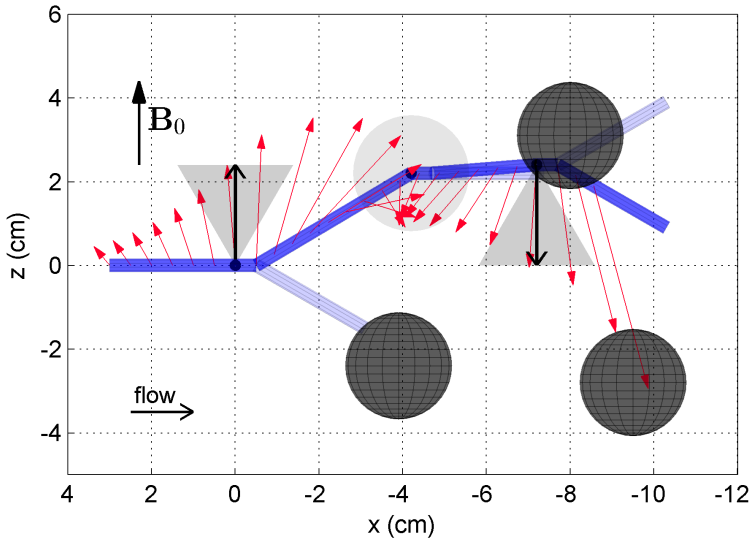

(a) Top view

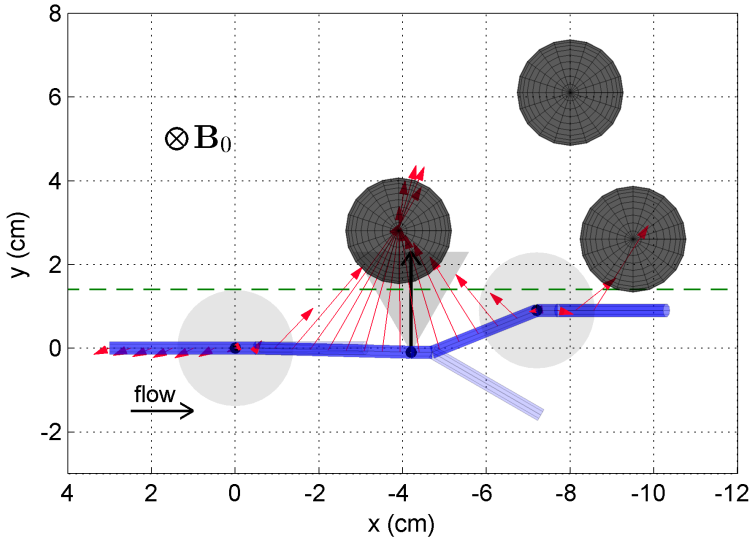

(b) Side view

Figure 4.7 Top and side views illustrating the experimental setup. The tube network is shown in blue, with the desired path in darker blue. The desired gradients and maximum angular errors are illustrated by the black open-tip arrows and gray cones. The red filled arrows depict the total gradients along the path, resulting from the positioned cores (black spheres). In (b), the green dashed line represents the top of the imaginary patient's body. Gradient scale is 6 cm/T.

yielded a flow velocity of 16.8, 8.4 and 4.2 cm/s before the first, second and third junctions respectively.

Magnetic particles were fabricated by the microencapsulation of water-based ferrofluid (Ferrotec EMG 700) using sodium alginate. This ferrofluid has a saturation magnetization of

25860 A/m and a density of 1.29 g/cc. The resulting particles varied in diameter between 200-400 μm. These magnetic particles were injected manually before the first junction. An MRI-compatible camera (MRC Systems GmbH, model 12M) was positioned in the tunnel of the MRI scanner in order to record videos of the experiment. Due to their magnetization, the magnetic particles (dark-brown color) formed small aggregates that were easily visible through the tubes in the images.

4.6.2 Results

Magnetic particles were injected continuously in the network for about 2 min 40 s, while the camera recorded a video of the experiment (30 fps, 640×480 pixels). The video was analyzed by a motion detection algorithm implemented in MATLAB. This algorithm performed a frame-by-frame differential analysis in order to detect moving particles or aggregates in the tubes. The distribution of the total motion detected for each pixel was plotted as a heat map, superimposed on the average video frame. Fig. 4.8b shows the result of this analysis (best viewed in colors). Clearly, most of the motion was detected along the desired path, indicating that the majority of particles were steered in the desired bifurcations. In fact, little motion was detected in the wrong branch of the first junction, and no motion was detected in the wrong branches of the second and the third bifurcations. In comparison, Fig. 4.8c shows the results of a control experiment, conducted in the same conditions but with no ferromagnetic cores. From these results, the influence of the cores on the direction taken by the particles is evident, especially in the first and second bifurcations where the flow velocity was the highest.

As a more precise evaluation of the navigation efficiency, the steering ratio is defined as the mass fraction of the particles reaching the targeted branch of a junction. In the present case, the steering ratio was estimated by counting the number of particles/aggregates reaching each branch of the three junctions. In order to obtain the most accurate counts as possible, this task was performed manually by analyzing the complete video frame by frame. For the first junction, a total number of 330 particles or aggregates were counted in the left branch, whereas 31 were spotted going through the right branch. This results in an estimated steering ratio of ~91% for the first bifurcation. For both the second and third bifurcations, where flow velocities were slower, no particles were seen in the wrong branches, thus yielding a steering ratio of 100% in those cases.

(a) Positioned cores above the tube network.

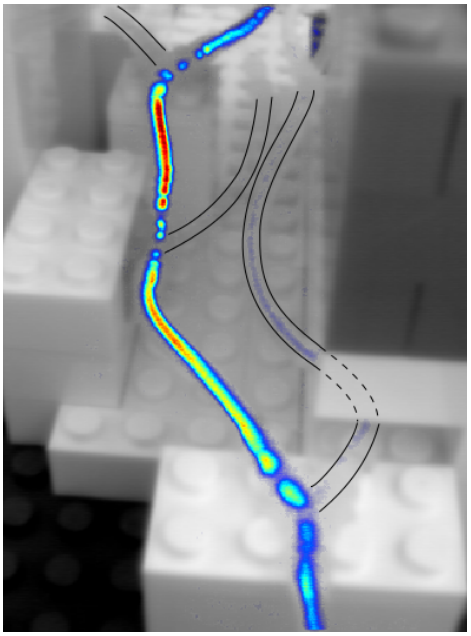

(b) Navigation experiment results.

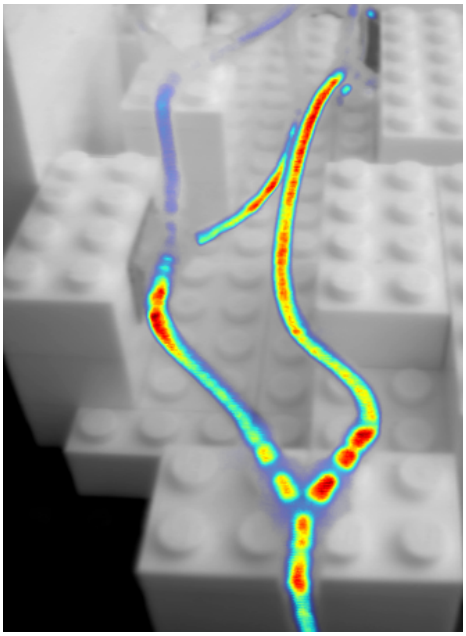

(c) Control experiment results (no cores).

Figure 4.8 Experimental setup and results. (a) shows the core configuration above the tube network. (b) and (c) show the detected particle motion for the navigation and control experiments respectively. The motion density is plotted as a heat map superimposed on the average video frame (red = high density, blue = low density). In (b), black lines were drawn to emphasize tube locations.

4.7 Discussion

The navigation experiment conducted demonstrates the potential of DFN for guiding magnetic particles in a vascular network. An interesting result is that core configurations could be found when the cores were constrained to be positioned above an imaginary patient body. Although the depth of the network inside the “body" was relatively small for this experiment, it could be increased using larger cores [24].

An issue worth discussing was encountered during the experiment, but does not appear in the results presented here. As depicted in Fig. 4.7, the core configuration used in this particular setup resulted in a strong gradient orthogonal to the flow in the targeted branch passed the third bifurcation. As they reached this region, the particles were trapped by this high gradient and could not move further. While it does not affect the validity of the results, this observation highlights the necessity to take into account the gradients generated through-out the vascular path and not only near the bifurcation points.

As mentioned earlier, it is in theory possible to generate virtually any magnetic path using DFN, provided that the rates of directional changes of the required gradients along the path are limited. The search algorithm presented in this paper is a first attempt at solving the positioning problem for multi-core DFN-S. One current limitation relates to the dipole approximation limit constraint, imposing a minimum separating distance between the cores. This constraint restrains the core combination possibilities, especially for the large cores required to navigate in deep tissues, and probably affects the gradient directional change resolution achievable with DFN-S. The characterization of this resolution under different conditions is subject to a future work. Another concern that would arise by using larger cores is the potentially much stronger magnetic interaction forces between the cores. The structure used to maintain the cores in place should be designed in consequence.

To cope with the anatomic variations of the vasculature between individuals, as well as to allow targeting any region in the body, it is crucial that the required gradients be adapted to the vascular path specific to each patient. The determination of the gradients should be based on various parameters, such as bifurcation angles, blood flow velocities and particle characteristics. This problem will be addressed in future works.

4.8 Conclusion

The targeted delivery of drugs to tumors in cancer therapy would significantly increase the efficiency of treatments, while minimizing their secondary toxicity for the patients. As such, Dipole Field Navigation is a promising method for navigating untethered magnetic therapeutic agents in a vascular network. It is the only method so far that can achieve both the depth-independent saturation magnetization of the agents and high gradient strengths, while being adapted to whole-body interventions.

The main challenge of DFN lies in the development of the models and methods required to adequately position the ferromagnetic cores around the patient. Here, we presented an algorithm for solving the problem of statically positioning multiple cores in order to generate a set of required gradients defined at some points in a vascular network. This algorithm was used to conduct an *in vitro* experiment, where magnetic particles were successfully guided through three consecutive bifurcations in a 3D network. The high targeting levels obtained demonstrate the feasibility and potential of DFN.

4.9 References

[1] N. Bertrand, J. Wu, X. Xu, N. Kamaly, et O. C. Farokhzad, "Cancer nanotechnology: the impact of passive and active targeting in the era of modern cancer biology." *Adv. Drug Deliv. Rev.*, vol. 66, pp. 2–25, 2014. DOI: 10.1016/j.addr.2013.11.009

[2] S. D. Steichen, M. Caldorera-Moore, et N. A. Peppas, "A review of current nanoparticle and targeting moieties for the delivery of cancer therapeutics", *Eur. J. Pharm. Sci.*, vol. 48, no. 3, pp. 416–427, 2013. DOI: 10.1016/j.ejps.2012.12.006

[3] S. Martel, "Magnetic therapeutic delivery using navigable agents", *J. Ther. Deliv.*, vol. 5, no. 2, pp. 189–204, 2014. DOI: 10.4155/tde.13.147

[4] C. Sun, J. S. H. Lee, et M. Zhang, "Magnetic nanoparticles in MR imaging and drug delivery", *Adv. Drug Deliv. Rev.*, vol. 60, no. 11, pp. 1252–1265, 2008. DOI: 10.1016/j.addr.2008.03.018

[5] O. Felfoul, J. B. Mathieu, G. Beaudoin, et S. Martel, "In vivo MR-tracking based on magnetic signature selective excitation", *IEEE Trans. Med. Imaging*, vol. 27, no. 1, pp. 28–35, 2008. DOI: 10.1109/TMI.2007.897375

[6] A. Senyei, K. Widder, et G. Czerlinski, "Magnetic guidance of drug-carrying microspheres", *J. Appl. Phys.*, vol. 49, no. 6, p. 3578, 1978. DOI: 10.1063/1.325219

[7] K. Mosbach et U. Schroder, "Preparation and application of magnetic polymers for targeting of drugs", *FEBS Lett.*, vol. 102, no. 1, pp. 112–116, 1979.

[8] K. J. Widder, R. M. Morrist, G. Pooret, D. P. Howard, et A. E. Senyeit, "Tumor remission in Yoshida sarcoma-bearing rats by selective targeting of magnetic albumin microspheres containing doxorubicin", dans *Proc. Natl. Acad. Sci. U. S. A.*, vol. 78, no. 1, 1981, pp. 579–581.

[9] J. Johnson, T. Kent, J. Koda, C. Peterson, S. Rudge, et G. Tapolsky, "The MTC Technology: A Platform Technology for the Site-Specific Delivery of Pharmaceutical Agents", *Eur. Cells Mater.*, vol. 3, pp. 12–15, 2002.

[10] A. Amirfazli et R. Virginia, "Magnetic nanoparticles hit the target", *Nat. Nanotechnol.*, vol. 2, no. August, pp. 467–468, 2007. DOI: 10.1038/nnano.2007.234

[11] S. Tognarelli, V. Castelli, G. Ciuti, C. Natali, E. Sinibaldi, P. Dario, et A. Menciassi, "Magnetic propulsion and ultrasound tracking of endovascular devices", *J. Robot. Surg.*, vol. 6, no. 1, pp. 5–12, 2011.

[12] H. Choi, K. Cha, J. Choi, S. Jeong, S. Jeon, G. Jang, J.-o. Park, et S. Park, "EMA system with gradient and uniform saddle coils for 3D locomotion of microrobot", *Sensors Actuators A Phys.*, vol. 163, no. 1, pp. 410–417, 2010. DOI: 10.1016/j.sna.2010.08.014

[13] S. Jeong, H. Choi, J. Choi, C. Yu, J. oh Park, et S. Park, "Novel electromagnetic actuation (EMA) method for 3-dimensional locomotion of intravascular microrobot", *Sensors Actuators, A Phys.*, vol. 157, no. 1, pp. 118–125, 2010. DOI: 10.1016/j.sna.2009.11.011

[14] M. D. Tehrani, M. O. Kim, et J. Yoon, "A Novel Electromagnetic Actuation System for Magnetic Nanoparticle Guidance in Blood Vessels", *IEEE Trans. Magn.*, vol. 50, pp. 1–12, 2014. DOI: 10.1109/TMAG.2014.2307271

[15] M. P. Kummer, J. J. Abbott, B. E. Kratochvil, R. Borer, A. Sengul, et B. J. Nelson, "Octomag: An electromagnetic system for 5-DOF wireless micromanipulation", *IEEE Trans. Robot.*, vol. 26, no. 6, pp. 1006–1017, 2010. DOI: 10.1109/TRO.2010.2073030

[16] H. Keller, A. Juloski, H. Kawano, M. Bechtold, A. Kimura, H. Takizawa, et R. Kuth,

"Method for navigation and control of a magnetically guided capsule endoscope in the human stomach", dans *Proc. IEEE RAS EMBS Int. Conf. Biomed. Robot. Biomechatronics*, 2012, pp. 859–865.

[17] C. Tremblay, B. Conan, D. Loghin, A. Bigot, et S. Martel, "Fringe Field Navigation for Catheterization", dans *6th Eur. Conf. Int. Fed. Med. Biol. Eng.*, 2014, pp. 379–382.

[18] J.-B. Mathieu, G. Beaudoin, et S. Martel, "Method of propulsion of a ferromagnetic core in the cardiovascular system through magnetic gradients generated by an MRI system." *IEEE Trans. Biomed. Eng.*, vol. 53, no. 2, pp. 292–299, 2006.

[19] S. Martel, J.-B. Mathieu, O. Felfoul, A. Chanu, E. Aboussouan, S. Tamaz, P. Pouponneau, L. Yahia, G. Beaudoin, G. Soulez, et M. Mankiewicz, "Automatic navigation of an untethered device in the artery of a living animal using a conventional clinical magnetic resonance imaging system", *Appl. Phys. Lett.*, vol. 90, no. 11, p. 114105, 2007.

[20] J. B. Mathieu et S. Martel, "Steering of aggregating magnetic microparticles using propulsion gradients coils in an MRI scanner", *Magn. Reson. Med.*, vol. 63, no. 5, pp. 1336–1345, 2010. DOI: 10.1002/mrm.22279

[21] P. Pouponneau, J. C. Leroux, G. Soulez, L. Gaboury, et S. Martel, "Co-encapsulation of magnetic nanoparticles and doxorubicin into biodegradable microcarriers for deep tissue targeting by vascular MRI navigation", *Biomaterials*, vol. 32, no. 13, pp. 3481–3486, 2011. DOI: 10.1016/j.biomaterials.2010.12.059

[22] J. A. McNab, B. L. Edlow, T. Witzel, S. Y. Huang, H. Bhat, K. Heberlein, T. Feiweier, K. Liu, B. Keil, J. Cohen-Adad, M. D. Tisdall, R. D. Folkerth, H. C. Kinney, et L. L. Wald, "The Human Connectome Project and beyond: Initial applications of 300mT/m gradients", *Neuroimage*, vol. 80, pp. 234–245, 2013.

[23] A. Bigot, C. Tremblay, G. Soulez, et S. Martel, "Temperature Response of a Magnetic Resonance Imaging Coil Insert for the Navigation of Theranostic Agents in Complex Vascular Networks", *IEEE Trans. Magn.*, vol. 50, no. 8, pp. 1–7, 2014. DOI: 10.1109/TMAG.2014.2309944

[24] M. Latulippe et S. Martel, "Dipole Field Navigation for Targeted Drug Delivery", dans *IEEE Int. Conf. Biomed. Robot. Biomechatronics*, 2014, pp. 320–325.

[25] B. Veron, A. Hubert, J. Abadie, et N. Andreff, “Geometric analysis of the singularities of a magnetic manipulation system with several mobile coils”, dans *IEEE Int. Conf. Intell. Robot. Syst.*, 2013, pp. 4996–5001. DOI: 10.1109/IROS.2013.6697078

[26] X. Luo et C. Foss, “Inverse of magnetic dipole field using a reversible jump Markov chain Monte Carlo”, dans *20th Int. Congr. Model. Simul.*, 2013, pp. 134–140.

[27] M. A. Jatoi, N. Kamel, A. S. Malik, I. Faye, et T. Begum, “A survey of methods used for source localization using EEG signals”, *Biomed. Signal Process. Control*, vol. 11, no. 1, pp. 42–52, 2014. DOI: 10.1016/j.bspc.2014.01.009

[28] N. C. Kapsalis, S.-D. J. Kakarakis, et C. N. Capsalis, “Prediction of Multiple Magnetic Dipole Model Parameters from Near Field Measurements Employing Stochastic Algorithms”, *Prog. Electromagn. Res. Lett.*, vol. 34, pp. 111–122, 2012. DOI: 10.2528/PIERL12030905

[29] R. Castañer, J. M. Medina, et M. J. Cuesta-Bolao, “The magnetic dipole interaction as measured by spring dynamometers”, *Am. J. Phys.*, vol. 74, no. 6, pp. 510–513, 2006. DOI: 10.1119/1.2180286

[30] Y. Kraftmakher, “Magnetic field of a dipole and the dipole-dipole interaction”, *Eur. J. Phys.*, vol. 28, no. 3, pp. 409–414, may 2007. DOI: 10.1088/0143-0807/28/3/003

[31] A. Mehdizadeh, R. Mei, J. F. Klausner, et N. Rahmatian, “Interaction forces between soft magnetic particles in uniform and non-uniform magnetic fields”, *Acta Mech. Sin.*, vol. 26, no. 6, pp. 921–929, 2010. DOI: 10.1007/s10409-010-0383-y

[32] J. C. Bezdek et R. J. Hathaway, “Convergence of alternating optimization”, *Neural, Parallel Sci. Comput.*, vol. 11, no. 4, pp. 351–368, 2003.

CHAPITRE 5 ARTICLE 2: ENABLING AUTOMATED MAGNETIC RESONANCE IMAGING-BASED TARGETING ASSESSMENT DURING DIPOLE FIELD NAVIGATION

Maxime Latulippe, Ouajdi Felfoul, Pierre E. Dupont and Sylvain Martel
Applied Physics Letters

5.1 Abstract

The magnetic navigation of drugs in the vascular network promises to increase the efficacy and reduce the secondary toxicity of cancer treatments by targeting tumors directly. Recently, Dipole Field Navigation (DFN) was proposed as the first method achieving both high field and high navigation gradient strengths for whole-body interventions in deep tissues. This is achieved by introducing large ferromagnetic cores around the patient inside a Magnetic Resonance Imaging (MRI) scanner. However, doing so distorts the static field inside the scanner, which prevents imaging during the intervention. This limitation constrains DFN to open-loop navigation, thus exposing the risk of a harmful toxicity in case of a navigation failure. Here, we are interested in periodically assessing drug targeting efficiency using MRI even in presence of a core. We demonstrate, using a clinical scanner, that it is in fact possible to acquire, in specific regions around a core, images of sufficient quality to perform this task. We show that the core can be moved inside the scanner to a position minimizing the distortion effect in the region of interest for imaging. Moving the core can be done automatically using the gradient coils of the scanner, which then also enables the core to be repositioned to perform navigation to additional targets. The feasibility and potential of the approach are validated in an in vitro experiment demonstrating navigation and assessment at two targets.

5.2 Main text

Controlled magnetic navigation of therapeutic carriers inside blood vessels is a promising technology for targeted drug delivery [1, 2]. By combining a drug with superparamagnetic nanoparticles, these carriers, if magnetized by an external magnetic field, can be steered via forces induced by magnetic gradients. To maximize the resulting forces, the magnetizing field must be strong enough to bring the particles to saturation magnetization. One approach is Magnetic Resonance Targeting (MRT) which exploits the strong static field of a Magnetic Resonance Imaging (MRI) scanner and uses the gradient coils of the scanner to cause

systemically circulating magnetized particles to accumulate at a desired location in the body [3]. Because superparamagnetic particles act as MRI contrast agents, MRT also provides the capability to assess particle accumulation. An alternative approach, explored in this paper, is to steer the particles along a predefined vascular route, from an injection point directly toward the targeted tumor, and thus minimize the toxicity and inefficiency of systemic circulation. Although the behavior of carriers is predictable, such navigation is ideally performed with closed-loop control in order to compensate for the uncertainties of the real-world vascular environment. This has been achieved with Magnetic Resonance Navigation (MRN) [4], which also uses an MRI scanner and enables real-time tracking of particles during the navigation process [5] using a specific imaging sequence such as MS-SET [6]. Considering the very small magnetic volume of the therapeutic carriers (e.g., max. 300 μm in size for liver chemoembolization), the capabilities of MRN in high blood flow velocities found in human arteries is, however, limited by the relatively weak gradients achievable with conventional clinical MRI scanners (typically 40 mT/m). While balloon catheters can be used to reduce the vascular flow rate, this approach translates to longer required intervention times. Electromagnetic actuation systems [7–9] can generate much higher gradients ($>$ 300 mT/m), but lack the required field strength to saturate the particles. The only method so far that combines a high magnetizing field with high gradient strengths ($>$ 300 mT/m) for whole-body interventions in deep tissues is Dipole Field Navigation (DFN) [10]. This method consists in inserting large ferromagnetic cores around the patient inside an MRI scanner to generate very strong gradients. However, the resulting distortion of the static field in the scanner prevents imaging. Indeed, MRI traditionally requires a homogeneous field for proper image reconstruction, and inhomogeneities can introduce imaging artifacts which affect the accuracy of anatomical details. Various approaches and algorithms have been developed to compensate for normal field inhomogeneities found in the MRI environment [11]. In particular, special imaging sequences have been shown to be more robust to field inhomogeneities and improve the image quality around metal implants [12, 13]. None of these methods, however, can cope with the much stronger and unusual field distortion caused by the ferromagnetic cores in DFN. As such, DFN has been limited to open-loop navigation and has relied on the accuracy of magnetic models and precise core positioning to achieve targeting accuracy. To ensure accurate targeting and to avoid potential morbidities from inaccurate targeting, drug delivery should be at least periodically assessed during an intervention so that core positions can be adjusted as necessary. Ideally, such an informed open-loop scheme would be achieved automatically and without retracting the cores from the scanner to speed up the intervention.

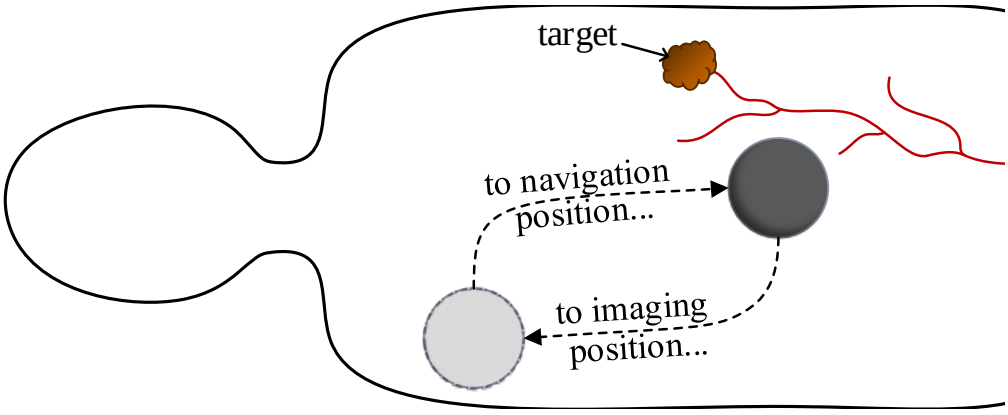

Figure 5.1 To assess targeting in DFN, the core can be moved between locations optimized for navigation and for imaging.

In this letter, we identify specific angular regions around a ferromagnetic core where imaging artifacts are minimized and exploit these regions for assessing targeting efficiency. Furthermore, using the imaging gradient coils as a propulsion mechanism [4, 14], we show that the core can be moved automatically between positions optimized for navigation and for imaging (see Fig. 5.1).

In DFN, both the nanoparticles and the cores are assumed to be magnetized at saturation by the static field $\mathbf{B}_0$ of the MRI scanner. The strong magnetic gradients result from the distortion of $\mathbf{B}_0$ around the cores and induce magnetic forces on the particles according to

$$\mathbf{F}_{mag} = \nabla(\mathbf{m}_p \cdot \mathbf{B}) \tag{5.1}$$

where $\mathbf{m}_p$ is the magnetic moment of a particle and $\mathbf{B} = \mathbf{B}_0 + \mathbf{B}_{core}$ is the total field experienced by the particle. For a single spherical core of radius R, volume V, saturation magnetization $\mathbf{M}_{sat}$ and magnetic moment $\mathbf{m} = V\mathbf{M}_{sat}$,

$$\mathbf{B}_{core}(r > R) = \frac{\mu_0}{4\pi}\left[3\frac{(\mathbf{m}\cdot\mathbf{r})\mathbf{r}}{r^5} - \frac{\mathbf{m}}{r^3}\right] \tag{5.2}$$

where $\mathbf{r}$ is the position vector relative to the core's center, $r = \|\mathbf{r}\|$ and $\mu_0 = 4\pi \times 10^{-7}\,\mathrm{H/m}$ is the vacuum permeability. Fundamentally in MRI, this non-uniform field added to $\mathbf{B}_0$ results in a position-dependent offset of the Larmor frequency $f = \frac{\gamma}{2\pi}B$ of the nucleus used for resonance signal acquisition, where γ is the gyromagnetic ratio of the nucleus. As shown in Fig. 5.2 for a chrome steel core ($M_{sat} = 1.4 \times 10^6\,\mathrm{A/m}$) and the hydrogen nucleus ($\gamma = 42.576\,\mathrm{MHz/T}$), this offset varies nonlinearly around the core and reaches zero at four location angles. Assuming

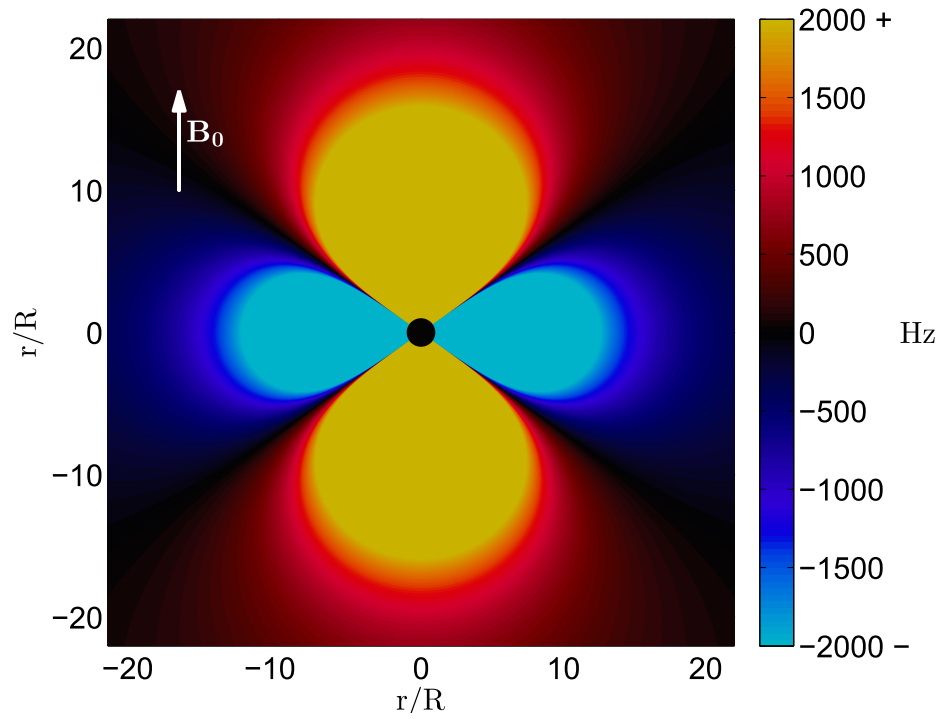

Figure 5.2 Simulated offset of the Larmor frequency of hydrogen around a chrome steel core (best viewed in color).

the core is magnetized in the z-axis direction (i.e., $\mathbf{B}_0 = B\hat{\mathbf{z}}$), the total field strength in the far field of the core can be approximated as

$$B \approx B_z = B_0 + \frac{\mu_0 m}{4\pi r^5}\left(3z^2 - r^2\right) \tag{5.3}$$

$$= B_0 + \frac{\mu_0 m}{4\pi r^3}\left(3\cos^2\theta - 1\right) \tag{5.4}$$

where θ is the angle between the position vector $\mathbf{r}$ and $\mathbf{B}_0$. For a chrome steel core in a 3 T field, this approximation yields an error below 0.1% at ~$2R$ from the core's center. From Eq. (5.4), which was obtained by substituting $z = r\cos\theta$, the contribution of the core to the total field is minimized when

$$3\cos^2\theta - 1 = 0 \tag{5.5}$$

which occurs at $\theta \approx \pm 54.7°$ and $\theta \approx \pm 125.3°$. Thus, while MRI distortion should be minimized at these angles, Fig. 5.2 suggests that an object of finite dimensions must be placed at a sufficient distance from the core to lie in the dark regions between the lobes.

This hypothesis was validated experimentally using a clinical Siemens Skyra 3 T scanner, by acquiring several images of an orange located at different positions (r, θ) relative to a

3.81 cm spherical chrome steel core. The orange was immersed in water and positioned at the boundary of the homogeneous volume of the scanner, while the core was placed at different positions inside this volume. The angle θ was varied for two distances (center to center) to the core, $r = 25\,\text{cm}$ ($\approx 13R$) and $r = 40\,\text{cm}$ ($\approx 21R$). The imaging sequence used was spin echo for its well-known robustness to field inhomogeneities. Fig. 5.3 compares the resulting images (coronal plane) with a reference image acquired before inserting the core inside the scanner. Whereas images acquired at $\theta = 0°$ and $\theta = 90°$ are significantly altered at $21R$ and show a complete loss of signal at $13R$, images taken around the theoretical optimal angle 54.7° are much more accurate. Although the image acquired at 25 cm at this angle is geometrically distorted, some small details remain visible in the lower distortion region (brighter area). One relevant observation is that, in all these images, the slice selected by the radiofrequency excitation pulse was also vertically distorted due to the non-uniform Larmor frequency. The slices were thus not perfectly horizontal as they should, nor exactly located at the expected vertical position. This is shown by the smaller diameter of the orange slice at $\theta = 0°$ and $\theta = 90°$, and by the visible seeds varying across images. On another hand, no pure scaling effects are observable in these experiments. Note that for drug targeting assessment, images need not be perfectly accurate from the anatomical point of view. Some level of alteration is acceptable as long as features can be recognized in order to localize the particles. Moreover, volume images (multiple slices) can be acquired so that the region of interest is covered even if slices are distorted.

These results motivated a navigation experiment using MRI to assess targeting in the presence of a core. The experiment consisted of sequentially navigating particles to two different targets in a vascular phantom. This phantom, which was made of transparent plastic tubes and junctions, had two levels of branching with a constant inner diameter of 1.59 mm. A filter was placed in each of the four output branches to capture the injected particles. The targeted regions were the rightmost branch for the first navigation and the leftmost branch for the second navigation. Both targets required navigating two consecutive bifurcations, separated by 2.5 cm and 3.3 cm respectively. The phantom was fixed in gelatin to increase the resonance signal for imaging. For the two targeting tasks, a single spherical core (chrome steel, diameter 3.81 cm) was positioned at coordinates (-7.3 cm, -1.5 cm) and (8 cm, -1.5 cm) respectively, relative to the first bifurcation (core's center vertically aligned with the phantom). These locations were selected using an optimization approach [10]. The imaging position of the core was set to $\theta = 55°$ and $r = 37\,\text{cm}$ from the center of the phantom. Due to the small gradient duty cycle during imaging, the core can remain stationary without being held at this position.

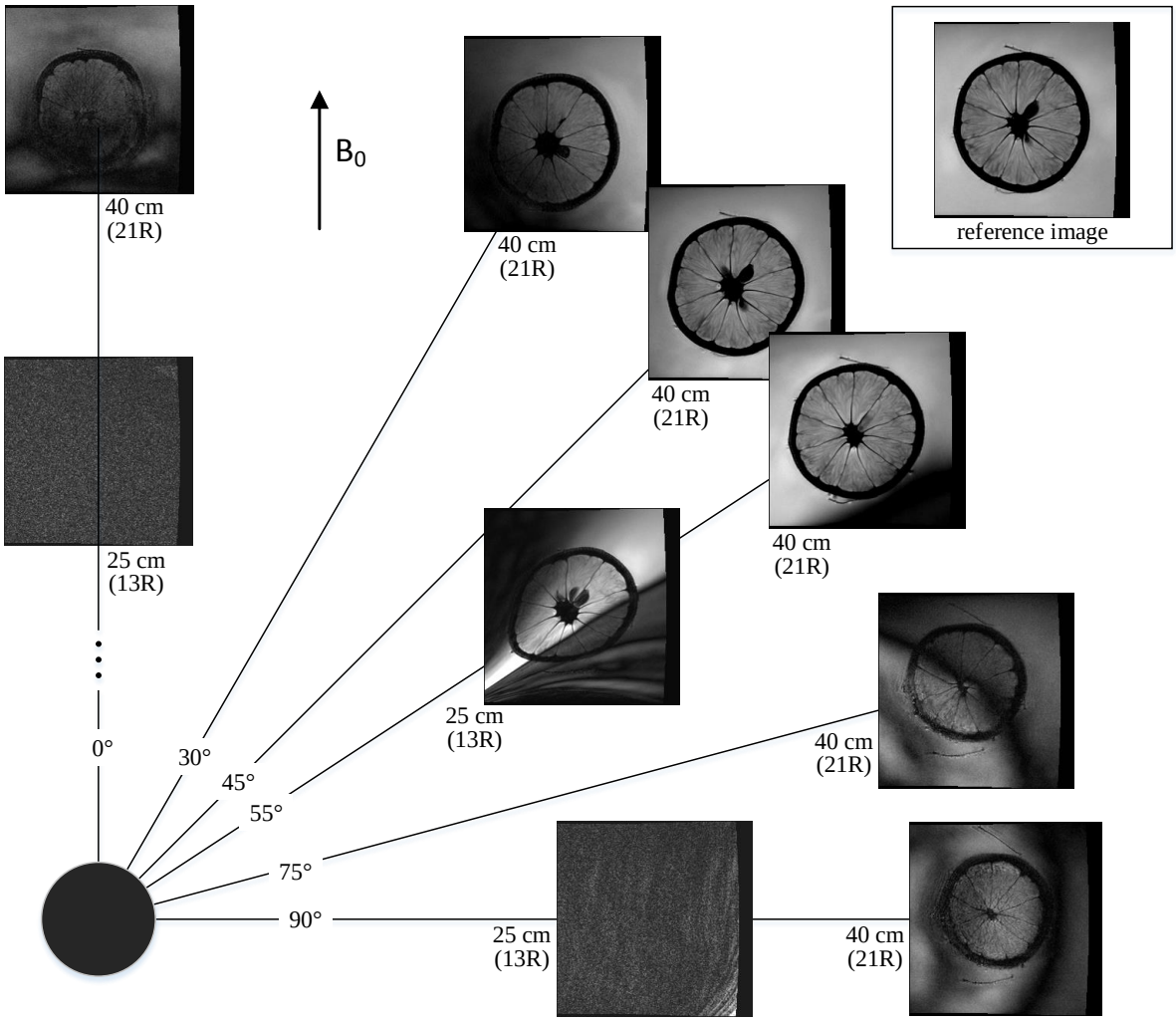

Figure 5.3 MR coronal images of an orange, acquired in presence of a 3.81 cm chrome steel core located at different positions. Imaging parameters: turbo spin echo, TE = 117 ms, TR = 3500 ms, ETL = 19, pixel bandwidth = 260 Hz, slice thickness = 3 mm.

The core was constrained to a track in the horizontal plane (Fig. 5.4a) and was moved between navigation and imaging positions using the scanner's gradient coils (manual control, pulses of 0.2 s at 10 mT/m in x and 0.5 s at 12 mT/m in z). Fig. 5.4b and 5.4c depict the theoretical particle steering gradients, which are generated by the core, along the desired paths on a schematic of the vascular phantom. The setup was placed in the homogeneous volume of the MRI scanner and oriented such that $\mathbf{B}_0$ was parallel to the general flow direction. To ensure equal flow at each bifurcation, water was pumped from each of the four output branches using syringes mounted on a Harvard Apparatus PHD 2000 pump. The input flow rate from a reservoir was 20 mL/min (16.8 cm/s). Magnetic particles encapsulating ferrofluid (Ferrotec EMG 700, $M_{sat} = 25860$ A/m) with an average diameter of 300 μm were injected individually

from the outside of the scanner to avoid their aggregation during their transit towards the phantom. A total of eight particles were injected for each target.

To cope with the vertical distortion of the imaging slices explained above, volume images for the entire thickness of the phantom were acquired. With the core located at its imaging position, we observed a vertical shift of the slices of about 3-5 mm in the center and up to 1 cm in some corners of the images. This resulted in a portion of the slices being shifted outside the phantom, where air generates no resonance signal. To facilitate visualization, slice images were blended together using transparency gradients so that a full view of the branches was obtained. Fig. 5.5 shows the resulting images corresponding to before, between and after the two navigation tasks. The artifacts created by the magnetic particles are clearly visible in images taken after their navigation. From these, we notice that all injected particles reached the targeted locations. For comparison, Fig. 5.6 shows a top view photograph of the phantom taken after removal from the scanner, where particles are also only visible in the desired branches.

In summary, we have demonstrated that MRI is possible in specific regions around a ferromagnetic core. The location and shape of these regions relative to the core depend on the resonance frequency offset induced by the core. In particular, the offset is minimized at specific angles relative to the central field and decreases with the distance from the core. Although the images acquired in these regions are likely to exhibit some distortion, we have shown that they can suffice for assessing targeting accuracy during DFN interventions. Furthermore, we have demonstrated that core positioning for both targeting and imaging can be performed using the gradient coils of the scanner. This approach enables efficient and automated navigation and delivery assessment at multiple target locations. While demonstrated here using spin echo, optimizing the imaging sequence used and the imaging parameters could potentially yields better imaging capabilities. For a given sequence, one could potentially calibrate and estimate particle accumulation at a target site from the size of the artifact. Finally, navigating in 3-D vasculatures generally requires multiple cores to generate the navigation gradient patterns needed [10]. Finding (and moving the cores to) proper positions for imaging in this case would be more challenging and will be addressed in future work.

This work was supported by the Fonds de recherche du Québec - Nature et technologies (FRQNT), the Canada Research Chair in Medical Nanorobotics, the US National Science Foundation under grant IIS-1208509 and the Wyss Institute for Biologically Inspired Engineering.

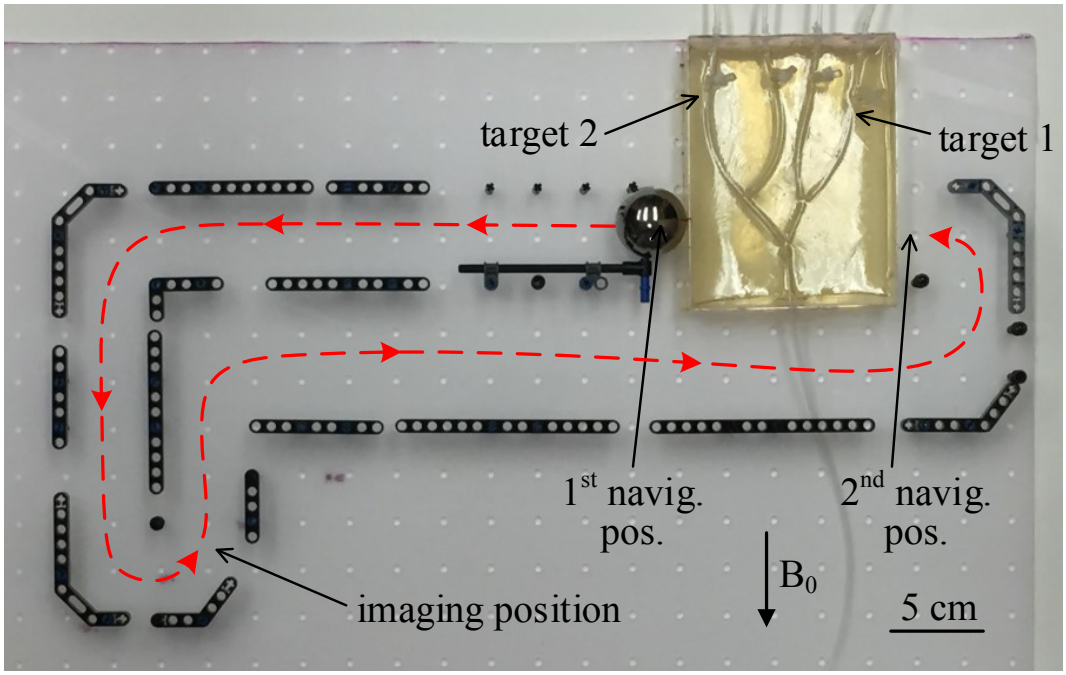

(a)

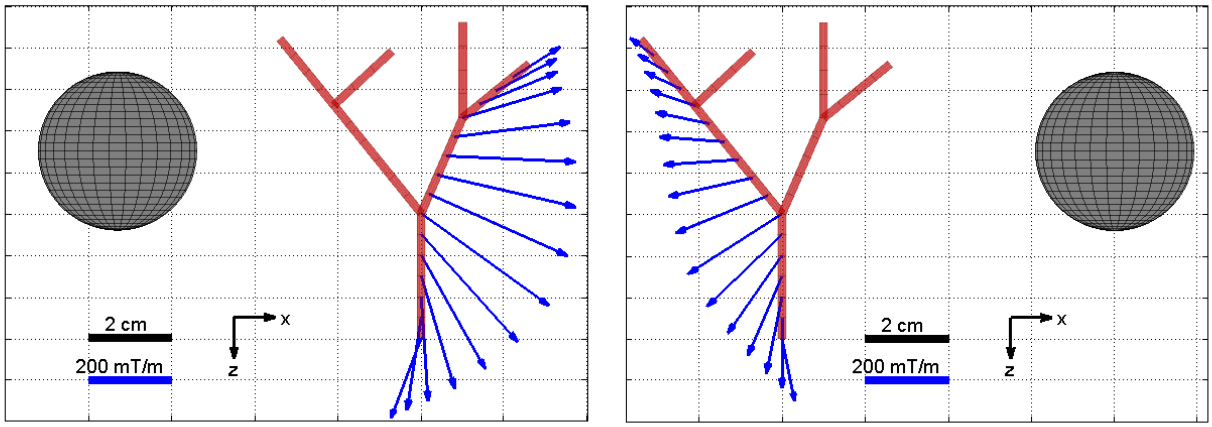

(b) (c)

Figure 5.4 a) Experimental setup used for the navigation and imaging experiment. b) and c) Optimized core positions (black spheres), for targets 1 and 2 respectively, and theoretical navigation gradients (blue arrows) resulting from the presence of the core along the desired path.

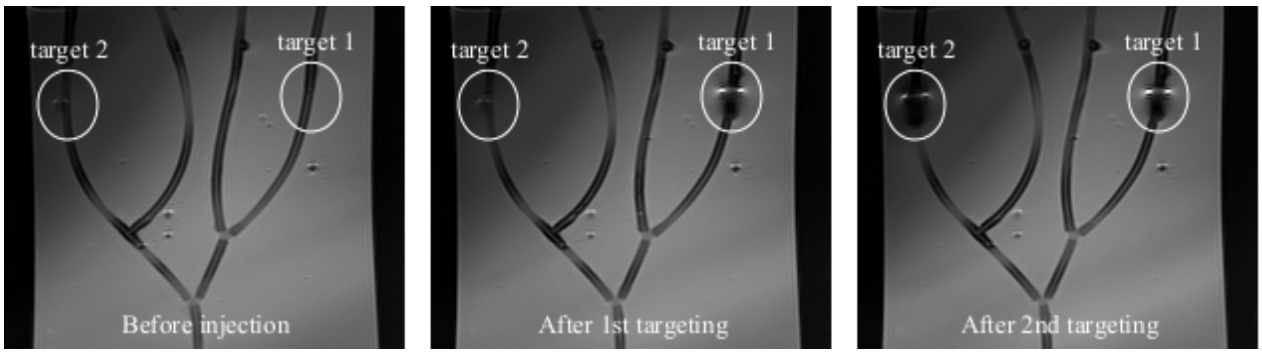

Figure 5.5 Coronal images of the phantom resulting from the combination of slice images acquired during the navigation experiment, with the core located at its imaging position. Each image is the result of 5 slice images blended together using transparency gradients in order to cope with slice depth distortions and provide a full view of the branches. Imaging parameters: spin echo, TE = 9.9 ms, TR = 800 ms, pixel bandwidth = 250 Hz, slice thickness = 3 mm, spacing between slices = 3.9 mm.

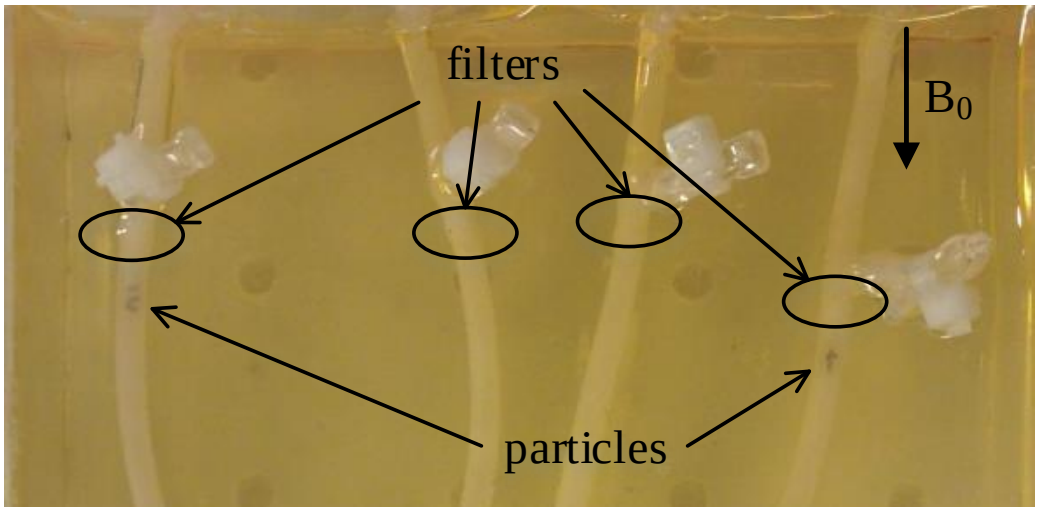

Figure 5.6 Post injection photograph of phantom showing particles in targeted branches. Note that particles shifted away from filters during removal from scanner for photographic imaging.

5.3 References

[1] P. Vartholomeos, M. Fruchard, A. Ferreira, et C. Mavroidis, "MRI-Guided Nanorobotic Systems for Therapeutic and Diagnostic Applications", *Annu. Rev. Biomed. Eng.*, vol. 13, no. 1, pp. 157–184, 2011. DOI: 10.1146/annurev-bioeng-071910-124724

[2] B. Shapiro, S. Kulkarni, A. Nacev, S. Muro, P. Y. Stepanov, et I. N. Weinberg, "Open challenges in magnetic drug targeting", *Wiley Interdiscip. Rev. Nanomedicine Nanobiotechnology*, vol. 7, no. 3, pp. 446–457, 2015.

[3] M. Muthana, A. J. Kennerley, R. Hughes, J. Richardson, M. Paul, C. Murdoch, F. Wright, M. Lythgoe, N. Farrow, J. Dobson, J. M. Wild, et C. Lewis, "Directing cell therapy to anatomic target sites in vivo with magnetic resonance targeting", *Nat. Commun.*, vol. 6, p. 8009, 2015.

[4] S. Martel, J.-B. Mathieu, O. Felfoul, A. Chanu, E. Aboussouan, S. Tamaz, P. Pouponneau, L. Yahia, G. Beaudoin, G. Soulez, et M. Mankiewicz, "Automatic navigation of an untethered device in the artery of a living animal using a conventional clinical magnetic resonance imaging system", *Appl. Phys. Lett.*, vol. 90, no. 11, p. 114105, 2007.

[5] A. Chanu, O. Felfoul, G. Beaudoin, et S. Martel, "Adapting the clinical MRI software environment for real-time navigation of an endovascular untethered ferromagnetic bead for future endovascular interventions", *Magn. Reson. Med.*, vol. 59, pp. 1287–1297, 2008.

[6] O. Felfoul, J. B. Mathieu, G. Beaudoin, et S. Martel, "In vivo MR-tracking based on magnetic signature selective excitation", *IEEE Trans. Med. Imaging*, vol. 27, no. 1, pp. 28–35, 2008. DOI: 10.1109/TMI.2007.897375

[7] M. P. Kummer, J. J. Abbott, B. E. Kratochvil, R. Borer, A. Sengul, et B. J. Nelson, "Octomag: An electromagnetic system for 5-DOF wireless micromanipulation", *IEEE Trans. Robot.*, vol. 26, no. 6, pp. 1006–1017, 2010. DOI: 10.1109/TRO.2010.2073030

[8] G. Go, H. Choi, S. Jeong, C. Lee, S. Y. Ko, J.-o. Park, et S. Park, "Electromagnetic Navigation System Using Simple Coil Structure (4 Coils) for 3-D Locomotive Microrobot", *IEEE Trans. Magn.*, vol. 51, no. 4, pp. 1–7, 2015.

[9] A. Mahmood, M. Dadkhah, M. O. Kim, et J. Yoon, "A Novel Design of an MPI-Based Guidance System for Simultaneous Actuation and Monitoring of Magnetic Nanoparticles",

IEEE Trans. Magn., vol. 51, no. 2, pp. 1–5, 2015. DOI: 10.1109/TMAG.2014.2358252

[10] M. Latulippe et S. Martel, "Dipole Field Navigation: Theory and Proof of Concept", *IEEE Trans. Robot.*, vol. 31, no. 6, pp. 1353–1363, 2015.

[11] U. Vovk, F. Pernuš, et B. Likar, "A review of methods for correction of intensity inhomogeneity in MRI", *IEEE Trans. Med. Imaging*, vol. 26, no. 3, pp. 405–421, 2007. DOI: 10.1109/TMI.2006.891486

[12] W. Lu, K. B. Pauly, G. E. Gold, J. M. Pauly, et B. A. Hargreaves, "SEMAC: Slice encoding for metal artifact correction in MRI", *Magn. Reson. Med.*, vol. 62, no. 1, pp. 66–76, 2009. DOI: 10.1002/mrm.21967

[13] M. Carl, K. Koch, et J. Du, "MR imaging near metal with undersampled 3D radial UTE-MAVRIC sequences", *Magn. Reson. Med.*, vol. 69, no. 1, pp. 27–36, 2013. DOI: 10.1002/mrm.24219

[14] P. Vartholomeos, C. Bergeles, L. Qin, et P. E. Dupont, "An MRI-powered and controlled actuator technology for tetherless robotic interventions", *Int. J. Rob. Res.*, vol. 32, no. 13, pp. 1536–1552, 2013. DOI: 10.1177/0278364913500362

CHAPITRE 6 ARTICLE 3: A PROGRESSIVE MULTIDIMENSIONAL PARTICLE SWARM OPTIMIZER FOR MAGNETIC CORE PLACEMENT IN DIPOLE FIELD NAVIGATION

Maxime Latulippe and Sylvain Martel

IEEE/RSJ International Conference on Intelligent Robots and Systems

6.1 Abstract

This paper tackles the inverse problem of finding optimal configurations of magnetic gradient sources in Dipole Field Navigation (DFN), a magnetic navigation method proposed recently for the direct targeting of drugs. In DFN, a limited number of these gradient sources, called the cores, must be positioned properly around a patient in a Magnetic Resonance Imaging scanner to induce the required directional forces on the navigated therapeutic carriers. To overcome some limitations of the previous approach for solving this problem, here we propose a novel and conceptually simple multidimensional variant of the well-known Particle Swarm Optimization (PSO) algorithm. This variant, called Progressive Multidimensional PSO (PMD-PSO), enables a tradeoff between the quality and the complexity of the solutions by progressively increasing the number of dimensions in the search space. We apply this algorithm to the core placement problem using an improved fitness function for the evaluation of a core configuration given a vascular path towards a target. Experiments on simulated vasculatures show that, while the approach can effectively solve this inverse problem, PMD-PSO exhibits better performances for DFN compared with two other multidimensional PSO variants.

6.2 Introduction

Direct targeting (DT) of drugs is a technology where drug-loaded microcarriers embedding superparamagnetic nanoparticles (MNPs) are navigated in the vascular network, from an injection point directly towards a targeted region. In cancer therapy for instance, such targeting of therapeutics to tumors would significantly increase the efficiency of treatments while reducing their secondary toxicity effects. In fact, despite the majority of cancers being initially localized, the common systemic administration of chemotherapeutic drugs generally leads to poor therapeutic effects (1-2% targeting) and to affected healthy organs and tissues.

The most effective method of DT to date that has been demonstrated *in vivo* is based on magnetic actuation [1] and is known as Magnetic Resonance Navigation (MRN) [2, 3]. This

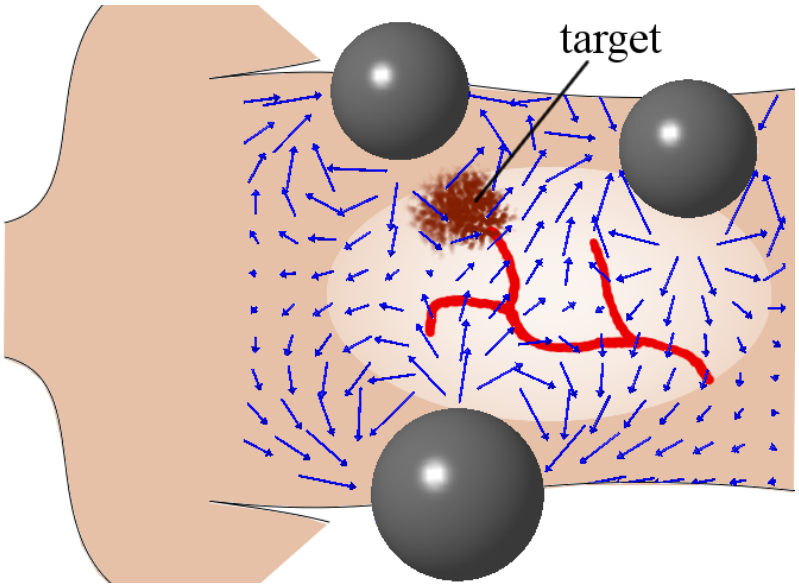

Figure 6.1 In DFN, ferromagnetic cores positioned around the patient in an MRI scanner generate gradients (arrows) for navigation towards a target.

method exploits the high magnetic field of a clinical Magnetic Resonance Imaging (MRI) scanner to bring the MNPs at saturation magnetization. Once magnetized, directional forces can be induced on the carriers by applying magnetic gradient fields using the scanner's imaging gradient coils. Conventional clinical scanners are however generally limited to gradient strengths around 40 mT/m, while at least ~300 mT/m is desirable for guiding the small carriers (~150 μm) needed to reach arterioles [4]. Although slowing down the blood flow would enable navigation using weaker gradients, this alternative would in return significantly increase the delivery time. Electromagnetic actuation systems or other coil-based systems [5–7], on another hand, are capable of much higher gradients, but only in smaller workspaces which prevent whole-body interventions.

A more recent approach that enable whole-body interventions with both a high field strength and high directional gradients is Dipole Field Navigation (DFN) [8]. In this approach, large ferromagnetic cores are inserted in an MRI scanner to distort the field, which generate gradients exceeding 300 mT/m in deep tissues. By adequately configuring a set of cores around a patient in the scanner, specific gradients can be generated to guide microcarriers along a desired vascular path (Fig. 6.1). This enhanced capability is however paid off by the much more complex models required for navigation. In fact, the nonlinear distortions around the cores as well as potential magnetic interactions render the inverse problem of finding proper core positions difficult, while the positioning precision directly affects the achievable navigation accuracy and resolution. Moreover, anatomical variations of the vasculature across

patients [9] limit the use of predefined core configurations. On another hand, the strong distortions of the static field *a priori* prevents imaging for real-time tracking and control of the carriers as achieved in MRN [10], although it was shown recently that imaging is possible in specific regions around a core in the scanner [11].

Thus, for the feasibility and practicality of DFN in a clinical setting, there is a need for an automatic system for the calculation of proper core configurations as a function of a patient's vasculature between an injection point and a target. Ideally, such a system should be able to minimize the required number of cores, while choosing them among a list of available core sizes or even geometries for an increased flexibility. In [8], we have proposed an optimization approach to solve this magnetic inverse problem and demonstrated the feasibility of DFN by guiding particles through three consecutive bifurcations in a 3-D *in vitro* network. To deal with some limitations of this approach however, which are mentioned in Section 6.3, here we propose in Section 6.4 a novel and conceptually simple multidimensional variant of Particle Swarm Optimization (PSO) [12], which we call Progressive Multidimensional PSO (PMD-PSO). In PMD-PSO, dimensions (cores) are progressively added to the search space while exploiting the best solutions found in lower dimensionality. In Section 6.5, we apply this algorithm to the DFN core placement problem using an improved, more adapted fitness function for the quality evaluation of a core configuration given a desired vascular path. Using this new function, navigation issues unaccounted for previously in [8] are avoided. Finally, we show in Section 6.6 that PMD-PSO exhibits better performances for DFN compared with two other multidimensional PSO approaches.

6.3 Previous Works

6.3.1 Magnetic Models for Dipole Field Navigation

The magnetic force induced by a total external field $\mathbf{B}_{tot}$ on a particle having a magnetic moment $\mathbf{m}_p$ is given by

$$\mathbf{F}_{mag} = \nabla(\mathbf{m}_p \cdot \mathbf{B}_{tot}) = m_p \nabla B_{tot} \tag{6.1}$$

where the right-hand side of the equation is valid for a particle magnetized by $\mathbf{B}_{tot}$, which is the case in DFN.

In presence of the scanner's homogeneous field $\mathbf{B}_0$, a ferromagnetic core becomes uniformly magnetized. For a spherical core, the magnetic field $\mathbf{B}_i$ generated by the core at any point $\mathbf{r}$

relative to the core center is that of a dipole:

$$\mathbf{B}_i(r > R_i) = \frac{\mu_0}{4\pi}\left[3\frac{(\mathbf{m}_i \cdot \mathbf{r})\mathbf{r}}{r^5} - \frac{\mathbf{m}_i}{r^3}\right] \tag{6.2}$$

where $\mu_0 = 4\pi \times 10^{-7}\,\mathrm{H/m}$ is the vacuum permeability, $r = \|\mathbf{r}\|$, R_i is the radius of the core and $\mathbf{m}_i$ its magnetic moment, which in the case of a sphere is

$$\mathbf{m}_i = \frac{4\pi R_i^3}{3}\mathbf{M}_{sat} \tag{6.3}$$

where $\mathbf{M}_{sat}$ is the volume magnetization of the material at saturation magnetization. In fact, a typical $\mathbf{B}_0$ strength of 1.5 T or 3 T is sufficient to bring most ferromagnetic materials close to or at full saturation magnetization. Thus, in DFN, the cores and particles can be considered saturated.

Assuming that the magnetic interactions between cores can be neglected, the total gradient field induced by N cores in the scanner is the linear sum of the individual gradient fields:

$$\nabla B_{tot} = \sum_{i=1}^{N} \nabla B_i = \sum_{i=1}^{N} \mathbf{G}_i \tag{6.4}$$

The validity of this assumption can be ensured by imposing minimum separating distances between cores (see Section 6.5.2). Note that the gradient of $\mathbf{B}_0$ is zero since this field is homogeneous.

In a high field strength B_0, the direction of $\mathbf{B}_{tot}$ around a core quickly becomes approximately parallel to $\mathbf{B}_0$ as the distance to the core increases. Thus, with the further assumption that $\mathbf{B}_{tot} \parallel \mathbf{B}_0$, it can be shown from (6.2) that [8]

$$\mathbf{G}_i \approx \frac{3\mu_0 m_i}{4\pi r^4}\begin{bmatrix} \sin\theta\cos\phi\,(1 - 5\cos^2\theta) \\ \sin\theta\sin\phi\,(1 - 5\cos^2\theta) \\ \cos\theta\,(3 - 5\cos^2\theta) \end{bmatrix} \tag{6.5}$$

where $\mathbf{r} = (r, \theta, \phi)$ is expressed in spherical coordinates [1] with $\theta = 0$ when $\mathbf{r} \parallel \mathbf{B}_0$. Without this latter assumption, the exact expression for ∇B_i, not included here, must be used. Despite the rapid decay of gradient magnitudes in r^{-4}, gradients can still exceed 300 mT/m in deep tissues [8].

1. The convention used here defines θ as the polar angle from an axis going in the direction of $\mathbf{B}_0$ and ϕ as the azimuthal angle.

Therefore, from the above equations, by properly positioning a set of cores around the patient, it is possible to generate a total magnetic gradient field in a vasculature such that particles are consecutively pushed in the desired vessel branches at bifurcations leading to a target.

6.3.2 Magnetic Core Positioning in DFN

In this work, we consider spherical cores made of the same ferromagnetic material. A core can thus be represented by its position and radius, i.e., $\mathcal{C}_i = \{x_i, y_i, z_i, R_i\}$. The magnetic inverse problem in DFN consists in finding a configuration of N cores $\{\mathcal{C}_1, \mathcal{C}_2, ..., \mathcal{C}_N\}$ that will generate an adequate gradient field ∇B_{tot} according to an evaluation function and given a vascular path. The complexity of this nonlinear and nonconvex problem increases with the number of cores.

Methods have been proposed for parameterizing a set of magnetic sources (e.g., currents in electromagnetic coils) to generate specific magnetic fields and gradients in magnetic actuation [5, 6, 13]. They do not apply to DFN however since the required number and locations of the sources (cores) are unknown. In DFN, core positioning must also take into account various constraints, such as minimum separating distances between cores to avoid magnetic interactions and physical constraints related to the patient body and scanner. Therefore, core positioning can be addressed as a constrained multidimensional optimization problem.

We have previously presented a search algorithm for solving this inverse problem [8]. This approach defines a set of target gradients on the vascular path and incrementally solves the problem by progressively considering those target gradients as partial solutions are found. At each step, the algorithm uses a local optimizer (gradient descent) to optimize various combinations of initial core positions determined using a heuristic based on the inverse magnetic model of (6.5). It is able to minimize the number of required cores and search using different discrete core radii. While being effective, disadvantages of this approach are its exponential computational complexity in the number of target gradients and available core radii, and its high dependence on the core initialization heuristic. More importantly, this incremental strategy considers the entire path up to the target only once all previous desired gradients are met. This can represent an issue if the algorithm fails before reaching the target.

6.3.3 Particle Swarm Optimization

Originally proposed in 1995, Particle Swarm Optimization (PSO) [12, 14] is an evolutionary algorithm where a swarm of particles (candidate solutions) fly through the search space to optimize a given objective (or fitness) function. After being initialized in the search space of dimension D with random position and velocity vectors $\mathbf{x}$ and $\mathbf{v}$, every particle is updated, at each iteration t and in each dimension d, according to

$$v_{t+1}^d = \omega v_t^d + r_1 c_1 \left(p_t^d - x_t^d\right) + r_2 c_2 \left(g_t^d - x_t^d\right) \tag{6.6}$$

$$x_{t+1}^d = x_t^d + v_{t+1}^d \tag{6.7}$$

where c_1 and c_2 are the personal and social acceleration coefficients, often set to 1.49 or 2, r_1 and r_2 are uniformly distributed random variables between 0 and 1, and ω is the inertia weight which balances between global exploration (larger value) and local exploitation (smaller value). The vectors $\mathbf{p}_t$ and $\mathbf{g}_t$ are the particle's personal best and the swarm's global best known positions, at iteration t, according to the objective function $F(\mathbf{x}_t)$. A maximum velocity parameter V_{max} is usually set to prevent the explosion of the swarm, as well as some mechanism to avoid particles from leaving a region of interest in the search space. This basic variant of PSO uses the global best neighborhood topology since each particle is aware of the entire swarm's best position. The best choice of topology is in fact problem dependent and can greatly impact the performances [15, 16]. Many variants of the algorithm have also been proposed since its introduction to improve its convergence properties [17].

PSO has shown good performances in a variety of optimization problems, including magnetic inverse problems such as the modeling of magnetic fields from measurements using dipoles [18] and the magnetoencephalography source localization [19]. Works in multidimensional optimization (i.e., when the global optimum has an unknown number of dimensions) are however limited. Multidimensional PSO (MD PSO) [20] and Dimension Adaptive PSO (DA-PSO) [21] provide mechanisms that allow particles to switch dimensionality during the optimization. These approaches, however, do not typically minimize the number of dimensions of the solutions, which is desired in DFN.

6.4 Progressive Multidimensional PSO

The PSO variant proposed in this work, called Progressive Multidimensional PSO (PMD-PSO), enable searching across a range of possible solution dimensionalities while providing an

optimum solution for each dimensionality considered.

PMD-PSO starts optimizing in D_{min} dimensions and progressively increases the number of dimensions D of the search space up to a given maximum D_{max}. Unlike an exhaustive search where PSO would be run separately in every considered dimensionality D, here the solutions coming from lower dimensionalities are injected in higher dimensionalities in order to find improved solutions. It is assumed that the improvement obtained by adding dimensions at some point becomes insubstantial. Therefore, an informed tradeoff can be made following PMD-PSO between the quality and the complexity (dimensionality) of the solution retained.

Let a particle be defined by a number of *components*. A component is a set of parameters (dimensions) that come altogether and cannot be separated. In DFN, for example, a component is one core $\mathcal{C} = \{x, y, z, R\}$ and represents four dimensions. The particle's position can then be defined as

$$\begin{aligned} \mathbf{x} = [a_{1,1}, a_{1,2}, ..., a_{1,q}, \quad & a_{2,1}, a_{2,2}, ..., a_{2,q}, \\ ..., \quad & a_{p,1}, a_{p,2}, ...a_{p,q}] \end{aligned} \tag{6.8}$$

where p is the number of components in the particle and q is the number of parameters that constitute a component. Note that q is problem dependent and can take any value.

Assume that $D_{min} = q$. At the beginning of the algorithm, a swarm of S particles is thus randomly initialized with one component. The usual iterations of PSO using update equations (6.6) and (6.7) are then performed until the progression of the swarm, s, falls below a threshold s_{th}, i.e., until the swarm appears to have converged (or stagnated) to an optimum of the search space according to a certain criteria. At this point, the improvement of the global best solution is slow and it is generally very unlikely to improve significantly in further iterations. Thus, after setting each particle's position back to its own personal best, another component is randomly added to every particle and all velocities, including those of the previous components, are randomized in order to reintroduce some diversity. As a result, those "new" particles now in a higher dimensionality include knowledge gained in the lower dimensionality. To be in accordance with the new dimensionality, the new particle positions become the initial personal bests and the swarm's global best $\mathbf{g}$ is replaced by the position of best new particle. The same process repeats until D_{max} (or another stopping criteria) is reached. The algorithm then returns the best solution found for every dimensionality. The pseudo-code is presented in Algorithm 1.

Note that any variant of PSO, including other neighborhood topologies, can be used inside PMD-PSO to perform the velocity and position updates. Different stagnation detection

Algorithm 1 PMDPSO(S, D_{min}, D_{max}, s_{th}, $maxIter$)

```
G ← empty list of solutions
Initialize S particles with dimensionality D_min
for t = 1 to maxIter do
    for i = 1 to S do
        Calculate F(x_i)
        Update p_i
    end for
    g ← the best p_i
    for i = 1 to S do
        Update v_i and x_i using (6.6) and (6.7)
    end for
    if s < s_th then                                  ▷ Stagnation detection
        Add g to solution list G
        if D < D_max then
            for i = 1 to S do
                x_i ← p_i
                Add component to particle i
                Randomize v_i
                p_i ← x_i
                Calculate F(x_i)
            end for
            g ← the best p_i
        else
            return G
        end if
    end if
end for
return G
```

methods [22] can also be tested and adapted to the optimization problem.

6.5 Core Placement in DFN Using PMD-PSO

This section first describes the proposed fitness evaluation function and the constraints applied on core positions. Details for the application of PMD-PSO to DFN are then given.

6.5.1 Proposed Fitness Function

The approach proposed in [8] for core placement in DFN considers a resulting gradient on the path only once all conditions for the previous target gradients are met. As a result, if the

algorithm stops before reaching the target, the last bifurcations are not taken into account in the objective function. Here, we emphasize that the global quality of a core configuration, taking into account the entire vascular path, should be evaluated throughout the optimization process. Particle clogging issues discussed in [8] also highlight the importance of avoiding very strong gradients on the path.

Ultimately, the goal of DFN is to maximize the proportion of injected particles reaching the target, referred to here as the targeting ratio $\mathcal{R}_{target}$. Let $\mathcal{B}_i$ be the i^{th} bifurcation on the desired path. We define the steering ratio $\mathcal{R}_i$ as the fraction of particles reaching $\mathcal{B}_i$ that are pushed into the targeted branch of $\mathcal{B}_i$. The targeting ratio $\mathcal{R}_{target}$ is therefore the product of all steering ratios $\mathcal{R}_i$ on this path. The proposed fitness function to maximize is

$$f(\mathbf{x}) = \left(\frac{1}{K} \sum_{i=1}^{K} \cos \xi_i(\mathbf{x}) \right) \mathcal{R}_{target}(\mathbf{x}) \tag{6.9}$$

where $\mathbf{x}$ is a vector describing a core configuration, K is the number of bifurcations towards the target and $\xi_i(\mathbf{x})$ is the error angle between an "ideal" gradient orientation defined at $\mathcal{B}_i$ and the actual gradient resulting from $\mathbf{x}$ at this point. The term in parentheses allows to discriminate solutions having similar targeting ratios but different gradient orientations. This avoids compensating a bad gradient orientation with a higher magnitude. Furthermore, the normalization by K ensures a maximum value $f = 1$ for any vascular path.

Each steering ratio $\mathcal{R}_i$ can be estimated from the gradients generated along the vascular segment preceding $\mathcal{B}_i$. Ideally, this estimation would depend on the flow velocity and other parameters, and would take into account the cumulative effects of the various forces encountered by the particles during their transit in this segment. Although this could be achieved from modeling and simulation [23], here for simplicity, the value of $\mathcal{R}_i$ is calculated from the projection b_i of the resulting gradient at $\mathcal{B}_i$ on the "ideal" gradient orientation. We assume that $\mathcal{R}_i = 1$ when b_i meets a minimum gradient magnitude $G_{min,i}$ defined at $\mathcal{B}_i$. The value of $\mathcal{R}_i$ is linearly decreased to 0.5 when $b_i = 0$ (even split in the two branches) and to 0 when $b_i \leq -G_{min,i}$. The resulting value, given by the following equation,

$$\mathcal{R}_i = \nu_i \left(0.5 + 0.5 \frac{b_i}{G_{min,i}} \right) \tag{6.10}$$

is weighted by a penalty factor ν_i used to avoid very strong gradients from blocking particles as mentioned earlier. This factor is $\nu_i = 1$ unless the maximum resulting gradient magnitude

$g_{max,i}$ encountered on the segment preceding $\mathcal{B}_i$ exceeds a maximum value G_{max}, i.e.,

$$\nu_i = \min\left(\frac{G_{max}}{g_{max,i}}, 1\right) \tag{6.11}$$

This latter parameter is included here to intentionally complexify the estimation of steering ratios with the need to consider the gradients generated all along the path instead of only at bifurcation points. For the test purposes, the value of G_{max} is nevertheless kept constant on the entire path, although it should depend on several parameters including the gradient orientation and flow velocity.

Admittedly, the estimation of steering ratios using (6.10) does not reflect the much more complex reality of navigation in the blood flow environment. It however remains adequate for testing different core positioning algorithms.

6.5.2 Core Positioning Constraints

The constraints on core placement, mentioned in Section 6.3, are handled in this work using a penalty function approach. The function to maximize becomes

$$F(\mathbf{x}) = f(\mathbf{x}) - \sum_{i=1}^{C} h_i(\mathbf{x}) \tag{6.12}$$

where h_i are the penalties of the individual constraints on core positions and C is the total number of constraints.

To avoid unfeasible positions, the N cores are constrained to lie outside a 3-D volume representing the patient body. The penalty is a function of the depth d_i of a core's material entering this volume and is normalized by the core radius:

$$h_{1,i} = d_i/R_i \quad \forall i \in [1, N] \tag{6.13}$$

Similarly, cores are constrained to lie inside a 3-D volume representing the scanner's homogeneous field volume:

$$h_{2,i} = d_i/R_i \quad \forall i \in [1, N] \tag{6.14}$$

where in this case d_i is the distance by which a core's material exceeds that volume's boundary. Note that the patient table of the scanner was not included in this work.

Finally, to avoid modeling inaccuracies from magnetic interactions between cores, minimum

separating distances [8] between cores are imposed using the following penalties:

$$h_{3,i,j} = d_{i,j} \geq 4\max(R_i, R_j) \quad \forall i,j \in [1,N]/i \neq j \tag{6.15}$$

$d_{i,j}$ being the distance between positions of cores $\mathcal{C}_i$ and $\mathcal{C}_j$.

6.5.3 Application of PMD-PSO to DFN

According to (6.8), a particle in DFN is represented by

$$\mathbf{x} = [x_1, y_1, z_1, R_1, \ ..., \ x_N, y_N, z_N, R_N] \tag{6.16}$$

The basic PSO update equations (6.6) and (6.7) are used in this work inside the PMD-PSO algorithm. The particles are initialized with one component ($D_{min} = 4$).

The stagnation detection method used, which has shown the best behavior for DFN in preliminary tests, is objective function based and is similar to the one proposed in [24]. At each iteration t, the following value is computed:

$$s = \left| \frac{1 - F_t\left(\mathbf{g}'_t\right) / F_{t-1}\left(\mathbf{g}'_t\right)}{1 - \bar{v}_t / \bar{v}_{t-1}} \right| \tag{6.17}$$

where $\mathbf{g}'_t$ and $\bar{v}_t$ denote the *current* best particle and the average of all particle velocities at iteration t. It is assumed that the swarm is stagnating when the moving average of s over three iterations falls below a threshold s_{th} (i.e., when the variation of $\mathbf{g}'$ is small relative to the variation of $\bar{v}$).

As a last consideration also mentioned before, the optimization of core configurations in DFN should be limited to some discrete values of available core radii. In this work, this is achieved by selecting the closest discrete value for each real value R_i when computing the fitness function. Keeping real values for R_i in the particle position vectors prevents the values of R_i to converge too quickly to their final values.

6.6 Experiments

PMD-PSO was tested on simulated problems and compared with two other multidimensional PSO approaches for solving the DFN core placement problem.

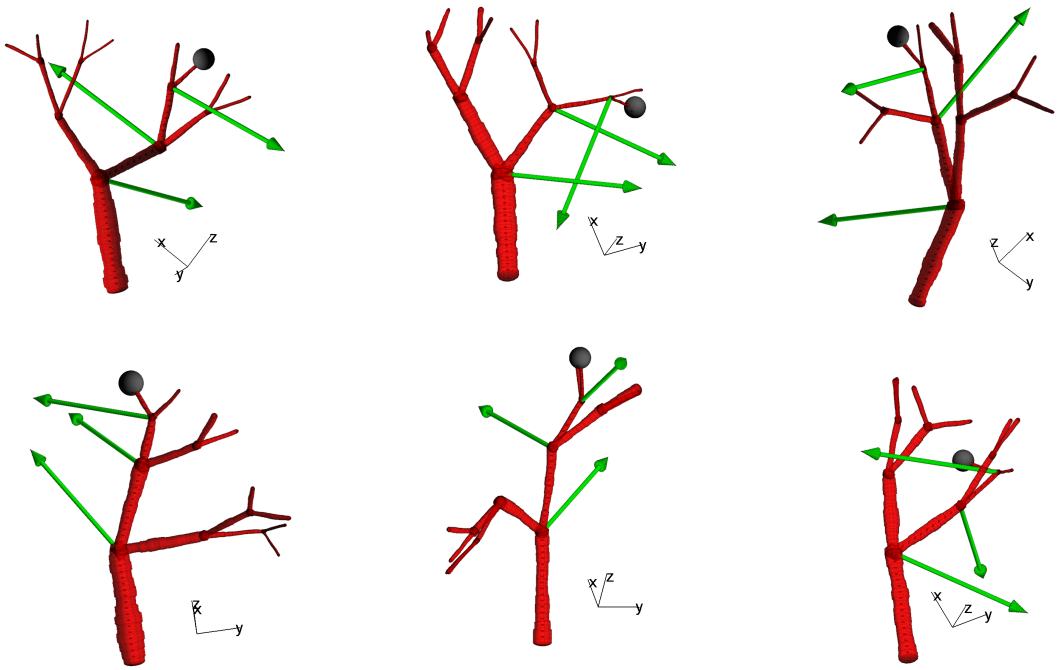

Figure 6.2 Examples of randomly generated vasculatures that were used to test the algorithms. The randomly selected targets are indicated by the dark spheres. The green arrows (which have a constant length in 3-D) show the "ideal" gradient orientations at bifurcation points in order to reach the target.

6.6.1 Test Framework

Random 3-D vascular networks were generated using Matlab. These networks had a tree-like structure with four levels (i.e., three bifurcations from the input to any of the output branches). For each network, one of the eight output branches was randomly selected as the target. For the test purposes, the "ideal" gradient orientations at bifurcation points were determined geometrically such that they lied in the bifurcation plane and were oriented perpendicular to the average direction of the two child branches, towards the desired branch. Fig. 6.2 shows vasculature examples with ideal gradient orientations at bifurcation points.

A total of 300 vasculatures were generated to test the algorithms. The average path length from the input point to the target was 7 cm. The average distance between the consecutive bifurcations was 2 cm between $\mathcal{B}_1$ and $\mathcal{B}_2$, and 1.4 cm between $\mathcal{B}_2$ and $\mathcal{B}_3$. The volume representing the patient body for constraints in (6.13) was defined as the axis-aligned bounding box of the vasculature padded by 5 cm on each side. This resulted in an average minimum depth of ≈ 6 cm of bifurcation points from the closest surface. The homogeneous field volume

for constraints in (6.14) was defined as a 50 cm sphere, which is a typical dimension for clinical MRI scanners. The value $G_{min} = 300\,\mathrm{mT/m}$ was set for all bifurcations and the constant defining the maximum gradient strength was set to $G_{max} = 2\,\mathrm{T/m}$.

6.6.2 Tested algorithms

The performance of PMD-PSO in solving the DFN inverse problem was compared to the following two algorithms:

Exhaustive dimensional search

The simplest approach for multidimensional optimization consists in trying each possible dimensionality independently. This approach is referred to here as Exhaustive PSO (E-PSO). To ensure an equivalent comparison with PMD-PSO, E-PSO was restarted with a higher number of cores when stagnation was detected.

Multidimensional PSO

Multidimensional PSO (MD PSO) [20] has been used successfully in multidimensional problems such as data clustering. In MD PSO, the particles have added parameters that enable them to switch between dimensionalities during the velocity and position updates. The algorithm however returns only one solution, which corresponds to the best dimensionality found, and thus does not enable a tradeoff between dimensionality and fitness value. It is nevertheless included here for comparison.

Note that Dimension Adaptive PSO [21], mentioned in Section 6.3, was not included in the tests of this work since it relies on an important weighting of the components in the particles. It is not evident what the best weighting criteria is for DFN and this was not investigated in this work.

6.6.3 Parameters Selection

Tests were conducted for swarm sizes $S = 20$ and $S = 50$. The particle velocity update parameters were set to $\omega = 0.65$ and $c_1 = c_2 = 1.49$. The maximum velocity V_{max} was set to 12.5 cm (1/4 the range of the scanner's volume) for positional dimensions (x, y, z), and to the full range of available radii for R. The stagnation threshold was set to $s_{th} = 10^{-5}$. These settings were determined from preliminary tests conducted using the basic PSO and were

used in all three algorithms. For an equivalent comparison of the algorithms, the number of iterations was not limited and the algorithms were stopped only once convergence (stagnation) was detected.

The tests were run assuming chrome steel cores ($M_{sat} = 1.4 \times 10^6$ A/m). The discrete values of available core radii provided were 1, 2, 3 and 4 cm. The maximum number of cores (components) was set to four ($D_{max} = 16$).

6.6.4 Results

Each algorithm was allowed three attempts per optimization problem. The average of these attempts was used as the result for each problem. Fig. 6.3a and 6.3b show the distributions of the results, for $S = 20$ and $S = 50$, over the 300 vasculatures as a function of the number of cores in the solution. Note that the random nature of the problems, combined with the various constraints on positions, did not guarantee the existence of an exact solution ($F = 1$) in all cases. As expected, E-PSO and PMD-PSO yielded very similar results for one core since they are the same algorithm at this stage. When dimensions are added to the search space however, PMD-PSO shows increased performances to solve the DFN problem. MD PSO on the other hand, which returns only one best solution found in a varying dimensionality, resulted in poorer solutions in our case. It was observed during experiments that MD PSO converged often rapidly to the final number of cores, thus preventing exploration in other dimensionalities.

We explain the observed improvement of PMD-PSO over E-PSO by the fact that particles in PMD-PSO, when a core is added to the search space, keep a knowledge of what good positions were in the lower dimensionality. With this knowledge and the randomization of the velocities, the particles have better chances to improve by adjusting these initial positions, but can also escape from this local optimum if better configurations are found from exploration. This behavior is clearly seen in Fig. 6.3c, which shows average fitness curves up to $t = 600$ for both algorithms ($S = 50$). The bumps on these curves are the result of the addition of a core to the search space. Whereas PMD-PSO benefits most of the time rapidly from the added core, restarting the optimization completely in E-PSO increases the risks of convergence to a poorer local optimum, which is sometimes worse than the previous solution found in the lower dimensionality.

Table I summarizes the results corresponding to the final solutions found by the algorithms (i.e., using four cores for E-PSO and PMD-PSO). Over all 300 problems, PMD-PSO yielded

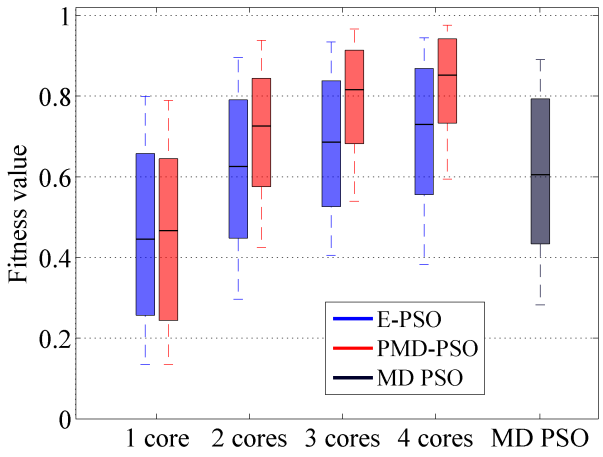

(a) $S = 20$.

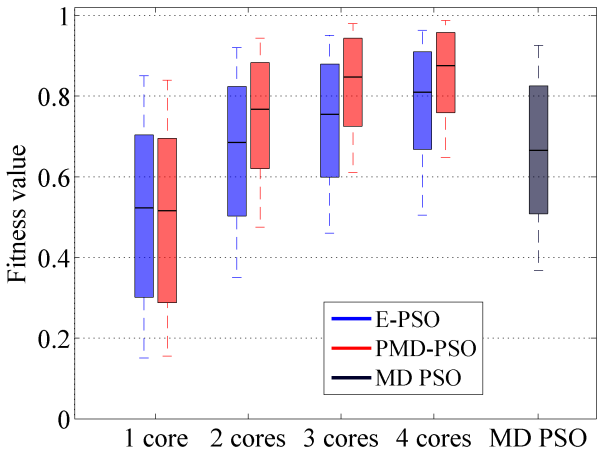

(b) $S = 50$.

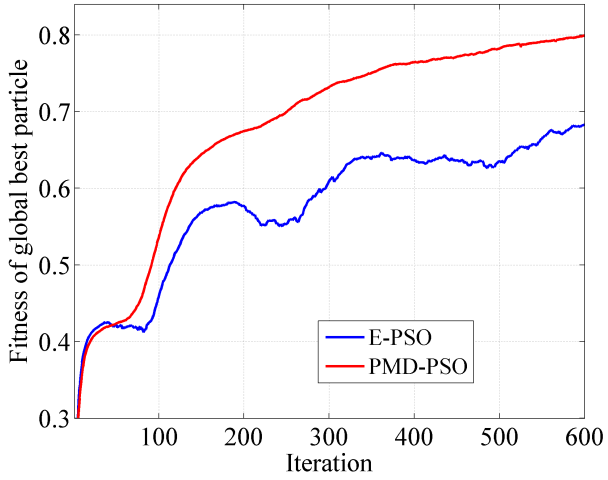

(c) $S = 50$.

Figure 6.3 a) Distribution of solution fitnesses (the closer to $F = 1$ the better) over the 300 problems solved, for different numbers of cores. Middle bars show the medians, box limits are the 1^{st} and 3^{rd} quartiles, whiskers extend to 10^{th} and 90^{th} percentiles. b) Average progression of fitness for E-PSO and PMD-PSO.

the final solution with the highest fitness value in close to 90% of the cases, followed by E-PSO. Interestingly, the amount of fitness by which PMD-PSO has "won" in these cases is also much more than the amount by which it was beaten in the other cases. Note that the small averages of the required number of iterations for MD PSO are due to its rapid convergence (stagnation) mentioned above.

Table 6.1 Overall performance of the tested algorithms on the 300 randomly generated navigation problems.

S	Algo	Mean	Med.	% win[a]	δ win[b]	# iter.[c]
20	E-PSO	0.697	0.730	8.3	0.025	784
	PMD-PSO	**0.813**	**0.852**	**91.0**	**0.117**	689
	MD PSO	0.603	0.605	0.7	0.008	171
50	E-PSO	0.764	0.810	12.0	0.026	807
	PMD-PSO	**0.841**	**0.875**	**87.3**	**0.087**	719
	MD PSO	0.651	0.665	0.7	0.009	182

[a] Pct. (%) of cases where this algorithm yielded the highest fitness.
[b] Amount of fitness by which this algo beat the others when it did.
[c] Average total number of iterations.

6.7 Discussion and Conclusion

The results presented above clearly show an advantage for using the proposed PMD-PSO over a basic exhaustive dimensional search (E-PSO) for the inverse problem of finding core configurations in DFN. Although both algorithms explore dimensionalities in a similar increasing fashion, PMD-PSO could find better solutions most of the time by exploiting the knowledge acquired in lower dimensionalities in the higher dimensionalities. Moreover, its capability to provide a solution for all possible dimensionalities enable an informed tradeoff to minimize the number of cores while ensuring a high targeting ratio. This is finally illustrated in Fig. 6.4 by an example of results obtained by PMD-PSO on a 2-D problem (for visualization purposes). In this case, the solution using two cores would probably be a good tradeoff considering its high fitness value, which is relatively close to that of the solution using three cores.

This novel approach for tackling the DFN inverse problem overcomes some limitations of the previous method presented in [8], notably by optimizing solutions according to the entire vascular path throughout the optimization process (instead of incrementally) and by using a fitness function more representative of the direct drug targeting problem. Nevertheless, although optimal core placements can be determined algorithmically, challenges remain for DFN to be used in a clinical settings. Among others, navigation errors can be expected resulting from complex flow conditions and flow variations, or from patient breathing and motion. Strategies will therefore be needed to deal with such uncertainties.

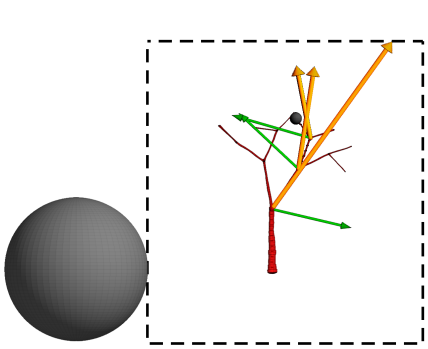

(a) Best solution using 1 core ($F = 0.296$).

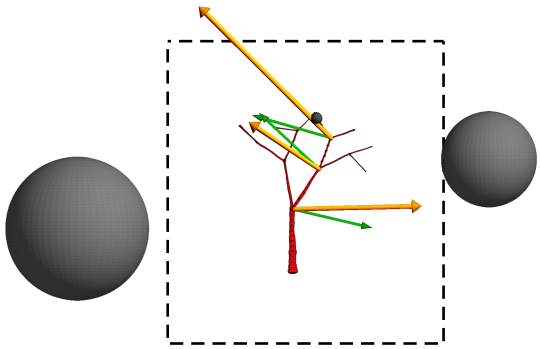

(b) Best solution using 2 cores ($F = 0.945$).

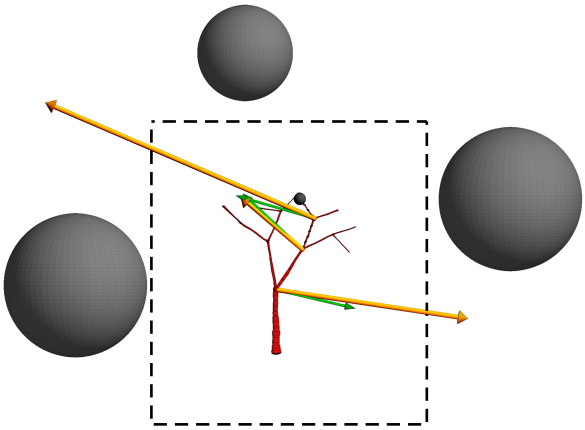

(c) Best solution using 3 cores ($F = 0.996$).

Figure 6.4 Illustration of the tradeoff in the number of cores using an example of the best solutions found by PMD-PSO on a 2-D problem. Green arrows show the "ideal" gradient orientations at bifurcation points towards the target, while thicker orange arrows show the resulting gradients generated by the cores (large spheres). Arrow lengths are proportional to gradient strengths. The dashed lines delimit the constraint representing the patient body.

Finally, in this work, the basic PSO algorithm was used inside PMD-PSO. More recent PSO variants, exhibiting better convergence properties, could be to incorporated inside PMD-PSO to see what improvements can be obtained using these variants. Additionally, it would be interesting to test PMD-PSO on different multidimentional problems such as, for example, the estimation of Gaussian mixture models.

6.8 References

[1] T. Xu, J. Yu, X. Yan, H. Choi, et L. Zhang, "Magnetic Actuation Based Motion Control for Microrobots: An Overview", *Micromachines*, vol. 6, no. 9, pp. 1346–1364, 2015.

[2] S. Martel, J.-B. Mathieu, O. Felfoul, A. Chanu, E. Aboussouan, S. Tamaz, P. Pouponneau, L. Yahia, G. Beaudoin, G. Soulez, et M. Mankiewicz, "Automatic navigation of an untethered device in the artery of a living animal using a conventional clinical magnetic resonance imaging system", *Appl. Phys. Lett.*, vol. 90, no. 11, p. 114105, 2007.

[3] P. Vartholomeos, M. Fruchard, A. Ferreira, et C. Mavroidis, "MRI-Guided Nanorobotic Systems for Therapeutic and Diagnostic Applications", *Annu. Rev. Biomed. Eng.*, vol. 13, no. 1, pp. 157–184, 2011. DOI: 10.1146/annurev-bioeng-071910-124724

[4] J. B. Mathieu et S. Martel, "Steering of aggregating magnetic microparticles using propulsion gradients coils in an MRI scanner", *Magn. Reson. Med.*, vol. 63, no. 5, pp. 1336–1345, 2010. DOI: 10.1002/mrm.22279

[5] M. P. Kummer, J. J. Abbott, B. E. Kratochvil, R. Borer, A. Sengul, et B. J. Nelson, "Octomag: An electromagnetic system for 5-DOF wireless micromanipulation", *IEEE Trans. Robot.*, vol. 26, no. 6, pp. 1006–1017, 2010. DOI: 10.1109/TRO.2010.2073030

[6] G. Go, H. Choi, S. Jeong, C. Lee, S. Y. Ko, J.-o. Park, et S. Park, "Electromagnetic Navigation System Using Simple Coil Structure (4 Coils) for 3-D Locomotive Microrobot", *IEEE Trans. Magn.*, vol. 51, no. 4, pp. 1–7, 2015.

[7] A. Mahmood, M. Dadkhah, M. O. Kim, et J. Yoon, "A Novel Design of an MPI-Based Guidance System for Simultaneous Actuation and Monitoring of Magnetic Nanoparticles", *IEEE Trans. Magn.*, vol. 51, no. 2, pp. 1–5, 2015. DOI: 10.1109/TMAG.2014.2358252

[8] M. Latulippe et S. Martel, "Dipole Field Navigation: Theory and Proof of Concept", *IEEE Trans. Robot.*, vol. 31, no. 6, pp. 1353–1363, 2015.

[9] M. S. Ugurel, B. Battal, U. Bozlar, M. S. Nural, M. Tasar, F. Ors, M. Saglam, et I. Karademir, "Anatomical variations of hepatic arterial system, coeliac trunk and renal arteries: an analysis with multidetector CT angiography." *Br. J. Radiol.*, vol. 83, no. 992, pp. 661–7, 2010. DOI: 10.1259/bjr/21236482

[10] A. Chanu, O. Felfoul, G. Beaudoin, et S. Martel, “Adapting the clinical MRI software environment for real-time navigation of an endovascular untethered ferromagnetic bead for future endovascular interventions”, *Magn. Reson. Med.*, vol. 59, pp. 1287–1297, 2008.

[11] M. Latulippe, O. Felfoul, P. E. Dupont, et S. Martel, “Enabling automated magnetic resonance imaging-based targeting assessment during dipole field navigation”, *Appl. Phys. Lett.*, vol. 108, no. 6, p. 062403, 2016. DOI: 10.1063/1.4941925

[12] J. Kennedy et R. Eberhart, “Particle swarm optimization”, *IEEE Int. Conf. Neural Networks*, vol. 4, pp. 1942–1948 vol.4, 1995. DOI: 10.1109/ICNN.1995.488968

[13] A. J. Petruska, A. W. Mahoney, et J. J. Abbott, “Remote manipulation with a stationary computer-controlled magnetic dipole source”, *IEEE Trans. Robot.*, vol. 30, no. 5, pp. 1222–1227, 2014. DOI: 10.1109/TRO.2014.2340111

[14] Y. Shi et R. Eberhart, “A modified particle swarm optimizer”, dans *Proc. IEEE Int. Conf. Evol. Comput.*, 1998, pp. 69–73. DOI: 10.1109/ICEC.1998.699146

[15] J. Kennedy et R. Mendes, “Population Structure and Particle Swarm Performance”, dans *IEEE Congr. Evol. Comput.*, 2002, pp. 1671–1676. DOI: 10.1109/CEC.2002.1004493

[16] A. P. Engelbrecht, “Particle swarm optimization: Global best or local best?” dans *BRICS Ctries. Congr. Comput. Intell.*, no. 1, 2013, pp. 124–135. DOI: 10.1109/BRICS-CCI-CBIC.2013.31

[17] M. R. Bonyadi et Z. Michalewicz, “A locally convergent rotationally invariant particle swarm optimization algorithm”, *Swarm Intell.*, vol. 8, pp. 159–198, 2014. DOI: 10.1007/s11721-014-0095-1

[18] S. Spantideas, N. Kapsalis, S. D. Kakarakis, et C. Capsalis, “A Method of Predicting Composite Magnetic Sources Employing Particle Swarm Optimization”, *Prog. Electromagn. Res. M*, vol. 39, pp. 161–170, 2014.

[19] K. E. Parsopoulos, F. Kariotou, G. Dassios, et M. N. Vrahatis, “Tackling magnetoencephalography with particle swarm optimization”, *Int. J. Bio-Inspired Comput.*, vol. 1, no. 1-2, pp. 32–49, 2009. DOI: 10.1504/IJBIC.2009.022772

[20] S. Kiranyaz, J. Pulkkinen, et M. Gabbouj, “Multi-dimensional particle swarm optimiza-

tion in dynamic environments", *Expert Syst. Appl.*, vol. 38, no. 3, pp. 2212–2223, 2011. DOI: 10.1016/j.eswa.2010.08.009

[21] Y. Yan et L. A. Osadciw, "Density estimation using a new dimension adaptive particle swarm optimization algorithm", *Swarm Intell.*, vol. 3, no. 4, pp. 275–301, 2009. DOI: 10.1007/s11721-009-0032-x

[22] F. Van Den Bergh, "An analysis of particle swarm optimizers", Ph.D. Thesis, University of Pretoria, South Africa, 2002.

[23] M. Larimi, A. Ramiar, et A. Ranjbar, "Numerical simulation of magnetic nanoparticles targeting in a bifurcation vessel", *J. Magn. Magn. Mater.*, vol. 362, pp. 58–71, 2014.

[24] C. Worasucheep, "A Particle Swarm Optimization with stagnation detection and dispersion", dans *IEEE World Congr. Comput. Intell.*, 2008, pp. 424–429.

CHAPITRE 7 ARTICLE 4: SEEKING OPTIMAL MAGNETIC CORE SHAPES FOR STRONG GRADIENT GENERATION IN DIPOLE FIELD NAVIGATION

Maxime Latulippe and Sylvain Martel

IEEE International Conference on Manipulation, Automation and Robotics at Small Scales

7.1 Abstract

Dipole Field Navigation (DFN) has been proposed previously as a promising remote magnetic actuation method for the navigation of microscale agents in vascular networks for the targeted delivery of therapeutics. This method exploits the strong magnetic field of a magnetic resonance imaging scanner to bring the agents at saturation magnetization, and relies on the proper positioning of ferromagnetic cores around the patient in the scanner to induce strong magnetic gradients for navigation. It is currently the only method providing both the high field and high gradient strengths required for the navigation of microparticles at the human scale. Because of the simpler magnetic models of this shape, previous works on DFN considered only spherical ferromagnetic cores. This work investigates different core shapes and shows that the sphere can be outperformed for deep tissue interventions. The gradients around different shapes, calculated by finite element modeling, are compared in the context of typical DFN conditions. Results show that, for the same amount of ferromagnetic material, the hemisphere and the disc generate significantly higher gradients (>50% gains) in deep tissues. Using those shapes instead of spheres would therefore improve the performances of DFN for targeting deep regions in the body.

7.2 Introduction

Controlled robotic agents inside the human body enable minimally invasive interventions for the enhanced treatment and diagnosis of diseases, while reducing the risks of complications and allowing for faster recovery. To this purpose, magnetic actuation has proven its effectiveness for the remote navigation of small devices or particles towards otherwise hard-to-reach regions inside the body. By applying magnetic fields and gradients, propelling forces and torques can be induced on magnetized agents to enable their control. Example applications using this approach include magnetically guided capsule endoscopes [1, 2], catheter steering platforms [3, 4] and controlled devices for microsurgery [5, 6]. At a smaller scale, the ability

to navigate microscale agents inside blood vessels would enable the targeted delivery of therapeutics to localized diseases, by guiding them through the vasculature from an injection point directly towards the target site. For the treatment of tumors notably, this ability would result in much more effective treatments compared with current chemotherapies where the free circulation of drugs yield poor therapeutic indexes while affecting healthy organs and tissues.

A simple approach for achieving such magnetic targeting consists in attracting magnetic nanoparticles coated with drug molecules using a magnet positioned near the target site [7, 8]. This approach, which relies on the diffusion of the nanoparticles through tissues, offers however poor control capabilities and, due to the rapid decay of the magnetic field and gradients, is limited to surface tissues. To enable more complex navigation inside vascular networks, magnetic microrobots capable of releasing drugs once at the target site can be fabricated. In particular, biology-inspired microrobots mimicking the propulsion mechanism of bacterial flagella have been proposed [9–11]. These can be actuated under low-strength rotating magnetic fields ($<$10 mT), but remain complex to produce in high numbers and in sufficiently small sizes to reach arterioles. Moreover, the relatively low translational forces achieved by these microrobots also limit the blood flow velocities in which they can navigate. An alternative consists in fabricating therapeutic magnetic microcarriers (TMMCs) encapsulating both drug molecules and superparamagnetic nanoparticles [12, 13]. These simpler structures are carried by the blood flow and, when magnetized, can be steered in the desired branches of the vascular network by applying magnetic gradients. Since they have no remanent magnetization, their aggregation is avoided once removed from the magnetic field, allowing these particles to disperse deeper in the targeted region. However, due to the very small volume of magnetic material embedded in these carriers, a high magnetic field strength is required to ensure the saturation magnetization of the particles, while strong magnetic gradients are needed to induce sufficient directional forces for steering.

Several platforms have been proposed for magnetic navigation in general, mainly using robotically controlled external magnets [14, 1, 15] or assemblies of electromagnetic coils [16, 17, 2, 6, 18]. These however lack the high field strength required for navigating microscale agents such as TMMCs when scaled to human size. Consequently, Magnetic Resonance Navigation (MRN) [19, 20] has been proposed, where the supraconducting magnet of a clinical magnetic resonance imaging (MRI) scanner is used to achieve a high field strength, typically 1.5-3 T, for whole-body interventions. It was shown that the imaging gradient coils of the scanner can be used to generate navigation gradients. The maximum gradient amplitudes of

these coils are however generally limited in the range 40-80 mT/m, which is not sufficient for navigating TMMCs without significantly reducing the blood flow.

A more recent method, which is investigated in this work, is Dipole Field Navigation (DFN) [21]. This method also exploits the strong field of an MRI scanner, but the navigation gradients are generated by distorting the scanner's field using large ferromagnetic cores precisely positioned around the patient. For spherical cores, it was shown that gradient strengths exceeding 300 mT/m could be achieved in deep tissues (~10 cm) for a core radius of 4 cm, although the gradient strengths in fact vary with the desired gradient orientations.

Due to the simpler magnetic models characterizing this shape, previous works on DFN only considered spherical cores. It is expected that, for a same amount of ferromagnetic material, stronger gradients could be achieved by optimizing the shape of the cores. Such improved gradients would translate to better steering capabilities, or allow using smaller cores to alleviate the attraction forces towards the scanner when inserting the cores. Consequently, in this paper, we investigate different core shapes for their potential use in DFN. The gradients generated by different shapes are compared in deep tissues, according to typical conditions of DFN interventions.

7.3 Magnetic Gradients in Dipole Field Navigation

When inserted in an MRI scanner's homogeneous field $\mathbf{B}_0 = B_0\hat{\mathbf{z}}$, a ferromagnetic core becomes uniformly magnetized and generates a magnetic field that adds to $\mathbf{B}_0$. This causes a distortion of the total field $\mathbf{B}_{tot}$, resulting in strong magnetic gradients around the core. Due to the high strength of $\mathbf{B}_0$, the ferromagnetic material of the core can be typically considered at saturation magnetization, which maximizes the gradients that are generated. The resulting force acting on a magnetic particle (e.g., TMMC), which is magnetized by the total field, is

$$\mathbf{F}_{mag} = \nabla(\mathbf{m}_p \cdot \mathbf{B}_{tot}) = m_p \nabla B_{tot} \tag{7.1}$$

where m_p is the magnetic moment of the particle. Thus, the steering force in DFN is directly proportional to the gradient of the total field strength. In the case of a spherical core, the resulting gradients are those of a magnetic dipole as shown in Fig. 7.1. Note that this gradient field is axisymmetric around the magnetization axis (z-axis) of the core. As referred to later, by convention, the gradient orientation angles ϑ are defined relative to the z-axis.

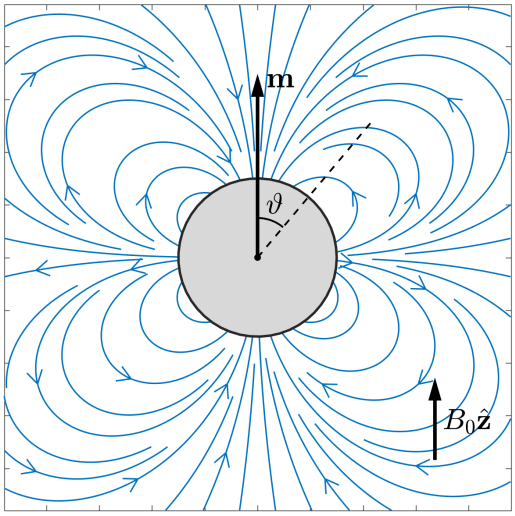

Figure 7.1 Magnetic gradient field lines around a magnetized sphere in a uniform field $\mathbf{B}_0$. Gradient orientation angles ϑ are defined relative to the z-axis.

7.3.1 Considerations on Magnetic Gradients

Since conventional clinical scanners generate the static field $\mathbf{B}_0$ along the longitudinal axis of the tunnel, the gradients that can be exploited for whole-body interventions in DFN are mainly those located on the lateral side of the core. This is illustrated in Fig. 7.2 where a plane is used to approximate this delimitation of usable versus unusable gradients. The vertical dashed line in Fig. 7.2b represents this plane and defines the *navigation gradient region* (NGR) in 2D inside the patient. Note that, for any shape, for a given core side being in contact with the plane (i.e., body), this 2D gradient field is independent of the angle of the plane around $\hat{\mathbf{z}}$ (i.e., independent of the core position around the body) and thus the gradients of different shapes can be compared within this 2D NGR. Besides, notice that the gradient directions vary around a core such that both repulsive and attractive gradients can be induced in the NGR.

The main advantages of shapes generating higher gradient strengths in this region of interest are threefold:

— ***Better steering capabilities:*** Gradient strengths vary depending on their orientation in the NGR (e.g., much weaker when oriented towards the body surface) and decrease exponentially with the distance to the core. Stronger gradients would enable steering in

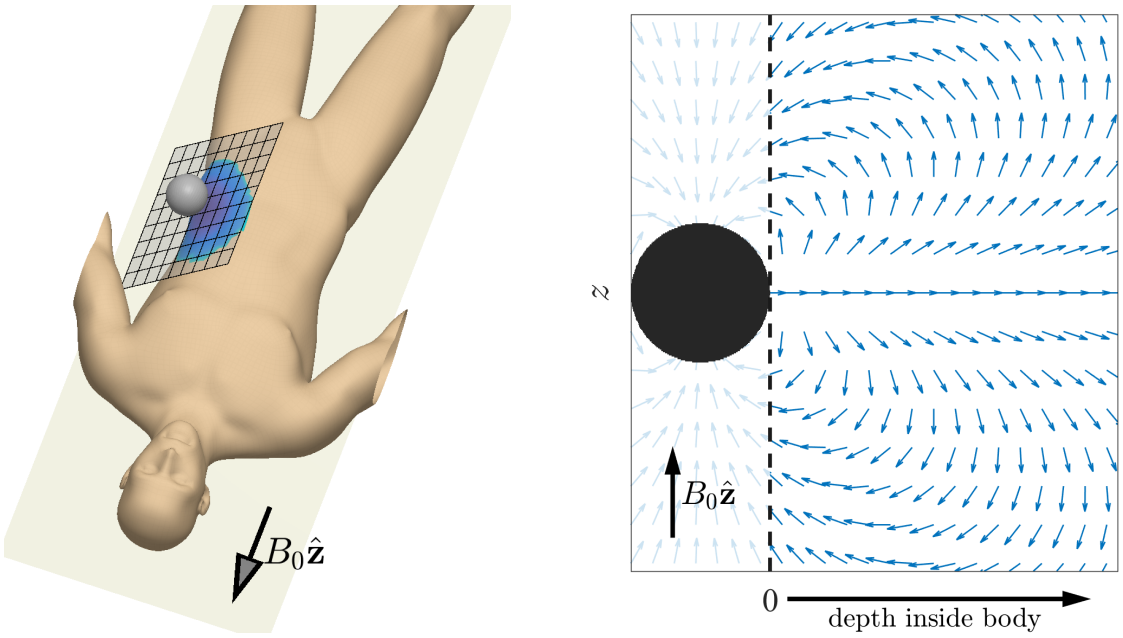

(a) (b)

Figure 7.2 Plane delimiting the gradients that are accessible (in blue, normalized) inside the body for DFN. a) Illustration of the patient on the scanner's table; b) Navigation gradient region, in 2D, delimited by the plane (dashed line).

any direction in deeper tissues, or in the presence of higher blood flows.

— ***Stronger directional changes:*** The rapid variations of the gradient directions required for steering through consecutive bifurcations can be achieved by positioning multiple cores. This implies, however, that gradients of different cores partially cancel each other, thus reducing the effective gradients. Better shapes would enable stronger varying gradients.

— ***Less magnetic material required:*** While stronger gradients can be achieved using larger cores, the core sizes are in practice limited by the strong attraction forces that must be sustained when inserting them in the scanner. Better shapes would allow using smaller cores while generating equivalent gradient strengths.

7.3.2 Expected Effect of Core Shape on Gradients

For a same volume V_{mag} of magnetic material at saturation magnetization M_{sat}, the magnetic moments of cores having different shapes remain the same, i.e. $m = V_{mag}M_{sat}$, but the distribution of the gradients around the cores changes. Although the gradients in the far field of any core shape eventually converge towards those of a magnetic dipole, due to the large

size of the cores needed in DFN, differences in gradients are expected between shapes even in deep tissues.

While multiple cores can be positioned to generate more complex or stronger gradient patterns, the performances of DFN depend on those of each individual core. Therefore, the "ideal" core shape can be defined as that yielding the strongest gradients in any direction in deep tissues inside the NGR.

7.4 Investigation of Core Shapes

7.4.1 Gradient Calculations

The COMSOL Multiphysics 5.2 software was used to calculate the gradients around different core shapes using finite element modeling. Although analytical models exist for some shapes, such as the sphere, using this approach for all shapes allowed for a fair comparison of the gradients. The following describes the models developed and solved by the software.

For a given core shape, a core volume was defined at the center of the xyz space. The core was assumed to be made of low carbon steel 1020, a common soft ferromagnetic material defined in the COMSOL AC/DC module's material library and having a saturation magnetization $M_{sat} \approx 1.74 \times 10^6\,\mathrm{A/m}$. The core was surrounded by a spherical volume of air having a diameter of 50 cm. This analysis region allowed to analyze gradients up to 25 cm from the core's center. This volume was extended by an outer infinite element layer of air to reduce boundary effects. A uniform background magnetic field $H_0 = B_0\hat{\mathbf{z}}/\mu_0\,\mathrm{A/m}$, where $\mathbf{B}_0 = 3\,\mathrm{T}$ and $\mu_0 = 4\pi \times 10^{-7}\,\mathrm{H/m}$ is the magnetic permeability of vacuum, was applied in the entire space. The core was magnetized (very close to or at saturation) by this field according to the material's magnetization curve. The COMSOL AC/DC module was used to solve this magnetostatic problem, whereas the Coefficient Form PDE module was used to calculate the spatial derivatives of the total field strength in order to obtain gradients. Due to the use of derivatives, a fine discretization of the space is needed to reduce gradient approximation errors to an acceptable level. As such, the meshing of the models was refined until no significant improvement was achieved in the quality of the solutions, with the solver's relative tolerance (convergence criterion) set to 10^{-10}. The final meshes were constructed according to a maximum element size of 10 mm.

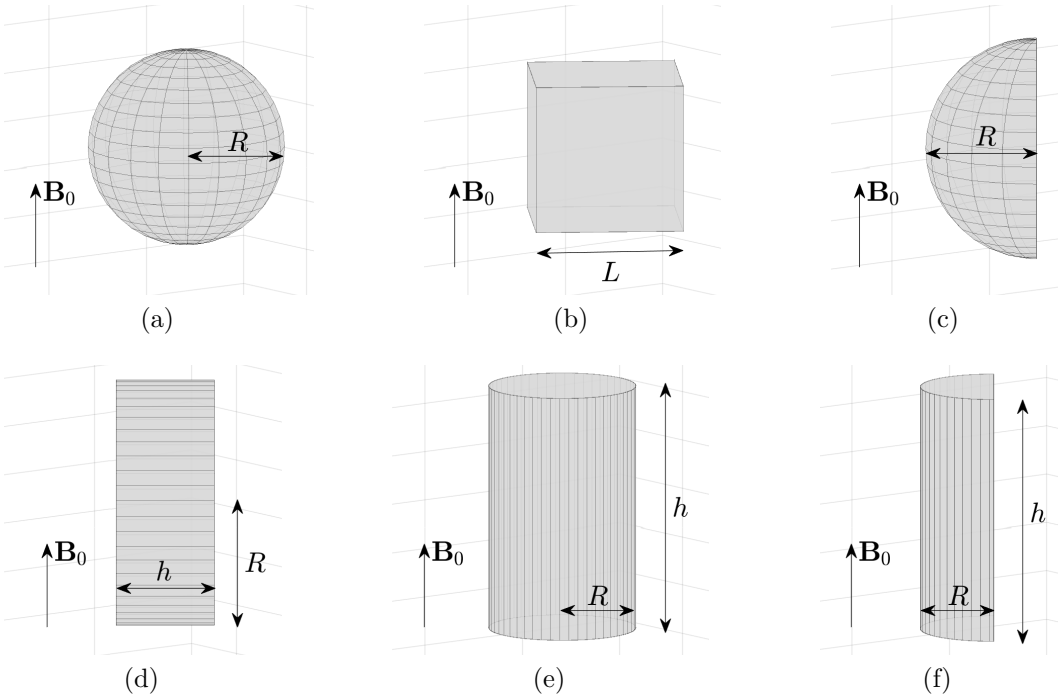

Figure 7.3 Tested core shapes and their natural alignment with $\mathbf{B}_0$. a) Sphere; b) Cube, flat side on body; c) Hemisphere, for both the flat or round side on body; d) Disc, flat side on body; e) Cylinder; f) Half cylinder, flat side on body.

7.4.2 Tested Core Shapes

One limitation of spherical cores relates to the distance separating the largest portion of ferromagnetic material from the body. It is expected that shapes allowing a larger portion of the material closer to the body, such as flat shapes, be able to generate stronger gradients in the NGR.

Consequently, the shapes tested are the sphere (reference shape), cube, hemisphere, disc, cylinder and half cylinder. These are shown in Fig. 7.3. Note that, except for the sphere, the magnetic anisotropy of these shapes makes them align with $\mathbf{B}_0$ according to preferential magnetization directions illustrated in Fig. 7.3. Due to the high torques required to rotate the cores away from these natural orientations in a strong 3 T field, other orientations were not considered in this work.

To isolate the influence of the shape itself on the gradients, core sizes were defined such that the volume of magnetic material V_{mag} was constant. In the case of the disc, cylinder and half cylinder, two core sizes with different h/R ratios were tested. The dimensions of all shapes were based on a spherical core of radius $R = 4\,\text{cm}$ and are reported in Table 7.1.

Table 7.1 Dimensions of the different core shapes tested, for a constant volume of ferromagnetic material in each core.

Shape	**Dimensions (cm)**	**Remarks**
Sphere	R = 4.00	Reference shape.
Cube	L = 6.45	
Hemisphere	R = 5.04	Tested for both the flat and the round side on the body surface.
Disc	R = 6.35, h = 2.12	$h/R = 1/3$.
	R = 5.04, h = 3.36	$h/R = 2/3$. Same diameter as the hemisphere (same footprint on body).
Cylinder	R = 3.49, h = 6.99	$h/R = 2$.
	R = 3.05, h = 9.16	$h/R = 3$.
Half cylinder	R = 4.40, h = 8.81	$h/R = 2$. Square footprint on body.
	R = 3.85, h = 11.54	$h/R = 3$.

7.4.3 Results

The COMSOL's solution data were exported and analyzed within Matlab R2016a. Using the Matlab's built-in `scatteredInterpolant` class with the natural neighbor interpolation method, the data were interpolated to obtain smoother approximations of the gradient fields.

To facilitate the comparison of the gradient strengths obtained across different shapes given a desired gradient orientation angle, the locations where this gradient orientation occurs inside the NGR were found numerically, for each shape, for depths up to 20 cm. This was repeated for gradient orientation angles (see convention in Fig. 7.1) of 90° (purely repulsive gradients), 45°, 0° (sideways gradients), −45° and −90° (attractive gradients towards body surface). The resulting isolines of these gradient orientations are shown, as an example, for the flat side of the hemisphere in Fig. 7.4.

Fig. 7.5 shows arrow and contour plots of the gradient fields, depicting gradient orientations and strengths (T/m) respectively, in the NGR for all the shapes tested. Fig. 7.6 presents the gradient strengths (left plots) obtained for specific gradient orientations, for the values of ϑ mentioned above, as a function of the depth inside the NGR and according to each shape's gradient orientation isolines. For a clearer distinction between shapes, the relative gains achieved on gradient strengths were also calculated (right plots), using the sphere as reference, along the isolines. Note that the curves ending prematurely, particularly for $\vartheta = -90°$, are

limited by the size of the analysis region defined in the COMSOL models (see Fig. 7.4).

7.5 Discussion

The results obtained clearly reveal that, despite being a simple model, the sphere is, among the shapes tested, the least effective in terms of gradient strengths achievable in deep tissues for DFN. This is unsurprising given that, compared with other shapes, only a small portion of a spherical core can be in contact with the surface of the body. It should be noted that, although the sphere can exceed the performances of other shapes at small depths, the gradients in these cases can reach several tesla per meter for all shapes and are therefore not limiting DFN.

In the case of the sphere and cylinders, it is observed that their flat counterparts (i.e., hemisphere and half cylinders) yield significantly higher gradients in deep tissues. The gains obtained by the hemisphere are especially noteworthy, reaching over 50% at a 10 cm depth. Besides, with the same footprint on the body surface than the flat side of the hemisphere, the disc having a ratio $h/R = 2/3$ also offers remarkable gains in gradient strengths. While being outperformed by the hemisphere for repulsive gradients, it becomes slightly more advantageous when $\vartheta < 0$. The other disc tested, which is thinner with a ratio $h/R = 1/3$, is observed to eventually take the lead among the shapes tested at larger depths, although gradients at such distances are much weaker.

Overall, among the core shapes tested, the hemisphere and the disc having $h/R = 2/3$ appear as the best candidates for DFN. Their resulting gradient strengths in deep tissues, combined with the strong scanner's field, confer a high potential for the navigation of microscale agents in the vasculature. For comparison, supposing that MRN could achieve continuous gradients of 80 mT/m, which is ambitious with current systems due to gradient limitations and overheating of the coils, the gradient strengths achieved in DFN using the hemispherical core on its flat side would exceed those of MRN up to a depth of ~18 cm for $\vartheta = 90°$. This however drops down to ~15.5 cm for $\vartheta = 0°$ and ~11.5 cm for $\vartheta = -90°$. Still, one challenge specific to DFN relates to the rapid spatial variations of the gradient directions that are needed to navigate in complex vasculatures. Inducing strong variations requires the accurate positioning of multiple cores that generate gradients in opposite directions, which reduces the effective steering gradient strengths. Although the shape of the cores can be optimized, a tradeoff is therefore expected between the gradient strengths and the gradient variations that can be achieved.

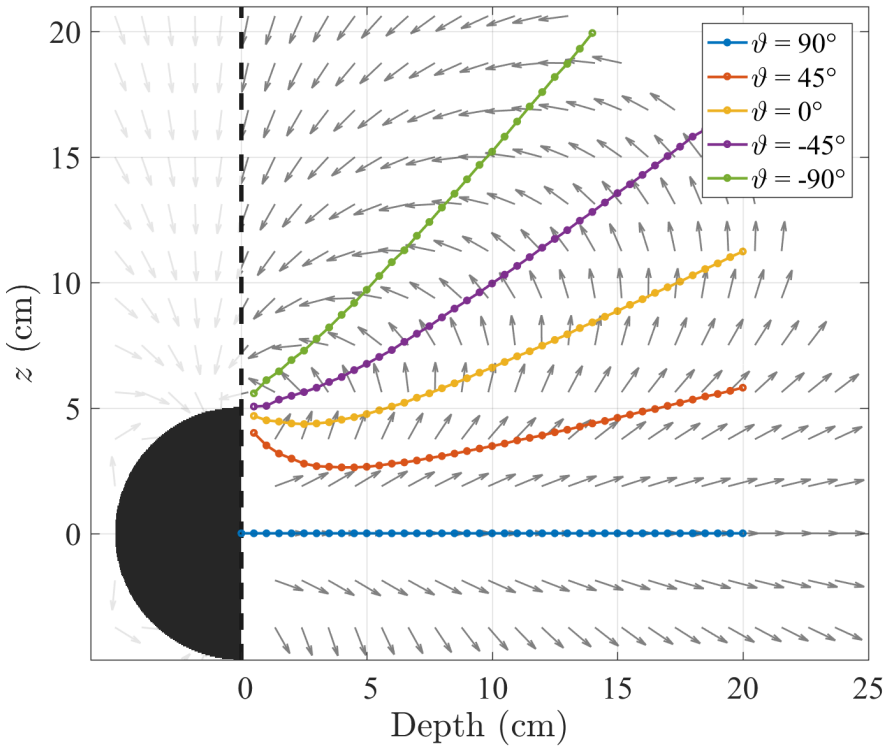

Figure 7.4 Example of gradient orientation isolines, which were used to compare gradient strengths across tested shapes given a desired gradient orientation.

7.6 Conclusion

It was previously shown that DFN can generate sufficiently high gradients for the navigation of microscale agents in deep tissues using spherical cores. Still, this method will always benefit from stronger gradients for improved steering capabilities. While larger cores generate higher gradients, their sizes are in practice limited by the magnetic attraction forces that must be sustained during their insertion in the scanner. In this paper, we have shown that the shape of the cores has a notable impact on the gradient strengths that can be achieved in deep tissues. In particular, the hemisphere and the disc yield, for a same volume of magnetic material, significantly stronger gradients compared with the sphere model considered in previous works. Using those shapes for DFN would consequently improve navigation performances.

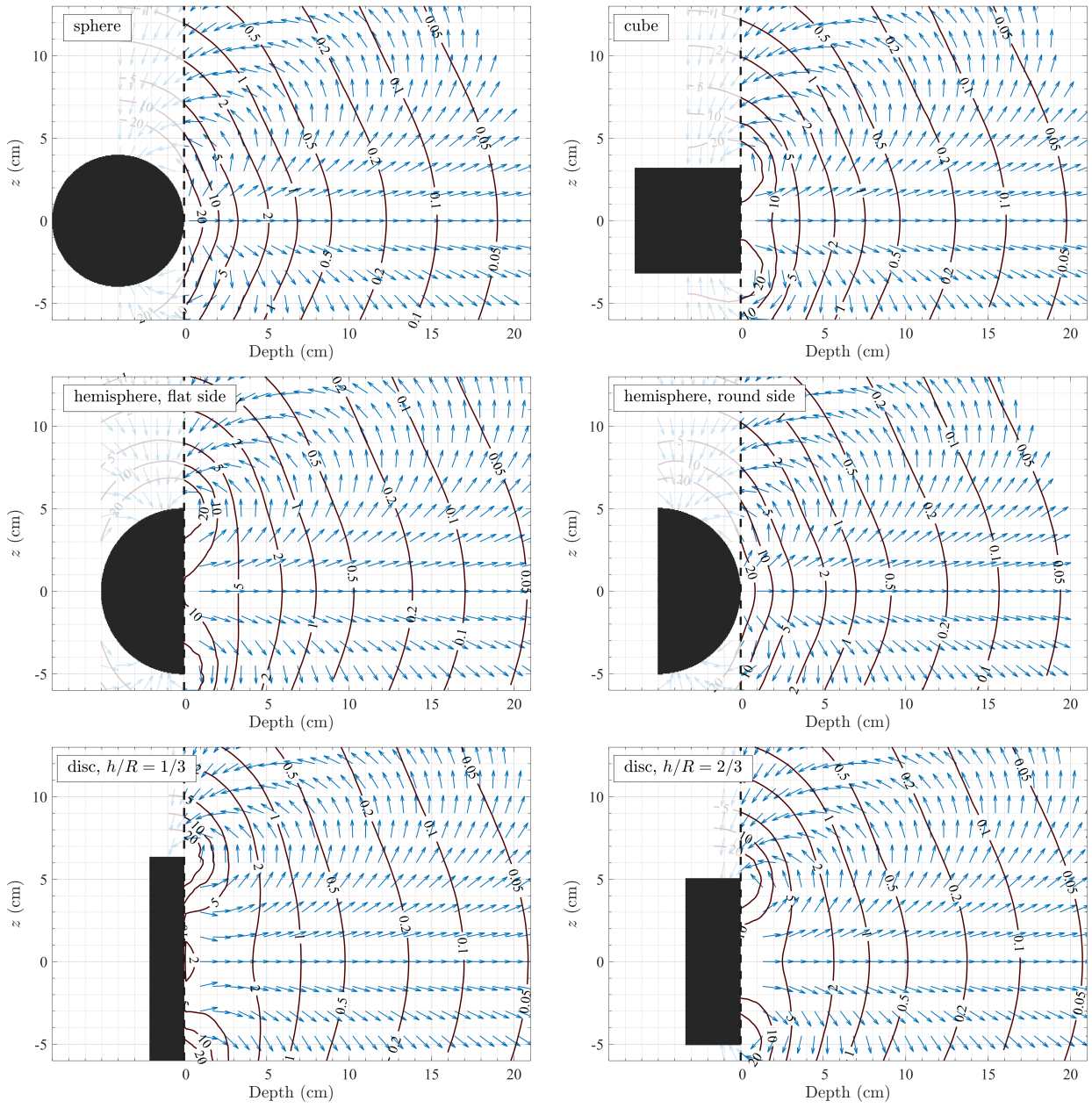

Figure 7.5 Results of the calculated gradients in the navigation gradient region (delimited by the vertical dashed line), for the different core shapes tested. Blue arrows depict gradient orientations. Red contour lines represent the gradient strengths in tesla per meter (T/m). Gradient fields are symmetric about $z = 0$.

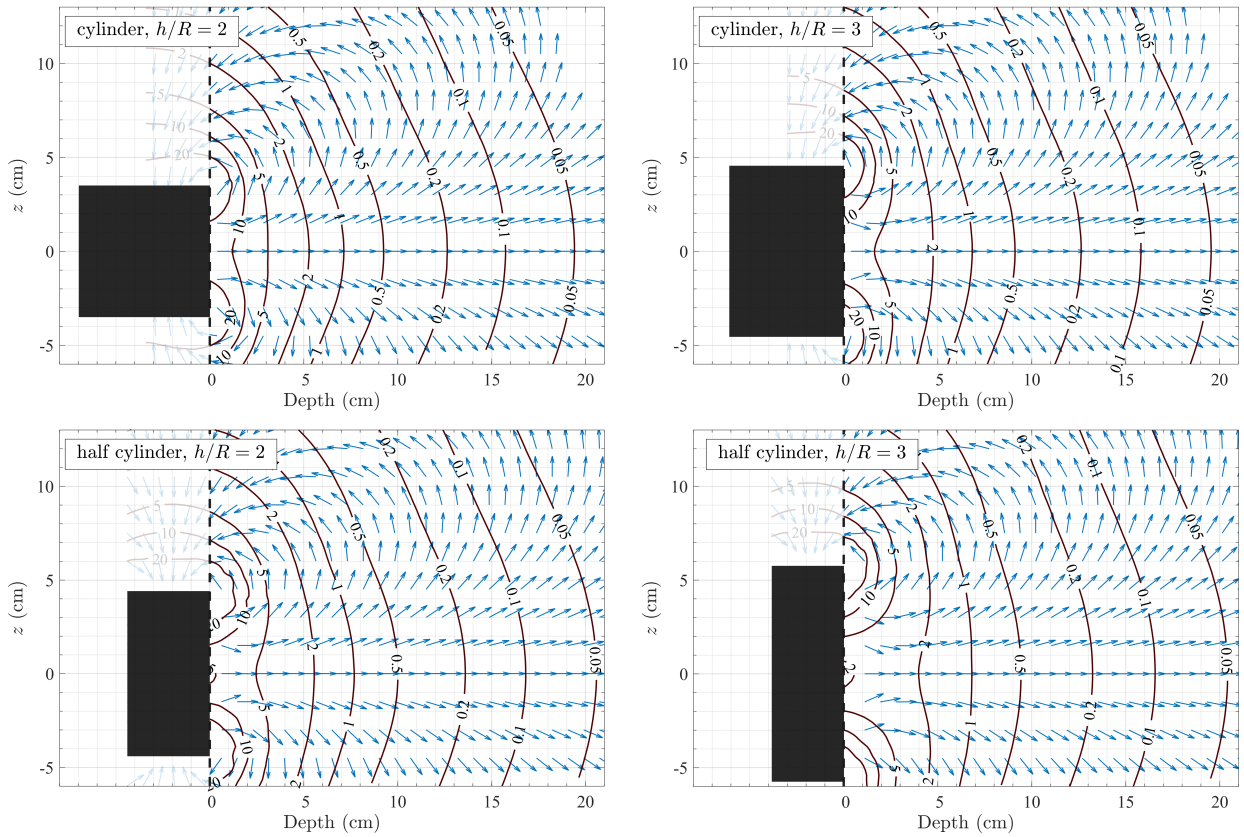

Figure 7.5 (Cont.)

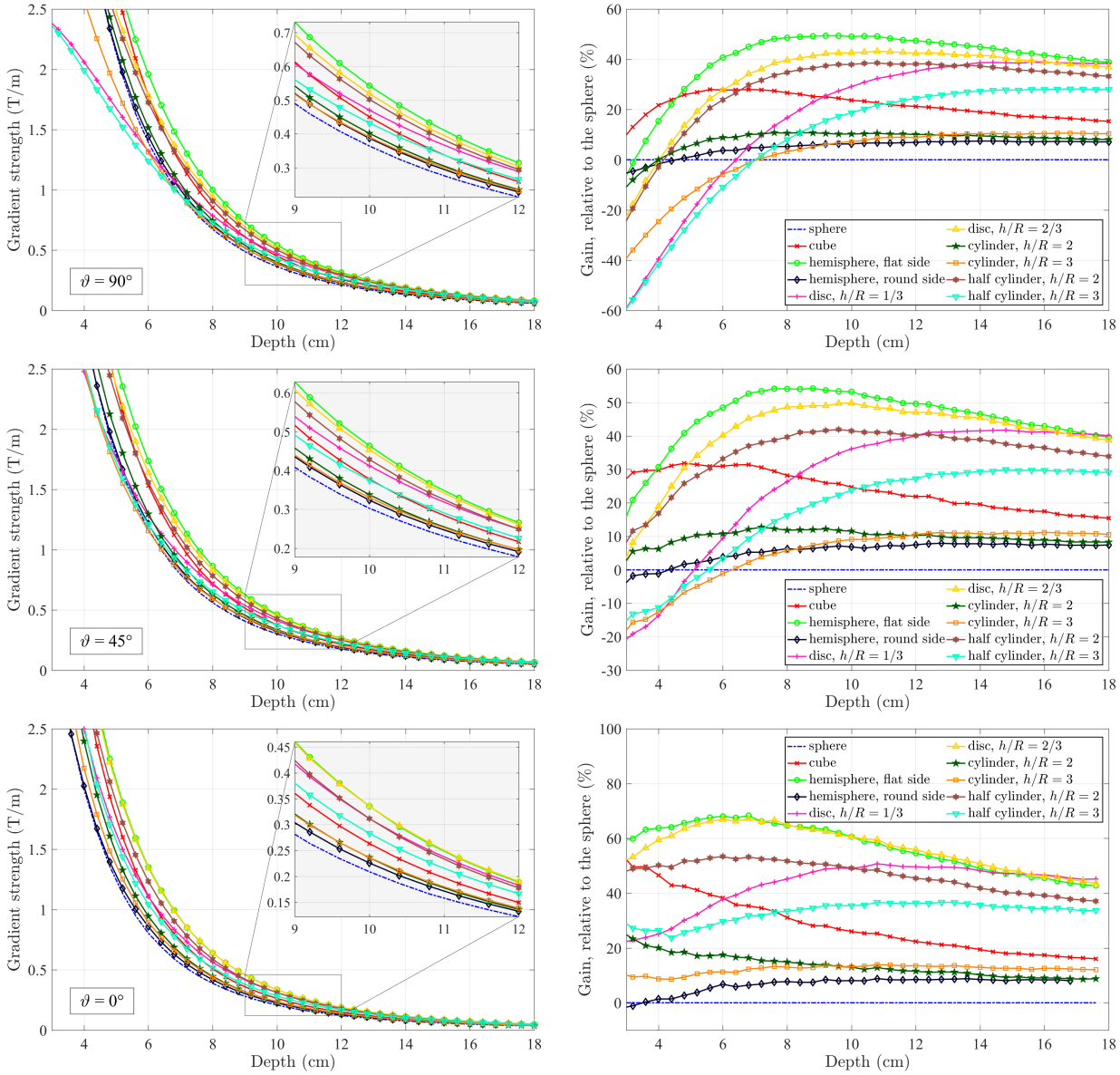

Figure 7.6 Gradient strengths (left plots) and gains relative to the sphere (right plots) obtained for the core shapes tested as a function of the depth inside the navigation gradient region, for desired gradient orientations ϑ of 90°, 45°, 0°, -45° and -90° (identified on left plots). Legends are shown on right plots.

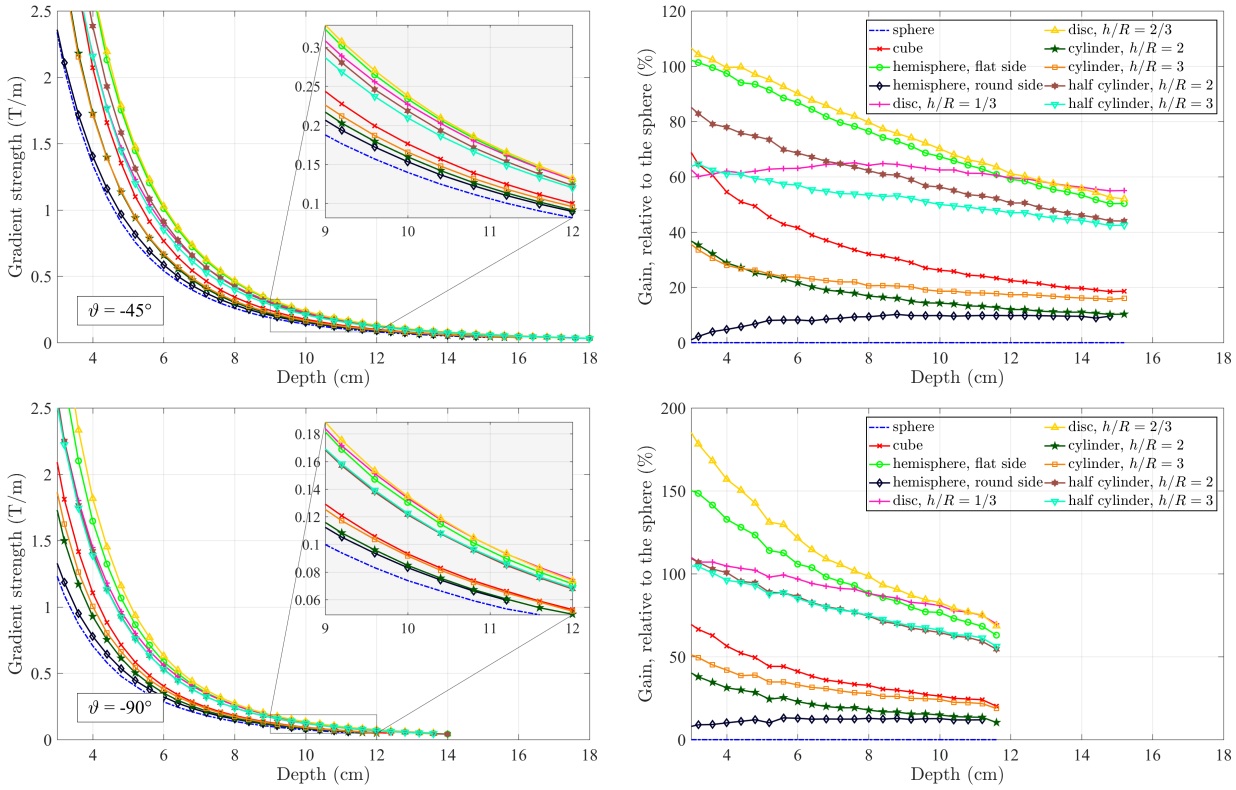

Figure 7.6 (Cont.)

7.7 References

[1] S. Tognarelli, V. Castelli, G. Ciuti, C. Natali, E. Sinibaldi, P. Dario, et A. Menciassi, "Magnetic propulsion and ultrasound tracking of endovascular devices", *J. Robot. Surg.*, vol. 6, no. 1, pp. 5–12, 2011.

[2] H. Keller, A. Juloski, H. Kawano, M. Bechtold, A. Kimura, H. Takizawa, et R. Kuth, "Method for navigation and control of a magnetically guided capsule endoscope in the human stomach", dans *Proc. IEEE RAS EMBS Int. Conf. Biomed. Robot. Biomechatronics*, 2012, pp. 859–865.

[3] "Stereotaxis". En ligne: `http://www.stereotaxis.com`

[4] "Aeon Scientific". En ligne: `www.aeon-scientific.com`

[5] F. Ullrich, C. Bergeles, J. Pokki, O. Ergeneman, S. Erni, G. Chatzipirpiridis, S. Pané, C. Framme, et B. J. Nelson, "Mobility experiments with microrobots for minimally invasive intraocular surgery", *Investig. Ophthalmol. Vis. Sci.*, vol. 54, no. 4, pp. 2853–2863, 2013.

[6] S. Jeong, H. Choi, G. Go, C. Lee, K. S. Lim, D. S. Sim, M. H. Jeong, S. Y. Ko, J. O. Park, et S. Park, "Penetration of an artificial arterial thromboembolism in a live animal using an intravascular therapeutic microrobot system", *Med. Eng. Phys.*, vol. 38, no. 4, pp. 403–410, 2016. DOI: `10.1016/j.medengphy.2016.01.001`

[7] A. S. Lübbe, C. Bergemann, H. Riess, A. S. Lãbbe, F. Schriever, P. Reichardt, K. Possinger, M. Matthias, B. Dã, F. Herrinann, R. Gurtler, P. Hohenberger, N. Haas, R. Sohr, B. Sander, A.-J. J. Lemke, D. Ohlendorf, W. Huhnt, D. Huhn, B. Dörken, F. Herrmann, R. Gürtler, P. Hohenberger, N. Haas, R. Sohr, B. Sander, A.-J. J. Lemke, D. Ohlendorf, W. Huhnt, D. Huhn, A. S. Lãbbe, F. Schriever, P. Reichardt, K. Possinger, M. Matthias, B. Dã, F. Herrinann, R. Gurtler, P. Hohenberger, N. Haas, R. Sohr, B. Sander, A.-J. J. Lemke, D. Ohlendorf, W. Huhnt, D. Huhn, B. Dörken, F. Herrmann, R. Gürtler, P. Hohenberger, N. Haas, R. Sohr, B. Sander, A.-J. J. Lemke, D. Ohlendorf, W. Huhnt, et D. Huhn, "Clinical Experiences with Magnetic Drug Targeting: A Phase I Study with 4'-Epidoxorubicin in 14 Patients with Advanced Solid Tumors", *Cancer Res.*, vol. 56, no. 20, pp. 4686–4693, 1996.

[8] A. Amirfazli et R. Virginia, “Magnetic nanoparticles hit the target”, *Nat. Nanotechnol.*, vol. 2, no. August, pp. 467–468, 2007. DOI: 10.1038/nnano.2007.234

[9] I. S. M. Khalil, H. C. Dijkslag, L. Abelmann, et S. Misra, “MagnetoSperm: A microrobot that navigates using weak magnetic fields”, *Appl. Phys. Lett.*, vol. 104, no. 22, 2014. DOI: 10.1063/1.4880035

[10] T. Y. Huang, M. S. Sakar, A. Mao, A. J. Petruska, F. Qiu, X. B. Chen, S. Kennedy, D. Mooney, et B. J. Nelson, “3D Printed Microtransporters: Compound Micromachines for Spatiotemporally Controlled Delivery of Therapeutic Agents”, *Adv. Mater.*, vol. 27, no. 42, pp. 6644–6650, 2015. DOI: 10.1002/adma.201503095

[11] F. Qiu et B. J. Nelson, “Magnetic Helical Micro- and Nanorobots: Toward Their Biomedical Applications”, *Engineering*, vol. 1, no. 1, pp. 21–26, 2015. DOI: 10.15302/J-ENG-2015005

[12] P. Pouponneau, J. C. Leroux, G. Soulez, L. Gaboury, et S. Martel, “Co-encapsulation of magnetic nanoparticles and doxorubicin into biodegradable microcarriers for deep tissue targeting by vascular MRI navigation”, *Biomaterials*, vol. 32, no. 13, pp. 3481–3486, 2011. DOI: 10.1016/j.biomaterials.2010.12.059

[13] L. Mellal, K. Belharet, D. Folio, et A. Ferreira, “Optimal structure of particles-based superparamagnetic microrobots: application to MRI guided targeted drug therapy”, *J. Nanoparticle Res.*, vol. 17, no. 2, 2015. DOI: 10.1007/s11051-014-2733-3

[14] M. Gao, C. Hu, Z. Chen, H. Zhang, et S. Liu, “Design and fabrication of a magnetic propulsion system for self-propelled capsule endoscope”, *IEEE Trans. Biomed. Eng.*, vol. 57, no. 12, pp. 2891–2902, 2010. DOI: 10.1109/TBME.2010.2051947

[15] A. W. Mahoney et J. J. Abbott, “Five-degree-of-freedom manipulation of an untethered magnetic device in fluid using a single permanent magnet with application in stomach capsule endoscopy”, *Int. J. Rob. Res.*, vol. 35, no. 1-3, pp. 129–147, 2015.

[16] M. P. Kummer, J. J. Abbott, B. E. Kratochvil, R. Borer, A. Sengul, et B. J. Nelson, “Octomag: An electromagnetic system for 5-DOF wireless micromanipulation”, *IEEE Trans. Robot.*, vol. 26, no. 6, pp. 1006–1017, 2010. DOI: 10.1109/TRO.2010.2073030

[17] H. Choi, K. Cha, J. Choi, S. Jeong, S. Jeon, G. Jang, J.-o. Park, et S. Park, “EMA system with gradient and uniform saddle coils for 3D locomotion of microrobot”, *Sensors*

Actuators A Phys., vol. 163, no. 1, pp. 410–417, 2010. DOI: 10.1016/j.sna.2010.08.014

[18] X. Zhang, T.-A. Le, et J. Yoon, "Development of a real time imaging-based guidance system of magnetic nanoparticles for targeted drug delivery", *J. Magn. Magn. Mater.*, vol. 427, no. October, pp. 345–351, 2017. DOI: 10.1016/j.jmmm.2016.10.056

[19] S. Martel, J.-B. Mathieu, O. Felfoul, A. Chanu, E. Aboussouan, S. Tamaz, P. Pouponneau, L. Yahia, G. Beaudoin, G. Soulez, et M. Mankiewicz, "Automatic navigation of an untethered device in the artery of a living animal using a conventional clinical magnetic resonance imaging system", *Appl. Phys. Lett.*, vol. 90, no. 11, p. 114105, 2007.

[20] K. Belharet, D. Folio, et A. Ferreira, "MRI-based microrobotic system for the propulsion and navigation of ferromagnetic microcapsules", *Minim. invasive Ther. allied Technol.*, vol. 19, pp. 157–169, 2010.

[21] M. Latulippe et S. Martel, "Dipole Field Navigation: Theory and Proof of Concept", *IEEE Trans. Robot.*, vol. 31, no. 6, pp. 1353–1363, 2015.

CHAPITRE 8 ARTICLE 5: EVALUATION OF THE POTENTIAL OF DIPOLE FIELD NAVIGATION FOR THE TARGETED DELIVERY OF THERAPEUTIC AGENTS IN A HUMAN VASCULAR NETWORK

Maxime Latulippe and Sylvain Martel
Soumis à : IEEE Transactions on Magnetics

8.1 Abstract

Magnetically guided agents in the vascular network are expected to enable the targeted delivery of therapeutics to localized regions while avoiding their systemic circulation. Due to the small size of the medically-applicable superparamagnetic microscale agents required to reach the smaller arteries, high magnetic fields and gradients are required to reach saturation magnetization and generate sufficient directional forces, respectively, for their effective navigation in the vascular environment. Currently, the only method that provides both a high field and high magnetic gradient strengths in deep tissues at the human scale is known as Dipole Field Navigation (DFN). This method relies on the controlled distortion of the field inside a magnetic resonance imaging scanner by precisely positioning ferromagnetic cores around the patient. This work builds on previous works that have experimentally demonstrated the feasibility of the method and proposed optimization algorithms for placing the cores. The maximum gradient strengths that can be generated for single and multi-bifurcation vascular routes are investigated while considering the major constraints on core positions (limited space in the scanner, magnetic interactions). Using disc cores, which were previously shown particularly effective for DFN, results show that gradient strengths exceeding 400 mT/m (a 10-fold increase w.r.t. typical gradients generated by clinical MRI scanners) can be achieved at 10 cm inside the patient, but decrease as the complexity of the vascular route increases. The potential of the method is evaluated for targeting regions of a vascular model of a human liver, segmented from clinical data, with encouraging results showing strengths up to 150 mT/m for generating gradients at three consecutive bifurcations within 20 degrees of average gradient direction error.

8.2 Introduction

The ability to deliver therapeutics locally, directly to a targeted region in the body, has the potential to dramatically increase the efficacy of some treatments and diagnostics without

exposing healthy organs and tissues to potentially harmful chemicals. In the fight against cancer notably, cytotoxic drugs are commonly administered systemically to patients with limited efficacy in treating tumors while inducing severe secondary effects. Even advanced chemotherapeutics designed to specifically target cancer cells yield poor therapeutic indexes (1-2%) due to their systemic circulation. Since the majority of cancers (>80%) are initially localized in a single region, these treatments would highly benefit from a targeted administration of the drugs directly to the diseased site.

As such, direct drug targeting consists in navigating therapeutic agents through the shortest vascular route between the injection point and a target region. Due to current limitations in miniaturization and technological constraints, the most promising approach for such navigation relies on the magnetic actuation of untethered agents [1]. By combining drug molecules with magnetic material into micro-structures [2–4], directional pulling forces for navigation can be induced by applying external magnetic fields and gradients. To avoid their aggregation and allow better dispersion in the target site after the intervention, a desirable property of such agents is to lose their magnetization once removed from the field. Superparamagnetic nanoparticles, which are already widely used in biomedical applications, are well suited for this purpose since they have no remanent magnetization [5].

One major challenge for navigating microscale agents, considering their small magnetic volume and the relatively high blood flow velocities, relates to the generation of sufficient magnetic force strengths for navigation. This requires both a high field strength, to bring the agents at saturation magnetization, and high magnetic gradient strengths for inducing strong directional forces. With the particles at saturation magnetization, previous works suggest that gradient strengths around 200-400 mT/m [6, 7] would be required for navigation, although this depends on various physical and physiological parameters. Generating such a high field and high gradient strengths in a workspace of the human size still represents a technological challenge.

Different magnetic actuation approaches have been proposed for the remote control of untethered agents in the human body. Statically positioned magnets have been used for attracting magnetic particles at a target site [8, 9]. A two-magnet system capable of pushing therapeutic particles in the inner ear has also been proposed [10]. Robotically controlled mobile magnets [11–13] can also be used for guiding relatively large agents such as capsule endoscopes. Other approaches, capable of fast control in up to 5 or 6 degrees of freedom, are based on assemblies of electromagnetic coils and include Electromagnetic Actuation (EMA) systems [14–18], such as the Omnimagnet [19] and actuation using a Magnetic Particle Imaging (MPI) system [20], to name but only two examples. All the above approaches, however, suffer

from a lack of magnetic field and/or gradient strengths for navigating microscale agents in deep tissues. Due to the rapid decay of the field and gradient strengths, permanent magnets are limited either to surface tissues or to larger devices. EMA and other coil-based systems can provide higher gradients, but they still lack field strength when scaled to human size. These platforms are currently limited to about 0.1 T and <400 mT/m for whole-body interventions and are therefore more adapted for guiding devices of millimeter scale.

One promising actuation method for drug targeting is known as Magnetic Resonance Navigation (MRN) [21, 22], which exploits the strong and homogeneous field inside a Magnetic Resonance Imaging (MRI) scanner (typ. 1.5-3 T) to bring the agents at saturation magnetization. It was shown that the imaging gradient coils of the scanner can be used to generate directional magnetic gradients for navigation. Conventional clinical scanners are however limited to relatively low gradient amplitudes, with maximums typically in the range 40-80 mT/m. Moreover, to prevent overheating of the coils, gradient strengths and/or duty cycles must be limited, which greatly reduces the effective gradient strengths. This method would consequently requires slowing down the blood flow in most cases to ensure effective navigation. Alternatively, in vivo targeting of microscale therapeutic agents has been achieved in a rabbit using MRN by adding custom propulsion gradient coils (up to 400 mT/m) inside the scanner [7], but the resulting narrower tunnel (~15 cm) prevents whole-body interventions on humans.

Currently, the method providing the strongest gradients in the whole body while ensuring saturation magnetization of the agents is Dipole Field Navigation (DFN) [23], illustrated in Fig. 8.1. Also exploiting the strong field of an MRI scanner, DFN generates the gradients by inserting large ferromagnetic cores in the scanner. The presence of the cores results in the distortion of the scanner's field, which produces strong magnetic gradients that can exceed 300 mT/m in deep tissues. Unlike a permanent magnet in the outside environment, a core in DFN can generate both attraction and repulsion forces. An adequate positioning of a set of cores around the patient can therefore induce complex gradient patterns in the body, allowing to guide therapeutic agents along a predefined vascular route.

The proper positioning of the cores in DFN is however non-trivial and must take into account the specific anatomy of the patient as well as the various constraints on core positions in the limited space inside the scanner. Moreover, since distortions of the scanner's field typically prevent magnetic resonance imaging for real-time tracking of the agents, this method is limited to mostly open-loop navigation, although it has been shown that periodic targeting assessments could be possible by temporarily moving the cores away in specific regions inside

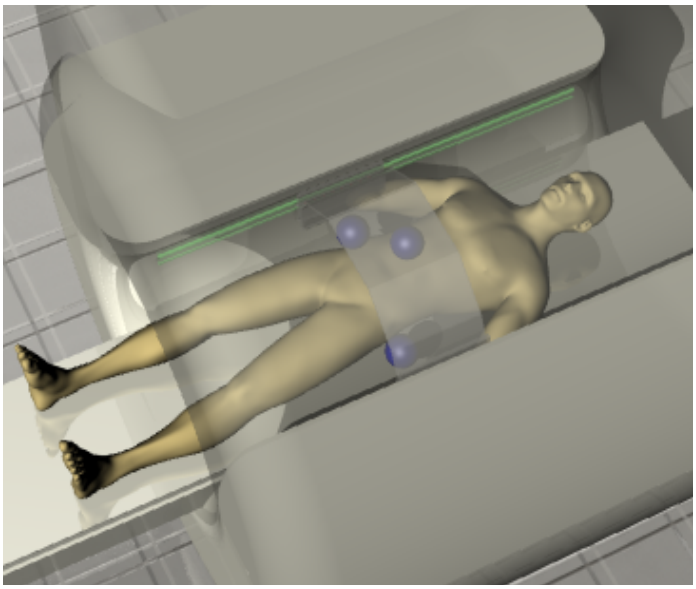

(a)

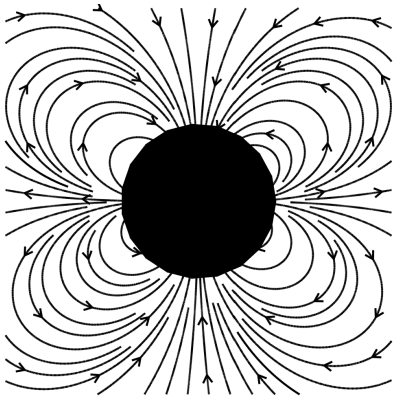

(b)

Figure 8.1 a) In Dipole Field Navigation, ferromagnetic cores are positioned around the patient inside an MRI scanner to distort the field, which generates strong directional forces for guiding therapeutic agents along a predefined vascular route; b) Magnetic gradient lines around a spherical core (dipole).

the scanner [24]. To ensure effective targeting, DFN must consequently rely on accurate models and algorithms for determining optimal core configurations.

Models and algorithms have been proposed for solving the core positioning problem [23, 25]. The feasibility of DFN has also been demonstrated experimentally by the in vitro navigation of particles through up to three consecutive bifurcations [23, 24]. The capabilities of this method for navigating agents in real vasculatures remain however unclear. In particular, the possible target organs and navigable vascular systems depend on the gradient strengths that can be generated considering all physical constraints related to the MRI environment, and on the spatial variations of the gradients that can be achieved to enable steering through multiple bifurcations.

The aim of this paper is to provide some insights on these aspects to help evaluate the capabilities and limitations of DFN using statically positioned cores. Magnetic models are used to optimize core parameters and identify the maximum gradient strengths and spatial variations that can be achieved in various conditions. The potential of the method is also evaluated for targeting regions of a real human liver model. The limited space for placing the cores around the patient inside the scanner as well as the constraints arising from magnetic

interactions between the cores are taken into account to ensure the applicability of the results.

The cores considered in this work have a disc shape. This shape was shown to generate much stronger gradients for DFN compared with the spherical cores considered previously [26]. It is assumed that the cores are made of low carbon steel 1020, a widely available soft ferromagnetic material having a high saturation magnetization $M_{sat} = 1.74 \times 10^6\,\mathrm{A/m}$. A 3 T scanner, such as the Siemens MAGNETOM Skyra system, is also assumed. This field strength is well over the ~0.8 T background field required to saturate cores of this material.

The paper is organized as follows. Section 8.3 presents the basics of DFN and introduces the core parameterizing algorithm used in this work. Section 8.4 presents magnetic models for calculating the gradients generated by a set of discs and investigates on minimum separating distances between discs to limit magnetic interactions. Section 8.5 explores the maximum gradient strengths achievable in various conditions, for one and two bifurcations. Sections 8.6 evaluate the potential of DFN for navigating particles in a human liver vasculature. Section 8.7 finally discusses and concludes.

8.3 Background on Dipole Field Navigation

Conventional clinical MRI scanners generate a strong static field $\mathbf{B}_0$, typically 1.5-3 T, along the longitudinal axis $\hat{\mathbf{z}}$ of the tunnel. A ferromagnetic core inserted in the scanner becomes magnetized and induces a magnetic field $\mathbf{B}_i$ that adds to $\mathbf{B}_0$. When N cores are inserted and magnetic interactions can be neglected, the cores are assumed to be uniformly magnetized, at saturation, in the direction of the scanner's field. The total magnetic field in the tunnel is

$$\mathbf{B}_{tot} = \mathbf{B}_0 + \sum_{i=1}^{N} \mathbf{B}_i \tag{8.1}$$

This distortion of the field $\mathbf{B}_0$ generates strong magnetic gradients in the vicinity of the cores, which can be used for navigation. For a navigable agent magnetized by $\mathbf{B}_{tot}$ and having a magnetic moment $\mathbf{m}_p$, the magnetic force exerted is proportional to the gradient of the total field strength:

$$\mathbf{F}_{mag} = \nabla(\mathbf{m}_p \cdot \mathbf{B}_{tot}) = m_p \nabla B_{tot} \tag{8.2}$$

Due to the high field $\mathbf{B}_0$, the total field lines around a core rapidly become approximately parallel to $\mathbf{B}_0 = B_0\hat{\mathbf{z}}$ as the distance to the core increases. Thus, if $\mathbf{B}_{tot}$ can be approximated

by its z-component only, (8.2) simplifies to

$$\widetilde{\mathbf{F}}_{mag} \approx m_p \nabla \left(B_0 + \sum_{i=1}^{N} B_{i,z} \right) = m_p \sum_{i=1}^{N} \nabla B_{i,z} \tag{8.3}$$

and the contributions of each core to the total gradient can be calculated independently [23]. However, to enable accurate predictions of gradients in the close vicinity of the cores, where navigation is also expected due to the relatively large core sizes needed for DFN, it is preferable to evaluate the exact expression of the gradient according to (8.2).

8.3.1 Optimization of Core Configurations

According to the equations above, an adequately configured set of cores around a patient body can, to a certain extent, generate the gradient patterns needed to guide particles in a vasculature. Optimization approaches have been proposed to parameterize core configurations (required number of cores, sizes, positions, etc.) given a vascular route towards a target [23, 25]. This problem has typically different possible solutions and many local extrema in the objective function. For further reference, the convention used in DFN for the system of coordinates is illustrated in Fig. 8.2a.

The optimization algorithm used in this work is Progressive Multidimensional Particle Swarm Optimization (PMD-PSO) [25], which has been shown well adapted to the core parameterization problem in DFN. PMD-PSO is based on the Particle Swarm Optimization (PSO) [27] algorithm. In the standard PSO, a swarm of S particles j (candidate solutions) with position and velocity vectors $\mathbf{x}^j$ and $\mathbf{v}^j$ having D dimensions fly through the search space, at each iteration t, according to the update equations

$$\mathbf{v}_{t+1}^j = \omega \mathbf{v}_t^j + c_1 \mathbf{R}_1 \left(\mathbf{p}_t^j - \mathbf{x}_t^j \right) + c_2 \mathbf{R}_2 \left(\mathbf{g}_t - \mathbf{x}_t^j \right) \tag{8.4}$$

$$\mathbf{x}_{t+1}^j = \mathbf{x}_t^j + \mathbf{v}_{t+1}^j \tag{8.5}$$

where $\mathbf{p}_t^j$ is the personal best known position of particle j at iteration t and $\mathbf{g}_t$ is the swarm's best known position, c_1 and c_2 are the cognitive and social acceleration constants, here both set to 1.49 as in [25], and $\mathbf{R}_1$ and $\mathbf{R}_2$ are diagonal matrices of uniformly distributed random numbers $\sim U(0,1)$. The coefficient $\omega \in [0,1]$ is the inertia weight, used to balance between exploration (high value) and exploitation (low value) of the search space. In the PMD-PSO variant, particles are first initialized with a minimum number of dimensions D_{min} (e.g. parameters of one core). The dimensionality of the search space is then progressively

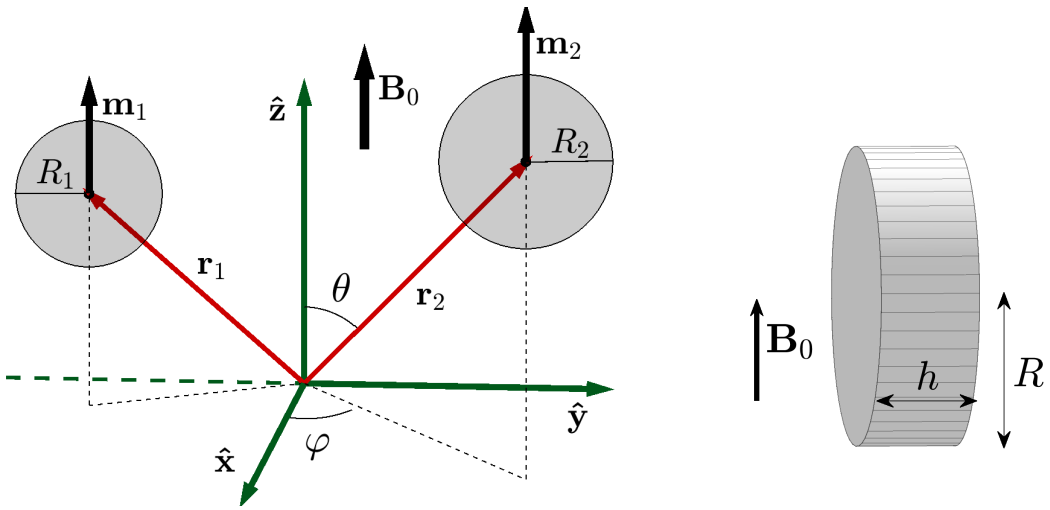

(a) (b)

Figure 8.2 a) Coordinate system used in DFN, where $\mathbf{B}_0$ is aligned with $\hat{\mathbf{z}}$; b) Alignment of a disc in the scanner's field (in this work, $h/R = 2/3$).

increased (e.g. a new core is added) each time the stagnation (convergence) of the swarm is detected, until a maximum dimensionality D_{max} is reached. The lower dimensionality solutions are memorized by the particles such that the swarm can build on them but can also escape from these local extrema if different, better configurations are found. This strategy has shown improved performances compared with the standard PSO for the core parameterizing problem in DFN.

In this work, a decreasing inertia weight $\omega_t = \omega_{t-1}u^{-1}$ is used, as proposed by [28], with $\omega_0 = 0.9$ and $u = 1.0001$. Such a decreasing scheme of ω has been shown to improve the convergence properties of PSO. The inertia weight is reset to ω_0 each time D is increased to allow for exploration. The particles in the swarm are also organized in a clan topology [29], which further improves convergence properties. Preliminary tests, not included here, were conducted to select these parameters and show that PMD-PSO remains superior to PSO for finding optimal core configurations.

8.4 Magnetic Models

Previous works on DFN considered spherical cores. In this particular case, the magnetic field induced by a core of radius R at any point with relative position $\mathbf{r} = (\mathbf{x}, \mathbf{y}, \mathbf{z})$ can be

represented by a dipole of equal magnetic moment $\mathbf{m}$ located at the center of the sphere:

$$\mathbf{B}(r > R) = \frac{\mu_0}{4\pi}\left[3\frac{(\mathbf{m}\cdot\mathbf{r})\mathbf{r}}{r^5} - \frac{\mathbf{m}}{r^3}\right] \tag{8.6}$$

where $\mu_0 = 4\pi \times 10^{-7}\,\mathrm{H/m}$ is the vacuum permeability. The magnetic moment of a core, $\mathbf{m} = V\mathbf{M}_{sat}$, is function of the saturation magnetization M_{sat} of the ferromagnetic material used and the volume V of the core.

8.4.1 Magnetic Field of Disc Cores

For disc cores, as used in this work, the dipole model in (8.6) is inadequate at work distances from the cores in DFN. Therefore, a mapping of the field was precomputed using finite element modeling (FEM) and used subsequently to estimate the field induced at any point around a disc. Note that discs are assumed to be magnetized in-plane, as caused by their natural orientation in the scanner's field (see Fig. 8.2b). For any disc size, the ratio of the disc height over the radius is kept constant at $h/R = 2/3$ as this was the best found in previous works for generating strong gradients inside the body [26].

The computations were done using the COMSOL Multiphysics 5.2 software. A disc of radius $R = 5\,\mathrm{cm}$ and height $h = 2R/3$ was defined at the center of a spherical volume of air having a diameter of 60 cm. This model was surrounded by an infinite element layer of air to minimize boundary effects. A uniform background field $H_0 = B_0\hat{\mathbf{z}}/\mu_0\,\mathrm{A/m}$ was defined in the entire space for $B_0 = 3\,\mathrm{T}$. The core was assumed to be made of low carbon steel 1020, a ferromagnetic material defined in the COMSOL's material library and having a saturation magnetization of $\sim 1.74 \times 10^6\,\mathrm{A/m}$. The magnetization of the core was calculated according the material's BH curve. The entire model was finely meshed according to a maximum element size of 2.5 mm and the COMSOL AC/DC module was finally used to solve this magnetostatic problem with the solver's relative tolerance set to 10^{-14}. The resulting field $\mathbf{B}_{model}$ in the entire space was then exported as a 3D data grid with resolution 2.5 mm. Using this grid, the field induced at any point by the magnetized core is estimated by trilinear interpolation of $\mathbf{B}_{model}$ and then calculating $\hat{\mathbf{B}} = \mathbf{B}_{model} - \mathbf{B}_0$. This procedure was validated (Fig. 8.3, top) using a spherical core model by comparing the estimated field values $\hat{\mathbf{B}}$ obtained by FEM with the analytical values $\mathbf{B}$ calculated using (8.6). The resulting errors are well below 1%.

Note that the mapping of the field obtained for the disc can be used to estimate the field induced for any disc size by exploiting the symmetry of scale. It can also be rotated to deal

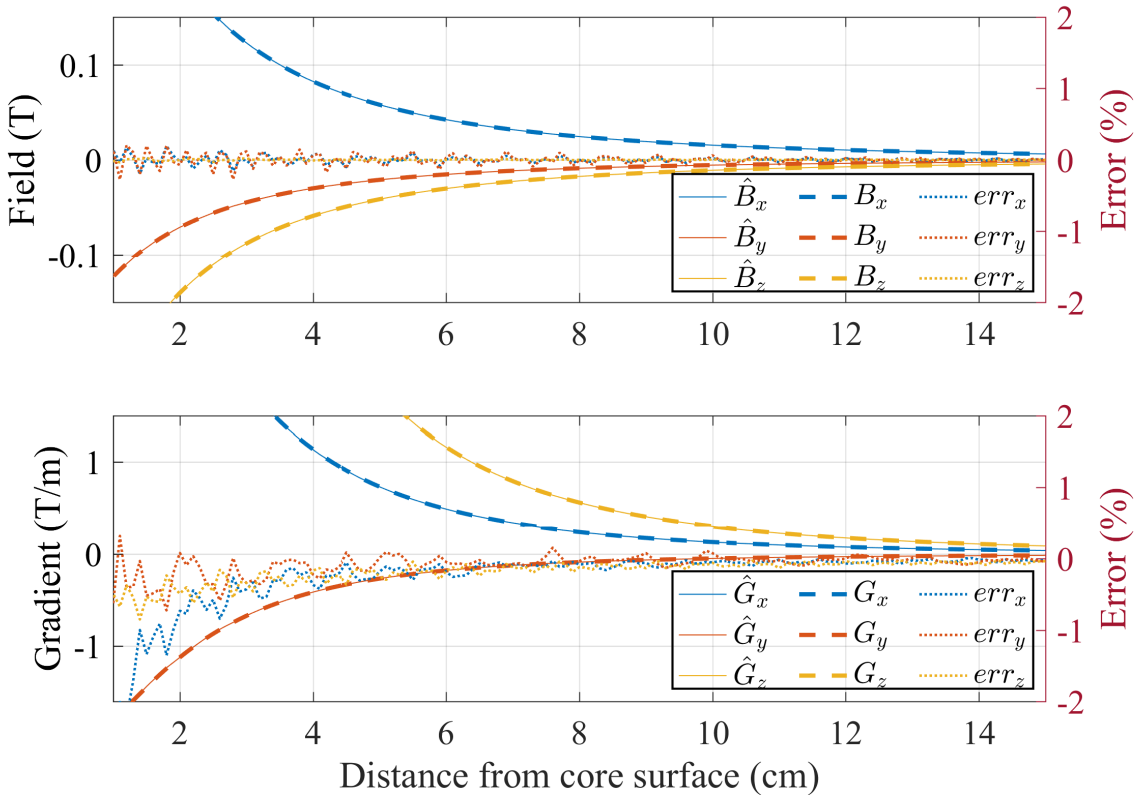

Figure 8.3 Validation of the field and gradient calculation approach, performed for a spherical core ($R = 4\,\text{cm}$) by comparison with analytical values. The curves shown correspond to gradients as the distance to the core surface increases when $\theta = 70°$ and $\phi = -20°$. Other directions show similar accuracy. Note the error scales on the right.

with any disc orientation around its magnetization axis.

8.4.2 Gradient Calculations

The gradients induced by N discs inside the scanner are calculated according to (8.2) by computing the central difference of the total field strength, with a differentiation step size equal to the resolution of the field mapping. The values obtained using this approach were also extensively validated for the spherical core model (Fig. 8.3, bottom). The expressions used to calculate the exact gradients $\nabla(\mathbf{B} + \mathbf{B}_0)$ for a sphere are provided in the Appendix. The numerical values of the gradients are well within 1-2% of the analytical values. It is assumed that the gradients calculated for the disc, using the same approach, have a similar accuracy.

8.4.3 Magnetic Interactions

One challenge in DFN relates to the potentially very strong magnetic interactions between the cores. On one hand, minimum separating distances must be defined such that the interaction forces at kept within an acceptable limit. Although this is subject to future works, it is assumed here that interaction forces at least up to 200 N could be supported by a core holding structure. On another hand, strong interactions may also alter the expected magnetizations of the cores. This can potentially reduce the accuracy of models, although this effect is diminished by the very strong field of the scanner.

In this work, disc core radii range from 2 cm to 5 cm [1] ($h = 2R/3$). The discs can be rotated about their magnetization axis such that their flat side always faces the surface of the patient body. Thus, it is expected that the contact point between two discs on a surface would be close or on their round sides. To limit the interactions to an acceptable level, the minimum center-to-center distance between two discs of radii R_1 and R_2 is empirically defined as

$$r_{min} = R_1 + R_2 + 27R_1R_2 \tag{8.7}$$

where the radii are expressed in meters. The precise elaboration of proximity limits is subject to future investigations. The goal here is to define reasonable limits that allow to evaluate the potential of DFN for generating complex gradient patterns in deep tissues. As such, the minimum gap (surface to surface distance) between two discs is, for example, 1.12 cm for $R_1 = R_2 = 2$ cm, 7.0 cm for $R_1 = R_2 = 5$ cm and 2.8 cm for $R_1 = 2$ cm and $R_2 = 5$ cm.

For two horizontal discs placed side by side at minimum separating distances defined by (8.7), Fig. 8.4 shows the force magnitudes and the alterations of the magnetizations, resulting from magnetic interactions, as a function of the relative positioning angle between the discs with respect to $\mathbf{B}_0$ and for various combinations of disc sizes. These values were obtained in COMSOL using similar models as in Section 8.4.1 above. In Fig. 8.4b, the values correspond to the average magnetization over the volume of the most affected disc (the smaller of the two in general). The simple constraint defined by (8.7) ensures that the maximum interaction force of 200 N is not exceeded, while the resulting errors on the expected magnetizations stay below 2° in orientation and reach at most ~0.18% in magnitude. Such errors on the models are likely to have a negligible impact on the navigation outcome. Besides, it is expected that

1. In previous works [23], it was shown that spherical cores with radius ~4 cm would be required to generate ~300 mT/m gradients in deep tissues. Here, a disc with radius 5 cm has an equivalent magnetic volume, although this shape yields better performances.

other arrangements of the discs (e.g., with different orientations on a curved surface) yield similar or weaker interactions due to the similar or larger gap between disc surfaces.

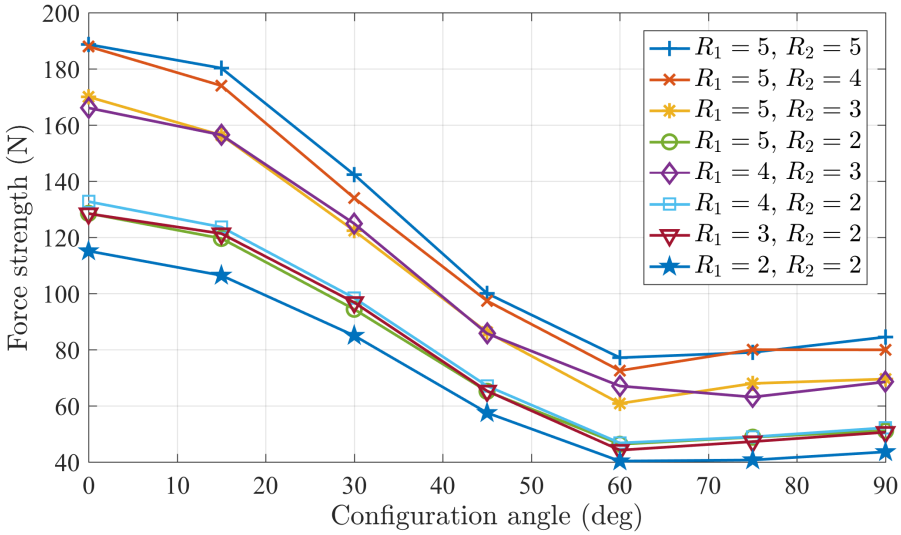

(a) Magnetic interaction forces.

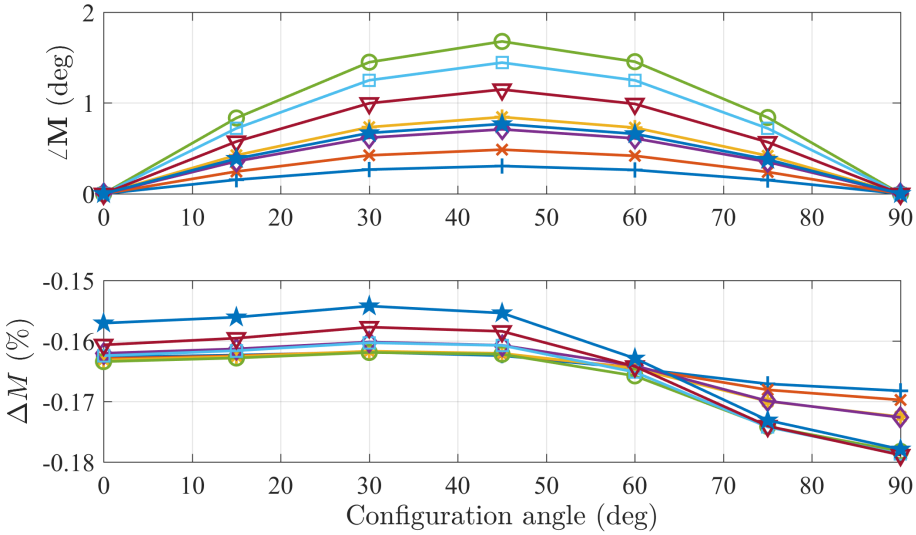

(b) Variations of the magnetization angle (top) and magnitude (bottom).

Figure 8.4 Results of the finite element modeling of the interactions forces between two discs and the variations from the expected magnetizations, as a function of the relative positioning angle between the discs, when the discs are placed at the minimum separating distance given by (8.7) ($M_{sat} = 1.74 \times 10^6$ A/m, $B_0 = 3$ T). Disc radii in the legend are in centimeters. The higher interaction forces are obtained for $R_1 = R_2 = 5$ cm, whereas the larger error on the expected magnetization direction is obtained for $R_1 = 5$ cm and $R_2 = 2$ cm.

8.5 Achievable Gradient Strengths

Using the models developed above, this section investigates the maximum steering gradient strengths that can be achieved when disc cores are constrained to lie above a horizontal plane (i.e. approximation of a patient body). Tests are conducted for different gradient orientations and depths under the plane. By symmetry around the z-axis, the obtained results can be transfered to any other plane orientation around $\hat{\mathbf{z}}$, e.g. for a core located on one side of the body.

8.5.1 Gradient Optimization Approach

A disc core with constant ratio h/R can be defined by its position (x, y, z) and radius R only. A core configuration is then represented by the parameter set

$$\mathbf{x} = \{x_1, y_1, z_1, R_1, x_2, y_2, z_2, R_2, ..., x_N, y_N, z_N, R_N\} \tag{8.8}$$

or, if core sizes are fixed,

$$\mathbf{x} = \{x_1, y_1, z_1, x_2, y_2, z_2, ..., x_N, y_N, z_N\} \tag{8.9}$$

The disc orientations (rotation about the magnetization axis $\hat{\mathbf{z}}$) are not included in the parameters since they can be defined by the surface of the patient body (i.e. here the plane).

The PMD-PSO algorithm described in Section 8.3.1 was used to search for optimal core configurations, starting with one core (i.e. $D_{min} = 3$ or 4). Given a target gradient orientation, desired at a specific location called the *gradient target point*, a fitness value is calculated as

$$f = \begin{cases} G, & \text{if } \xi < \xi_{max} \\ -100\left[(\xi - \xi_{max})^2 - 1\right], & \text{otherwise} \end{cases} \tag{8.10}$$

where G is the resulting gradient norm at the target point and ξ is the error angle, constrained to be smaller than ξ_{max}, on the resulting gradient orientation. For K target gradient orientations desired at K target points, with $k \in [1, K]$, the objective function maximized is

$$F = \begin{cases} \arg\min_k G_k, & \text{if } (\xi_k < \xi_{max})\, \forall k \\ \sum_k f_k, & \text{otherwise} \end{cases} \tag{8.11}$$

where f_k are the fitnesses defined in (8.10). Note that this function implicitly forces the

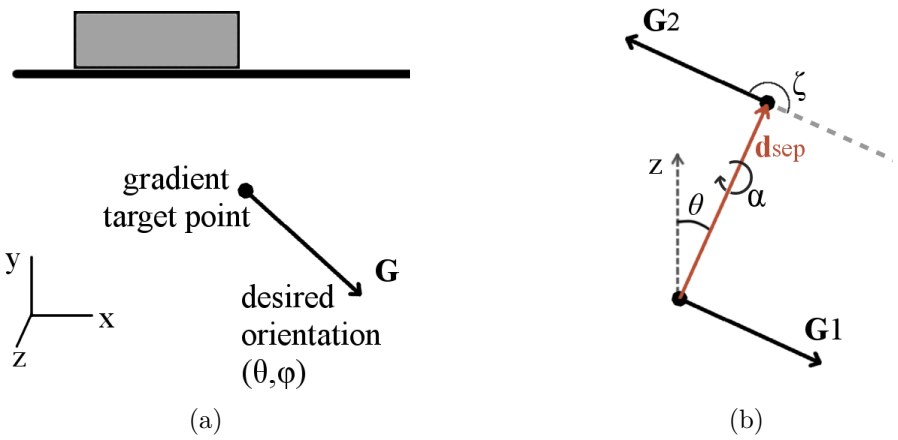

Figure 8.5 Illustration of the achievable gradient tests, a) for a single bifurcation; b) for two bifurcations. Disc cores are constrained by a horizontal plane for generating desired gradient orientation(s) at specific target point(s). For two bifurcations, α is the out-of-plane rotation of the desired gradient orientations, whereas ζ is the required angular variation of the gradient.

resulting gradients to have equal strengths when possible. The function value otherwise corresponds to the minimum strength achieved. This function was the most effective found in preliminary tests for maximizing gradient strengths while dealing with the extra parameter ξ_{max}. Besides, the constraints associated with the plane and the minimum disc separating distances are handled by a penalty approach as in [25].

8.5.2 Single bifurcation

For a single target point located a certain depth under the plane (see Figure 8.5a), desired gradient orientations were uniformly sampled on the unit sphere, for $\theta \in [0, 90°]$ and $\varphi \in [-90°, 90°]$, according to convention in Figure 8.2a. These ranges cover all the possible orientations since the problem is symmetric for the other values of θ and φ. For convenience, reference regions in the (θ, φ) space are identified in Fig. 8.6a.

The position of a disc core with fixed radius $R = 5\,\text{cm}$ was optimized for target point depths of 5 cm and 10 cm. For each orientation, 5 independent runs of the PMD-PSO algorithm were performed ($S = 100$ particles, organized in 5 clans) with $\xi_{max} = 1°$. Although the algorithm converges well most of the time, there is a certain variance across the solutions found and it occasionally fails due to its stochastic behavior and because of the hard constraint related to ξ_{max}. Running multiple attempts allowed to increase the probability of finding the very best solution in each case. The maximum gradient strengths achieved are presented in Figure 8.6b

as heat maps function of θ and φ. As one can see, not only upward gradients are weaker than downward gradients in general, but approximately horizontal gradients are much harder to achieve using a single core, except for gradients aligned within a certain angle from the z-axis.

To increase flexibility and enable generating any gradient orientation effectively, one solution consists in splitting the core into two smaller cores. Doing so, by keeping the same total amount of ferromagnetic material, the second core can cancel undesired components of the gradient generated by the first core and conversely. This hypothesis was validated by running the same tests as above using two discs of radius $R = 3.97\,\text{cm}$, with the corresponding results presented in Figure 8.6c. As expected, the increased flexibility enables all gradient orientations, with strengths ranging between ~80-400 mT/m at 10 cm depth. Thus, the same volume of material can be used more effectively if divided in two separate cores, although some gradient orientations are achieved with higher strengths using a single core.

For comparison purposes, the maximum gradient strengths obtained at a 10 cm depth using smaller discs and their two-core equivalents are presented in Fig. 8.7 for two characteristic sweeps in the (θ, φ) space, namely $(\theta = 90°, \varphi \in [-90°, 90°])$ and $(\theta \in [-90°, 90°], \varphi = 90°)$. These latter are depicted in Fig. 8.6a by the green and orange paths respectively. These plots emphasize that, depending on the desired gradient orientations, either using one or two cores can be best. Note that for gradient orientations that can be generated using a single core, the solutions with two cores are particularly limited by the constraints on minimum separating distances in (8.7).

8.5.3 Two bifurcations

The efficacy of DFN for navigating particles along relatively complex vascular routes (more than one bifurcation) depends on its ability to induce pronounced spatial variations of the gradient orientations while achieving sufficient strengths.

Here, the achievable steering strengths corresponding to a worst-case variation $\zeta = 180°$ of the gradient between two target points are investigated. The two target points are assumed to be located a certain depth under the plane and separated by a distance d_{sep}. The direction of the separation distance (in the xz-plane) is given by the angle θ, whereas the desired gradient orientations at the two points are set perpendicular to the vector $\mathbf{d}_{sep}$ and in opposite directions from each other (see Figure 8.5b). To also test for upward and downward steering gradients, the desired out-of-plane orientations of the gradients are further given by an angle α (rotation about $\mathbf{d}_{sep}$).

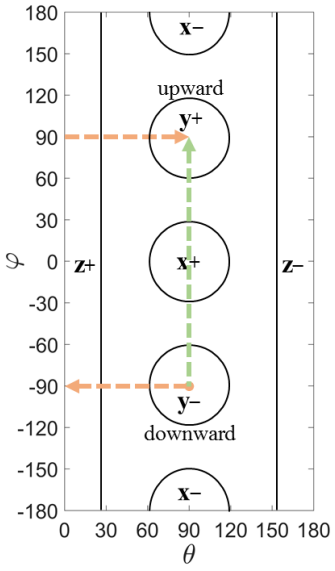

(a) Regions of the (θ, φ) space.

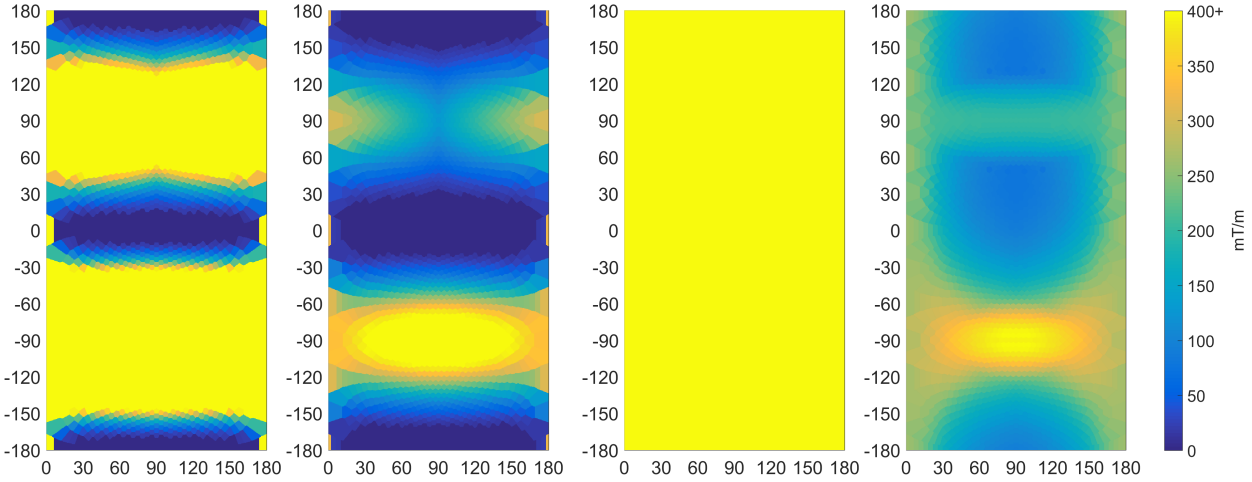

(b) One disc, $R = 5\,\text{cm}$.

(c) Two smaller discs, $R = 3.97\,\text{cm}$ (same total volume).

Figure 8.6 Maximum gradient strengths obtained using disc core(s) constrained to lie above a horizontal plane (approximation of patient body) as a function of the desired gradient orientation (θ, φ), at depths of 5 cm and 10 cm under the plane ($M_{sat} = 1.74 \times 10^6\,\text{A/m}$, $B_0 = 3\,\text{T}$). Proximity between cores is constrained by (8.7). Color scale is on the right. In a), dashed colored paths are for further reference in Fig 8.7.

The values of θ and α were both sampled in the range $[0, 90°]$, the problem being symmetric for other values of these angles. Because of a certain tolerance on gradient directions for steering in practice, an error angle $\xi_{max} = 10°$ was allowed. Note that even at this maximum error angle, a resulting gradient still produces >98% of the force in the desired direction. Based on the above results showing that some gradient orientations are more effectively achieved using

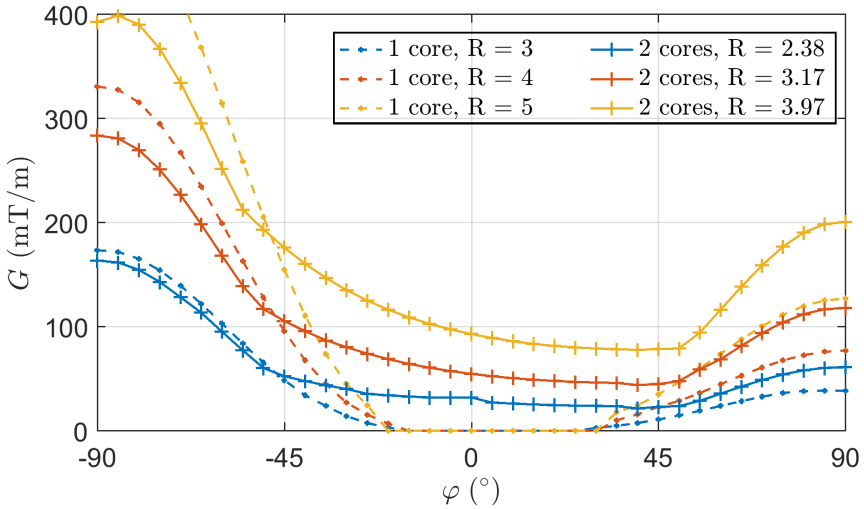

(a) Fixed $\theta = 90°$, varying φ (along green path in Fig. 8.6a).

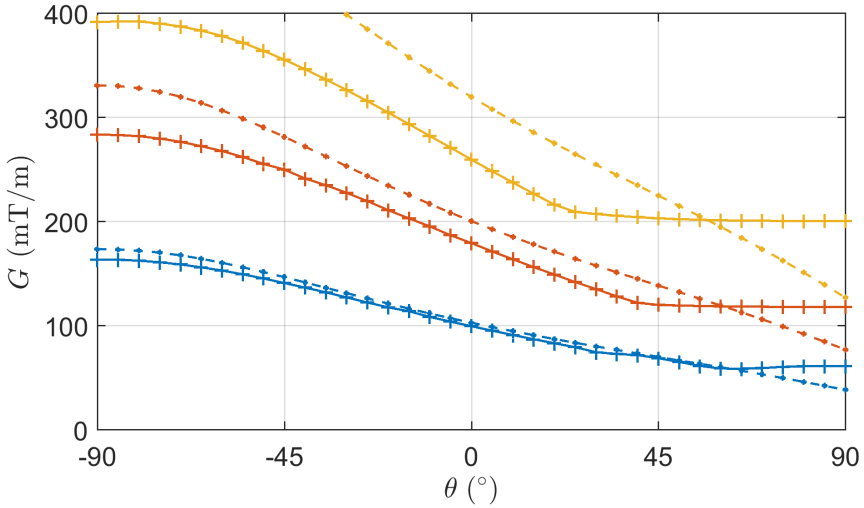

(b) Varying θ, fixed $\varphi = 90°$ (along orange path in Fig. 8.6a).

Figure 8.7 Performances comparison between different disc core sizes for generating desired gradient orientations at a 10 cm depth, for two characteristic sweeps in the (θ, φ) space. Disc radii in the legend are in centimeters. Curves of the same color indicate equal total magnetic volumes.

two cores, the tests were conducted for both using two and four cores. Furthermore, it was observed in preliminary tests that combining different core sizes in certain cases significantly increases the performances. Consequently, a continuous range of disc radii $R \in [2, 5]$ cm was allowed when using two cores, and $R \in [2, 3.97]$ cm when using four cores (same maximum total amount of magnetic material).

For each pair of desired gradient orientations, the PMD-PSO algorithm was used to find

optimal core configurations for different separation distances d_{sep} and depths ($S = 200$ particles organized in 5 clans, 10 runs). Figure 8.8 presents the heat maps corresponding to the gradient strengths obtained. In agreement with previous results, the increased flexibility when using four cores yields better performances overall. With similar patterns between different values of d_{sep}, it is also clear that the capabilities progressively decrease when the distance allowed for the variation decreases. In fact, inducing a strong change of the gradient orientation implies that opposite gradients generated by the different cores partially cancel, which inevitably results in weaker gradients at the target points. More importantly, the achievable strengths are greatly affected by an increased depth, falling for example from well over 200 mT/m (up to ~420 mT/m) at 5 cm when $d_{sep} = 2$ cm with four cores to ~30-40 mT/m at 10 cm. Recall, however, that this corresponds to worst cases since $\zeta = 180°$.

Finally, to support the aforementioned statement about the possible performance gains when different core sizes are combined, Fig. 8.9 compares the gradient strengths obtained for both fixed and variable disc sizes, for the parameter sweep ($\theta = 0°, \alpha \in [0°, 90°]$) when $d_{sep} = 3$ cm. Due to the higher constraints imposed by magnetic interactions for larger cores, better solutions generating stronger gradients are in certain cases achieved using smaller cores. Even more interestingly, combining different disc sizes yield even stronger gradients in some cases. It was observed, notably, that for α values near 90°, the optimal two-core solutions consist in a smaller core for generating the downward gradient combined with a larger core for generating the upward gradient. Consequently, it is preferable to allow for different core sizes when parameterizing core configurations, although the optimization is then more challenging due to the increased number of parameters.

8.6 Real Case Scenario - Targeting in the Human Liver with Dipole Field Navigation

Transarterial chemoembolization is a common treatment for hepatocellular carcinoma, a primary form of liver cancer. Typically, embolization particles and drugs are injected through a catheter inserted beyond the proper hepatic artery (PHA), as close as possible to the targeted lobe or region. It is an example of intervention that could benefit from magnetic navigation, either by guiding the therapeutic agents from the PHA and avoid the risks associated with repeated catheterization of the smaller vessels, or by allowing to target even more precisely the tumors by guiding agents in further bifurcations that cannot be reached with the catheter.

The potential of DFN for guiding particles in real vasculatures was consequently evaluated

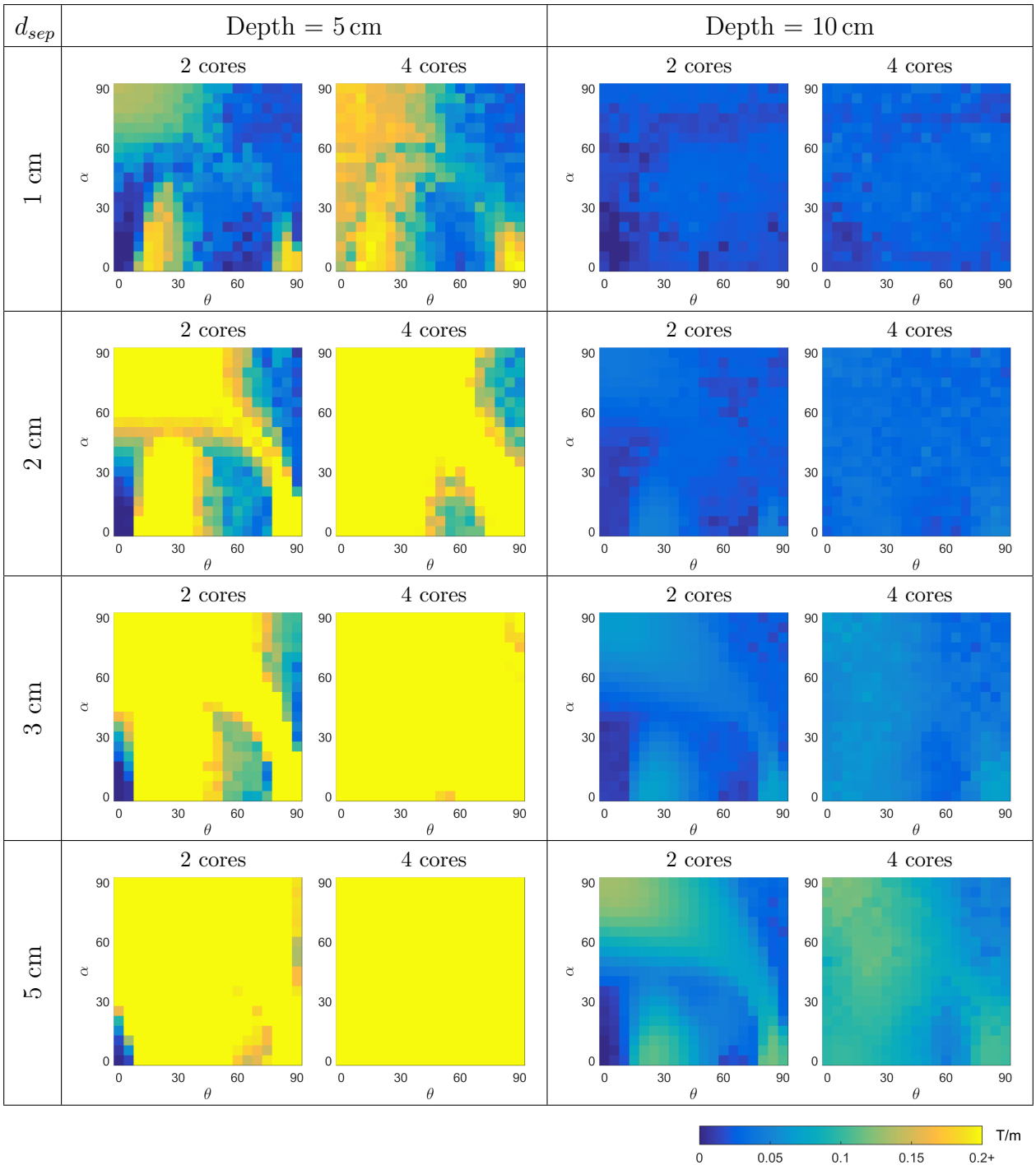

Figure 8.8 Maximum gradient strengths obtained for generating a 180° variation (worst case) of the gradient over a distance d_{sep} using disc cores constrained to lie above a horizontal plane (approximation of a patient body), for different gradient orientations ($M_{sat} = 1.74 \times 10^6$ A/m, $B_0 = 3$ T). Color scale is shown at the bottom right. Core sizes are optimized by the algorithm, in ranges $R \in [2, 5]$ cm for two cores and $R \in [2, 3.97]$ cm for four cores (same maximum total magnetic volume). Proximity between cores is constrained by (8.7).

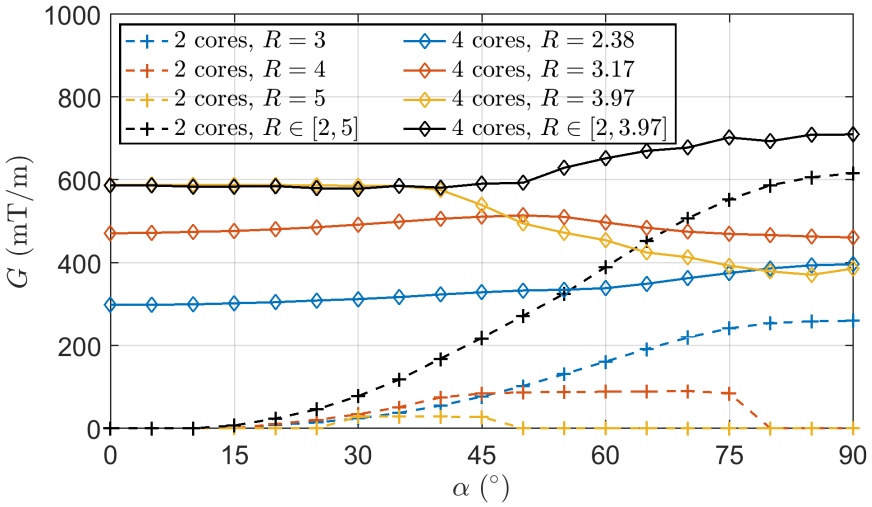

(a) Depth = 5 cm

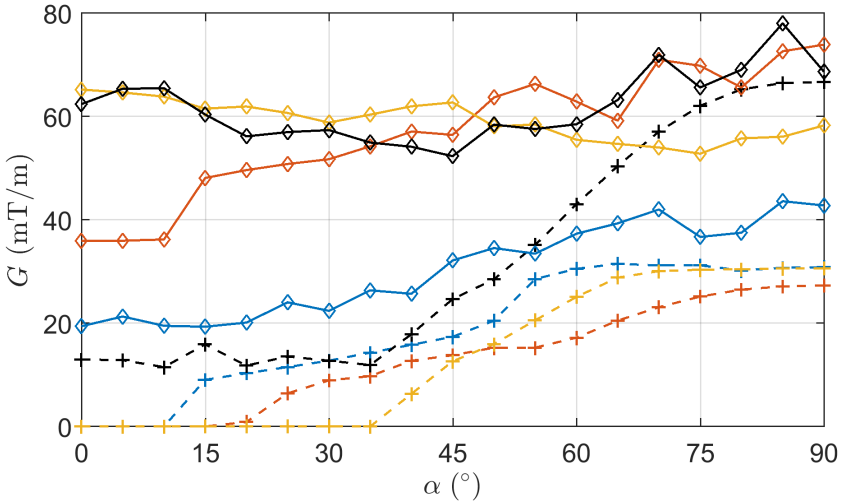

(b) Depth = 10 cm

Figure 8.9 Performance comparison between different disc core sizes for generating 180° variations of the gradient at 5 and 10 cm depths when $d_{sep} = 3$ cm, for the parameter sweep ($\theta = 0°, \alpha \in [0°, 90°]$). As a result, larger cores are not necessarily better and combining different sizes in some cases improves the performance. Disc radii in the legend are in centimeters. Curves of the same color indicate equal maximum total magnetic volumes.

using a model of a human liver vasculature obtained from anonymized clinical data. A computed tomography image, which covered the full abdomen of a patient, was segmented to create the vascular model, from the PHA to the different liver lobes. The patient skin was also segmented to generate a model of the body surface. To account for the core positioning constraints of a realistic intervention scenario, these models, shown in Fig. 8.10, were aligned on an MRI table inside a spherical homogeneous field volume of 50 cm in diameter. This size

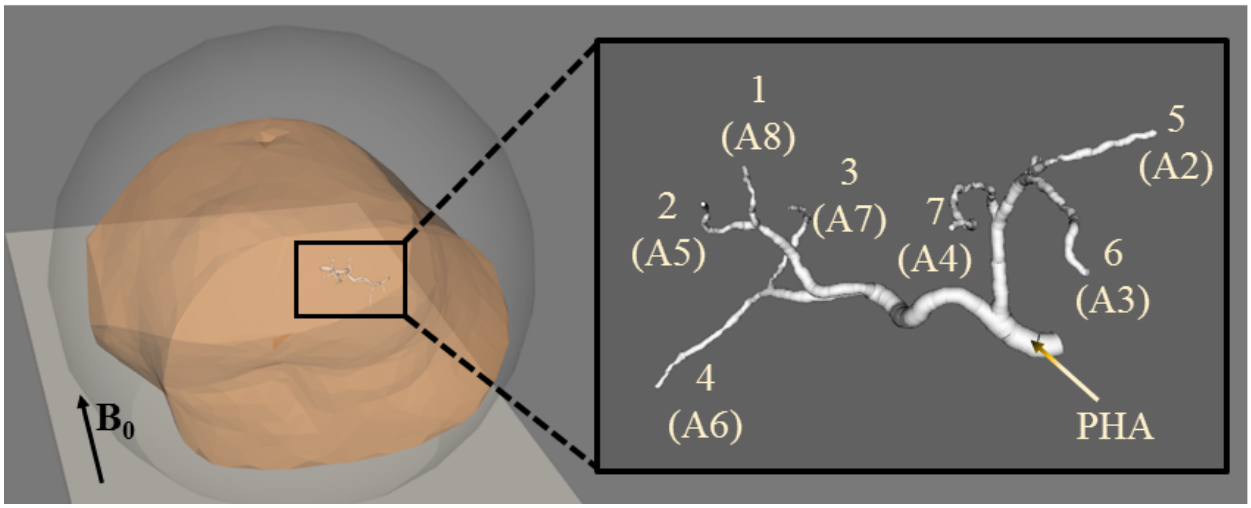

Figure 8.10 Realistic scenario tested for DFN in a real human liver model, taking into account the limited space around the patient body inside an MRI scanner. The transparent sphere represents the homogeneous field volume of a conventional scanner. Vascular routes are numbered for the tests, with the corresponding segmental arteries (Couinaud classification) in parentheses.

of homogeneous volume is typical of conventional scanners. Seven vascular routes, going from the PHA towards each of the seven possible targets (segmental arteries) in this vasculature, are numbered on this figure. The values in parentheses identify the segmental arteries according to the Couinaud classification of the liver.

For the seven vascular routes, the desired gradient orientations at bifurcations were defined based on the geometry of the vascular branches. For each bifurcation, the desired gradient orientation was set perpendicular to both the mother branch and the normal of the bifurcation plane (i.e. the plane defined by $\mathbf{v}_1 \times \mathbf{v}_2$, where $\mathbf{v}_1$ and $\mathbf{v}_2$ are the directions of the child branches) towards the desired branch. Consequently, the desired gradients for steering in the two possible branches of any given bifurcation have opposite directions. The characteristics of the seven vascular routes and their corresponding target gradients are provided in Table 8.1. Note that all routes except Route 7 have three bifurcations. The average target point depth, defined as the closest distance from the skin in the 3D model, is ~10.1 cm. The distance d_{sep} between consecutive bifurcation points vary between ~1.0 cm and ~2.8 cm, whereas the variation angles ζ between consecutive target gradient orientations vary between 61° and 112°.

The purpose of the following tests is to assess the steering gradient strengths that can be generated along these vascular routes and their coupling with the resulting angular errors

Table 8.1 Target Gradient Parameters and Characteristics for the Seven Vascular Routes Tested in the Human Liver Model.

Route	Target gradient orientations (θ, φ) (°)			Target gradient variations				Average depth (cm)
	Bifurcation 1	Bifurcation 2	Bifurcation 3	Bifu 1 → Bifu 2		Bifu 2 → Bifu 3		
				d_{sep} (cm)	ζ (°)	d_{sep} (cm)	ζ (°)	
1	(147.3, -26.1)	(59.5, 20.0)	(41.3, -170.5)	2.7	96	2.8	100	10.0
2	(147.3, -26.1)	(59.5, 20.0)	(128.0, -4.5)	2.7	96	2.8	72	10.0
3	(147.3, -26.1)	(116.3, -147.6)	(49.3, -106.8)	2.7	83	2.3	77	10.1
4	(147.3, -26.1)	(116.3, -147.6)	(130.3, 57.5)	2.7	83	2.3	109	10.1
5	(25.2, 167.7)	(84.7, 152.4)	(74.6, -93.3)	1.8	61	1.0	112	10.3
6	(25.2, 167.7)	(84.7, 152.4)	(99.1, 82.1)	1.8	61	1.0	72	10.3
7	(25.2, 167.7)	(88.0, -32.8)	-	1.8	112	-	-	10.2

on gradient directions. The maximum number of cores was set to four discs with varying sizes $R \in [2, 5]$ cm and $h = 2R/3$ ($D_{max} = 16$). Contrary to previous tests in Section 8.5, here the orientations of the discs (rotation angle about the magnetization axis $\hat{\mathbf{z}}$) are varied to maximize the gradient strengths generated inside the body [26]. As such, the orientation of a disc is determined from the normal of the closest point on the body surface from the disc, such that its flat side is *as parallel as possible* to the body (rotation about $\hat{\mathbf{z}}$ only). Note that only a rotation about $\hat{\mathbf{z}}$ is allowed to keep the disc in its natural alignment with the scanner's field [2] (see Fig. 8.2b). This simple approach avoids the need for extra optimization parameters in (8.8).

For these tests, the objective function maximized for K target gradients is, inspired from [25],

$$F = \prod_{k=1}^{K} \left(0.5 + 0.5 \min \left\{ \frac{G_k}{G_{min}}, 1.0 \right\} \cos(\xi_k) \right) \tag{8.12}$$

which balances between a tentative minimum gradient strength G_{min} and the resulting angular errors on gradient directions. This function can be seen as a geometric estimation of the targeting efficiency ($F \in [0, 1]$) where a gradient strength G_{min} is assumed to yield 100% steering at a bifurcation k if perfectly oriented ($\xi_k = 0$). The PMD-PSO algorithm was used to search for optimal core configurations corresponding to different values of $G_{min} = 20, 50, 100, 150, 200$ and $250\,\mathrm{mT/m}$ ($S = 200$ particles organized in 5 clans, 5 runs). The cores were constrained to lie above the scanner table, inside the homogeneous field volume and outside the patient body, with minimum separation distances defined in (8.7).

2. For large discs, deviations from this preferential magnetization axis are expected to generate high torques, and pre-computed field maps would be needed for various deviation angles.

For each route and each value of G_{min}, the solution with the highest value F found is reported in Fig. 8.11 as the average resulting error angle of the gradients on the route versus the average resulting gradient strength. These results clearly highlight the compromise between strengths and angular accuracies for navigating through multiple bifurcations. As such, the average accuracies for gradients of 20-50 mT/m are within ~10° or less for most of the tested routes, but degrade to ~30° or more at 250 mT/m. Note that these higher gradient strengths could not be achieved for Routes 1 and 7. Examples of core configurations found by the algorithm are provided in Fig. 8.12 for Routes 1, 3 and 7, along with the gradient strengths and angular errors resulting at each bifurcation point.

8.7 Discussion

The capabilities of DFN depend on several parameters, in particular the depth of the vasculature, the number and sizes of the cores used, and the strength of magnetic interactions allowed between the cores. Although not exhaustive, the tests conducted in this work allow to draw significant conclusions about the potential of the method.

First, when physical constraints are taken into account, using a single core may restrains the

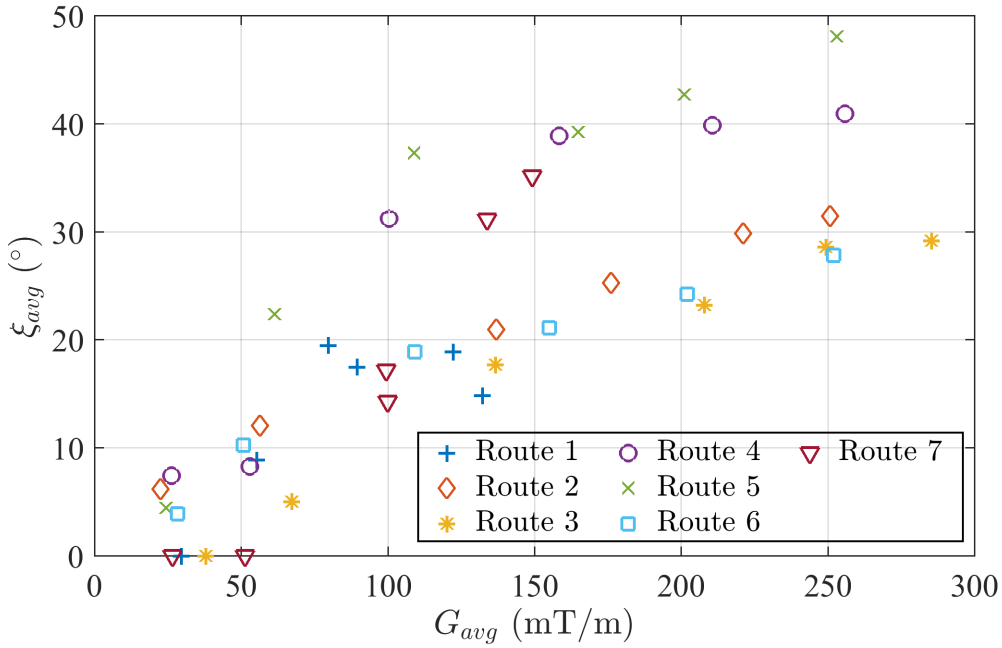

Figure 8.11 Results of different compromises between the average error angle and the average strength of the resulting gradients on the vascular routes in the liver model. Solutions have four discs with sizes $R \in [2, 5]$ cm.

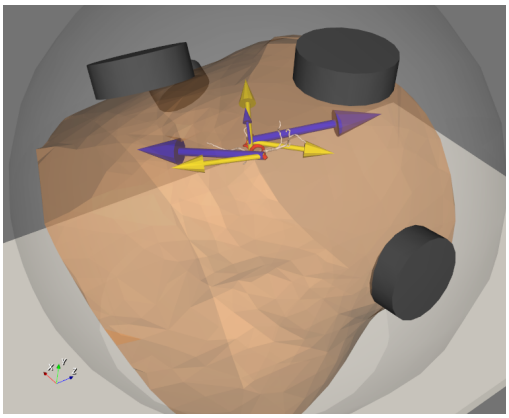

(a) Route 1. $R = 5.0, 5.0, 3.4, 4.4\,\text{cm}$; $G = 153, 54, 159\,\text{mT/m}$; $\xi = 26°, 10°, 21°$.

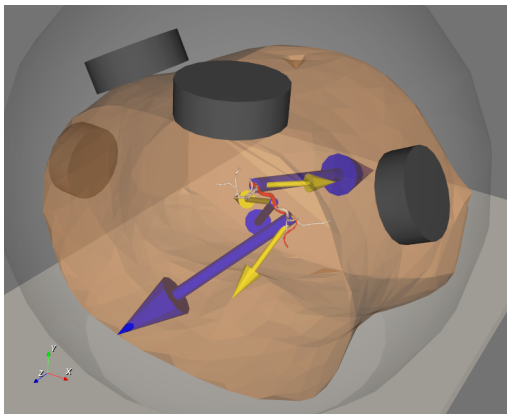

(b) Route 3. $R = 5.0, 4.5, 5.0, 4.1\,\text{cm}$; $G = 250, 150, 223\,\text{mT/m}$; $\xi = 23°, 22°, 25°$.

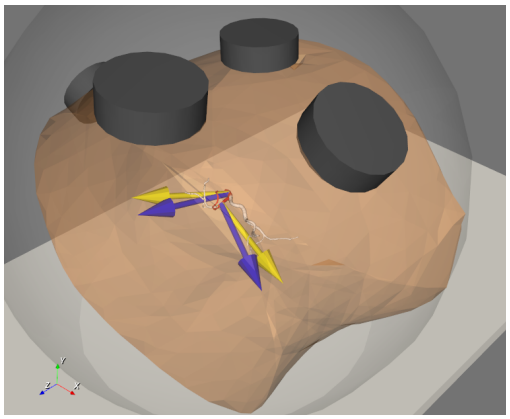

(c) Route 7. $R = 5.0, 4.0, 5.0, 3.5\,\text{cm}$; $G = 100, 100\,\text{mT/m}$; $\xi = 11°, 17°$.

Figure 8.12 Example core configurations obtained for three vascular routes in the liver model. Yellow and blue arrows depict desired and resulting gradients respectively, with arrow sizes proportional to the gradient strengths (here yellow arrows correspond to 100 mT/m). Disc radii are provided for each core configuration ($h = 2R/3$). The resulting gradient strengths and error angles are given, in each case, in the same order as they appear on the route.

gradient orientations that can be generated with sufficient strengths (see Fig. 8.6). These orientations are increasingly limited as the depth of the desired gradient increases. One effective solution consists in splitting the core into two smaller cores which, for the same total amount of ferromagnetic material, enable generating any gradient orientation. Results show that gradients ranging between 80-400 mT/m can in this manner be achieved at a 10 cm depth using two discs of radius $R = 3.97\,\text{cm}$ and height $h = 2R/3$. Second, the ability to induce strong variations of the gradient, which is a general requirement for navigating in vascular routes having two or more bifurcations, is greatly affected by the depth and by

the distance allowed for the variation (see Fig. 8.8). Again, dividing two cores into four smaller cores improves the overall performances by increasing the flexibility for generating all gradient orientations. Still, at a 10 cm depth, although worst-case 180° variations of the gradient can be generated with strengths around 80-120 mT/m for a wide range of orientations when $d_{sep} = 5$ cm, these decrease to ~30-40 mT/m when $d_{sep} = 2$ cm and ~20-30 mT/m when $d_{sep} = 1$ cm. We emphasize that these values may serve as lower bounds on the achievable gradients at two bifurcations, since bifurcations requiring a lower angular variation of the gradient are expected to allow for stronger gradients. Third, results also show that larger cores are not necessarily better when magnetic interactions are taken into account and limit the proximity between cores. In some cases, significantly better performances can even be obtained by combining different core sizes.

The potential of DFN for guiding particles in real vasculatures was evaluated using a vascular model of a human liver and considering the constraints associated with the limited space for placing the cores around a patient in a conventional MRI scanner. Despite the depth (~10 cm) of the bifurcations and the relatively complex vascular routes for targeting different regions in this model, encouraging results were obtained. In fact, for most routes, gradients exceeding 100 mT/m could be achieved within ~20° of average angular accuracy. For three routes out of seven, gradients reaching 250 mT/m could be achieved within ~30° accuracy. Although the acceptable angular errors on gradient orientations are still unknown and subject to future works, these results demonstrate that an important part in parameterizing core configurations will consist of establishing the best possible compromise between gradient strengths and gradient accuracies to maximize the targeting efficiency in each case.

Different aspects could be investigated to achieve higher gradient capabilities. Undoubtedly, allowing stronger interactions between the cores would improve the capabilities through an increased positioning flexibility. Therefore, the simple rule used in this work for determining minimum separating distances between disc cores could be further studied to account, in particular, for the nonlinearity of magnetic interactions as a function of the relative angle between the cores. Stronger gradients could also be generated using larger cores, but the increased interactions would in turn impose larger separating distances which, as stated before, could limit the gains in a range of cases. Instead, it is possible that using a higher number of cores further improves the capabilities, although optimizing the configuration parameters of a large number of cores becomes more challenging. This aspect also leads to another consideration, not discussed in this work, related to an additional compromise between the quality of the gradients generated and the increased complexity of inserting a larger total

quantity of magnetic material in the scanner.

Compared with Magnetic Resonance Navigation (MRN), which also exploits the high field of an MRI scanner, DFN in its present form has the advantage of being able to generate stronger directional gradients even in deep tissues, although with limited resolutions between bifurcation points. This is achieved at the cost of losing imaging capabilities due to the highly distorted field, thus preventing the real-time tracking of particles during navigation. Still, with reliable magnetic models and algorithms, DFN would enable a continuous injection of the therapeutic agents once the cores are positioned. This would allow for much shorter intervention times for administering a given dose of drugs compared with other methods, such as MRN, where particle boluses must be guided individually, one by one.

In conclusion, the results presented in this work show a promising potential for targeting therapeutics using DFN, with the highest field and gradient strengths currently available at the human scale. Other challenges remain to be addressed, such as for inserting and holding the cores in the scanner, but current advancements in this approach motivate future works towards in vivo experiments.

Appendix - Exact Gradient Model for One Spherical Core

The gradient around a core is function of the total field strength

$$\mathbf{G} = \nabla\sqrt{B_{tot,x}^2 + B_{tot,y}^2 + B_{tot,z}^2} \tag{8.13}$$

where, for a spherical core (dipole) in Cartesian coordinates and according to the coordinate convention shown in Fig. 8.2a,

$$B_{tot,x} = \frac{\mu_0 m}{4\pi}\frac{3xz}{r^5} \tag{8.14}$$

$$B_{tot,y} = \frac{\mu_0 m}{4\pi}\frac{3yz}{r^5} \tag{8.15}$$

$$B_{tot,z} = \frac{\mu_0 m}{4\pi}\frac{3z^2 - r^2}{r^5} + B_0 \tag{8.16}$$

This expression of the gradient was developed using the Symbolic Math Toolbox in Matlab R2016a. The expressions output by Matlab for G_x, G_y and G_z are not included here due to

their lengths. After substitutions, the following expressions can be obtained:

$$G_x = \frac{\partial B_{tot}}{\partial x} = \frac{bkx}{er}\left(1 - \frac{5z^2}{r^2}\right) + \frac{k^2xz^2}{er^2}\left(1 - \frac{5\rho^2}{r^2}\right) \tag{8.17}$$

$$G_y = \frac{\partial B_{tot}}{\partial y} = \frac{bky}{er}\left(1 - \frac{5z^2}{r^2}\right) + \frac{k^2yz^2}{er^2}\left(1 - \frac{5\rho^2}{r^2}\right) \tag{8.18}$$

$$G_z = \frac{\partial B_{tot}}{\partial z} = \frac{bkz}{er}\left(3 - \frac{5z^2}{r^2}\right) + \frac{k^2z\rho^2}{er^2}\left(1 - \frac{5z^2}{r^2}\right) \tag{8.19}$$

where the following variables are defined for concision:

$$k = \frac{3\mu_0 m}{4\pi r^4} \tag{8.20}$$

$$\rho = \sqrt{x^2 + y^2} \tag{8.21}$$

$$b = B_0 + k/r\left(z^2 - r^2/3\right) \tag{8.22}$$

$$e = \sqrt{b^2 + k^2z^2\rho^2/r^2} \tag{8.23}$$

Substituting $\cos^2\theta = z^2/r^2$ and $\sin^2\theta = \rho^2/r^2$ yields

$$G_x = \frac{bkx}{er}\left(1 - 5\cos^2\theta\right) + \frac{k^2x\cos^2\theta}{e}\left(1 - 5\sin^2\theta\right) \tag{8.24}$$

$$G_y = \frac{bky}{er}\left(1 - 5\cos^2\theta\right) + \frac{k^2y\cos^2\theta}{e}\left(1 - 5\sin^2\theta\right) \tag{8.25}$$

$$G_z = \frac{bkz}{er}\left(3 - 5\cos^2\theta\right) + \frac{k^2z\sin^2\theta}{e}\left(1 - 5\cos^2\theta\right) \tag{8.26}$$

The gradient can then be expressed as

$$\mathbf{G} = \frac{b}{e}\widetilde{\mathbf{G}} + \frac{k^2}{e}\begin{bmatrix} x\cos^2\theta\left(1 - 5\sin^2\theta\right) \\ y\cos^2\theta\left(1 - 5\sin^2\theta\right) \\ z\sin^2\theta\left(1 - 5\cos^2\theta\right) \end{bmatrix} \tag{8.27}$$

where

$$\widetilde{\mathbf{G}} = k\begin{bmatrix} \sin\theta\cos\varphi\left(1 - 5\cos^2\theta\right) \\ \sin\theta\sin\varphi\left(1 - 5\cos^2\theta\right) \\ \cos\theta\left(3 - 5\cos^2\theta\right) \end{bmatrix} \tag{8.28}$$

is the far field approximation model ($B_{tot} \approx B_{tot,z}$) used in previous works [23]. Note the presence of B_0 in (8.22) for the exact model in (8.27). As B_0 increases, b/e tends towards the unit ratio and k_1^2/e tends towards zero, thus the gradient approaches the far field

approximation $\widetilde{\mathbf{G}}$.

Acknowledgments

The authors would like to thank Dr Pierre Perreault, radiologist at CHUM Montréal, for providing the anonymized computed tomography image.

8.8 References

[1] T. Xu, J. Yu, X. Yan, H. Choi, et L. Zhang, "Magnetic Actuation Based Motion Control for Microrobots: An Overview", *Micromachines*, vol. 6, no. 9, pp. 1346–1364, 2015.

[2] P. Pouponneau, G. Bringout, et S. Martel, "Therapeutic Magnetic Microcarriers Guided by Magnetic Resonance Navigation for Enhanced Liver Chemoembilization: A Design Review", *Ann. Biomed. Eng.*, vol. 42, no. 5, pp. 929–939, 2014. DOI: 10.1007/s10439-014-0972-1

[3] L. Mellal, K. Belharet, D. Folio, et A. Ferreira, "Optimal structure of particles-based superparamagnetic microrobots: application to MRI guided targeted drug therapy", *J. Nanoparticle Res.*, vol. 17, no. 2, 2015. DOI: 10.1007/s11051-014-2733-3

[4] T. Y. Huang, M. S. Sakar, A. Mao, A. J. Petruska, F. Qiu, X. B. Chen, S. Kennedy, D. Mooney, et B. J. Nelson, "3D Printed Microtransporters: Compound Micromachines for Spatiotemporally Controlled Delivery of Therapeutic Agents", *Adv. Mater.*, vol. 27, no. 42, pp. 6644–6650, 2015. DOI: 10.1002/adma.201503095

[5] M. Arruebo, R. Fernández-pacheco, M. R. Ibarra, et J. Santamaría, "Magnetic nanoparticles for drug delivery", *Nano Today*, vol. 2, no. 3, pp. 22–32, 2007.

[6] J. B. Mathieu et S. Martel, "Steering of aggregating magnetic microparticles using propulsion gradients coils in an MRI scanner", *Magn. Reson. Med.*, vol. 63, no. 5, pp. 1336–1345, 2010. DOI: 10.1002/mrm.22279

[7] P. Pouponneau, J. C. Leroux, G. Soulez, L. Gaboury, et S. Martel, "Co-encapsulation of magnetic nanoparticles and doxorubicin into biodegradable microcarriers for deep tissue targeting by vascular MRI navigation", *Biomaterials*, vol. 32, no. 13, pp. 3481–3486, 2011. DOI: 10.1016/j.biomaterials.2010.12.059

[8] A. S. Lübbe, C. Bergemann, H. Riess, A. S. Lãbbe, F. Schriever, P. Reichardt, K. Possinger, M. Matthias, B. Dã, F. Herrinann, R. Gurtler, P. Hohenberger, N. Haas, R. Sohr, B. Sander, A.-J. J. Lemke, D. Ohlendorf, W. Huhnt, D. Huhn, B. Dörken, F. Herrmann, R. Gürtler, P. Hohenberger, N. Haas, R. Sohr, B. Sander, A.-J. J. Lemke, D. Ohlendorf, W. Huhnt, D. Huhn, A. S. Lãbbe, F. Schriever, P. Reichardt, K. Possinger, M. Matthias, B. Dã, F. Herrinann, R. Gurtler, P. Hohenberger, N. Haas, R. Sohr, B. Sander, A.-J. J. Lemke, D. Ohlendorf, W. Huhnt, D. Huhn, B. Dörken, F. Herrmann, R. Gürtler, P. Hohenberger, N. Haas, R. Sohr, B. Sander, A.-J. J. Lemke, D. Ohlendorf, W. Huhnt, et D. Huhn, "Clinical Experiences with Magnetic Drug Targeting: A Phase I Study with 4'-Epidoxorubicin in 14 Patients with Advanced Solid Tumors", *Cancer Res.*, vol. 56, no. 20, pp. 4686–4693, 1996.

[9] A. Amirfazli et R. Virginia, "Magnetic nanoparticles hit the target", *Nat. Nanotechnol.*, vol. 2, no. August, pp. 467–468, 2007. DOI: 10.1038/nnano.2007.234

[10] B. Shapiro, K. Dormer, et I. B. Rutel, "A two-magnet system to push therapeutic nanoparticles", dans *AIP Conf. Proc.*, vol. 1311, no. 1, 2010, pp. 77–88. DOI: 10.1063/1.3530064

[11] M. Gao, C. Hu, Z. Chen, H. Zhang, et S. Liu, "Design and fabrication of a magnetic propulsion system for self-propelled capsule endoscope", *IEEE Trans. Biomed. Eng.*, vol. 57, no. 12, pp. 2891–2902, 2010. DOI: 10.1109/TBME.2010.2051947

[12] S. Tognarelli, V. Castelli, G. Ciuti, C. Natali, E. Sinibaldi, P. Dario, et A. Menciassi, "Magnetic propulsion and ultrasound tracking of endovascular devices", *J. Robot. Surg.*, vol. 6, no. 1, pp. 5–12, 2011.

[13] A. W. Mahoney et J. J. Abbott, "Five-degree-of-freedom manipulation of an untethered magnetic device in fluid using a single permanent magnet with application in stomach capsule endoscopy", *Int. J. Rob. Res.*, vol. 35, no. 1-3, pp. 129–147, 2015.

[14] M. P. Kummer, J. J. Abbott, B. E. Kratochvil, R. Borer, A. Sengul, et B. J. Nelson, "Octomag: An electromagnetic system for 5-DOF wireless micromanipulation", *IEEE Trans. Robot.*, vol. 26, no. 6, pp. 1006–1017, 2010. DOI: 10.1109/TRO.2010.2073030

[15] H. Choi, K. Cha, J. Choi, S. Jeong, S. Jeon, G. Jang, J.-o. Park, et S. Park, "EMA system with gradient and uniform saddle coils for 3D locomotion of microrobot", *Sensors Actuators A Phys.*, vol. 163, no. 1, pp. 410–417, 2010. DOI: 10.1016/j.sna.2010.08.014

[16] H. Keller, A. Juloski, H. Kawano, M. Bechtold, A. Kimura, H. Takizawa, et R. Kuth, "Method for navigation and control of a magnetically guided capsule endoscope in the human stomach", dans *Proc. IEEE RAS EMBS Int. Conf. Biomed. Robot. Biomechatronics*, 2012, pp. 859–865.

[17] E. Diller, J. Giltinan, G. Z. Lum, Z. Ye, et M. Sitti, "Six-degree-of-freedom magnetic actuation for wireless microrobotics", *Int. J. Rob. Res.*, vol. 35, no. 1-3, pp. 114–128, 2016. DOI: 10.1177/0278364915583539

[18] S. Jeong, H. Choi, G. Go, C. Lee, K. S. Lim, D. S. Sim, M. H. Jeong, S. Y. Ko, J. O. Park, et S. Park, "Penetration of an artificial arterial thromboembolism in a live animal using an intravascular therapeutic microrobot system", *Med. Eng. Phys.*, vol. 38, no. 4, pp. 403–410, 2016. DOI: 10.1016/j.medengphy.2016.01.001

[19] A. J. Petruska, J. B. Brink, et J. J. Abbott, "First demonstration of a modular and reconfigurable magnetic-manipulation system", dans *Proc. - IEEE Int. Conf. Robot. Autom.*, vol. 2015-June, no. June, 2015, pp. 149–155. DOI: 10.1109/ICRA.2015.7138993

[20] X. Zhang, T.-A. Le, et J. Yoon, "Development of a real time imaging-based guidance system of magnetic nanoparticles for targeted drug delivery", *J. Magn. Magn. Mater.*, vol. 427, no. October, pp. 345–351, 2017. DOI: 10.1016/j.jmmm.2016.10.056

[21] S. Martel, J.-B. Mathieu, O. Felfoul, A. Chanu, E. Aboussouan, S. Tamaz, P. Pouponneau, L. Yahia, G. Beaudoin, G. Soulez, et M. Mankiewicz, "Automatic navigation of an untethered device in the artery of a living animal using a conventional clinical magnetic resonance imaging system", *Appl. Phys. Lett.*, vol. 90, no. 11, p. 114105, 2007.

[22] K. Belharet, D. Folio, et A. Ferreira, "MRI-based microrobotic system for the propulsion and navigation of ferromagnetic microcapsules", *Minim. invasive Ther. allied Technol.*, vol. 19, pp. 157–169, 2010.

[23] M. Latulippe et S. Martel, "Dipole Field Navigation: Theory and Proof of Concept", *IEEE Trans. Robot.*, vol. 31, no. 6, pp. 1353–1363, 2015.

[24] M. Latulippe, O. Felfoul, P. E. Dupont, et S. Martel, "Enabling automated magnetic resonance imaging-based targeting assessment during dipole field navigation", *Appl. Phys. Lett.*, vol. 108, no. 6, p. 062403, 2016. DOI: 10.1063/1.4941925

[25] M. Latulippe et S. Martel, “A Progressive Multidimensional Particle Swarm Optimizer for Magnetic Core Placement in Dipole Field Navigation”, dans *IEEE Int. Conf. Intell. Robot. Syst.*, 2016, pp. 2314–2320.

[26] M. Latulippe et S. Martel, “Seeking Optimal Magnetic Core Shapes for Strong Gradient Generation in Dipole Field Navigation”, dans *IEEE Int. Conf. Manip. Autom. Robot. Small Scales*, 2017.

[27] Y. Shi et R. Eberhart, “A modified particle swarm optimizer”, dans *Proc. IEEE Int. Conf. Evol. Comput.*, 1998, pp. 69–73. DOI: 10.1109/ICEC.1998.699146

[28] B. Jiao, Z. Lian, et X. Gu, “A dynamic inertia weight particle swarm optimization algorithm”, *Chaos, Solitons and Fractals*, vol. 37, no. 3, pp. 698–705, 2008. DOI: 10.1016/j.chaos.2006.09.063

[29] D. F. D. Carvalho et C. J. A. Bastos-Filho, “Clan particle swarm optimization”, *Int. J. Intell. Comput. Cybern.*, vol. 2, no. 2, pp. 197–227, 2009. DOI: 10.1108/17563780910959875

CHAPITRE 9 DISCUSSION GÉNÉRALE

De manière générale, l'actionnement magnétique a bien démontré son efficacité pour le guidage et le contrôle de petits dispositifs dans des régions autrement difficiles d'accès du corps humain. Cette approche a été utilisée pour développer notamment des plateformes de guidage de capsules endoscopiques [44, 46, 61] et de cathéter [50, 69, 133]. Elle a aussi été employée pour le contrôle à distance de petits outils chirurgicaux pour effectuer des microchirurgies minimalement invasives [68, 59]. Pour le guidage de micro-agents à l'intérieur du réseau vasculaire, obtenir la saturation magnétique des agents en plus de gradients magnétiques forts dans les tissus profonds représente toutefois un défi. Hormis la méthode proposée de guidage par champs de dipôles (DFN), la seule méthode permettant à l'heure actuelle de garantir la saturation magnétique des agents thérapeutiques, peu importe leur profondeur dans le corps du patient, est MRN [75]. Cette méthode est cependant fortement limitée par les amplitudes de gradients pouvant être générées par les appareils cliniques conventionnels d'imagerie par résonance magnétique.

Les corps ferromagnétiques positionnés autour du patient dans DFN permettent d'atteindre des amplitudes de gradients nettement supérieures à ceux des appareils d'IRM conventionnels. Les résultats montrent qu'en utilisant des corps en forme de disque, les gradients peuvent excéder 400 mT/m à une profondeur de 10 cm. Les capacités de guidage de DFN sont par contre fortement affectées par la profondeur et la complexité de la trajectoire vasculaire visée. Pour des trajectoires relativement complexes à plusieurs bifurcations, un compromis est nécessaire entre les amplitudes de gradients générés et leurs précisions angulaires. La quantification des erreurs angulaires acceptables et l'identification des meilleurs compromis pourraient être investiguées à l'aide de modélisations fluidiques du transit des agents dans l'environnement vasculaire [129, 134–136].

En général, sauf pour des cas simples, la combinaison de plusieurs corps ferromagnétiques est requise pour le guidage. Bien qu'augmenter le nombre et la taille des corps ferromagnétiques pourraient possiblement jusqu'à un certain point améliorer les performances de DFN pour diriger des agents le long de trajectoires complexes, la quantité de matériau magnétique insérée dans l'appareil doit être minimisée afin de limiter non seulement les forces d'interaction magnétique, mais également les forces d'attraction à soutenir lors de leur insertion dans l'appareil d'IRM. À ce titre, il est pertinent d'inclure ici, pour référence, quelques graphiques de la force d'insertion d'un corps ferromagnétique en fonction de la distance à parcourir

jusqu'au centre de l'appareil. Ces graphiques, présentés à la Fig. 9.1, ont été produits à partir de données provenant de Siemens Healthcare et décrivant le champ et le gradient à l'intérieur et à l'extérieur d'un appareil MAGNETOM Skyra de 3 T. Les forces d'attraction ont été calculées en utilisant ces valeurs et en considérant la courbe de magnétisation $M(H)$ d'un corps ferromagnétique en acier à faible teneur en carbone 1020 ($M_{sat} \approx 1.74 \times 10^6$ A/m) [1]. Chaque graphique correspond à l'insertion d'un disque ferromagnétique avec un certain décalage latéral par rapport à l'axe central du tunnel. Pour cet appareil, le diamètre interne du tunnel est de 70 cm. Le décalage le plus élevé, soit de 30 cm, correspond donc à l'insertion du disque très près de la paroi du tunnel. Il est à noter que les insertions décalées entraînent une composante radiale de la force. Pour minimiser les forces d'insertion, les corps ferromagnétiques volumineux doivent idéalement être insérés le long de l'axe du tunnel, en plein centre. Ceci est possible si les corps ferromagnétiques sont insérés dans l'appareil avant d'y faire entrer le patient. Actuellement, le robot Kuka installé près de l'appareil d'IRM au Laboratoire de NanoRobotique a une capacité de soutenir une force d'attraction d'environ 300 kg. Utiliser ce robot, d'ailleurs requis pour la méthode de guidage de cathéter FFN [51], est une possibilité pour insérer les corps ferromagnétiques, un seul ou plusieurs à la fois. Autrement, un mécanisme d'insertion sera nécessaire. Une alternative serait de conserver des corps ferromagnétiques en permanence dans un appareil d'IRM dédié à DFN.

Il serait aussi envisageable de combiner plusieurs formes différentes de corps ferromagnétiques afin d'exploiter les avantages de chacune pour le guidage. L'espace de recherche plus grand qui en résulterait complexifierait cependant l'optimisation des configurations de corps ferromagnétiques. Aussi, bien que les formes les plus performantes identifiées dans cet ouvrage soient le disque et l'hémisphère, il est possible que d'autres formes encore plus avantageuses puissent être exploitées. L'optimisation de la forme des corps ferromagnétiques pourraient donc être étudiée davantage pour améliorer la distorsion du champ et les capacités de guidage.

La minimisation de la quantité totale de matériau magnétique utilisé pour le guidage est en partie gérée par l'algorithme PMD-PSO, qui permet de faire un compromis entre la qualité d'une solution et le nombre de corps ferromagnétiques utilisés. Une approche améliorée serait d'intégrer le volume total de matériau magnétique d'une solution comme deuxième objectif d'optimisation afin de permettre d'identifier des solutions optimales différentes, correspondant aux différents compromis possibles (frontière de Pareto) entre la quantité de matériau et la qualité des gradients générés. D'autre part, pour augmenter les amplitudes de gradients

1. L'approximation d'un corps ferromagnétique uniformément magnétisé est faite pour simplifier le problème. Les valeurs de champ et de gradient considérées sont celles au centre du corps ferromagnétique.

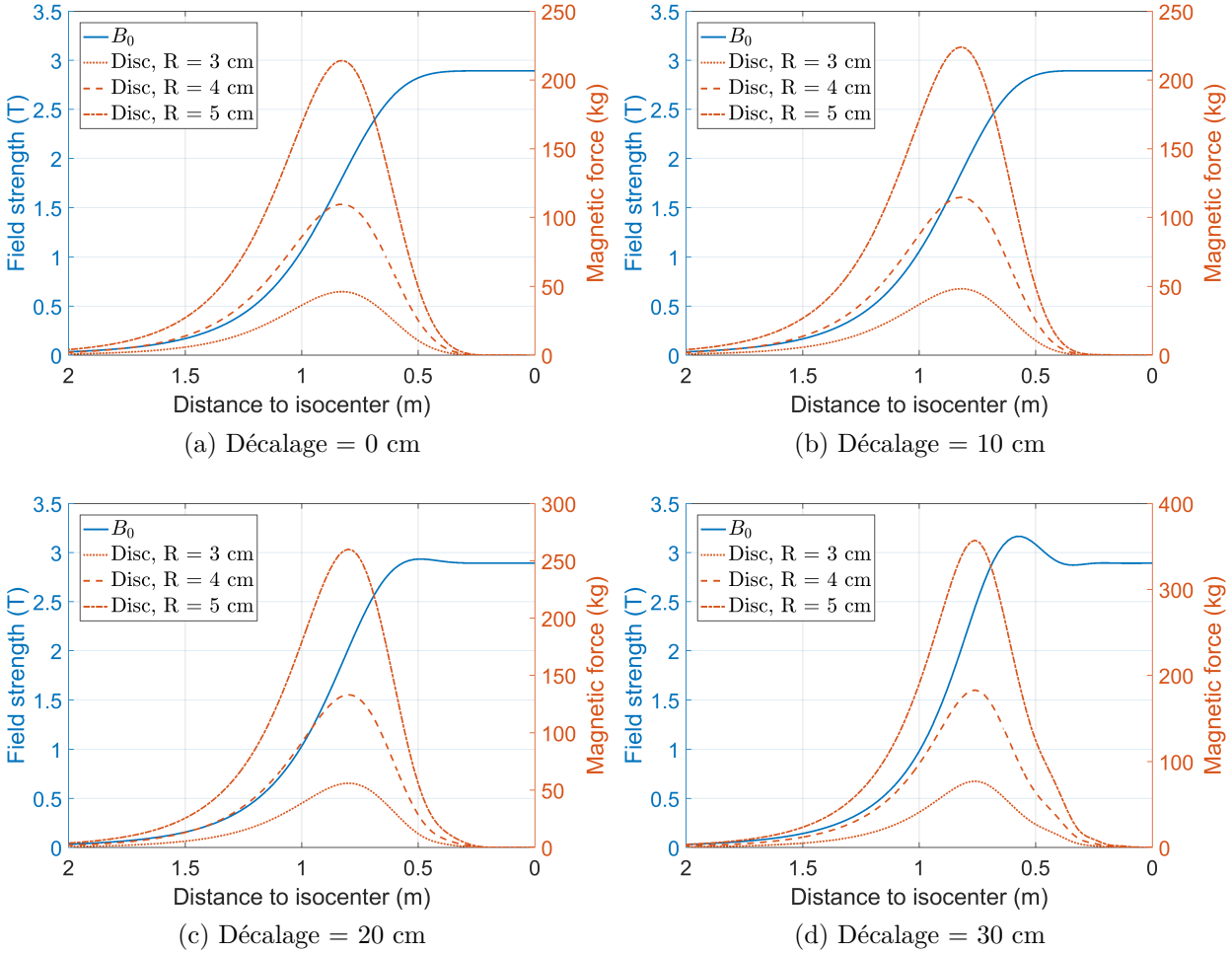

(a) Décalage = 0 cm

(b) Décalage = 10 cm

(c) Décalage = 20 cm

(d) Décalage = 30 cm

Figure 9.1 Forces d'insertion de disques ferromagnétiques dans un appareil d'IRM de modèle MAGNETOM Skyra 3 T, pour l'insertion d'un disque avec différents décalages latéraux par rapport à l'axe central du tunnel de l'appareil. Noter la direction inversée des abscisses. L'épaisseur des disques est fonction du rayon ($h = 2R/3$). Valeurs calculées selon la courbe de magnétisation de l'acier à faible teneur en carbone 1020.

générés par un volume donné de matériau magnétique, une solution simple pourrait être d'utiliser un matériau avec une saturation plus élevée. En particulier, le matériau disponible en bloc ayant la plus haute magnétisation à saturation connue à ce jour est un alliage de fer-cobalt contenant 35% de cobalt et dont la magnétisation est $M_{sat} = 1.95 \times 10^6$ A/m [137]. Ce dernier offrirait un gain potentiel de ~12% par rapport à l'acier 1020 dernièrement considéré, quoique les forces d'interaction et d'insertion sont susceptibles d'augmenter tout autant.

Par ailleurs, sans capacité d'imagerie permettant le contrôle en boucle fermée des agents navigués avec DFN, il est clair que la précision des modèles et algorithmes développés est cruciale afin de correctement paramétrer les corps ferromagnétiques et prédire les résultats

du guidage. Ceci est sans compter le système de positionnement des corps ferromagnétiques dans l'appareil d'IRM, qui devra permettre de placer et de maintenir ces derniers aux emplacements prévus par rapport au patient avec une précision suffisante (à déterminer). De plus, la validation périodique du ciblage, bien que possible en déplaçant le ou les corps ferromagnétiques à des positions spécifiques dans le tunnel de l'appareil, est probablement limitée pour des corps ferromagnétiques de grande taille en raison de la distance à laquelle ceux-ci devraient être éloignés du patient. En autant que le signal d'IRM puisse être acquis dans la région d'intérêt, une approche à explorer serait d'identifier la localisation de la cible dans les images distordues (voir Fig. 5.3), acquises avec les corps placés à leurs positions d'imagerie, par correspondance avec des images acquises sans corps ferromagnétiques. Il serait ainsi possible d'ensuite valider périodiquement le ciblage à l'aide d'images acquises avec les corps ferromagnétiques déplacés à ces mêmes positions.

Le positionnement statique des corps ferromagnétiques limite la résolution spatiale maximale atteignable pour le guidage à travers plusieurs bifurcations consécutives. Pour possiblement pallier cette limitation, une version dynamique de DFN pourrait être envisagée, dans laquelle un ou plusieurs corps ferromagnétiques seraient rapidement déplacés autour du patient afin d'ajuster les gradients en temps réel pendant le guidage d'un agrégat de micro-agents le long de la trajectoire vasculaire. Une approche hybride pourrait aussi être considérée, en combinant à la fois des corps statiques et dynamiques. Ces variantes entraînent toutefois un problème de synchronisation des gradients, similaire à MRN mais probablement sans imagerie possible, en fonction du transit des micro-agents le long de la trajectoire.

À l'instar de MRN, la méthode proposée permet le contrôle d'agents magnétiques selon trois degrés de liberté. La distorsion angulaire du champ autour des corps ferromagnétiques n'est en effet pas suffisante pour permettre d'orienter un agent dans des directions significativement différentes de celle du champ de l'appareil (voir Fig. 1.2b). Pour des corps ferromagnétiques fixés autour du patient, les gradients générés sont statiques, ce qui permet l'injection continue des TMMCs. Ainsi, contrairement à MRN, DFN n'est pas sujette aux difficultés liées à la synchronisation des gradients et l'administration d'une dose donnée de médicament est plus rapide. Le Tableau 9.1 résume les principaux avantages et inconvénients de DFN en comparaison avec la méthode MRN. En pratique, il est possible que MRN soit mieux adaptée que DFN dans certains cas et inversement. Il est aussi possible qu'une combinaison des deux soit employée.

Tableau 9.1 Avantage et inconvénients de la méthode proposée, DFN, en comparaison avec la méthode MRN.

Avantages	**Inconvénients**
Champ magnétique aussi fort que MRN (typ. 1.5-3 T) assurant la saturation des agents	Erreur angulaire sur les gradients générés (compromis, limite de résolution)
Gradients forts (~10 fois plus élevés dans les tissus profonds)	Guidage principalement à l'aveugle (boucle ouverte), en assumant l'exactitude des modèles
Injection continue des agents (pas de problème de synchronisation)	Complexité accrue (insertion et positionnement des corps ferromagnétiques)

CHAPITRE 10 CONCLUSION ET RECOMMANDATIONS

En permettant d'acheminer des agents thérapeutiques directement vers une région ciblée, le guidage magnétique de microtransporteurs thérapeutiques magnétiques promet d'augmenter significativement l'efficacité des traitements contre le cancer tout en réduisant leurs effets secondaires. Non seulement cette technologie a le potentiel d'améliorer les chances de survie des patients, mais elle pourrait aussi entraîner une diminution des coûts de santé en réduisant le nombre de traitements requis et les durées d'hospitalisation.

Dans cette thèse, le guidage par champs de dipôles, ou *Dipole Field Navigation*, a été proposé pour pallier certaines limitations des méthodes existantes. La méthode proposée a l'avantage de bénéficier à la fois d'un champ magnétique fort et de gradients magnétiques élevés dans les tissus profonds à l'échelle humaine, permettant ainsi de maximiser les forces de guidages qui peuvent être induites sur les agents navigués. Ceci est possible au prix des modèles mathématiques et algorithmes complexes qui sont requis pour paramétrer adéquatement les dispositions de corps ferromagnétiques dans l'appareil d'IRM en fonction d'une trajectoire vasculaire désirée.

Les résultats de recherche obtenus jusqu'à présent pour DFN sont prometteurs et motivent la poursuite des travaux, notamment pour la validation in vivo de la méthode. Selon le modèle animal utilisé, il est possible que des corps ferromagnétiques relativement gros soient requis. L'insertion manuelle de ceux-ci n'est alors fortement pas recommandée [1] !

Une prochaine étape majeure du projet consiste donc à concevoir et fabriquer le système d'insertion (robot ou autre) et de positionnement des corps ferromagnétiques à l'intérieur de l'appareil d'IRM. En plus des aspects de sécurité reliés aux forces d'insertion et d'interactions magnétiques, ce système doit permettre de placer les corps ferromagnétiques le plus près possible de la peau du patient. Afin d'en tenir compte dans la conception de ce système, il serait avisé d'étudier plus en profondeur la sensibilité des gradients générés aux erreurs de positionnement des corps ferromagnétiques. La précision requise attendue est actuellement de l'ordre de quelques millimètres pour les trajectoires multi-bifurcations. Pour des raisons de sécurité, il serait préférable que tous les corps ferromagnétiques soient insérés avant le patient dans l'appareil. Un mécanisme permettant de surélever ou de rabattre les corps

1. Par expérience, l'insertion manuelle de corps ferromagnétiques équivalents à une sphère ayant jusqu'à environ 2.5 cm de diamètre est relativement sécuritaire. À titre informatif, le corps ferromagnétique le plus volumineux inséré à la main dans le cadre de ce projet est une sphère en acier chromé ($M_{sat} \approx 1.4 \times 10^6$ A/m) de 5 cm de diamètre (appareil d'IRM 1.5 T).

ferromagnétiques temporairement contre les parois du tunnel est donc sans doute nécessaire afin d'y laisser entrer le patient, avant d'ensuite rapprocher ceux-ci de la peau à leurs positions prédéterminées. Par ailleurs, pour tenir compte de la position réelle du patient dans l'appareil, qui pourrait être déterminée par un recalage intra-opératoire avec les modèles, mais aussi pour corriger des erreurs de guidage éventuelles, le système de positionnement devrait permettre d'ajuster légèrement, au besoin, la position de chaque corps ferromagnétique une fois ceux-ci placés autour du patient.

Avec la méthode proposée, les erreurs angulaires sur les gradients générés sont pratiquement inévitables dans le cas général pour obtenir des gradients suffisamment forts. La détermination des meilleurs compromis entre l'amplitude et la précision des gradients, via la modélisation du guidage en fonction des différents paramètres de l'environnement vasculaire et des agents navigués, devrait être étudiée. Mieux encore, l'efficacité du guidage dépend en réalité des effets cumulés des gradients générés sur l'ensemble de la trajectoire vasculaire. Parce que les amplitudes et orientations des gradients varient dans l'espace le long d'un segment de trajectoire, il n'est pas nécessairement suffisant d'observer les gradients à des points précis. Le positionnement des corps ferromagnétiques devrait donc idéalement tenir compte de l'effet global des différentes forces agissant sur les micro-agents. Par le fait même, la direction optimale des gradients précédant une bifurcation n'est pas nécessairement perpendiculaire au flot, alors que les gradients devraient être beaucoup plus forts aux premières bifurcations en raison des débits sanguins plus élevés. Une telle modélisation, plus fidèle à la réalité, devrait être intégrée au processus de paramétrage des corps ferromagnétiques.

Plusieurs aspects restent à être étudiés et intégrés afin d'obtenir un protocole d'intervention applicable pour DFN dans un environnement clinique. Des modèles préopératoires du réseau vasculaire ciblé ainsi que de la surface du patient doivent être obtenus avec une précision adéquate, suivis de la planification du positionnement (et autres paramètres) des corps ferromagnétiques. Un recalage intra-opératoire avec ces modèles est ensuite probablement nécessaire une fois le patient entré dans l'appareil d'IRM, afin d'ajuster les positions finales des corps ferromagnétiques par rapport au patient. Des tests d'ajustement du guidage pourraient être réalisés avant l'injection des agents thérapeutiques, en injectant d'abord des « scouts » inoffensifs et en vérifiant que ceux-ci soient bien dirigés vers la cible. Pour assurer une efficacité maximale, les mouvements involontaires ou de respiration du patient devront probablement aussi être pris en compte.

RÉFÉRENCES

[1] Comité consultatif de la Société canadienne du cancer, “Statistiques canadiennes sur le cancer 2014”, Société canadienne du cancer, Toronto (Ontario), 2014.

[2] J. Ferlay, I. Soerjomataram, M. Ervik, R. Dikshit, S. Eser, C. Mathers, M. Rebelo, D. Parkin, D. Forman, et F. Bray, “GLOBOCAN 2012 v1.0, Cancer Incidence and Mortality Worldwide : IARC CancerBase No. 11 [Internet]”, Lyon, France : International Agency for Research on Cancer, 2013. En ligne : `http://globocan.iarc.fr`

[3] V. P. Torchilin, “Passive and Active Drug Targeting : Drug Delivery to Tumors as an Example”, dans *Handb. Exp. Pharmacol.*, M. Schäfer-Korting, éd. Springer, 2010, vol. 197, pp. 3–53.

[4] Cancer Network, “Chemotherapeutic Agents and Their Uses, Dosages, and Toxicities [Internet]”, 2014. En ligne : `http://www.cancernetwork.com/cancer-management/chemotherapeutic-agents-and-their-uses-dosages-and-toxicities`

[5] T. Xu, J. Yu, X. Yan, H. Choi, et L. Zhang, “Magnetic Actuation Based Motion Control for Microrobots : An Overview”, *Micromachines*, vol. 6, no. 9, pp. 1346–1364, 2015.

[6] B. Shapiro, S. Kulkarni, A. Nacev, S. Muro, P. Y. Stepanov, et I. N. Weinberg, “Open challenges in magnetic drug targeting”, *Wiley Interdiscip. Rev. Nanomedicine Nanobiotechnology*, vol. 7, no. 3, pp. 446–457, 2015.

[7] M. Arruebo, R. Fernández-pacheco, M. R. Ibarra, et J. Santamaría, “Magnetic nanoparticles for drug delivery”, *Nano Today*, vol. 2, no. 3, pp. 22–32, 2007.

[8] J. Estelrich, E. Escribano, J. Queralt, et M. A. Busquets, “Iron oxide nanoparticles for magnetically-guided and magnetically-responsive drug delivery”, *Int. J. Mol. Sci.*, vol. 16, no. 4, pp. 8070–8101, 2015.

[9] G. Liu, J. Gao, H. Ai, et X. Chen, “Applications and potential toxicity of magnetic iron oxide nanoparticles”, *Small*, vol. 9, no. 9-10, pp. 1533–1545, 2013. DOI : `10.1002/smll.201201531`. En ligne : `http://www.ncbi.nlm.nih.gov/pubmed/23019129`

[10] A. J. Cole, V. C. Yang, et A. E. David, “Cancer theranostics : The rise of targeted magnetic nanoparticles”, *Trends Biotechnol.*, vol. 29, no. 7, pp. 323–332, 2011. DOI :

10.1016/j.tibtech.2011.03.001

[11] Wahajuddin et S. Arora, "Superparamagnetic iron oxide nanoparticles : Magnetic nanoplatforms as drug carriers", *Int. J. Nanomedicine*, vol. 7, pp. 3445–3471, 2012. DOI : 10.2147/IJN.S30320

[12] P. A. Voltairas, D. I. Fotiadis, et L. K. Michalis, "Hydrodynamics of magnetic drug targeting", *J. Biomech.*, vol. 35, no. 6, pp. 813–821, 2002.

[13] P. Pouponneau, G. Bringout, et S. Martel, "Therapeutic Magnetic Microcarriers Guided by Magnetic Resonance Navigation for Enhanced Liver Chemoembilization : A Design Review", *Ann. Biomed. Eng.*, vol. 42, no. 5, pp. 929–939, 2014. DOI : 10.1007/s10439-014-0972-1

[14] L. Mellal, K. Belharet, D. Folio, et A. Ferreira, "Optimal structure of particles-based superparamagnetic microrobots : application to MRI guided targeted drug therapy", *J. Nanoparticle Res.*, vol. 17, no. 2, 2015. DOI : 10.1007/s11051-014-2733-3

[15] J. B. Mathieu et S. Martel, "Steering of aggregating magnetic microparticles using propulsion gradients coils in an MRI scanner", *Magn. Reson. Med.*, vol. 63, no. 5, pp. 1336–1345, 2010. DOI : 10.1002/mrm.22279

[16] P. Pouponneau, J. C. Leroux, G. Soulez, L. Gaboury, et S. Martel, "Co-encapsulation of magnetic nanoparticles and doxorubicin into biodegradable microcarriers for deep tissue targeting by vascular MRI navigation", *Biomaterials*, vol. 32, no. 13, pp. 3481–3486, 2011. DOI : 10.1016/j.biomaterials.2010.12.059

[17] S. H. Kim et K. Ishiyama, "Magnetic robot and manipulation for active-locomotion with targeted drug release", *IEEE/ASME Trans. Mechatronics*, vol. 19, no. 5, pp. 1651–1659, 2014. DOI : 10.1109/TMECH.2013.2292595

[18] V. Iacovacci, G. Lucarini, L. Ricotti, P. Dario, P. E. Dupont, et A. Menciassi, "Untethered magnetic millirobot for targeted drug delivery", *Biomed. Microdevices*, vol. 17, no. 3, p. 63, 2015. DOI : 10.1007/s10544-015-9962-9

[19] T. Y. Huang, M. S. Sakar, A. Mao, A. J. Petruska, F. Qiu, X. B. Chen, S. Kennedy, D. Mooney, et B. J. Nelson, "3D Printed Microtransporters : Compound Micromachines for Spatiotemporally Controlled Delivery of Therapeutic Agents", *Adv. Mater.*, vol. 27, no. 42, pp. 6644–6650, 2015. DOI : 10.1002/adma.201503095

[20] L. Zhang, J. J. Abbott, L. Dong, K. E. Peyer, B. E. Kratochvil, H. Zhang, C. Bergeles, et B. J. Nelson, "Characterizing the swimming properties of artificial bacterial flagella", *Nano Lett.*, vol. 9, no. 10, pp. 3663–3667, 2009. DOI : 10.1021/nl901869j

[21] F. Qiu et B. J. Nelson, "Magnetic Helical Micro- and Nanorobots : Toward Their Biomedical Applications", *Engineering*, vol. 1, no. 1, pp. 21–26, 2015. DOI : 10.15302/J-ENG-2015005

[22] H. Li, S. Member, J. Tan, M. Zhang, et S. Member, "Dynamics Modeling and Analysis of a Swimming Microrobot for Controlled Drug Delivery", *IEEE Trans. Autom. Sci. Eng.*, vol. 6, no. 2, pp. 220–227, 2009. DOI : 10.1109/TASE.2008.917137

[23] R. Dreyfus, J. Baudry, M. L. Roper, M. Fermigier, H. A. Stone, et J. Bibette, "Microscopic artificial swimmers", *Nature*, vol. 437, no. 7060, pp. 862–865, 2005. DOI : 10.1038/nature04090

[24] I. S. M. Khalil, H. C. Dijkslag, L. Abelmann, et S. Misra, "MagnetoSperm : A microrobot that navigates using weak magnetic fields", *Appl. Phys. Lett.*, vol. 104, no. 22, 2014. DOI : 10.1063/1.4880035

[25] H.-W. Huang, M. S. Sakar, A. J. Petruska, S. Pane, et B. J. Nelson, "Soft micromachines with programmable motility and morphology", *Nat Commun*, vol. 7, p. 12263, 2016. DOI : 10.1038/ncomms12263

[26] D. de Lanauze, O. Felfoul, J.-P. Turcot, M. Mohammadi, et S. Martel, "Three-dimensional remote aggregation and steering of magnetotactic bacteria microrobots for drug delivery applications", *Int. J. Rob. Res.*, vol. 33, no. 3, pp. 359–374, 2014. DOI : 10.1177/0278364913500543

[27] I. S. M. Khalil, M. P. Pichel, L. Abelmann, et S. Misra, "Closed-loop control of magnetotactic bacteria", *Int. J. Rob. Res.*, vol. 32, no. 6, pp. 637–649, 2013. DOI : 10.1177/0278364913479412

[28] D. Loghin, C. Tremblay, et S. Martel, "Improved three-dimensional remote aggregations of magnetotactic bacteria for tumor targeting", *2016 Int. Conf. Manip. Autom. Robot. Small Scales, MARSS 2016*, 2016. DOI : 10.1109/MARSS.2016.7561739

[29] O. Felfoul, M. Mohammadi, S. Taherkhani, D. de Lanauze, Y. Zhong Xu, D. Loghin, S. Essa, S. Jancik, D. Houle, M. Lafleur, L. Gaboury, M. Tabrizian, N. Kaou, M. Atkin,

T. Vuong, G. Batist, N. Beauchemin, D. Radzioch, et S. Martel, "Magneto-aerotactic bacteria deliver drug-containing nanoliposomes to tumour hypoxic regions." *Nat. Nanotechnol.*, no. August, pp. 1–5, 2016. DOI : 10.1038/nnano.2016.137

[30] M. W. Freeman, A. Arrott, et J. H. L. Watson, "Magnetism in Medicine", *J. Appl. Phys.*, vol. 31, no. 5, pp. 404S–405S, 1960. DOI : 10.1063/1.1984765

[31] A. Senyei, K. Widder, et G. Czerlinski, "Magnetic guidance of drug-carrying microspheres", *J. Appl. Phys.*, vol. 49, no. 6, p. 3578, 1978. DOI : 10.1063/1.325219

[32] K. J. Widder, A. E. Senyel, G. D. Scarpelli, A. E. Senyei, et D. G. Scarpelli, "Magnetic microspheres : a model system of site specific drug delivery in vivo", *Proc. Soc. Exp. Biol. Med.*, vol. 158, no. 2, pp. 141–146, 1978. DOI : 10.3181/00379727-158-40158

[33] K. Mosbach et U. Schroder, "Preparation and application of magnetic polymers for targeting of drugs", *FEBS Lett.*, vol. 102, no. 1, pp. 112–116, 1979.

[34] Y. Morimoto, K. Sugibayashi, M. Okumura, et Y. Kato, "Biomedical applications of magnetic fluids. i. Magnetic guidance of ferro-colloid-entrapped albumin microsphere for site specific drug delivery in vivo", *J. Pharmacobiodyn.*, vol. 3, pp. 264–267, 1980. DOI : 10.1248/bpb1978.3.264

[35] K. J. Widder, R. M. Morrist, G. Pooret, D. P. Howard, et A. E. Senyeit, "Tumor remission in Yoshida sarcoma-bearing rats by selective targeting of magnetic albumin microspheres containing doxorubicin", dans *Proc. Natl. Acad. Sci. U. S. A.*, vol. 78, no. 1, 1981, pp. 579–581.

[36] D. J. A. Crommelina, G. Scherphofb, et G. Storma, "Active targeting with particulate carrier systems in the blood compartment", *Adv. Drug Deliv. Rev.*, vol. 17, no. 1, pp. 49–60, 1995.

[37] A. S. Lübbe, C. Bergemann, H. Riess, A. S. Lãbbe, F. Schriever, P. Reichardt, K. Possinger, M. Matthias, B. Dã, F. Herrinann, R. Gurtler, P. Hohenberger, N. Haas, R. Sohr, B. Sander, A.-J. J. Lemke, D. Ohlendorf, W. Huhnt, D. Huhn, B. Dörken, F. Herrmann, R. Gürtler, P. Hohenberger, N. Haas, R. Sohr, B. Sander, A.-J. J. Lemke, D. Ohlendorf, W. Huhnt, D. Huhn, A. S. Lãbbe, F. Schriever, P. Reichardt, K. Possinger, M. Matthias, B. Dã, F. Herrinann, R. Gurtler, P. Hohenberger, N. Haas, R. Sohr, B. Sander, A.-J. J. Lemke, D. Ohlendorf, W. Huhnt, D. Huhn, B. Dörken, F. Herrmann, R. Gürtler, P. Ho-

henberger, N. Haas, R. Sohr, B. Sander, A.-J. J. Lemke, D. Ohlendorf, W. Huhnt, et D. Huhn, "Clinical Experiences with Magnetic Drug Targeting : A Phase I Study with 4'-Epidoxorubicin in 14 Patients with Advanced Solid Tumors", *Cancer Res.*, vol. 56, no. 20, pp. 4686–4693, 1996.

[38] J. Johnson, T. Kent, J. Koda, C. Peterson, S. Rudge, et G. Tapolsky, "The MTC technology : A platform technology for the site-specific delivery of pharmaceutical agents", *Eur. Cells Mater.*, vol. 3, no. SUPPL. 2, pp. 12–15, 2002.

[39] S. Goodwin, C. Peterson, C. Hoh, et C. Bittner, "Targeting and retention of magnetic targeted carriers (MTCs) enhancing intra-arterial chemotherapy", *J. Magn. Magn. Mater.*, vol. 194, no. 1-3, pp. 132–139, apr 1999. DOI : 10.1016/S0304-8853(98)00584-8

[40] A. Amirfazli et R. Virginia, "Magnetic nanoparticles hit the target", *Nat. Nanotechnol.*, vol. 2, no. August, pp. 467–468, 2007. DOI : 10.1038/nnano.2007.234

[41] A. Al Faraj, A. S. Shaik, A. P. Shaik, et B. Al Sayed, "Enhanced magnetic delivery of superparamagnetic iron oxide nanoparticles to the lung monitored using noninvasive MR", *J. Nanoparticle Res.*, vol. 16, no. 10, 2014. DOI : 10.1007/s11051-014-2667-9

[42] U. O. Häfeli, K. Gilmour, A. Zhou, S. Lee, et M. E. Hayden, "Modeling of magnetic bandages for drug targeting : Button vs. Halbach arrays", *J. Magn. Magn. Mater.*, vol. 311, no. 1 SPEC. ISS., 2007.

[43] B. Shapiro, K. Dormer, et I. B. Rutel, "A two-magnet system to push therapeutic nanoparticles", dans *AIP Conf. Proc.*, vol. 1311, no. 1, 2010, pp. 77–88. DOI : 10.1063/1.3530064

[44] M. Gao, C. Hu, Z. Chen, H. Zhang, et S. Liu, "Design and fabrication of a magnetic propulsion system for self-propelled capsule endoscope", *IEEE Trans. Biomed. Eng.*, vol. 57, no. 12, pp. 2891–2902, 2010. DOI : 10.1109/TBME.2010.2051947

[45] S. Tognarelli, V. Castelli, G. Ciuti, C. Natali, E. Sinibaldi, P. Dario, et A. Menciassi, "Magnetic propulsion and ultrasound tracking of endovascular devices", *J. Robot. Surg.*, vol. 6, no. 1, pp. 5–12, 2011.

[46] F. Carpi, N. Kastelein, M. Talcott, et C. Pappone, "Magnetically controllable gastrointestinal steering of video capsules", *IEEE Trans. Biomed. Eng.*, vol. 58, no. 2, pp. 231–234, 2011. DOI : 10.1109/TBME.2010.2087332

[47] A. W. Mahoney et J. J. Abbott, “Five-degree-of-freedom manipulation of an untethered magnetic device in fluid using a single permanent magnet with application in stomach capsule endoscopy”, *Int. J. Rob. Res.*, vol. 35, no. 1-3, pp. 129–147, 2015.

[48] L. B. Kratchman, T. L. Bruns, J. J. Abbott, et R. J. W. III, “Guiding Elastic Rods With a Robot-Manipulated Magnet for Medical Applications”, *IEEE Trans. Robot.*, vol. 33, no. 1, pp. 227–233, 2016. DOI : 10.1109/TRO.2016.2623339

[49] A. Hosney, A. Klingner, S. Misra, et I. S. M. Khalil, “Propulsion and steering of helical magnetic microrobots using two synchronized rotating dipole fields in three-dimensional space”, *IEEE Int. Conf. Intell. Robot. Syst.*, vol. 2015-Decem, pp. 1988–1993, 2015. DOI : 10.1109/IROS.2015.7353639

[50] “Stereotaxis”. En ligne : http://www.stereotaxis.com

[51] C. Tremblay, B. Conan, D. Loghin, A. Bigot, et S. Martel, “Fringe Field Navigation for Catheterization”, dans *6th Eur. Conf. Int. Fed. Med. Biol. Eng.*, 2014, pp. 379–382.

[52] S. Nishijima, S.-i. Takeda, F. Mishima, Y. Tabata, M. Yamamoto, J.-i. Joh, H. Iseki, Y. Muragaki, A. Sasaki, K. Jun, et N. Saho, “A study of magnetic drug delivery system using bulk high temperature superconducting magnet”, *IEEE Trans. Appl. Supercond.*, vol. 18, no. 2, pp. 874–877, 2008. DOI : 10.1109/TASC.2008.921967

[53] M. Tomita et M. Murakami, “High-temperature superconductor bulk magnets that can trap magnetic fields of over 17 tesla at 29 K.” *Nature*, vol. 421, no. 6922, pp. 517–520, 2003. DOI : 10.1038/nature01350

[54] J. H. Durrell, A. R. Dennis, J. Jaroszynski, M. D. Ainslie, K. G. B. Palmer, Y.-H. Shi, A. M. Campbell, J. Hull, M. Strasik, E. E. Hellstrom, et D. A. Cardwell, “A trapped field of 17.6 T in melt-processed, bulk Gd-Ba-Cu-O reinforced with shrink-fit steel”, *Supercond. Sci. Technol.*, vol. 27, no. 8, p. 082001, 2014. DOI : 10.1088/0953-2048/27/8/082001

[55] A. J. Petruska et B. J. Nelson, “Minimum Bounds on the Number of Electromagnets Required for Remote Magnetic Manipulation”, *IEEE Trans. Robot.*, vol. 31, no. 3, pp. 714–722, 2015. DOI : 10.1109/TRO.2015.2424051

[56] P. Berkelman et M. Dzadovsky, “Magnetic levitation over large translation and rotation ranges in all directions”, *IEEE/ASME Trans. Mechatronics*, vol. 18, no. 1, pp. 44–52, 2013. DOI : 10.1109/TMECH.2011.2161614

[57] E. Diller, J. Giltinan, G. Z. Lum, Z. Ye, et M. Sitti, "Six-degree-of-freedom magnetic actuation for wireless microrobotics", *Int. J. Rob. Res.*, vol. 35, no. 1-3, pp. 114–128, 2016. DOI : 10.1177/0278364915583539

[58] M. P. Kummer, J. J. Abbott, B. E. Kratochvil, R. Borer, A. Sengul, et B. J. Nelson, "Octomag : An electromagnetic system for 5-DOF wireless micromanipulation", *IEEE Trans. Robot.*, vol. 26, no. 6, pp. 1006–1017, 2010. DOI : 10.1109/TRO.2010.2073030

[59] F. Ullrich, C. Bergeles, J. Pokki, O. Ergeneman, S. Erni, G. Chatzipirpiridis, S. Pané, C. Framme, et B. J. Nelson, "Mobility experiments with microrobots for minimally invasive intraocular surgery", *Investig. Ophthalmol. Vis. Sci.*, vol. 54, no. 4, pp. 2853–2863, 2013.

[60] S. Schuerle, S. Erni, M. Flink, B. E. Kratochvil, et B. J. Nelson, "Three-Dimensional Magnetic Manipulation of Micro- and Nanostructures for Applications in Life Sciences", *IEEE Trans. Magn.*, vol. 49, no. 1, pp. 321–330, 2013.

[61] H. Keller, A. Juloski, H. Kawano, M. Bechtold, A. Kimura, H. Takizawa, et R. Kuth, "Method for navigation and control of a magnetically guided capsule endoscope in the human stomach", dans *Proc. IEEE RAS EMBS Int. Conf. Biomed. Robot. Biomechatronics*, 2012, pp. 859–865.

[62] B. Veron, A. Hubert, J. Abadie, et N. Andreff, "Geometric analysis of the singularities of a magnetic manipulation system with several mobile coils", dans *IEEE Int. Conf. Intell. Robot. Syst.*, 2013, pp. 4996–5001. DOI : 10.1109/IROS.2013.6697078

[63] V. H. Le, H. L. Rodriguez, C. Lee, G. Go, J. Zhen, V. D. Nguyen, H. Choi, S. Y. Ko, J. O. Park, et S. Park, "A soft-magnet-based drug-delivery module for active locomotive intestinal capsule endoscopy using an electromagnetic actuation system", *Sensors Actuators, A Phys.*, vol. 243, pp. 81–89, 2016. DOI : 10.1016/j.sna.2016.03.020

[64] H. Choi, K. Cha, J. Choi, S. Jeong, S. Jeon, G. Jang, J.-o. Park, et S. Park, "EMA system with gradient and uniform saddle coils for 3D locomotion of microrobot", *Sensors Actuators A Phys.*, vol. 163, no. 1, pp. 410–417, 2010. DOI : 10.1016/j.sna.2010.08.014

[65] S. Jeong, H. Choi, K. Cha, J. Li, J. O. Park, et S. Park, "Enhanced locomotive and drilling microrobot using precessional and gradient magnetic field", *Sensors Actuators, A Phys.*, vol. 171, no. 2, pp. 429–435, 2011. DOI : 10.1016/j.sna.2011.08.020

[66] K. Belharet, D. Folio, et A. Ferreira, “Control of a magnetic microrobot navigating in microfluidic arterial bifurcations through pulsatile and viscous flow”, *2012 IEEE/RSJ Int. Conf. Intell. Robot. Syst.*, vol. 1, pp. 2559–2564, oct 2012. DOI : 10.1109/IROS.2012.6386030

[67] G. Go, H. Choi, S. Jeong, C. Lee, S. Y. Ko, J.-o. Park, et S. Park, “Electromagnetic Navigation System Using Simple Coil Structure (4 Coils) for 3-D Locomotive Microrobot”, *IEEE Trans. Magn.*, vol. 51, no. 4, pp. 1–7, 2015.

[68] S. Jeong, H. Choi, G. Go, C. Lee, K. S. Lim, D. S. Sim, M. H. Jeong, S. Y. Ko, J. O. Park, et S. Park, “Penetration of an artificial arterial thromboembolism in a live animal using an intravascular therapeutic microrobot system”, *Med. Eng. Phys.*, vol. 38, no. 4, pp. 403–410, 2016. DOI : 10.1016/j.medengphy.2016.01.001

[69] “Aeon Scientific”. En ligne : www.aeon-scientific.com

[70] “Magnetecs”. En ligne : http://www.magnetecs.com

[71] A. J. Petruska, A. W. Mahoney, et J. J. Abbott, “Remote manipulation with a stationary computer-controlled magnetic dipole source”, *IEEE Trans. Robot.*, vol. 30, no. 5, pp. 1222–1227, 2014. DOI : 10.1109/TRO.2014.2340111

[72] A. J. Petruska, J. B. Brink, et J. J. Abbott, “First demonstration of a modular and reconfigurable magnetic-manipulation system”, dans *Proc. - IEEE Int. Conf. Robot. Autom.*, vol. 2015-June, no. June, 2015, pp. 149–155. DOI : 10.1109/ICRA.2015.7138993

[73] X. Zhang, T.-A. Le, et J. Yoon, “Development of a real time imaging-based guidance system of magnetic nanoparticles for targeted drug delivery”, *J. Magn. Magn. Mater.*, vol. 427, no. October, pp. 345–351, 2017. DOI : 10.1016/j.jmmm.2016.10.056

[74] S. Martel, “Advantages and Limitations of the Various Magnetic Manipulation Methods of Untethered Agents in the Human Body”, dans *IEEE/ASME Int. Conf. Adv. Intell. Mechatronics*, no. 1, 2014. DOI : 10.1109/AIM.2014.6878039

[75] S. Martel, J.-B. Mathieu, O. Felfoul, A. Chanu, E. Aboussouan, S. Tamaz, P. Pouponneau, L. Yahia, G. Beaudoin, G. Soulez, et M. Mankiewicz, “Automatic navigation of an untethered device in the artery of a living animal using a conventional clinical magnetic resonance imaging system”, *Appl. Phys. Lett.*, vol. 90, no. 11, p. 114105, 2007.

[76] A. Bigot, C. Tremblay, G. Soulez, et S. Martel, "Temperature Response of a Magnetic Resonance Imaging Coil Insert for the Navigation of Theranostic Agents in Complex Vascular Networks", *IEEE Trans. Magn.*, vol. 50, no. 8, pp. 1–7, 2014. DOI : 10.1109/TMAG.2014.2309944

[77] A. Chanu, O. Felfoul, G. Beaudoin, et S. Martel, "Adapting the clinical MRI software environment for real-time navigation of an endovascular untethered ferromagnetic bead for future endovascular interventions", *Magn. Reson. Med.*, vol. 59, pp. 1287–1297, 2008.

[78] K. Belharet, D. Folio, et A. Ferreira, "MRI-based microrobotic system for the propulsion and navigation of ferromagnetic microcapsules", *Minim. invasive Ther. allied Technol.*, vol. 19, pp. 157–169, 2010.

[79] P. Vartholomeos, C. Bergeles, L. Qin, et P. E. Dupont, "An MRI-powered and controlled actuator technology for tetherless robotic interventions", *Int. J. Rob. Res.*, vol. 32, no. 13, pp. 1536–1552, 2013. DOI : 10.1177/0278364913500362

[80] P. Pouponneau, G. Soulez, G. Beaudoin, J.-C. Leroux, et S. Martel, "MR imaging of therapeutic magnetic microcarriers guided by magnetic resonance navigation for targeted liver chemoembolization." *Cardiovasc. Intervent. Radiol.*, vol. 37, no. 3, pp. 784–90, 2014.

[81] "Siemens MRI systems". En ligne : http://usa.healthcare.siemens.com/magnetic-resonance-imaging

[82] "GE Healthcare MRI systems". En ligne : http://www3.gehealthcare.com/en/products/categories/magnetic_resonance_imaging

[83] "Philips MRI systems". En ligne : http://www.healthcare.philips.com/ca_en/products/mri/systems/

[84] J. A. McNab, B. L. Edlow, T. Witzel, S. Y. Huang, H. Bhat, K. Heberlein, T. Feiweier, K. Liu, B. Keil, J. Cohen-Adad, M. D. Tisdall, R. D. Folkerth, H. C. Kinney, et L. L. Wald, "The Human Connectome Project and beyond : Initial applications of 300mT/m gradients", *Neuroimage*, vol. 80, pp. 234–245, 2013.

[85] A. Bigot, C. Tremblay, G. Soulez, et S. Martel, "Magnetic resonance navigation of a bead inside a three-bifurcation PMMA phantom using an imaging gradient coil insert", *IEEE Trans. Robot.*, vol. 30, no. 3, pp. 719–727, 2014. DOI : 10.1109/TRO.2014.2300591

[86] M. Muthana, A. J. Kennerley, R. Hughes, J. Richardson, M. Paul, C. Murdoch, F. Wright, M. Lythgoe, N. Farrow, J. Dobson, J. M. Wild, et C. Lewis, "Directing cell therapy to anatomic target sites in vivo with magnetic resonance targeting", *Nat. Commun.*, vol. 6, p. 8009, 2015.

[87] J. Paul, V. Jacobi, M. Farhang, B. Bazrafshan, T. J. Vogl, et E. C. Mbalisike, "Radiation dose and image quality of X-ray volume imaging systems : Cone-beam computed tomography, digital subtraction angiography and digital fluoroscopy", *Eur. Radiol.*, vol. 23, no. 6, pp. 1582–1593, 2013. DOI : 10.1007/s00330-012-2737-2

[88] T. Sugahara, Y. Korogi, K. Nakashima, S. Hamatake, S. Honda, et M. Takahashi, "Comparison of 2D and 3D digital subtraction angiography in evaluation of intracranial aneurysms", *AJNR. Am. J. Neuroradiol.*, vol. 23, no. 9, pp. 1545–52, 2002.

[89] N. Olamaei, F. Cheriet, S. Deschênes, A. Sharafi, et S. Martel, "Three-dimensional reconstruction of a vascular network by dynamic tracking of magnetite nanoparticles", *Med. Phys.*, vol. 42, no. 10, pp. 5702–5710, 2015.

[90] O. Felfoul, J. B. Mathieu, G. Beaudoin, et S. Martel, "In vivo MR-tracking based on magnetic signature selective excitation", *IEEE Trans. Med. Imaging*, vol. 27, no. 1, pp. 28–35, 2008. DOI : 10.1109/TMI.2007.897375

[91] S. Martel, "Magnetic Navigation Control of Microagents in the Vascular Network", *IEEE Control Syst.*, vol. 33, no. 6, pp. 119–134, 2013.

[92] O. Felfoul, A. T. Becker, G. Fagogenis, et P. E. Dupont, "Simultaneous steering and imaging of magnetic particles using MRI toward delivery of therapeutics", *Sci. Rep.*, vol. 6, no. August, p. 33567, 2016.

[93] N. Panagiotopoulos, R. L. Duschka, M. Ahlborg, G. Bringout, C. Debbeler, M. Graeser, C. Kaethner, K. L ? ?dtke-Buzug, H. Medimagh, J. Stelzner, T. M. Buzug, J. Barkhausen, F. M. Vogt, et J. Haegele, "Magnetic particle imaging : Current developments and future directions", *Int. J. Nanomedicine*, vol. 10, pp. 3097–3114, 2015. DOI : 10.2147/IJN.S70488

[94] M. Latulippe et S. Martel, "Dipole Field Navigation : Theory and Proof of Concept", *IEEE Trans. Robot.*, vol. 31, no. 6, pp. 1353–1363, 2015.

[95] M. Latulippe et S. Martel, “Dipole Field Navigation for Targeted Drug Delivery”, dans *IEEE Int. Conf. Biomed. Robot. Biomechatronics*, 2014, pp. 320–325.

[96] M. Latulippe, O. Felfoul, P. E. Dupont, et S. Martel, “Enabling automated magnetic resonance imaging-based targeting assessment during dipole field navigation”, *Appl. Phys. Lett.*, vol. 108, no. 6, p. 062403, 2016. DOI : 10.1063/1.4941925

[97] M. Latulippe et S. Martel, “A Progressive Multidimensional Particle Swarm Optimizer for Magnetic Core Placement in Dipole Field Navigation”, dans *IEEE Int. Conf. Intell. Robot. Syst.*, 2016, pp. 2314–2320.

[98] M. Latulippe et S. Martel, “Seeking Optimal Magnetic Core Shapes for Strong Gradient Generation in Dipole Field Navigation”, dans *IEEE Int. Conf. Manip. Autom. Robot. Small Scales*, 2017.

[99] N. Bertrand, J. Wu, X. Xu, N. Kamaly, et O. C. Farokhzad, “Cancer nanotechnology : the impact of passive and active targeting in the era of modern cancer biology.” *Adv. Drug Deliv. Rev.*, vol. 66, pp. 2–25, 2014. DOI : 10.1016/j.addr.2013.11.009

[100] S. D. Steichen, M. Caldorera-Moore, et N. A. Peppas, “A review of current nanoparticle and targeting moieties for the delivery of cancer therapeutics”, *Eur. J. Pharm. Sci.*, vol. 48, no. 3, pp. 416–427, 2013. DOI : 10.1016/j.ejps.2012.12.006

[101] S. Martel, “Magnetic therapeutic delivery using navigable agents”, *J. Ther. Deliv.*, vol. 5, no. 2, pp. 189–204, 2014. DOI : 10.4155/tde.13.147

[102] C. Sun, J. S. H. Lee, et M. Zhang, “Magnetic nanoparticles in MR imaging and drug delivery”, *Adv. Drug Deliv. Rev.*, vol. 60, no. 11, pp. 1252–1265, 2008. DOI : 10.1016/j.addr.2008.03.018

[103] S. Jeong, H. Choi, J. Choi, C. Yu, J. oh Park, et S. Park, “Novel electromagnetic actuation (EMA) method for 3-dimensional locomotion of intravascular microrobot”, *Sensors Actuators, A Phys.*, vol. 157, no. 1, pp. 118–125, 2010. DOI : 10.1016/j.sna.2009.11.011

[104] M. D. Tehrani, M. O. Kim, et J. Yoon, “A Novel Electromagnetic Actuation System for Magnetic Nanoparticle Guidance in Blood Vessels”, *IEEE Trans. Magn.*, vol. 50, pp. 1–12, 2014. DOI : 10.1109/TMAG.2014.2307271

[105] J.-B. Mathieu, G. Beaudoin, et S. Martel, “Method of propulsion of a ferromagnetic

core in the cardiovascular system through magnetic gradients generated by an MRI system." *IEEE Trans. Biomed. Eng.*, vol. 53, no. 2, pp. 292–299, 2006.

[106] X. Luo et C. Foss, "Inverse of magnetic dipole field using a reversible jump Markov chain Monte Carlo", dans *20th Int. Congr. Model. Simul.*, 2013, pp. 134–140.

[107] M. A. Jatoi, N. Kamel, A. S. Malik, I. Faye, et T. Begum, "A survey of methods used for source localization using EEG signals", *Biomed. Signal Process. Control*, vol. 11, no. 1, pp. 42–52, 2014. DOI : 10.1016/j.bspc.2014.01.009

[108] N. C. Kapsalis, S.-D. J. Kakarakis, et C. N. Capsalis, "Prediction of Multiple Magnetic Dipole Model Parameters from Near Field Measurements Employing Stochastic Algorithms", *Prog. Electromagn. Res. Lett.*, vol. 34, pp. 111–122, 2012. DOI : 10.2528/PIERL12030905

[109] R. Castañer, J. M. Medina, et M. J. Cuesta-Bolao, "The magnetic dipole interaction as measured by spring dynamometers", *Am. J. Phys.*, vol. 74, no. 6, pp. 510–513, 2006. DOI : 10.1119/1.2180286

[110] Y. Kraftmakher, "Magnetic field of a dipole and the dipole-dipole interaction", *Eur. J. Phys.*, vol. 28, no. 3, pp. 409–414, may 2007. DOI : 10.1088/0143-0807/28/3/003

[111] A. Mehdizadeh, R. Mei, J. F. Klausner, et N. Rahmatian, "Interaction forces between soft magnetic particles in uniform and non-uniform magnetic fields", *Acta Mech. Sin.*, vol. 26, no. 6, pp. 921–929, 2010. DOI : 10.1007/s10409-010-0383-y

[112] J. C. Bezdek et R. J. Hathaway, "Convergence of alternating optimization", *Neural, Parallel Sci. Comput.*, vol. 11, no. 4, pp. 351–368, 2003.

[113] P. Vartholomeos, M. Fruchard, A. Ferreira, et C. Mavroidis, "MRI-Guided Nanorobotic Systems for Therapeutic and Diagnostic Applications", *Annu. Rev. Biomed. Eng.*, vol. 13, no. 1, pp. 157–184, 2011. DOI : 10.1146/annurev-bioeng-071910-124724

[114] A. Mahmood, M. Dadkhah, M. O. Kim, et J. Yoon, "A Novel Design of an MPI-Based Guidance System for Simultaneous Actuation and Monitoring of Magnetic Nanoparticles", *IEEE Trans. Magn.*, vol. 51, no. 2, pp. 1–5, 2015. DOI : 10.1109/TMAG.2014.2358252

[115] U. Vovk, F. Pernuš, et B. Likar, "A review of methods for correction of intensity

inhomogeneity in MRI", *IEEE Trans. Med. Imaging*, vol. 26, no. 3, pp. 405–421, 2007. DOI : 10.1109/TMI.2006.891486

[116] W. Lu, K. B. Pauly, G. E. Gold, J. M. Pauly, et B. A. Hargreaves, "SEMAC : Slice encoding for metal artifact correction in MRI", *Magn. Reson. Med.*, vol. 62, no. 1, pp. 66–76, 2009. DOI : 10.1002/mrm.21967

[117] M. Carl, K. Koch, et J. Du, "MR imaging near metal with undersampled 3D radial UTE-MAVRIC sequences", *Magn. Reson. Med.*, vol. 69, no. 1, pp. 27–36, 2013. DOI : 10.1002/mrm.24219

[118] M. S. Ugurel, B. Battal, U. Bozlar, M. S. Nural, M. Tasar, F. Ors, M. Saglam, et I. Karademir, "Anatomical variations of hepatic arterial system, coeliac trunk and renal arteries : an analysis with multidetector CT angiography." *Br. J. Radiol.*, vol. 83, no. 992, pp. 661–7, 2010. DOI : 10.1259/bjr/21236482

[119] J. Kennedy et R. Eberhart, "Particle swarm optimization", *IEEE Int. Conf. Neural Networks*, vol. 4, pp. 1942–1948 vol.4, 1995. DOI : 10.1109/ICNN.1995.488968

[120] Y. Shi et R. Eberhart, "A modified particle swarm optimizer", dans *Proc. IEEE Int. Conf. Evol. Comput.*, 1998, pp. 69–73. DOI : 10.1109/ICEC.1998.699146

[121] J. Kennedy et R. Mendes, "Population Structure and Particle Swarm Performance", dans *IEEE Congr. Evol. Comput.*, 2002, pp. 1671–1676. DOI : 10.1109/CEC.2002.1004493

[122] A. P. Engelbrecht, "Particle swarm optimization : Global best or local best ?" dans *BRICS Ctries. Congr. Comput. Intell.*, no. 1, 2013, pp. 124–135. DOI : 10.1109/BRICS-CCI-CBIC.2013.31

[123] M. R. Bonyadi et Z. Michalewicz, "A locally convergent rotationally invariant particle swarm optimization algorithm", *Swarm Intell.*, vol. 8, pp. 159–198, 2014. DOI : 10.1007/s11721-014-0095-1

[124] S. Spantideas, N. Kapsalis, S. D. Kakarakis, et C. Capsalis, "A Method of Predicting Composite Magnetic Sources Employing Particle Swarm Optimization", *Prog. Electromagn. Res. M*, vol. 39, pp. 161–170, 2014.

[125] K. E. Parsopoulos, F. Kariotou, G. Dassios, et M. N. Vrahatis, "Tackling magnetoencephalography with particle swarm optimization", *Int. J. Bio-Inspired Comput.*, vol. 1,

no. 1-2, pp. 32–49, 2009. DOI : 10.1504/IJBIC.2009.022772

[126] S. Kiranyaz, J. Pulkkinen, et M. Gabbouj, "Multi-dimensional particle swarm optimization in dynamic environments", *Expert Syst. Appl.*, vol. 38, no. 3, pp. 2212–2223, 2011. DOI : 10.1016/j.eswa.2010.08.009

[127] Y. Yan et L. A. Osadciw, "Density estimation using a new dimension adaptive particle swarm optimization algorithm", *Swarm Intell.*, vol. 3, no. 4, pp. 275–301, 2009. DOI : 10.1007/s11721-009-0032-x

[128] F. Van Den Bergh, "An analysis of particle swarm optimizers", Ph.D. Thesis, University of Pretoria, South Africa, 2002.

[129] M. Larimi, A. Ramiar, et A. Ranjbar, "Numerical simulation of magnetic nanoparticles targeting in a bifurcation vessel", *J. Magn. Magn. Mater.*, vol. 362, pp. 58–71, 2014.

[130] C. Worasucheep, "A Particle Swarm Optimization with stagnation detection and dispersion", dans *IEEE World Congr. Comput. Intell.*, 2008, pp. 424–429.

[131] B. Jiao, Z. Lian, et X. Gu, "A dynamic inertia weight particle swarm optimization algorithm", *Chaos, Solitons and Fractals*, vol. 37, no. 3, pp. 698–705, 2008. DOI : 10.1016/j.chaos.2006.09.063

[132] D. F. D. Carvalho et C. J. A. Bastos-Filho, "Clan particle swarm optimization", *Int. J. Intell. Comput. Cybern.*, vol. 2, no. 2, pp. 197–227, 2009. DOI : 10.1108/17563780910959875

[133] B. L. Nguyen, J. L. Merino, et E. S. Gang, "Remote navigation for ablation procedures - a new step forward in the treatment of cardiac arrhythmias", *Eur. Cardiol.*, vol. 6, no. 3, pp. 50–56, 2010.

[134] A. D. Grief et G. Richardson, "Mathematical modelling of magnetically targeted drug delivery", *J. Magn. Magn. Mater.*, vol. 293, pp. 455–463, 2005. DOI : 10.1016/j.jmmm.2005.02.040

[135] K. Gitter et S. Odenbach, "Investigations on a Branched Tube Model in Magnetic Drug Targeting—Systematic Measurements and Simulation", *IEEE Trans. Magn.*, vol. 49, no. 1, pp. 343–348, 2013.

[136] P. Plötner, K. Harada, N. Sugita, et M. Mitsuishi, “Theoretical analysis of magnetically propelled microrobots in the cardiovascular system”, dans *Conf. Proc. ... Annu. Int. Conf. IEEE Eng. Med. Biol. Soc. IEEE Eng. Med. Biol. Soc. Annu. Conf.*, vol. 2014, no. 1, 2014, pp. 870–873. DOI : 10.1109/EMBC.2014.6943729

[137] D. Jiles, “Recent advances and future directions in magnetic materials”, *Acta Mater.*, vol. 51, no. 19, pp. 5907–5939, nov 2003. DOI : 10.1016/j.actamat.2003.08.011